Structure and Reactivity in Self-Organised Ionic Liquids

Christopher Patrick Cabry

PhD

University of York

Chemistry

September 2017

Abstract

The research presented within this thesis aimed to contribute to the understanding of the structure of, and reactivity in, self-organised ionic liquids (ILs). This thesis comprises of three studies.

The first relates to the local, short-range ordering in both pure and binary mixtures of 1-alkyl-3-methylimidazolium bis(trifluoromethylsulfonyl)imides ($[C_nC_1im][Tf_2N]$). Following the synthesis of selectively deuterated materials, in order to provide the necessary contrast, small-angle neutron scattering data were collected and fit to a range of scattering models. It was found that pure ILs with short alkyl chain lengths (n = 2, 4, 6) have no alkyl chain ordering, while longer alkyl chained ILs (n = 8, 10, 12) displayed bicontinuous (percolated) structures, where one network consists of alkyl chains and the other of imidazolium head groups and $[Tf_2N]^-$ anions. The bilayer separations were related directly to chain length. Neutron data were also collected for two series of binary IL mixtures, namely $[C_2C_1im]_{x-1}[C_nC_1im]_x[Tf_2N]$ and $[C_mC_1im]_{x-1}[C_{12}C_1im]_x[Tf_2N]$ (n = 2, 4, 6, 8, 10, 12, m = 2, 4, 6, 8). Analysis of the data revealed that several fitting models could be used and the most appropriate often depends on the composition of the mixture. The mixtures can be described as either having no alkyl chain structure, consisting of small alkyl chain aggregates, or as a bicontinuous network, depending upon the mixture, mole fraction, and alkyl chain length.

The second study reports on the effect of the long-range order present in liquid-crystalline ILs (LCILs) to influence the rate of an aza-Claisen rearrangement. *Ex situ* ^1H nuclear magnetic resonance spectroscopy indicated that a small rate change occurs through a cubic-to-columnar transition, while no change is observed through a cubic-to-isotropic transition.

The third study reports on the thermal properties of fan-shaped, stilbazolium-based salts, in the search for new LCILs. Polarising optical microscopy and differential scanning calorimetry experiments determined that the stilbazolium-based salts were not liquid-crystalline.

Contents

List of Tables

List of Figures

List of Schemes

Acknowledgements

Firstly, I would like to thank my supervisors Duncan Bruce and John Slattery for their invaluable support and advice throughout my PhD studies. They have also given me the opportunity to present my research at many conferences across the world, which have been invaluable experiences.

I thank the University of York chemistry department for awarding me a teaching scholarship and providing me with the opportunity to teach alongside my PhD studies.

My research would not have been possible without the help from the technical staff in the department, all of whom I thank. I am grateful for the help of the beamline scientists at the ILL and ISIS, namely Isabelle Grillo, Richard Campbell, Sarah Rogers, and Maximilian Skoda. I also thank Karen Edler for helpful SANS fitting discussions.

I must also thank members of the Bruce and Slattery research groups, past and present, for making every day enjoyable. Additional thanks go to Yanan Gao, Iman Khazal, Lucía D'Andrea, and Sarah Kirchhecker for synthesising some of the ionic liquids presented in this thesis.

Finally, I would like to thank my family and friends, especially my parents, Theresa and Patrick, and my brothers, Marc and James, for their support and encouragement. I am also very grateful to Katie Whiteside for her patience and understanding over the last four years.

Declaration

I declare that this thesis is a presentation of original work and I am the sole author. This work has not previously been presented for an award at this, or any other, University. All sources are acknowledged as References.

Some of the compounds used in this work were prepared by Yanan Gao, Iman Khazal, Lucía D'Andrea and Sarah Kirchhecker, specific details can be found under Heading 5.1.

Part of the work present in Chapter 2 has been published in:

- D. W. Bruce, C. P. Cabry, J. N. C. Lopes, M. L. Costen, L. D'Andrea, I. Grillo, B. C. Marshall, K. G. McKendrick, T. K. Minton, S. M. Purcell, S. Rogers, J. M. Slattery, K. Shimizu, E. Smoll and M. A. Tesa-Serrate, *J. Phys. Chem. B*, 2017, **121**, 6002-6020.
- C. P. Cabry, L. D'Andrea, K. Shimizu, I. Grillo, P. Li, S. E. Rogers, D. W. Bruce, J. N. Canongia Lopes and J. M. Slattery, *Faraday Discussions*, 2017, DOI: 10.1039/C7FD00167C.

Christopher Patrick Cabry

September 2017

1. Introduction

1.1. Ionic liquids

Ionic liquids (ILs) can be defined as salts that melt, below 100 ˚C, into liquids that are comprised entirely of cations and anions, with many ionic liquids being further classified as room-temperature ILs. While the first room-temperature IL (RTIL) to be reported in the literature was ethanolammonium nitrate by Gabriel in 1888,[1] however research into RTILs is considered to have started when Walden synthesised ethylammonium nitrate in 1914,[2] research into ILs entered a new phase with the discovery of the organic chloroaluminates in 1951.[3] More recently IL research has been subdivided into many categories, for example protic, [4] aprotic, and chiral ILs.[5] Aprotic IL research began when Wilkes *et al.* reported the synthesis of 1-ethyl-3-methylimidazolium ILs with $[PF_6]^-$ and $[BF_4]^-$ as weakly coordinating anions.[6] Aprotic ILs are typically based on alkylated ammonium, phosphonium, pyrrolidinium, or imidazolium salts as the cations, along with halides and other inorganic anions, due to these usually being facile to prepare and stable to air, Figure 1.1.

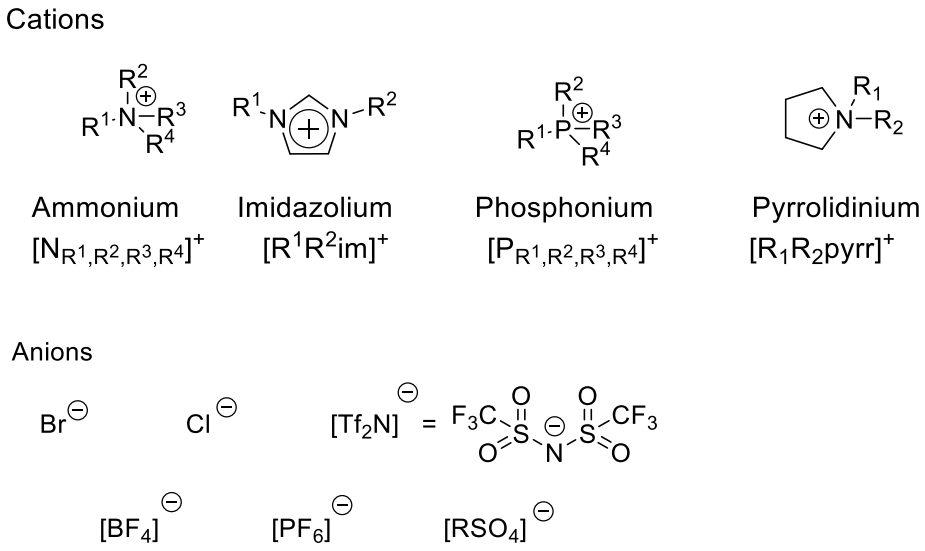

Figure 1.1: Examples of some widely used cations and anions.

Many research groups are active in the area of ILs and, as a consequence, the nomenclature has become fragmented, with many research groups choosing their own abbreviations for ILs. What they all agree on is that ILs should be grouped by

cation and not anion structure, due to the relatively facile substitution of the anionic part in most cases. The nomenclature Welton outlines in his 2011 review will be used throughout this report, such that alkyl chain lengths are denoted by C_n in the abbreviated form instead of using abbreviations derived from their literature names, *e.g.*, $[C_4C_1im]^+$ rather than $[BMIM]^+$ or $[bmim]^+$ for the 1-butyl-3-methylimidazolium cation.[7]

Ionic liquids are appealing to many scientists due to their advantageous properties, which can be wide ranging depending on the structure of the anion and cation species. However, it is possible to make generalisations such as ILs generally have low volatilities, large liquid state ranges and possess higher viscosities and densities than common molecular solvents. Having low or negligible vapour pressures makes ILs very attractive for use as solvents as they are generally safer to use as the solvent does not evaporate into the air, so they are less flammable. For the same reasons, they are often considered to be 'green' solvents as they are less likely to be released and damage the atmosphere. However, they are not always environmentally friendly as they may be toxic depending on their anion/cation structure or through the use toxic reagents in their synthesis. Other advantageous properties of ILs include high thermal, electrochemical and chemical stabilities.[8] ILs tend to be versatile solvents due to their ability to solubilise a wide range of substrates and many have the ability to dissolve both polar and apolar solutes as they are often amphiphilic. As the structure of an IL can be changed systematically, a range of properties can easily be attained, which has led to the current generation of ILs being branded as 'designer solvents'.

1.1. Liquid crystals

Liquid crystals (LCs) are materials that display a liquid-crystalline state of matter. The liquid-crystalline states exist between the crystalline phase, which has long-range, three-dimensional positional and orientational order, and the isotropic liquid phase, which has no molecular ordering. A range of LC states are known to exist, with each phase being characterised by the orientation and/or positional ordering within the phase. The ordering in LCs is less than that in the crystalline phase but higher than that in the isotropic liquid phase and for this reason they are often described as *mesophases*, from the Greek *mesos* meaning 'in the middle' or 'intermediate'; molecules that display mesophases are usually called mesogens or mesomorphic compounds. Unlike in the crystalline phases, where the molecules are constrained to

a specific point on a three-dimensional lattice, in both position and orientation, liquid-crystalline phases have reduced order, in that the mesogens have a degree of mobility. This can vary from complete positional freedom and constrained long-range orientational freedom, in the most disordered mesophase, to mesophases that also have some long-range positional ordering. Due to this long-range order, properties of LCs such as refractive index, viscosity and permittivity can be anisotropic.

Liquid crystals can be categorised into two families, *thermotropic* and *lyotropic* LCs. Thermotropic LCs exhibit mesophases upon heating from the solid state into a LC phase and, on further heating, they may pass through more than one LC phase before reaching the isotropic liquid phase; this last temperature is known as the clearing point. If a LC phase is found on both heating and cooling, it is designated as *enantiotropic* and is thermodynamically stable, whereas it is possible to observe phases only on cooling, in which case they are termed *monotropic* and are thermodynamically metastable. LC-to-LC transitions are usually thermodynamically controlled transitions occurring at the same temperature on both heating and cooling, unlike crystallisation which usually has a kinetic component leading to supercooling. Lyotropic mesophases occur when a solid lattice is perturbed by the addition of a solvent; they are sensitive to concentration, pressure and temperature. As this thesis concentrates on thermotropic LCs, lyotropic LCs will not be discussed in any more detail.

1.1.1. Thermotropic Liquid Crystals

Thermotropic LCs lose their order step-wise, melting into a LC phase before clearing into the isotropic phase. LC phases are true thermodynamically stable phases. A number of factors can influence the type of phase displayed by a LC, with molecular shape possibly being the most important. The two most common molecular shapes that display LC behaviour are the rod-like (calamitic) and disc-like (discotic) architectures, Figure 1.2, although other shapes are known to promote LC behaviour.[9] The orange cores in Figure 1.2 represent the average shape of the rigid parts of the molecules upon rotation around the unique molecular axes.

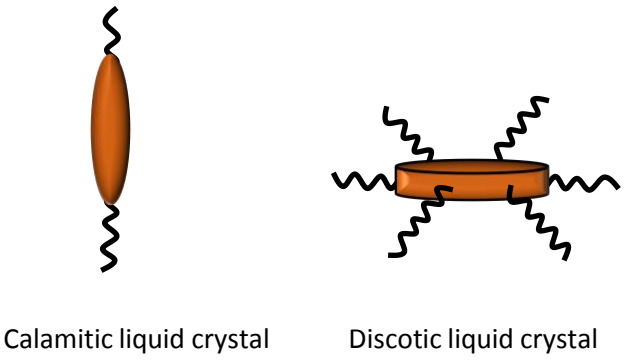

Figure 1.2: Generalised shapes for calamitic and discotic liquid crystals.

1.1.2. Liquid Crystal Phases formed by Calamitic Molecules

Calamitic mesogens can form a wide range of mesophases, the most common of which are discussed.

1.1.2.1. Nematic Phase

The nematic phase (N) is the least ordered LC phase and has no positional ordering, showing only one-dimensional orientational order with the long molecular axes, on average, pointing in the same direction. This direction is described as a vector known as the director, $\hat{n}$, Figure 1.1.

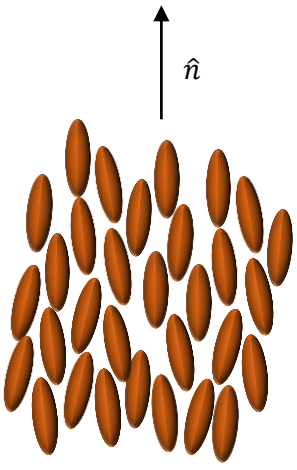

Figure 1.3: Schematic structure of the nematic phase.

The degree of this ordering can be defined by the order parameter (S, Equation 1.1), where S is the order parameter, θ is the angle between the director and the long axis of the individual molecules. This equation, which averages over all molecules in the phase, can describe a crystalline solid (S = 1) and an isotropic liquid (S = 0). For the nematic phase, the order parameter usually has a value between 0.35 and 0.7.[10]

Equation 1.1 $$S = 0.5 < 3\ \cos^2\theta - 1 >$$

1.1.2.2. Smectic Phases

Smectic phases have lamellar (layered) structures and as such are more ordered than the nematic phase. They have orientational ordering, like the nematic phase, while also having partial translational ordering. Several types of smectic mesophases are known, some are shown in Figure 1.4. The layered structures are not well defined, rather they are dynamic and show a sinusoidal density fluctuation. The apparent thickness of the layers is described by the layer periodicity.

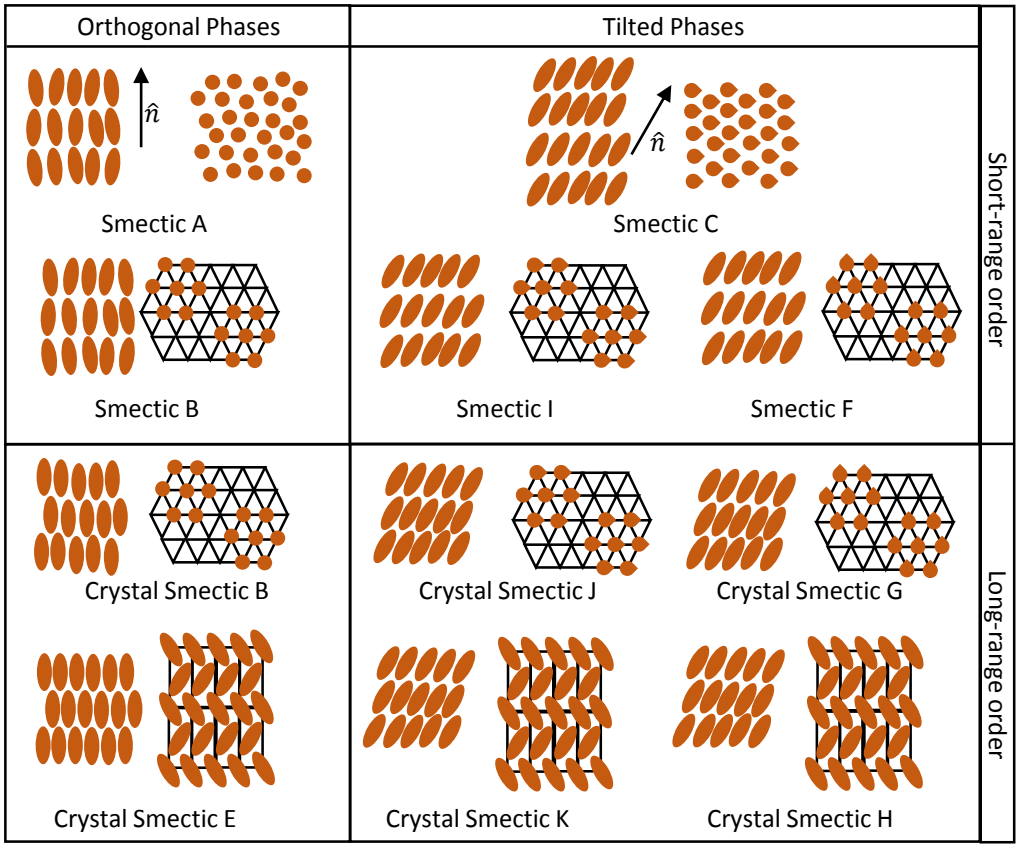

Figure 1.4: Schematic diagram showing the organisation in some smectic phases.

As in the nematic phase, the shape of the molecules result in the orientational ordering, whereas the translational ordering can be represented as arising from nano-segregation of incompatible parts, usually a rigid core and flexible side chains. This will be discussed in more detail later.

The smectic A (SmA) phase is the least ordered of the smectic phases and is described as an orthogonal mesophase as the director ($\hat{n}$) is parallel to the layer normal, Figure 1.4. In the smectic C (SmC) phase, the director is tilted with respect to the layer normal.

The smectic B phase (SmB) is similar to the SmA phase except that in the layers, the molecules are arranged in a two-dimensional hexagonal lattice, with the molecules still able to move between layers and past each other.

Analogous to the SmB phase, the smectic I (SmI) and smectic F (SmF) phases have a hexagonal lattice but the molecules are tilted as in the SmC phase. In the SmI phase, the molecules tilt towards the vertex of the hexagonal net whereas in the SmF phase, the tilt is towards the edge of the hexagon. These more highly ordered hexatic smectic phases (SmB, SmF, and SmI) can repeat their lattices on a scale of ~1500 – 6000 nm.[11]

The crystal smectic phases are related to the hexatic phases except their ordering is predictable over a longer range and in three-dimensions.[12] The crystal B, crystal J and crystal G phases are analogous to the SmB, SmF and SmI phases, respectively. The molecules in these soft crystal phases are confined to a lattice point but they are able to rotate. These are not considered as true liquid-crystalline phases as they have long-range, three-dimensional order.[13]

1.1.2.3. Chiral Phases of Calamitic Molecules

Introducing chirality into liquid crystals can have a profound effect upon the mesophase structure. Chirality can be introduced by either incorporating a chiral centre into the LC molecules, or by using a chiral dopant. A chiral dopant is a chiral molecule that is added into an achiral LC host that induces a chiral mesophase. Chiral phases are denoted by an asterisk, for example the chiral nematic (N*) and chiral smectic C (SmC*) phases.

The chiral nematic phase is analogous to the nematic phase, in that it has no positional ordering, only orientational ordering. However, unlike in the N phase where the director is constant, in the N* phase the director precesses around a perpendicular

axis, forming a helix owing to the way chiral molecules self-organise, Figure 1.5. The chiral nematic phase is sometime referred to as the cholesteric phase as the first N* phases discovered were based on cholesterol.[14]

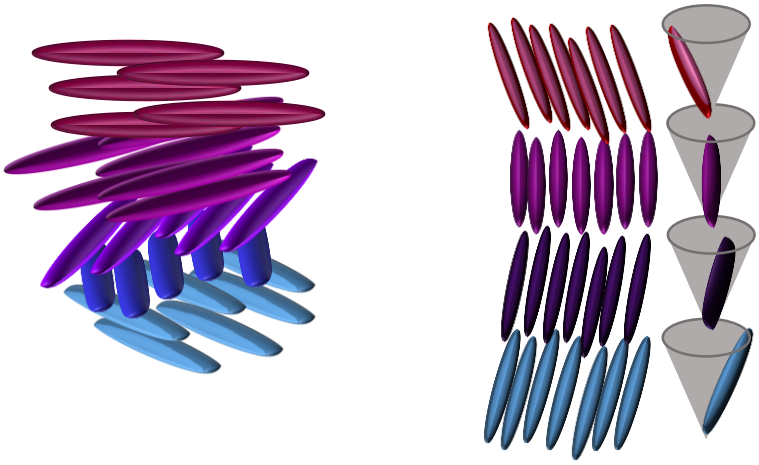

Figure 1.5: The chiral nematic phase, adapted from M. Mitov, *Adv. Mater*. 2012, **24**, 6260-6276,[15] and the chiral smectic C phase.

The chiral smectic C phase (SmC*), like the SmC phase, is layered and the molecules in each layer are tilted with respect to the layer normal, Figure 1.5. A helical structure is formed as in each layer the director rotates, however the angle between the director and layer normal remains constant.

1.1.3. Liquid Crystal Phases of Discotic Molecules

Disc-shaped (discotic) molecules can also display a range of different mesophases (Figure 1.6). Molecules that are able to aggregate into disc-like shapes, for example fan-, wedge-, and cone-shaped molecules, can display similar LC phases.[16]

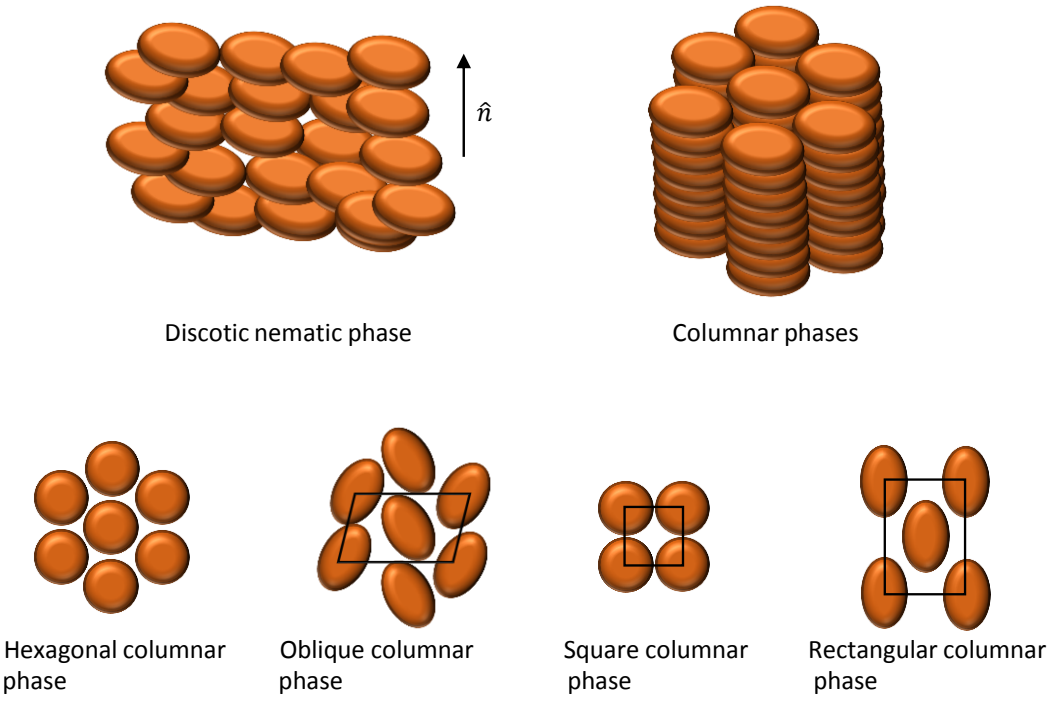

Figure 1.6: Liquid crystal phases of disc-like molecules. Elliptical shapes represent stacks of discs that are tilted within the columns.

1.1.3.1. Discotic nematic phases

The discotic nematic phase (N_D) is similar to the nematic phase of calamitic mesogens, in that it only has orientational order (Figure 1.6), except that for the N_D phase, it is the short molecular axis that is correlated.

1.1.3.2. Columnar phases

More ordered columnar phases are possible as the columns of the discotic molecules (or aggregates) arrange themselves onto a two-dimensional lattice. The different columnar phases are named after the shape of their lattice, for example, columnar hexagonal (Col_h) columnar rectangular (Col_r) and columnar oblique (Col_o), Figure 1.6.

1.1.4. Cubic Phases

Another class of liquid crystal phases are the cubic phases, which are unlike the phases previously discussed as they present long-range, three-dimensional positional

ordering with cubic symmetry, although the molecules have freedom to rotate and move within the structure (Figure 1.7). Several different types of cubic phase symmetries are known including, *Ia*$\bar{3}$*d*, *Pm*$\bar{3}$*m*, *Pn*$\bar{3}$*m* and *Im*$\bar{3}$*m*.[17] Cubic phases can be subdivided into two categories, these are micellar and continuous cubic phases. Micellar cubic phases consist of spherical aggregates, while continuous cubic mesophases consist of interwoven continuous networks, for example *Ia*$\bar{3}$*d* is a bicontinuous cubic phase as it consists of two continuous interwoven networks.

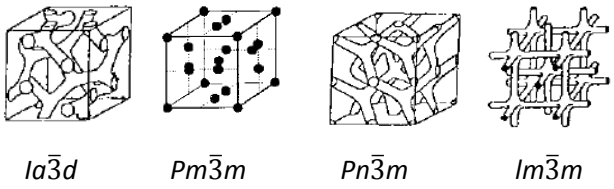

Figure 1.7: Cubic mesophases, adapted from *J. Mater. Chem*. 1998, **8**, 1485–1508.[18]

1.1.5. Origins of Liquid-crystalline Behaviour

When a crystalline solid, which has long-range, three-dimensional order, melts it can either melt directly into the isotropic liquid phase or it can melt in a step-wise manner through one or more liquid crystal phases as shown in Figure 1.8. Thus, any given liquid crystal could have one, or more than one mesophase, which if present must be determined experimentally.

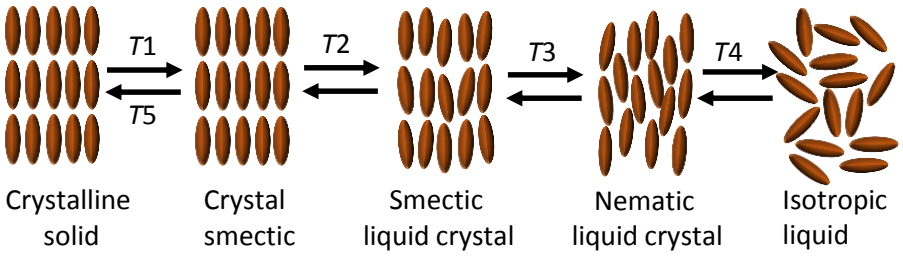

Figure 1.8: Schematic melting sequence for a liquid-crystalline material. Often $T1 \neq T5$ owing to supercooling of the melting point.

On heating a conventional crystal, the molecules within the crystal lattice gain vibrational energy. When a particular temperature is reached, the molecules have enough energy to overcome the intermolecular forces confining them to the lattice point, resulting in an isotropic liquid with full orientational and positional freedom.

On heating a liquid crystal from its crystalline phase, melting happens in stages with greater motional freedom being realised as the temperature increases. A liquid-crystalline material may go through one or more different mesophases before clearing into the isotropic phase. A schematic of a melting sequence for a liquid-crystalline material is given in Figure 1.8. At *T*1 some of the intermolecular forces are overcome leading to a crystal smectic phase, where the molecules have some rotational freedom and there is long-range positional order in three dimensions. Then, at a higher temperature (*T*2), there will be complete rotational freedom and the dimensionality of their long-range positional ordering reduces forming a smectic liquid-crystalline phase. When the temperature is further increased to *T*3, all long-range positional order is lost to give way to a nematic phase, where only orientational order remains. Then, when *T*4 is reached, the molecules have enough energy to lose the remaining orientational correlations resulting in an isotropic liquid, where all ordering is lost.[a] These intermediate states of aggregation between the solid and isotropic liquid phases are stabilised by the additional, anisotropic dispersion forces that arise owing to the structural anisotropy in the molecules.[18] Melting sequences of discotics are analogous to calamitics.

Along with intermolecular forces, structural or chemical incompatibility can be used to rationalise liquid crystal formation- this is known as nanosegregation.[18-22] Incompatible structures can be rigid sections and flexible chains, while chemical incompatibility could be from polar and apolar parts, hydrophilic and hydrophobic parts, and hydrocarbon and fluorocarbon parts, *etc*. The incompatible parts segregate from each other and the compatible parts aggregate together to create separate domains. The forces involved in nanophase segregation are enough to result in liquid crystalline phase formation in mesogens that are not anisotropic. The example of an amphiphilic molecule will be used to illustrate how nanosegregation occurs. An amphiphilic molecule has a hydrophobic part covalently attached to a hydrophilic part so that the incompatible parts cannot phase separate. Similar arguments can be made for any molecule containing two incompatible parts.

[a] As will be seen in later chapters, it is long-range order that is lost. Short range order can persist for some time above the clearing temperature and is also found in some materials that are not liquid-crystalline in nature.

Another concept used to understand the formation of liquid-crystalline phase formation is the idea of interfacial curvature, Figure 1.9. The interface is where the structure changes from one incompatible part to the other, in this case hydrophobic to hydrophilic. If the two incompatible parts have similar shape and volume, then the molecules will pack next to each other, segregating the incompatible parts into a lamellar phase, in this example the SmA phase, with alternating hydrophobic and hydrophilic domains. Increasing the volume (or changing the shape) of one of the incompatible parts will change the mesophase displayed, as the molecules will fill space differently. The curvature that results from one incompatible part being larger (or a different shape) than the other part is termed interfacial curvature and it is this that determines the mesophase structure. For example, increasing the volume fraction of the hydrophilic part of the amphiphile in Figure 1.9 results in an increase in interfacial curvature, giving rise to the smectic A phase then a bicontinuous cubic phase, followed by a hexagonal columnar phase and finally a micellar cubic phase. Conversely, increasing the volume fraction of the hydrophobic part of the amphiphile increases the interfacial curvature in the opposite direction leading to a change in mesophase.

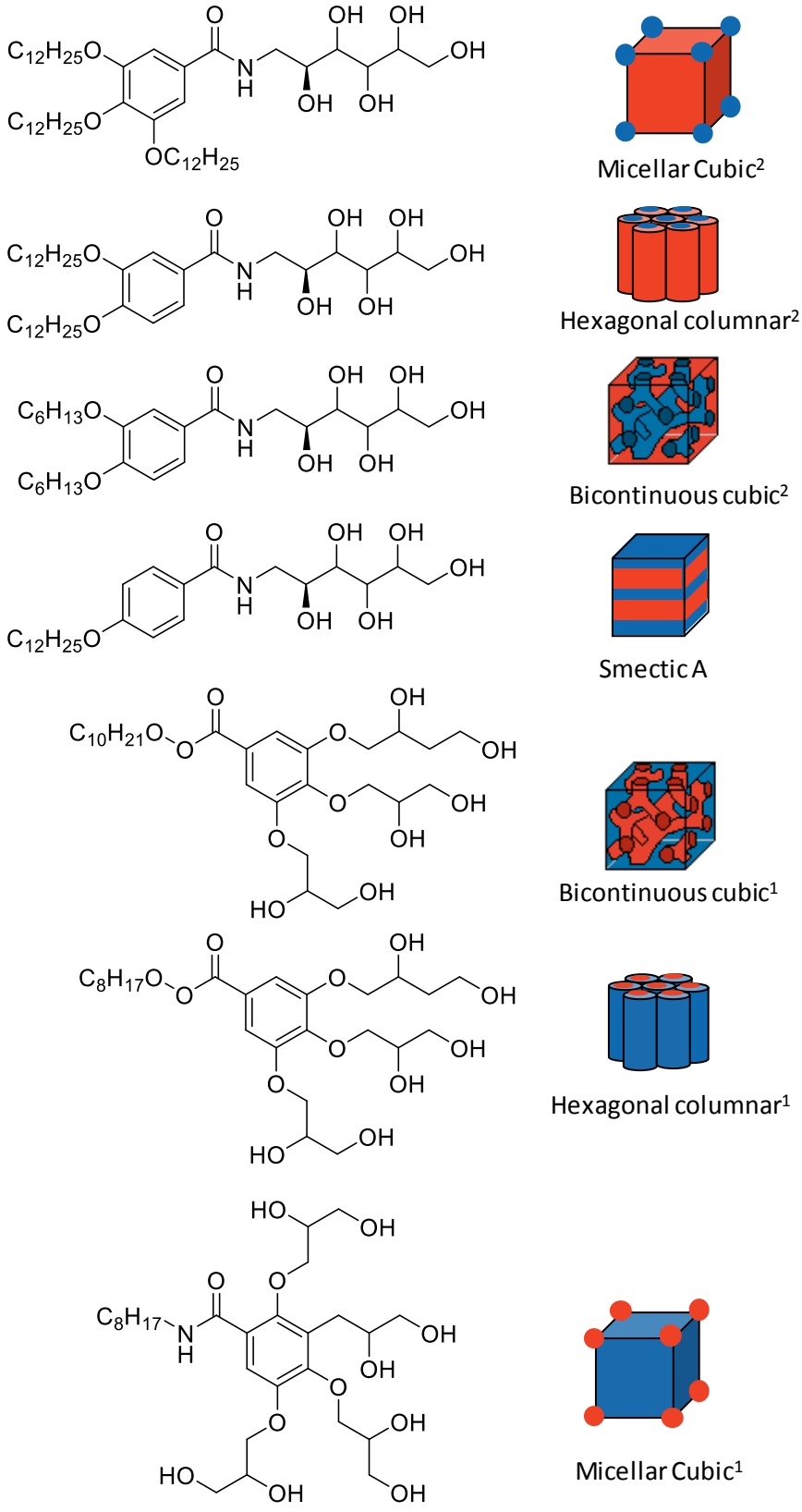

Figure 1.9: Shape based mesophase formation. [1]Normal type phase, [2] inverted type phase. Blue represents apolar rich regions while red represents polar rich regions. Information taken from *Angew. Chem. Int. Ed.* 2002, **41**, 628-631.[23]

1.2. Liquid-crystalline ionic liquids

Liquid crystalline ionic liquids (LCILs) are liquid-crystalline compounds that are made from cations and anions and have received considerable interest as they combine the advantageous properties of ILs with the molecular ordering inherent in LCs. Hence, LCILs display interesting properties such as ionic conductivity, low vapour pressures and molecular ordering in their liquid phases. While the first LCILs reported were 4-alkylpyridines salts by Knight in 1938,[24] research into LCILs was rather slow until the 1990s, when it intensified; several review articles have been published on the subject.[5, 25-29]

LCILs are commonly categorised by the cation type, just like the convention for ionic liquids. Most of the research has been aimed at ammonium, phosphonium, imidazolium, and pyridinium LCILs, again due to ease of synthesis with alkyl halides. Several different architectures have been used to design LCILs (Figure 1.10), including those that have the cationic group attached to an alkyl chain long enough to induce mesomorphism, for example $[C_nC_1im]^+$ ILs can show liquid-crystalline behaviour when $n \geq 12$ (Figure 1.10. a).[30, 31] There are also examples where: the cationic group is attached directly to a rigid core (Figure 1.10. b); the cationic group is appended to a liquid-crystalline moiety by a flexible spacer (Figure 1.10. c), and where the cationic group is part of a fan-shaped group (Figure 1.10. d).

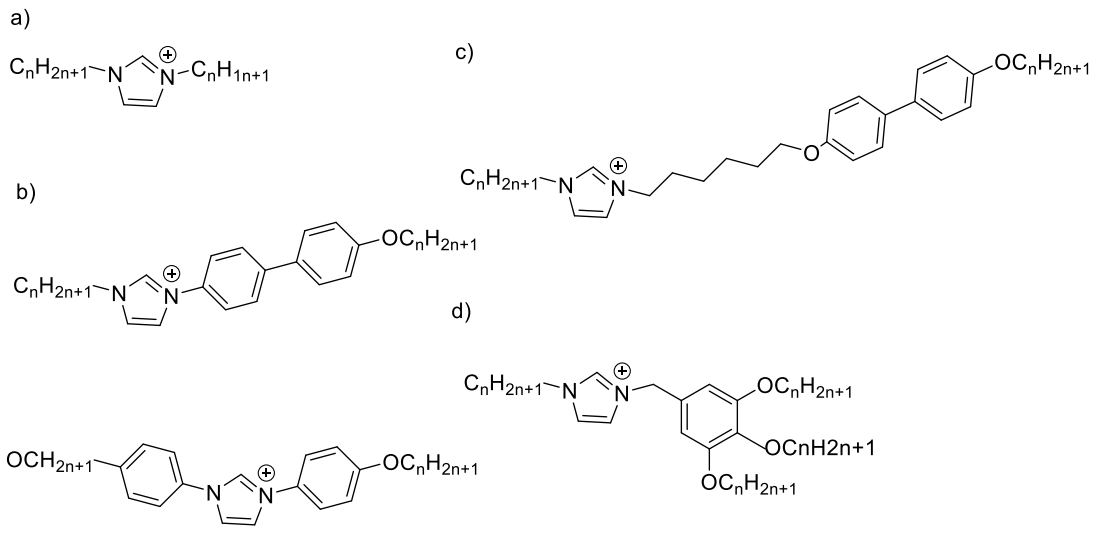

Figure 1.10: Liquid-crystalline ionic liquid architectures.

While the same factors governing the organisation of neutral thermotropic liquid crystals also apply to LCILs, there are, of course, additional electrostatic forces at play, such as ion-ion and ion-dipole interactions. These long-range, non-directional interactions, typically up to 250 kJ mol^{-1} in strength, are appreciably stronger than other types of intermolecular interactions such as hydrogen/halogen bonds, which are the strongest non-ionic interactions, with a typical strength of ~ 20 kJ mol^{-1}. [32]

By introducing charges into the system, nanosegregation is increased as the charged parts are incompatible with the apolar parts of the molecule, and the ionic parts have a tendency to stick together, thus the phases that are driven by nanosegregation are common.[5, 25] Conversely the nematic phase is very rare in ionic systems, as the weak dispersion forces are easily overcome by the stronger electrostatic forces. [33, 34] Even when strong nematic-promoting groups are attached to the cationic group *via* a spacer, or when the cationic group is incorporated into an anisotropic rigid section, smectic phases still dominate. However, nematic phases can present themselves if, for example, there is tight ion pairing between the cation and anion, or there are large amounts of nematogenic groups attached as sidechains to a polymeric backbone.[33, 35-38]

While smectic A phases are common in LCILs, the smectic C phase is rare, although examples exist where a mesogenic group is attached to an ionic group through a flexible spacer (*e.g.* as in Figure 1.10.c). [39-41]

A new type of crystal smectic phase was found in 1993 through the research into LCILs.[42] This new phase is called the crystal smectic T phase and is named such as it had two-dimensional tetragonal symmetry, although this phase has only been found to occur in a small number of LCILs.[42-44] The structure of the crystal smectic T phase is shown in Figure 1.11. The alkyl chains are molten while the ionic parts are arranged in a tetragonal lattice that is held together by strong electrostatic interactions. For the crystal smectic T phase to form the cationic and anionic groups need to be charge dense and spherical in shape.

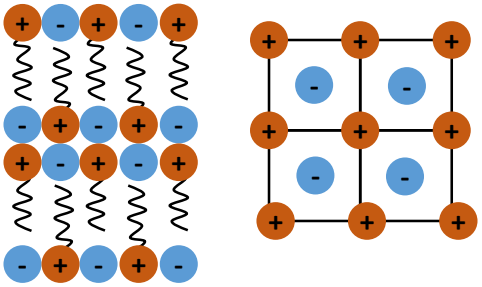

Figure 1.11: Crystal smectic T phase. Left, side view and right, top view.

1.3. Methods of Identifying Liquid Crystal Phases

Identification of liquid-crystalline phases are achieved primarily using polarising optical microscopy, differential scanning calorimetry and X-ray diffraction.

1.3.1. Polarising Optical Microscopy

Polarising optical microscopy (POM), used in conjunction with a temperature-controlled hot stage, allows the study of the optical textures of LC materials as a function of temperature. POM is the technique used first and most commonly to identify a mesophase.

Polarising optical microscopy exploits the optical anisotropy of most mesophases resulting in the mesophase being birefringent. Birefringence (double refraction) is when a single incident beam of light is separated into two different rays, which occurs as the mesophases have at least two different refractive indices, thus when a ray of light travels through the mesophase, it will travel at two different speeds, hence two different directions, Figure 1.12. These two rays are called the ordinary (n_o) and extraordinary (n_e) rays, and the birefringence can be quantified as the difference between the two rays ($\Delta n = n_e - n_o$). A characteristic pattern, or optical texture, is observed due to how the two rays recombine as they exit the material.

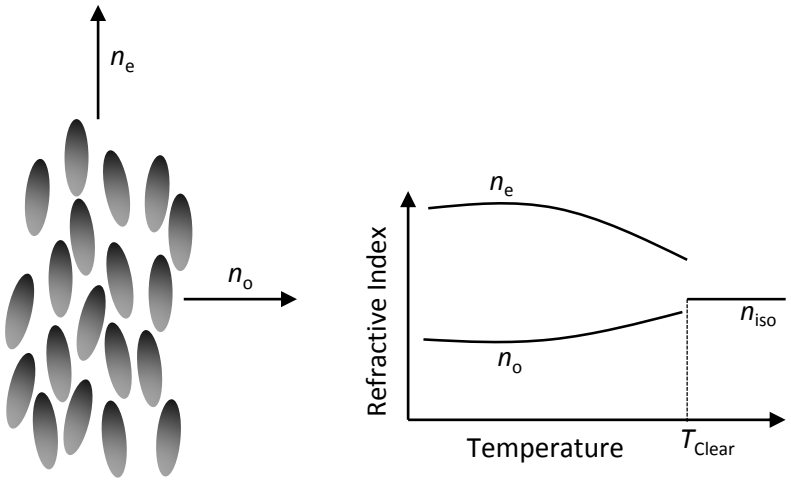

Figure 1.12: The relationship between refractive indices and temperature.

A schematic of a polarised optical microscope with a hot-stage is depicted in Figure 1.13. The optical microscope has two polarisers, one before and after the sample, that are positioned with their polarisation directions perpendicular to each other. They are orientated this way so that when light passes through the polariser and then through an isotropic liquid (which has one refractive index) the light is extinguished by the analyser, as the isotropic liquid does not affect the polarisation which impinges on the analyser at 90° to the preferred direction. In a typical experiment, a small amount (*ca* mg) of a LC sample is placed between two glass slides and these are placed on the hot-stage. The temperature is cycled up and down and the optical textures are observed, which can be used to identify the mesophase. There are instances when mesophases do not show an optical texture, for example cubic phases, which are isotropic, or if the mesogens are aligned homeotropically. There are two extremes of alignment, homeotropic and homogeneous. Homeotropic alignment is where the main axes of the molecules are perpendicular to the glass slides, thus the light travels down the molecules optical axis and no interference is seen, while homogeneous alignment is where the main axes of the molecules lie parallel to the glass slide.[12]

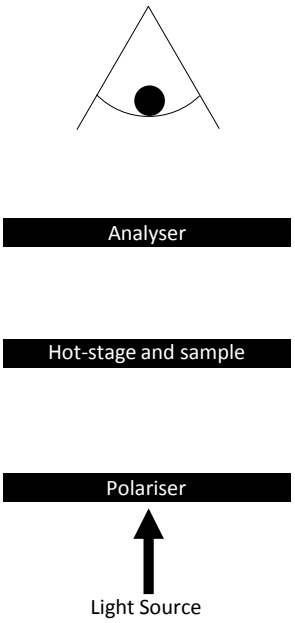

Figure 1.13: Schematic of a polarised optical microscope, with a hot-stage.

1.3.2. Differential Scanning Calorimetry

A differential scanning calorimeter is used to measure the enthalpy change at a phase transition; Differential Scanning Calorimetry (DSC) is usually used in conjunction with POM to determine the mesophase type and temperature of transition. A differential scanning calorimeter has two independent furnaces that are kept at the same temperature under a flow of nitrogen, Figure 1.14. In one furnace, there is a sealed aluminium pan containing the sample under investigation (1-3 mg), while the other furnace has an empty sealed aluminium reference pan. The calorimeter is programmed to heat and cool the sample and reference pans, keeping their temperatures identical and the power difference required to achieve this is recorded against the sample temperature. Thus, when a phase transition occurs, more (or less) power is supplied to the sample pan and the trace is a plot of this power as a function of temperature, as seen in Figure 1.15. The change in enthalphy (ΔH) can be obtained by integration of the peak area.

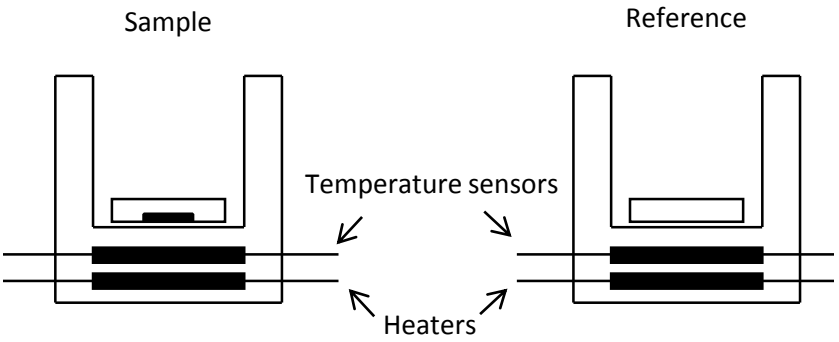

Figure 1.14: Schematic of a differential scanning calorimeter.

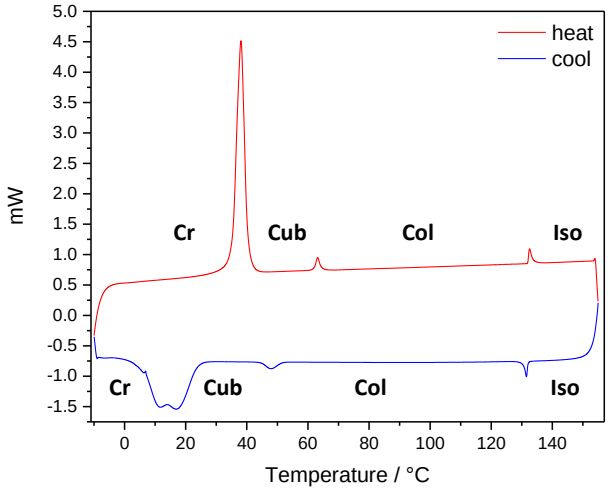

Figure 1.15: DSC trace of a LC, where Cr is a crystal phase, Cub is a cubic phase, Col is a columnar phase and Iso is the isotopic phase.

1.3.3. X-Ray Diffraction

X-Ray diffraction studies are a way to investigate the short-range nanostructuring of liquid crystal phases and a schematic of typical diffractometer is depicted in Figure 1.16.

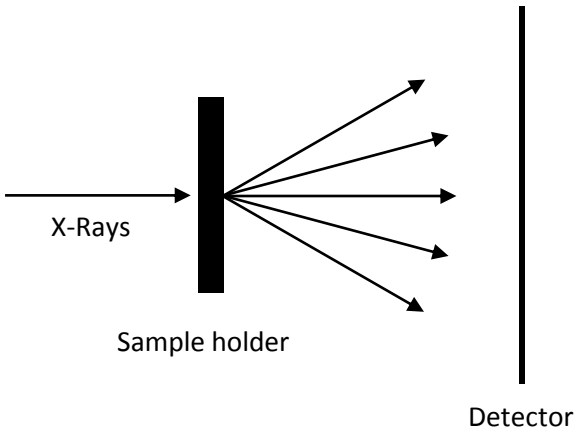

Figure 1.16: Schematic of a typical diffractometer.

X-Rays are diffracted by electron density, the diffracted X-rays will interact with each other and any periodic arrangement are depicted by a diffraction pattern. A diffraction peak is seen when the diffracted X-rays interact constructively, which occurs when the distance the X-rays travel is equal to a multiple of the wavelength, Bragg's Law (Equation 1.2).[45] This can be illustrated by the difference in path length between the two X-ray beams, which are in phase, in Figure 1.17. The blue beam diffracts from the top layer (α), whereas the red beam has to travel further to diffract from layer β. The difference in path length is AB + BC, which can be calculated as $2d\sin\theta$ as AB = BC, Figure 1.17.

Equation 1.2 $$2d \sin\theta = n\lambda$$

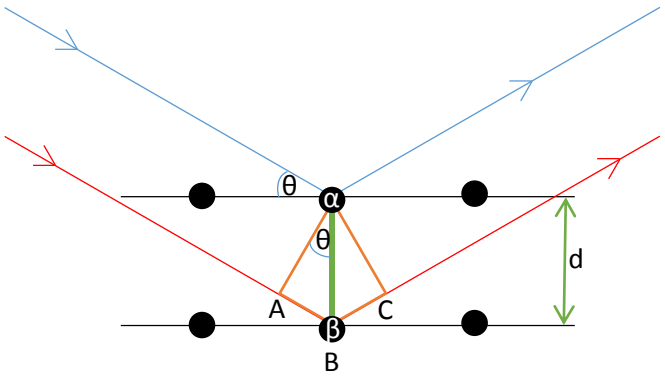

Figure 1.17: Illustration of Bragg's Law, Equation 1.2.

An example for the Col_h phase is shown in Figure 1.18. The two-dimensional symmetry of the mesophase can be assigned from analysis of the *d*-spacings from the data.

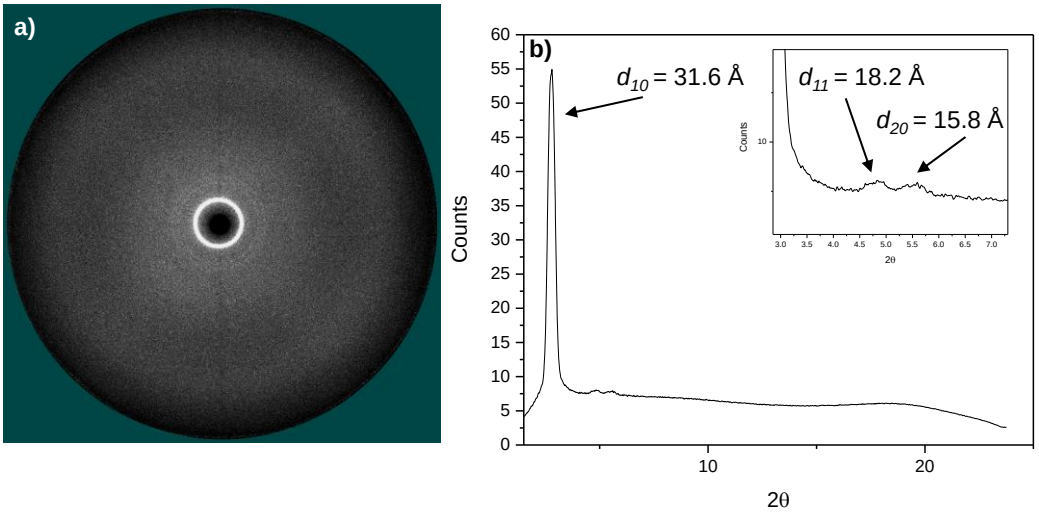

Figure 1.18: a) 2D X-ray scattering pattern of a LC in the Col_h phase and b) the corresponding spherical integration.

1.4. Aims of the Work Described in this Thesis

The research detailed in the thesis aimed to contribute to the understanding of the structure of, and reactivity in, self-organised ionic liquids. This thesis is split into three different areas. The first is the study of the bulk nanostructure in pure $[C_nC_1im][Tf_2N]$ (n = 2, 4, 6, 8, 10, 12) and their mixtures, using small-angle neutron scattering, Chapter 2; note that these are not liquid crystals. The second study investigates the use of liquid-crystalline ionic liquids as reaction media for an aza-Claisen rearrangement, Chapter 3, while the third study is the search for new LCILs based upon stilbazolium cations, Chapter 4.

2. Bulk Structure of Binary Ionic Liquid Mixtures

2.1. Introduction

The benefits of ionic liquids (ILs) stem from their remarkable properties, including their negligible vapour pressure, large liquid range and high thermal stability, which has resulted in their adoption in a wide range of areas. ILs are often referred to as designer solvents due to the simplicity of changing their properties by altering the structure of the anion, cation, or both. This has led to large libraries of ionic liquids being synthesised with the aim of achieving specific properties. A simpler alternative methodology is to mix two or more ionic liquids together.[46 47] Although the structure of ionic liquids has been an intense research area, mixtures have received less attention. One of the most intensively studied ILs are the imidazolium-based salts, including those in this chapter, 1-alkyl-3-methylimidazolium salts. These are abbreviated as [$C_nC_1$im][X], where *n* is the alkyl-carbon number and X the anion.

A range of models have been used to describe ionic liquid bulk structure, including ion pairs,[48-51] hydrogen-bonded networks,[52-61] ion clusters[62-64] and self-assembled nanoscale structuring.[46, 65-74] The most appropriate model depends upon the type of IL under investigation. Indirect evidence from viscosity, conductivity and Raman spectroscopy proposed long-range ordering from as early as 2000.[65, 75, 76] Since then, the structure of ionic liquids has been an intense research area with several reviews on ionic liquid bulk structure being written.[52, 53, 77-80]

Early molecular dynamic (MD) simulations postulated nanostructure for several different systems of [$C_nC_1$im][X].[66, 68-70] When alkyl chains were sufficiently long, the chains start to aggregate to form alkyl domains.[69, 70] Originally it was reported that nanoscale ordering is only due to alkyl chain aggregation, while the imidazolium heads are distributed homogeneously.[70] However, an atomistic simulation of [$C_nC_1$im][PF_6] introduced the concept of head-group aggregation to form continuous domains.[71] Diffraction patterns were exported from several simulations predicting the appearance of a low-*q* peak due to alkyl chain aggregation. ILs frequently display three peaks in small-angle scattering experiments: a peak at higher-*q* (~ 13 nm^{-1}) that relates to characteristic close-contact separations between ions, the so-called 'contact-peak' (CP); a peak at intermediate-*q* (~ 8 nm^{-1}) that relates to the average distances between ions of the same charge, the 'charge-ordering peak' (COP); and a

peak at lower-*q* (~ 2.5 nm^{-1}) that is related to ion-ion distances separated by the non-polar network, the 'polar/non-polar peak' (PNPP), Figure 2.1.[81]

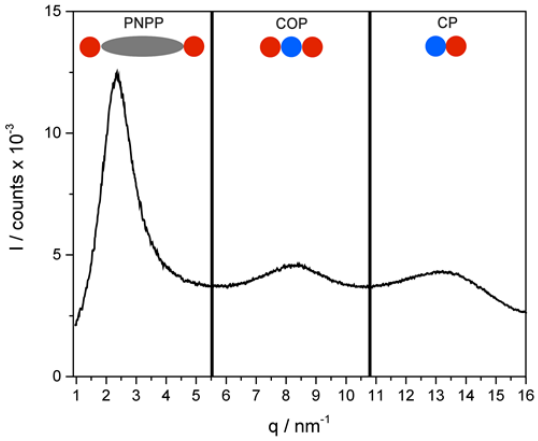

Figure 2.1: Small-angle X-ray scattering data for $[C_{12}C_1im][Tf_2N]$ showing the three peaks (CP, COP and PNPP) commonly seen in nanostructured ILs. Cation head groups are represented as red circles, anions as blue circles and alkyl chains as grey ellipses.

The PNPP was first identified experimentally by Triolo *et al.* by X-ray diffraction studies,[82] along with many others afterwards.[67, 83] A dependence on alkyl chain length with the correlation distance (PNPP position) is observed, and as the chain length increases the peak sharpens, its intensity increases and it moves to lower *q* (longer correlation length). This is rationalised as the apolar alkyl chains segregating from the polar imidazolium group and the anion. X-Ray diffraction studies on liquid-crystalline ILs in their liquid-crystalline and isotropic states indicate that the structural ordering is similar in both, with only the PNPP intensity decreasing upon the transition into the isotropic phase. This was concluded as being due to the long-range order of the liquid crystal phase being lost and not an intrinsic structural change.[30, 84]

Small-angle neutron scattering (SANS) techniques have been utilised to investigate ionic liquid structure further.[72, 85, 86] The results tend to agree with the notion that the PNPP is due to nanostructuring in the IL. However, some contributions put forward an argument that the PNPP does not arise from nanoscale ordering, but simply from a second-shell radial distribution.[72, 87] The PNPP observed in SANS experiments agrees with the data obtained from X-ray measurements, in that the peak increases in intensity, sharpens and the correlation length increases upon increasing alkyl chain length.[72]

The structure of pure ionic liquids has received attention in the last decade whereas ionic liquid-ionic liquid mixtures have had little consideration. [46, 84, 86] The research into the structure of IL mixtures can be generally split into two classes, one being where the mixtures have common cations and different anions, [88, 89] and the second being mixtures of ILs that have common anions and different cations, such as the work described within this chapter. Small-angle X-ray scattering (SAXS) has been used to study binary ionic liquids mixtures, of $[C_1C_1im][Tf_2N]$ and $[C_{12}C_1im][Tf_2N]$, where the two components have different cations and common anions.[86] Low concentrations of $[C_{12}C_1im][Tf_2N]$ in $[C_1C_1im][Tf_2N]$ have been modelled as pseudospherical aggregates that do not interact with each other, while at higher concentrations the model uses interacting pseudospherical hard-sphere aggregates. A similar model has been used on a related system where solid $[C_nC_1im][Cl]$ (n = 14, 16, 18) was dissolved in liquid $[C_nC_1im][FeCl_4]$ (n = 1, 2).[90] In a recent study, it was shown that both the bulk and surface properties of the IL mixture system $[C_2C_1im]_{1-x}[C_{12}C_1im]_x[Tf_2N]$, which contains an IL with a relatively amphiphilic cation, $[C_{12}C_1im][Tf_2N]$, dissolved in a relatively polar IL, $[C_2C_1im][Tf_2N]$, behave in a non-ideal way as the composition of the mixture changes.[91] Using a range of experimental and computational approaches, including preliminary SANS data, for a small selection of compositions and one isotopic contrast, it was possible to relate this non-ideal behaviour to the surface and bulk structure of these mixtures. These data suggest that IL structure, in some binary IL mixtures, may depend strongly on composition.

2.2. Small-Angle Scattering

SANS and SAXS are powerful techniques to probe the nanostructure of ordered materials.[92-94] They are typically used in the studies of polymers, micelles and liquid crystals to determine the size, shape and the size/shape polydispersity of the material.

2.2.1. X-Rays

X-Rays are massless, electrically neutral (zero charge) electromagnetic radiation with a wavelength (λ) from ~ 10^{-2} to 10^2 Å. However, in small-angle X-ray scattering experiments, the X-rays used usually have wavelengths of 0.5 to 2.5 Å and are generated by a copper Kα (λ = 1.54056 Å) target tube. When a synchrotron radiation source is used, a monochromator is employed to harvest the wavelength required.

X-rays are defined by their wavelength (λ), Equation 2.1, energy (E) Equation 2.2, and momentum (ρ) Equation 2.3, where c is the speed of light (2.998×10^8 m s^{-1}), ν is the frequency, h is Planck's constant (6.636×10^{-34} J s). X-Rays scatter by interacting with the electrons of the atoms.

Equation 2.1 $$\lambda = \frac{c}{\nu}$$

Equation 2.2 $$E = h\nu$$

Equation 2.3 $$\rho = \frac{h}{\lambda}$$

2.2.2. Neutrons

The neutron was first discovered in 1932 by Chadwick.[95] A neutron is a sub-atomic particle with a mass of $m = 1.675 \times 10^{-27}$ kg that is electrically neutral. Its kinetic energy, E, is defined in Equation 2.4 and its momentum, ρ, is defined in Equation 2.5, where v is its velocity.

Equation 2.4 $$E = \frac{1}{2}mv^2$$

Equation 2.5 $$\rho = mv$$

When neutrons are produced they have a high velocity, hence they are high energy neutrons. These are then moderated so that they have a higher probability of interacting with the material. Neutrons exhibit wave-particle duality thus they have a wavelength, as given by the Broglie equation, Equation 2.6, Neutrons are known as being hot (~1 Å), thermal (~ 2 Å) or cold (~6 Å) depending upon their wavelength.[93]

Equation 2.6 $$\lambda = \frac{h}{\rho} = \frac{h}{mv}$$

2.2.3. Scattering Theory

The theory of scattering of particles by matter is the same for most techniques, including light, electrons, X-rays and neutrons. Light interacts with matter through

polarisability, electrons through electrostatic interactions, X-rays through electromagnetic interactions with electron clouds and neutrons interact with matter through nuclear interactions.

The probability of a neutron interacting with a nucleus is low due to the nucleus being small compared to the atom. This means that neutrons are able to penetrate well through materials. When a neutron does interact it can do so in three different ways, by absorption, refraction or scattering, Figure 2.2. Absorption occurs when the intensity of the neutron beam is reduced and the neutron vector remains unchanged. Refraction occurs when the beam intensity is not weakened and the neutron vector is refracted. Scattering occurs when the beam intensity is not weakened and is scattered spherically outwards from the material.

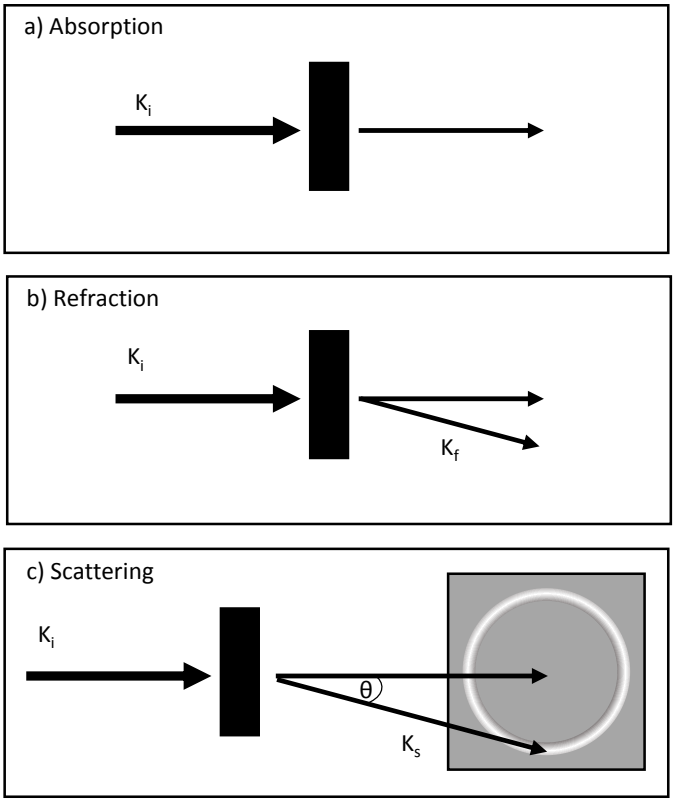

Figure 2.2: Neutron interactions with matter: a) absorption; b) refraction; c) scattering.

Neutron scattering is a powerful technique as it can differentiate between different atoms and even between isotopes of the same atom as they poses different scattering length densities (*b*). The difference in scattering length between hydrogen (b = – 3.7406 10^{-15} m) and deuterium (b = 6.671 10^{-15} m) can be used to great effect

by using contrast (isotopic) variation. Scattering lengths, along with the density of a substance, are used to calculate the scattering length density of molecule.

2.2.4. Neutron Generation

There are two main methods of neutron generation used for neutron experiments, these are the continuous sources and spallation sources.

Continuous sources of neutrons are from fission processes in nuclear reactors, such as at the Institute Laue-Langevin (ILL) in Grenoble, France. Fission is the process of splitting heavy nuclides into smaller ones and when this happens, high-energy neutrons are released along with electromagnetic radiation and kinetic energy in the fission fragments. These neutrons can either be harvested for neutron experiments or they go on to initiate more fission events. The ILL uses ^{235}U-enriched uranium as its fissionable material.

Spallation sources produce neutrons by projecting a beam of hydrogen ions at a spallation target. At the ISIS facility, STFC Rutherford Appleton Laboratory, UK, hydride ions are injected into a linear accelerator, where they are bunched into discrete packets and accelerated into a synchrotron. As the H^- ions enter the synchrotron they pass through an aluminium oxide foil which removes the two electrons, producing a proton (H^+). The synchrotron continues to accelerate and bunch the protons to packets with 100 ns pulse travelling at 84% of the speed of light. These are then dumped into the extracted proton beam tube, where they are directed at a tungsten target. The protons collide with the tungsten target releasing high-energy neutrons. This results in a pulsed source that repeats 50 times per second.

2.2.5. Scattering Vector

By defining the wavevector of both the incident ($\boldsymbol{k}_i$) and scattered ($\boldsymbol{k}_s$) neutrons (Figure 2.2, where $\boldsymbol{k}_i = \frac{2\pi}{\lambda}$), the scattering vector (q) can be calculated, Equation 2.7, which characterises the scattering geometry. The scattering centre can be considered as a point scatterer, thus the scattered wave will be spherically symmetrical. When coherent scattering occurs from several scattering centers a scattering pattern is observed.

Equation 2.7 $$q = |q| = |\boldsymbol{k}_s - \boldsymbol{k}_i| = \frac{4\pi}{\lambda} \sin\left(\frac{\vartheta}{2}\right)$$

2.2.6. Scattering Cross Section

The intensity of scattering, $I(q)$, is measured during a neutron scattering experiment. $I(q)$ is a function of the instrument and environmental specific functions, along with the scattering cross section. The total scattering cross section is a sum of the coherent cross section and the incoherent cross section. The coherent cross section contains structural information as it is a function of the average scattering length against q. While the incoherent cross section contains no structural information as it is a function of the variance of the scattering length density and usually appears as background noise. The coherent differential scattering cross section ($\frac{d\Sigma}{d\Omega}$) can be described as a function of the density of scattering centres (N), the volume of a scattering centers (V), the contrast ($\Delta\rho$), along with the particle form factor ($P(q)$) and the structure factor ($S(q)$), Equation 2.8. All the structural information is contained within the scattering cross section.

Equation 2.8 $$\frac{d\Sigma}{d\Omega}(q) = NV^2 (\Delta\rho)^2 P(q) S(q)$$

The particle form factor, $P(q)$, is a function of interference between scattered neutrons from different parts of the same scattering centre. The structure factor, $S(q)$, is a function of the interference between scattered neutrons from different scattering centres. As such the particle form factor contains information on the size and shape of a scattering object and the structure factor contains information on the interactions between scattering objects.

2.3. Scattering Models

To obtain information about the nanostructure of liquids, the scattering data are fitted to a range of different models. The model has to be appropriate for the system under study and the model output values, such as correlation length, need to be related to the molecular length scales. The scattering data in this chapter was fit using the SasView software and the models used are described below.[96]

2.3.1. Shape-Based Models

Shape-based models describe the scattering objects as shapes that have a scattering length density, inside a solvent that has a uniform scattering length density.

2.3.1.1. Sphere Model

The sphere model describes the particle form factor for a system of monodisperse spherical particles, with a uniform scattering length density (SLD), within a solvent also with uniform SLD, Figure 2.3.[96] The form factor is normalised by the particle volume (V) and incoherent scattering is accounted for by the addition of a background value (bkg), Equation 2.9, where, r is the radius of the sphere and $\Delta\rho$ is the difference is SLDs between the sphere and the solvent.

Figure 2.3: An illustration of the sphere model, where r is the radius of the sphere.

Equation 2.9
$$P(q) = \frac{\text{scale}}{V}\left[3V(\Delta\rho)\frac{(\sin(qr)-qr\cos(qr))}{(qr)^3}\right]^2 + bkg$$

2.3.1.2. Ellipsoid Model

The ellipsoid model describes the particle form factor for a system of monodisperse ellipsoids with uniform SLD, within a solvent also with uniform SLD, Figure 2.4.[96] The form factor ($P(q,\alpha)$) is normalised by the particle volume (V) and the incoherent scattering is accounted for by the addition of a background value (bkg), Equation 2.10, where α is the angle between the ellipsoid axis and the q-vector, R_a is the radius of

the rotational axis of the ellipsoid (axial), R_b is the radius perpendicular to the rotational axis of the ellipsoid (equatorial), $\Delta\rho$ is the difference in SLDs between the ellipsoid and the solvent. If $R_a > R_b$ the ellipsoid is oblate and if $R_a < R_b$ then the ellipsoid is prolate, if $R_a = R_b$ the ellipsoid is a sphere.

Figure 2.4: An illustration of the ellipsoid model where R_a is the axial radius and R_b is the equatorial radius.

Equation 2.10

$$P(q,\alpha) = \frac{Scale}{v} f^2(q) + bkg$$

where

$$f(q) = \frac{3(\Delta\rho)V(\sin[qr(R_a,R_b,\alpha)] - qr\cos[qr(R_a,R_b,\alpha)])}{[qr(R_a,R_b,\alpha)]^3}$$

and

$$r(R_a,R_b,\alpha) = \left[R_b^2 \sin^2\alpha + R_a^2 \cos^2\alpha\right]^{\frac{1}{2}}$$

2.3.2. Shape-Independent Models

Shape-independent models describe the scattering intensity ($I(q)$) based on empirical formulae. A sum model, that is, a sum of two (or more) models, can be used to describe the scattering data, Equation 2.11.

Equation 2.11

$$Sum\ Model = scale\ (Model_1 + Model_2)$$

2.3.2.1. Lorentz Model

The Lorentz (or Ornstein-Zernicke) model describes broad scattering at low-q and is defined by Equation 2.12, where L is the correlation length.[96]

Equation 2.12 $$I(q) = \frac{scale}{(1+ (qL)^2)} + background$$

2.3.2.2. Peak Lorentz Model

The peak Lorentz (PL) model describes a Lorentzian-shaped peak on a flat background, Equation 2.13, where the peak has a height of I_0 centered at q_0 which has a half-width at half-maximum of B.[96]

Equation 2.13 $$I(q) = \frac{scale}{\left(1+\left(\frac{q-q_0}{B}\right)^2\right)} + background$$

The *d*-spacing associated with the Lorentzian peak can be calculated from Equation 2.14 and the correlation length (scatterer size) is given in Equation 2.15.

Equation 2.14 $$d\text{-Spacing} = \frac{2\pi}{q_0}$$

Equation 2.15 $$\text{Scatterer size} = \frac{1}{B}$$

The *d*-spacing is associated with the characteristic distances between scattering inhomogeneities. The scatterer size is associated with the length scale over which structural correlation decays as expressed in Equation 2.16. For large, highly correlated structures, such as lamellar or bicontinuous structures, the scatterer size can be related to the domain size.

Equation 2.16 $$\text{structural decay} \propto \frac{e^{\frac{-r}{\xi}}}{r}$$

2.3.2.3. Teubner-Strey Model

The Teubner-Strey model is an empirical model that was first used to describe the scattering intensities of two-component microemulsions, where the intensity is proportional to the density-density association of the two components. [97] It is used to describe a range of structures including micelles, bicontinuous networks, lamellar and disordered structures. The Teubner-Strey model is described in Equation 2.17, where a, c_1 and c_2 are empirical fitting parameters.

Equation 2.17 $$I(q) = \frac{1}{a + c_1 q^2 + c_2 q^2} + background$$

a, c_1 and c_2 can be used to derive length scale values that relate to the structure of the system, d-spacing (Equation 2.18) and the correlation length (Equation 2.19).

Equation 2.18 $$d\text{-Spacing} = \frac{2\pi}{\sqrt{\frac{1}{2}\sqrt{\frac{a}{c_2}} - \frac{1}{4}\frac{c_1}{c_2}}}$$

Equation 2.19 $$\text{Correlation length } (\xi) = \frac{1}{\sqrt{\frac{1}{2}\sqrt{\frac{a}{c_2}} + \frac{1}{4}\frac{c_1}{c_2}}}$$

The d-spacing is associated with the characteristic distances between scattering structures, while the correlation length is associated with the length scale over which structural correlation decays. The correlation function ($\gamma(r)$), Equation 2.20, gives the probability of finding a scattering structure at r, given that one exits at the origin, when $-1 < \gamma < 1$.

Equation 2.20 $$\gamma(r) = \frac{d}{2\pi r} e^{\frac{-r}{\xi}} \sin\left(\frac{2\pi r}{d}\right)$$

Another factor can be derived from the Teubner-Strey model, this is known as the amphiphile strength (γ) which suggests the structural type of the system, Equation 2.21. The system is regarded as being disordered when $\gamma > 1$, the correlation function decays monotonically and no order is present. Aggregate/micelle formation occurs

when $0 < \gamma < 1$ and the system is bicontinuous when $-1 < \gamma < 0$. Lamellar structures exist when $\gamma < -1$. The point at which the amphiphile strength changes from negative to positive values is known as the Lifshitz line.

Equation 2.21 $$\gamma = \frac{c_1}{4ac_2}$$

In aggregate systems, the *d*-spacing is related to the scattering domain size and the correlation length is associated with the density fluctuations within the domain. For correlated structures, such as lamellar or bicontinuous structures systems, the *d*-spacing is related to the average distance between the scattering objects or the periodic distance in structures, while the correlation length is the length scale of the short-range correlation within the domain.

2.4. Aims

The research detailed in this chapter aimed to contribute to the understanding of the self-organised structure of ionic liquids and their mixtures. The ionic liquids under study are [$C_nC_1$im][Tf_2N] ionic liquids (*n* = 2, 4, 6, 8, 10, 12), these were chosen as these are liquid at the temperatures used in this study. SANS experiments were carried out on two instruments, D22 at the ILL and on Sans2d at ISIS. D22 covered a *q*-range of 9×10^{-2} to 9 nm^{-1}, while Sans2d covered a *q*-range of 4.5×10^{-2} to 7 nm^{-1}, which was chosen as the larger length scale features, such as the PNPP, resides in this range, the PNPP is associated with the organisation of the alkyl chains in these systems.[81]

To provide a contrast between the different components of the ILs, several isotopically labelled ILs were prepared, and their nomenclature is defined in Figure 2.5.

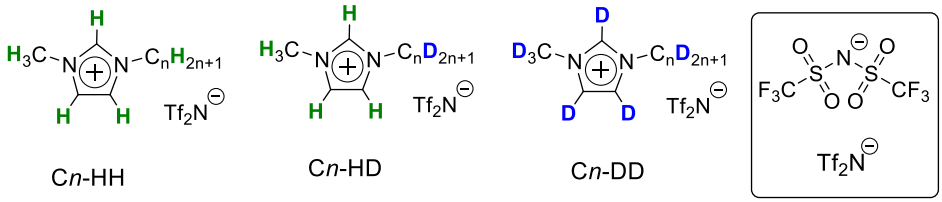

Figure 2.5: The chemical structures and nomenclature of the ions under investigation.

The studies are broken up into different sections, first the structure of the pure ILs will be discussed followed by binary mixtures of *n* = 12, 10, 8, 6, 4 in *n* = 2, and then *n* = 4, 6, 8, in *n* = 12.

2.5. SANS of Pure [$C_nC_1$im][Tf_2N] Ionic Liquids

SANS experiments were carried out on pure [$C_nC_1$im][Tf_2N] ionic liquids (*n* = 2, 4, 6, 8, 10, 12), with two different contrasts, C*n*-HH and C*n*-DD. The SANS data for these ILs are shown in Figure 2.6. The SANS data are presented in two different sections. First the discussion of the smaller alkyl chain ILs, where *n* = 2, 4, 6, followed by the ILs with longer alkyl chains, *n* = 8, 10, 12. Then a more detailed discussion of the SANS data is presented, for [$C_{12}C_1$im][Tf_2N] collected on separately synthesised batches, followed by a summary of the structural changes upon increasing *n*.

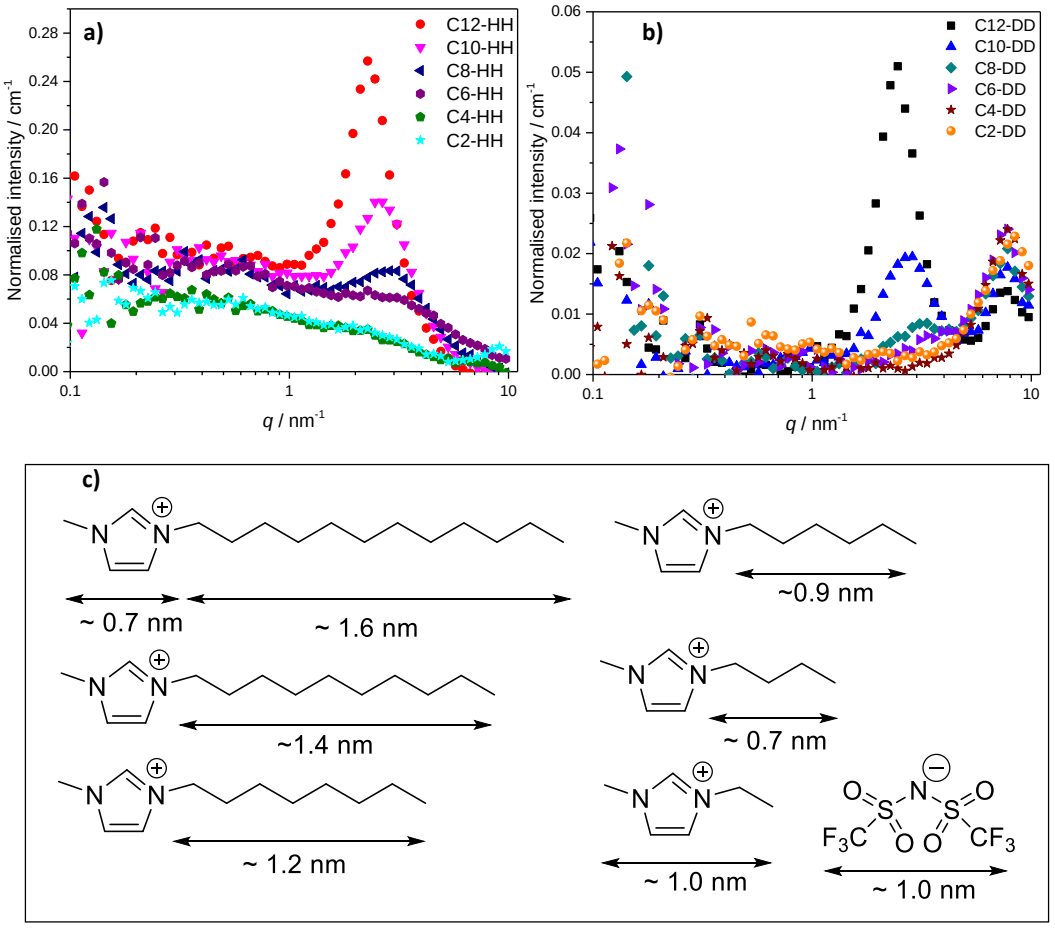

Figure 2.6: SANS data, normalised to the background, for: a) C*n*-HH; b) C*n*-DD, (*n* = 2, 4, 6, 8, 10, 12); c) the molecular length scales for the ions in the system, these are approximate values due to conformational flexibility.

2.5.1. Pure Ionic Liquids [C$_n$C$_1$im][Tf$_2$N] where n = 2, 4, 6

The SANS data for the [C$_n$C$_1$im][Tf$_2$N] ILs where n < 8 are shown in Figure 2.7. The data for these ILs feature a charge-order peak (COP) that appears around 8 nm^{-1}, which is seen in all the fully deuterated contrasts and C2-HH. This is because the scattering intensity, for the COP, is a function of the difference in SLDs between the cationic imidazolium head-group and the anion, which is large in C*n*-DD and small in C*n*-HH. This, in combination with high backgrounds due to the high degree of incoherent scattering from the proteo-rich molecules, results in the COP not being visible. The rest of the data range shows little scattering for the C*n*-DD contrasts, while the C*n*-HH contrasts show some scattering at lower-*q*, due to incoherent scattering. The SANS fitting parameters and the derived parameters are found in Table 2.1.

All the C*n*-DD contrasts fit well to a peak Lorentz model for the COP suggesting there is no alkyl chain ordering in these systems. The C*n*-HH contrasts fit well to the Lorentz model or the Lorentz + peak Lorentz model, where the COP is visible. The COP shifts to lower *q* values on increasing *n*, which has been found previously and is related to the stretching of the polar network.[81, 91, 98-102]

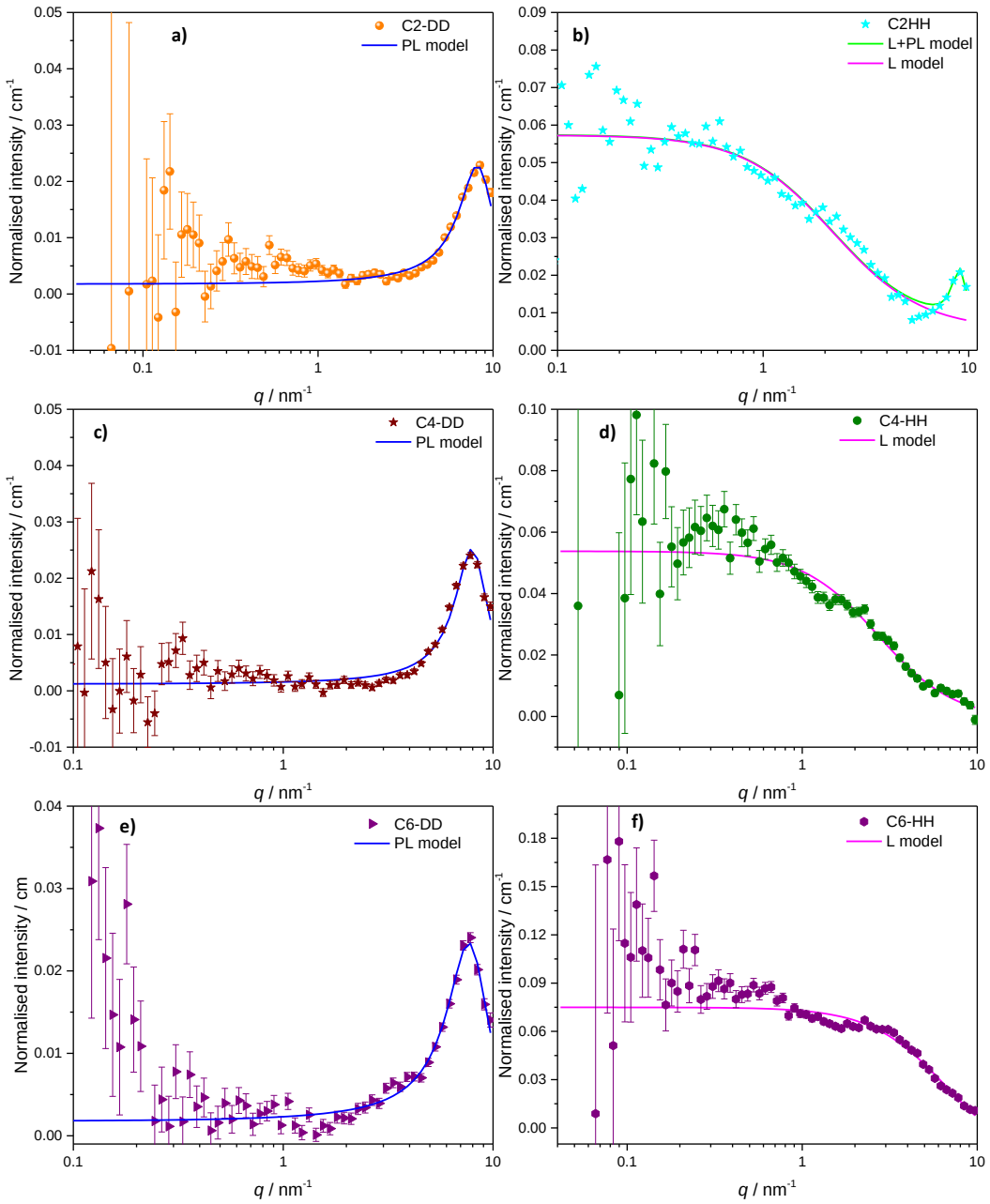

Figure 2.7: Fits to the SANS data for $[C_nC_1im][Tf_2N]$ n = 2, 4, 6. Peak Lorentz (PL, blue: a, c, d) model, Lorentz + peak Lorentz (L+PL, green: b) model and the Lorentz (L, magenta: b, d, f) model. All the data are normalised to the background.

Table 2.1: SANS fitting parameters and derived parameters for C*n*-HH and C*n*-DD (*n* = 6, 4, 2).

	Lorentz + Peak Lorentz		
	Correlation length / nm	COP *d*-Spacing / nm	COP position / nm^{-1}
C2-HH	0.5	0.7	9.0
C2-DD	–	0.8	8.1
C4-HH	0.4	–	–
C4-DD	–	0.8	7.8
C6-HH	0.1	–	–
C6-DD	–	0.8	7.7

2.5.2. Pure Ionic Liquids [$C_nC_1$im][Tf_2N] where *n* = 12, 10, 8.

The SANS data for the [$C_nC_1$im][Tf_2N] (*n* = 12, 10, 8) ILs show two features, Figure 2.8. The first is a PNPP that appears around 2.5 nm^{-1}, which moves to lower *q* and increases in intensity as *n* increases. The PNPP is characteristic of the scattering seen in nanostructured ILs. The second feature is the COP that appears around 8 nm^{-1}, which is seen only in the fully deuterated contrasts, for reasons detailed above. These SANS data have been fitted to, where appropriate, the: Lorentz + peak Lorentz model, peak Lorentz + peak Lorentz model, and the Teubner-Strey model, Figure 2.8. The SANS fitting parameters and the derived parameters are summarised in Table 2.2.

For these ILs, the scattering for the PNPP can be described by a single Lorentzian peak and where the COP is visible, a peak Lorentz + peak Lorentz model. However, the C*n*-HH contrasts have additional scattering at low-*q* (below ~ 4 nm^{-1}), which can be accounted for by the addition of a Lorentzian component. The Teubner-Strey model can also be applied to these systems, although these models also underestimate the scattering at lower *q*. Poor fits to the Teubner-Strey model have also been seen in ultra-flexible microemulsions due to a lack of a 'sharp' interface between the two phases.[103]

For imidazolium ILs where *n* ≥ 8, the system can be described as a bicontinuous network of continuous apolar domains, comprising of the alkyl chains and a polar network of the $[Tf_2N]^-$ anions and imidazolium head groups. This is indicated by the clear PNPP and the negative amphiphile strength given by the Teubner-Strey model. This bicontinuous network undergoes changes upon increasing chain length (*n*), and the PNPP shifts to lower *q* with increasing *n*, which is associated with an increase in

d-spacing, seen in the fitting and derived parameters in Table 2.2 for all models. The *d*-spacing increases from ~ 2.0 nm for $[C_8C_1im][Tf_2N]$, to ~2.3 nm for $[C_{10}C_1im][Tf_2N]$, and to ~ 2.5 nm for $[C_{12}C_1im][Tf_2N]$, which can be related directly to the length of the molecules, Figure 2.5. Thus, a bilayer structure, constructed of interdigitated or highly folded alkyl chains, is present. The scatterer size, and correlation length from the Teubner-Strey models both relate to the size of the scattering object. For both models these values increase upon increasing alkyl chain length from ~ 0.6 nm to 1.7 nm, suggesting that the length scale of the alkyl chain regions is becoming larger upon increasing *n* and the alkyl chains are either interdigitated or highly folded, agreeing with the picture given by the *d*-spacings.

The difference between the *d*-spacing and correlation length, in the TS or PL models, gives a length scale associated with the polar network. In all cases this length scale is ~1.2 nm which corresponds to the molecular lengths of the $[Tf_2N]^-$ anion and the imidazolium head group of $[C_nC_1im]^+$ cation.

The Teubner-Strey, peak Lorentz + peak Lorentz and the peak Lorentz component of the Lorentz + peak Lorentz models all suggest similar *d*-spacing and correlation lengths for each contrast.

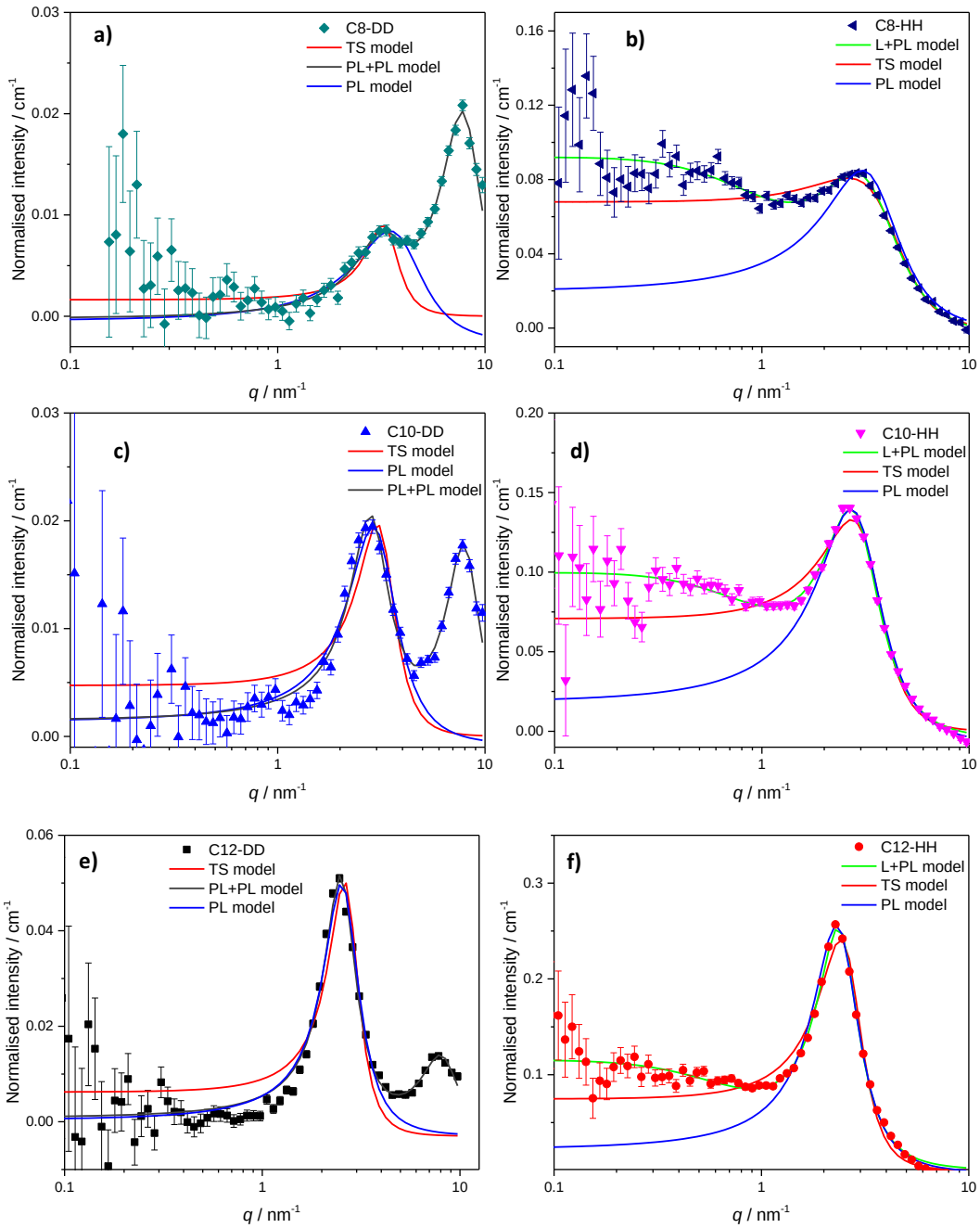

Figure 2.8: Fits to the Teubner-Strey (TS, red: a, b, c, d, e, f) model, peak Lorentz (PL, blue: a, b, c, d, e, f) model, Lorentz + peak Lorentz (L+PL, green: b, d, f),model and the peak Lorentz + peak Lorentz (PL+PL, grey: a, c, e) model, for the SANS data for $[C_nC_1im][Tf_2N]$ n = 8, 10, 12. All the data are normalised to the background.

Table 2.2: Selected SANS fitting parameters and derived parameters for C*n*-HH and C*n*-DD (*n* = 12, 10, 8, 6, 4, 2).

	Lorentz + Peak Lorentz			Teubner-Strey			Peak Lorentz + Peak Lorentz				
$[C_nC_1im][Tf_2N]$, *n*	correlation length / nm	*d*-Spacing / nm	Scatterer size / nm	Correlation Length / nm	*d*-Spacing / nm	Amphiphile strength, γ	COP *d*-Spacing / nm	COP scatterer size / nm	PNPP *d*-Spacing / nm	PNPP scatterer size / nm	COP position/ nm^{-1}
C8-HH	1.0	2.1	0.6	0.5	1.8	-0.7	–	–	2.1	0.6	–
C8-DD	–	1.8	0.6	0.8	1.8	-0.9	0.8	0.4	2.0	1.0	7.8
C10-HH	1.0	2.3	0.9	0.8	2.1	-0.7	–	–	2.3	0.8	–
C10-DD	–	2.2	1.0	0.8	2.0	-0.9	0.8	0.5	2.3	1.3	7.9
C12-HH	1.3	2.7	1.4	1.3	2.5	-0.8	–	–	2.7	1.3	–
C12-DD	–	2.5	1.5	1.7	2.4	-0.9	0.8	0.4	2.5	1.7	8.0

2.5.3. SANS of [$C_nC_1$im][Tf_2N] (n = 12, 2)

The SANS data for [$C_nC_1$im][Tf_2N] ionic liquids (n = 2, 4, 6, 8, 10, 12) discussed above was all collected on Sans2d during July 2016. In total three visits were made to carry out SANS experiments reported in this chapter, two to Sans2d and one to D22. In each visit SANS data was collected on a newly synthesised batch of C12-HH, Figure 2.9. The SANS fitting and derived parameters are summarised in Table 2.3.

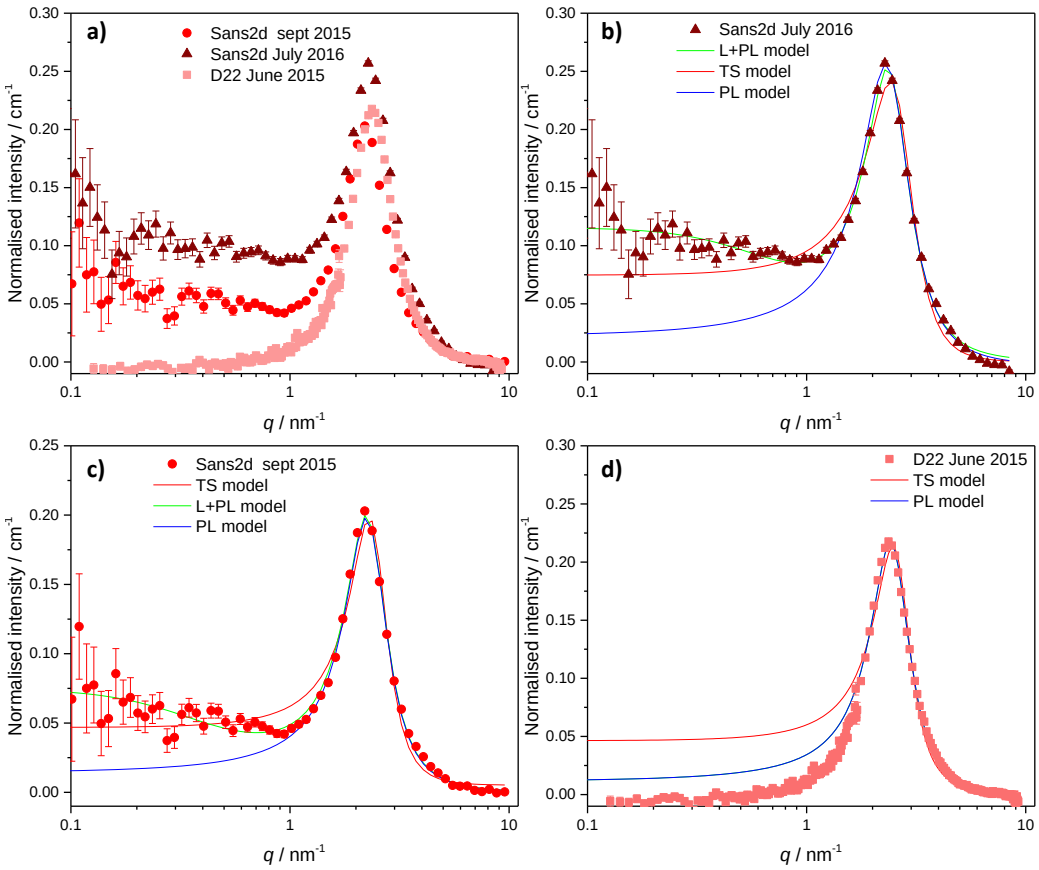

Figure 2.9: SANS data of C12-HH and fits to the Teubner-Strey (TS, red: b, c, d), model the Lorentz + peak Lorentz (L+PL, green: b, c) model, and the peak Lorentz model (PL, blue: b, c, d). All the data are normalised to the background.

Table 2.3: Selected SANS fitting parameters and derived parameters for C12-HH.

	Lorentz + Peak Lorentz			Teubner-Strey Model		
C12-HH collected on	Correlation length / nm	d-Spacing / nm	Scatterer size / nm	Correlation Length / nm	d-Spacing / nm	Amphiphile strength, γ
ILL June 2015[a]	–	2.7	1.9	1.6	2.5	-0.9
ISIS Sept 2015	2.5	2.8	1.6	1.7	2.6	-0.9
ISIS July 2016	1.3	2.7	1.4	1.3	2.5	-0.8
Average	1.9 ± 0.6	2.73 ± 0.04	1.6 ± 0.1	1.5 ± 0.1	2.53 ± 0.06	-0.87 ± 0.02

[a]No Lorentz model was used to fit.

The SANS data of the repeats of C12-HH all show a PNPP and differing amounts of low-*q* (below ~ 4 nm^{-1}) scattering, with the data collected on D22 in June 2015 having the least low-*q* scattering and the data collected on Sans2d in July 2016 having the most. The appearance of scattering at lower *q* has an effect on the fitting models used. With the data collected on D22, both the peak Lorentz and Teubner-Strey fitting models overestimate the amount of the scattering at low-*q*, while the same models underestimate the data collected on Sans2d. To make the peak Lorentz model fit better a Lorentzian model was added.

The fitting parameters and the derived parameters obtained from the fitting models all agree, apart from the correlation length from the Lorentz + peak Lorentz model, as shown by the average of the parameters for the three data sets having small standard errors, Table 2.3.

The correlation length from the Lorentz + peak Lorentz model seems to be acting as a correction factor, to take into account the extra low-*q* scattering between the different SANS data sets. All the SANS data depict a system where there is a bicontinuous network (γ ~ -0.87) of continuous apolar domains, comprising of the alkyl chains and a polar network of $[Tf_2N]^-$ anions and imidazolium head groups. The distance between the scattering objects is ~2.6 nm (*d*-spacing) and the size of the scattering objects is ~1.6 nm (scatterer size and Teubner-Strey correlation length), portraying a bilayer structure constructed of either interdigitated or folded alkyl chains.

The extra low-*q* scattering is not seen for the SANS data for separately synthesised batches of C12-DD, that were collected at different times on Sans2d, or on repeats of the same sample, Figure 2.10.a. SANS data collected on separately synthesised batches of $[C_2C_1im][Tf_2N]$, at different times displays a similar trend, in that extra low-*q* scattering is seen for C2-HH and not C2-DD as collected on Sans2d, Figure 2.10.b and c. Again this is only seen for SANS data collected on Sans2d for the fully-proteo

IL. The most likely reason for the difference in scattering at low-*q* is a function of how the data have been reduced, along with the higher incoherent scattering in the proteo-ILs, resulting in a non-linear background.

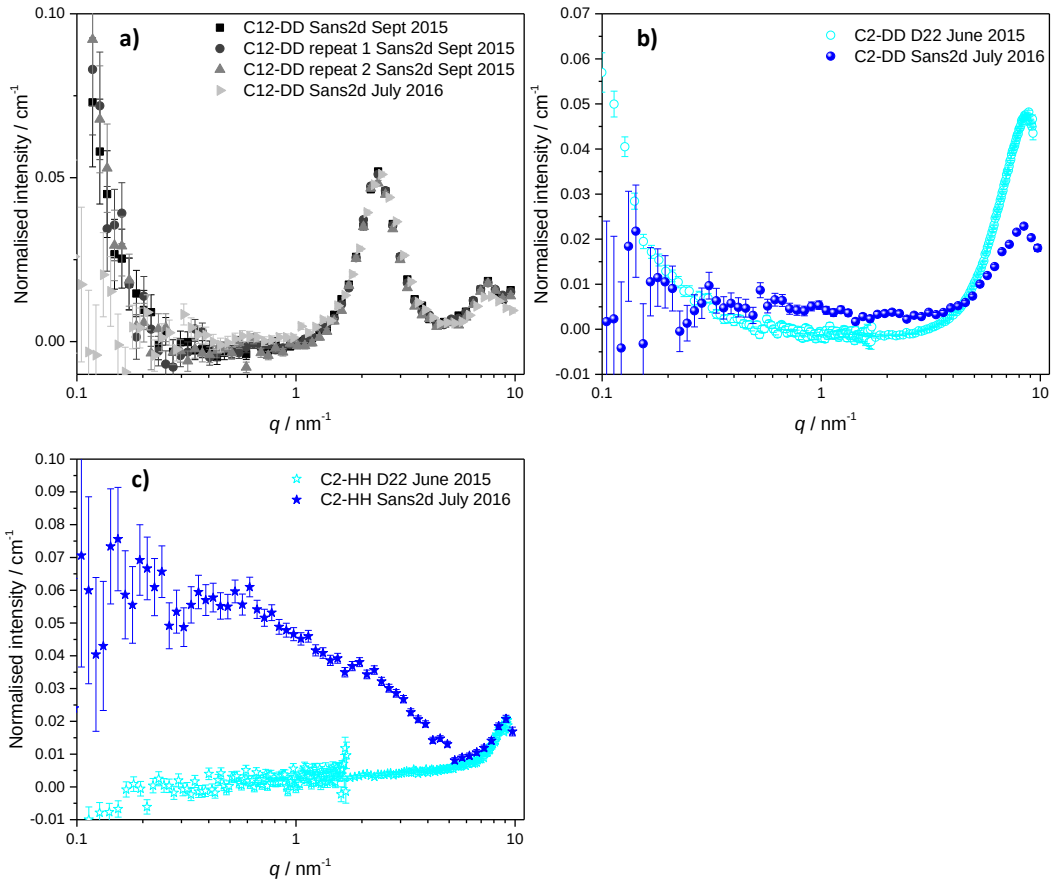

Figure 2.10: SANS data for: a) C12-DD; b) C2-DD; c) C2-HH. All the data are normalised to the background.

2.5.4. Summary of Structural Changes for [$C_nC_1$im][Tf_2N] Ionic Liquids

A summary of all the derived parameters from the Teubner-Strey model, Lorentz + peak Lorentz, and peak Lorentz + peak Lorentz models are show in Figure 2.11. When the alkyl chain is short, (n = 2, 4, and 6) the SANS data show little or no scattering in the lower q region (below ~ 4.0 nm^{-1}), suggesting that the alkyl chains are disordered in these ionic liquids. When n = 8, 10, or 12, the SANS data have a predominant PNPP that fitted to both the Teubner-Strey and peak Lorentz models; for the proteo-ILs, a Lorentz component was added to the peak Lorentz model to account for the extra scattering at lower q. In all cases, the amphiphile strength parameter is negative (~ – 0.8) suggesting a bicontinuous structure within these ILs. A cartoon of

the proposed ordering is presented in Figure 2.12. All the fitting models show that on increasing *n,* the *d*-spacing increases, relating to the length scale of the local bilayer in the IL. The models also show that the length scale of the scattering objects increase with increasing *n*, (Teubner-Strey correlation length and peak Lorentz scatterer size). The overall picture is that on increasing the chain length, *n,* of $[C_nC_1im][Tf_2N]$, the bilayer length scale increases, due to the increasing length of the alkyl chain increasing the distance between the polar network. This interpretation is consistent with the MD simulations carried out by Shimizu *et al*. who suggest that the PNPP is well defined by $[C_7C_1im][Tf_2N]$ and that the length scale of the apolar network increases with increasing *n*.[81]

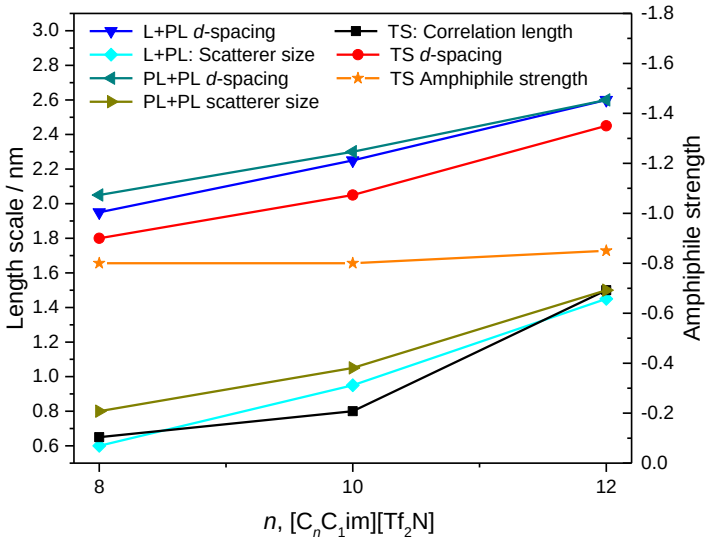

Figure 2.11: A summary of selected fitting and derived parameters from the Teubner-Strey model (TS), Lorentz (L) + peak Lorentz (PL) model for $[C_nC_1im][Tf_2N]$ (n = 12, 10, 8). Data are averaged values for the $[C_nC_1im\text{-}d_{2n+7}][Tf_2N]$ and $[C_nC_1im][Tf_2N]$ contrasts.

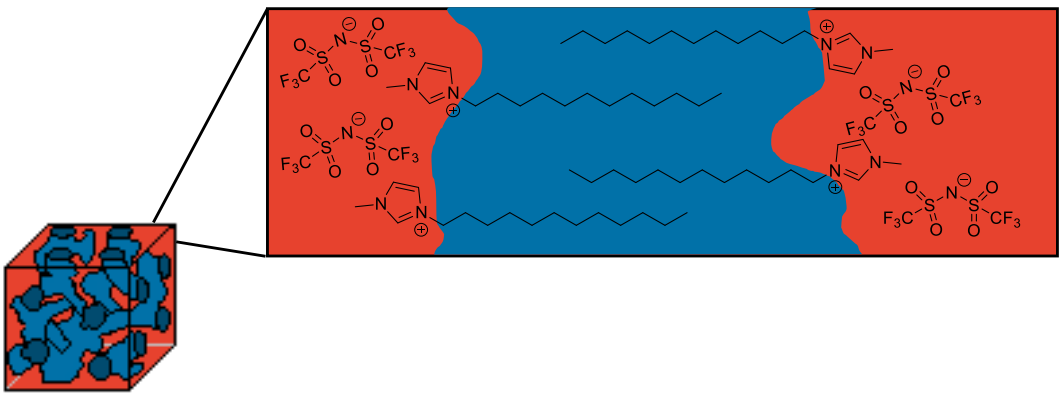

Figure 2.12: A cartoon representation of the bicontinuous structure proposed in this thesis.

All atom molecular dynamic simulations carried out by Canongia Lopes *et al*. on $[C_nC_1im][PF_6]$ (n = 2, 4, 6, 8, 12) support the picture of a nanostructured liquid, with a bicontinuous structure occurring when n > 4.[71] This value of n is lower than that found within this study, where a bicontinuous structure occurs when n > 6. This could be attributed to the different anions used in the two studies ($[PF_6]^-$ vs $[Tf_2N]^-$).

A more recent study by Canongia Lopes *et al*. provides a comprehensive study of $[C_nC_1im][Tf_2N]$ ($2 \leq n \leq 10$), in which molecular dynamics simulations are compared to X-ray scattering data collected by Triolo *et al*.[81, 83] The bicontinuous nanostructure was reported to occur when n > 5, with the bicontinuous domains being well defined by n > 6, which is in good agreement with the interpretation of the SANS data presented within this chapter.

Empirical potential structure refinement has been used by Hardacre *et al*. to interpret neutron scattering data from a series of $[C_nC_1im][PF_6]$ (n = 4, 6, 8) ILs.[72] The overall trends seen agree in the data presented here, in that increasing the chain length (n) results in the PNPP moving to lower q (larger distances) and increasing in intensity. The empirical potential structure refinement models reported rule out a micellar structure. The authors suggest that the PNPP is a result of a second coordination, shell along the vector of the long alkyl chains, and not from well-defined separated domains, such as that present in liquid-crystalline systems. This second coordination shell is proposed to be an outcome of the increasing anisotropy of the cation, however this does not rule out poorly organised domains of alternating cations and anions, such as the ones proposed to occur in the systems under study in this chapter.

2.6. SANS of Binary mixtures of $[C_{12}C_1im][Tf_2N]$ in $[C_2C_1im][Tf_2N]$

SANS experiments were performed on a range of compositions of a binary mixture of $[C_{12}C_1im][Tf_2N]$ in $[C_2C_1im][Tf_2N]$ ($[C_2C_1im]_{1-x}[C_{12}C_1im]_x[Tf_2N]$) ionic liquids; the contrasts, compositions and selected experimental conditions are given in Table 2.4. The SANS data are presented in seven different sections: firstly a discussion of the low compositions of $[C_{12}C_1im][Tf_2N]$ where $x \leq 0.24$; secondly, intermediate compositions where $0.24 \leq x \geq 0.52$; thirdly, higher compositions where $x > 0.52$. These are followed by a summary of the structural changes upon increasing x, after which the effect of temperature and water are discussed.

Table 2.4: Details of the mixtures and contrasts used in the SANS studies.

Isotopic contrast	Compositions	Temperature / ^{o}C	Other details
$[C_2C_1im\text{-}d_{11}]_{1-x}[C_{12}C_1im]_x[Tf_2N]$ (C12-HH in C2-DD)	x = 0, 0.01, 0.04, 0.16, 0.24, 0.32, 0.52, 0.74, 0.87, 0.96, 0.99, 1	20	
$[C_2C_1im\text{-}d_{11}]_{1-x}[C_{12}C_1im]_x[Tf_2N]$ ((C12-HH in C2-DD))	x = 0.01, 0.24, 0.74	60	
$[C_2C_1im]_{1-x}[C_{12}C_1im\text{-}d_{31}]_x[Tf_2N]$ ((C12-DD in C2-HH))	x = 0.01, 0.24, 0.74	60	
$[C_2C_1im]_{1-x}[C_{12}C_1im\text{-}d_{31}]_x[Tf_2N]$ (C12-DD in C2-HH)	x = 0, 0.01, 0.04, 0.16, 0.24, 0.32, 0.52, 0.74, 0.87, 0.96, 0.99, 1	20	
$[C_2C_1im]_{1-x}[C_{12}C_1im\text{-}d_{25}]_x[Tf_2N]$ (C12-HD in C2-HH)	x = 0.04, 0.24, 0.52, 0.87	20	
$[C_2C_1im\text{-}d_5]_{1-x}[C_{12}C_1im]_x[Tf_2N]$ (C12-HH in C2-HD)	x = 0.04, 0.24, 0.52, 0.87	20	
$[C_2C_1im]_{1-x}[C_{12}C_1im]_x[Tf_2N]$ (C12-HH in C2-HH)	x = 0.04, 0.24, 0.52, 0.87	20	
$[C_{12}C_1im\text{-}d_{31}][Tf_2N]$ (C12-DD)	–	20	Saturated with H_2O
$[C_2C_1im\text{-}d_{11}]_{1-x}[C_{12}C_1im]_x[Tf_2N]$ (C12-HH in C2-DD)	x = 0.24	20	Saturated with H_2O

2.6.1. Low Compositions of $[C_{12}C_1im][Tf_2N]$ where $x \leq 0.24$

SANS data for the ionic liquid mixtures where $x \leq 0.24$ are shown in Figure 2.13 and five different compositions were studied (x = 0, 0.01, 0.04, 0.16, 0.24) for two isotropic contrasts, C12-HH in C2-DD and C12-DD in C2-HH. Three additional contrasts (C12-HD in C2-HH, C12-HH in C2-HD, and C12-HH in C2-HH) were studied for two compositions (x = 0.04, 0.24).

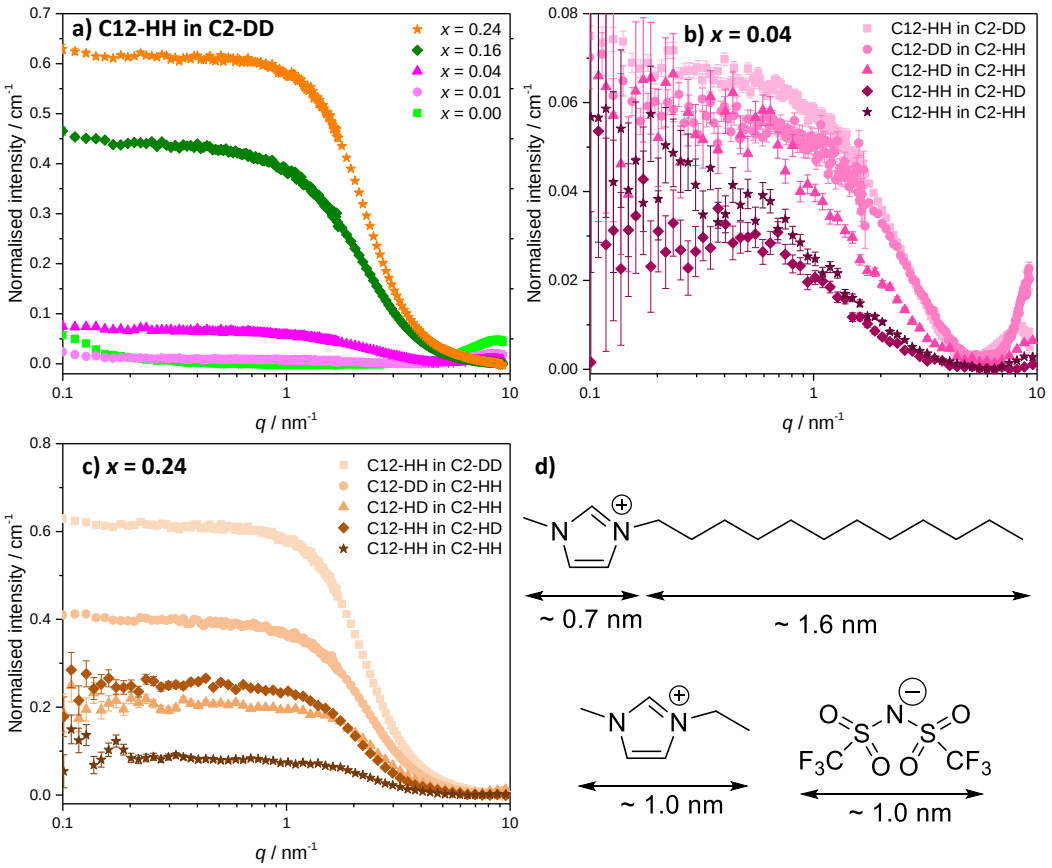

Figure 2.13: SANS data for $x \leq 0.24$: a) $[C_2C_1im\text{-}d_{11}]_{1-x}[C_{12}C_1im]_x[Tf_2N]$ (C12-HH in C2-DD); b) all contrasts for $x = 0.04$; c) all contrasts for $x = 0.24$; d) approximate molecular length scales for the ions in this systems. All the data are normalised to the background.

The SANS data in this compositional range have two features. The COP and low-q (below ~ 4 nm^{-1}) scattering that increases in relative intensity with increasing x and is related to the formation of small aggregates of C12 alkyl chains from $[C_{12}C_1im]^+$ ions within a polar network. These SANS data have been fitted to, where appropriate, the: sphere model; ellipsoid model; Teubner-Strey model; Lorentz; peak Lorentz; and Lorentz + peak Lorentz model. Selected fitting parameters and derived parameters are shown in Table 2.5.

Table 2.5: Selected SANS fitting parameters and derived parameters. Data are average values from fitting of both the C12-HH in C2-DD and C12-DD in C2-HH contrasts at that composition, except at x = 0.04 and 0.24 where averages and standard errors from five compositions and repeat measurements are given. The Lorentz + Peak Lorentz model is not included, as in most cases fits are poorer than the shape-based or Teubner-Strey models for this compositional range.

		Sphere model		Ellipsoid model			Teubner-Strey model		
Composition, x	COP position / nm^{-1}	Radius / nm	Volume fraction	Axial radius / nm	Equatorial radius / nm	Volume fraction	Correlation length / nm	d-spacing / nm	Amphiphile strength, γ
0	8.8	–	–	–	–	–	–	–	–
0.01	8.7	0.8	0.01	0.9	0.8	0.01	0.5	4.5	0.3
0.04	8.6	0.93±0.05	0.017±0.005	2.0±.03	0.62±0.02	0.02±0.01	0.50±0.04	7.51±1.66	0.62±0.09
0.16	–	0.9	0.07	1.4	0.6	0.10	0.5	4.4	0.4
0.24	–	0.82±0.02	0.11±0.02	1.24±0.06	0.65±0.01	0.11±0.02	0.57±0.02	3.9±0.1	0.09±0.02

When x = 0 (pure [C_2C_1im][Tf_2N]) the data essentially show no scattering at low q and can be modelled to a Lorentzian or a Lorentz + peak Lorentz model peak for the COP. When x = 0.01 and 0.04, all the scattering models fit well as the scattering data at low-q have large error bars, Figure 2.14. The system can be described as consisting of small aggregates of C12 alkyl chains that are either spherical or prolate ellipsoids. When $x \geq 0.16$ the sphere and ellipsoid models fit the data less well, although, all compositions fit well to the TS model.

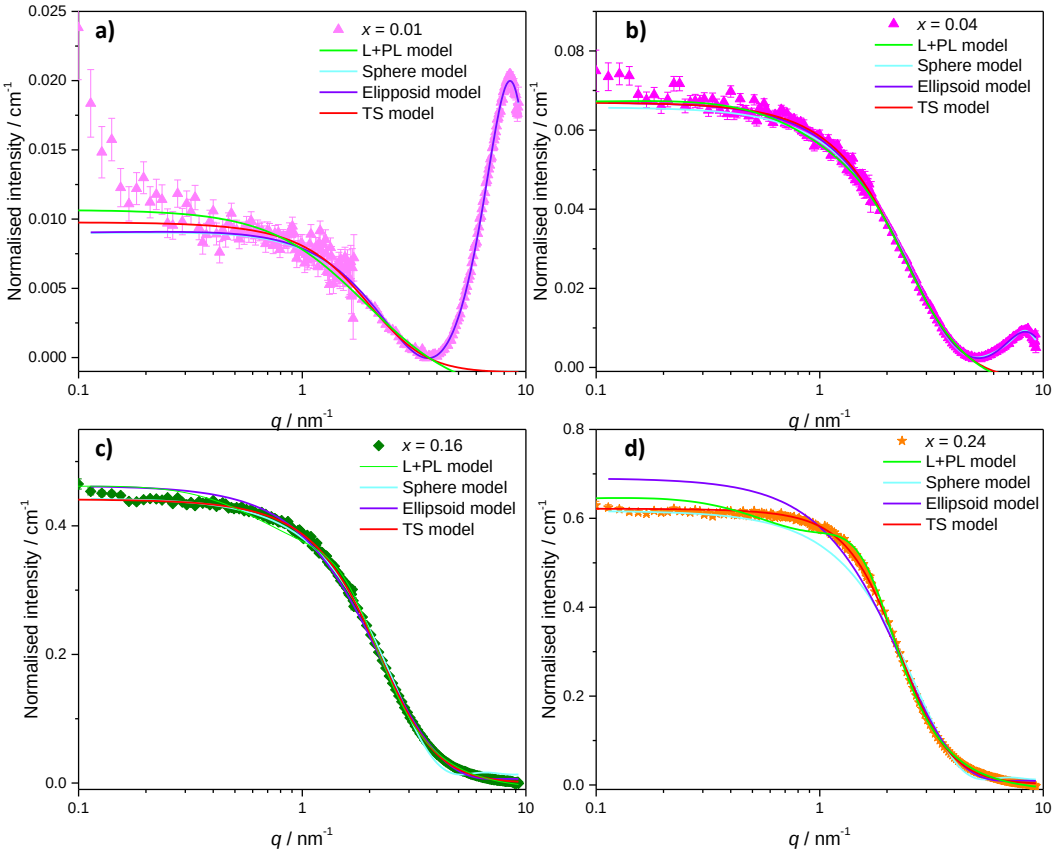

Figure 2.14: SANS data at: a) x = 0.01; b) x = 0.04; c) x = 0.16; d) x = 0.24, for [C_2C_1im-d_{11}]$_{1-x}$[$C_{12}C_1$im]$_x$[Tf_2N] (fits to other contrasts are similar). Fits to the Lorentz + Peak Lorentz (L+PL model), sphere, ellipsoid, Teubner-Strey (TS model) and are shown in green, cyan, violet, and red respectively. All the data are normalised to the background.

To gain insight into the liquid structure, the parameters derived from the fitting models (Table 2.5) can be compared to the molecular length scales for the anions and cations in the system, Figure 2.13. When $x \leq 0.24$, the system consists of relatively small scattering objects, with length scales of ~1.6 nm for the spherical model and ~2.5 × 1.2 nm for the ellipsoid model. The TS model agrees with this model suggesting an aggregated/micellar structure ($0 < \gamma < 1$), but the scatterer size from

the TS model suggests the aggregates are ~0.5 nm in length, which is smaller than the sphere and ellipsoid models. This could be due to the way the shape-based models were fitted. The SLD of the solvent was set to the calculated SLD of the solvent, while the SLD of the scattering objects were set to the calculated SLD of the alkyl chains, modelling the size of the alkyl chain aggregates directly. However, the TS model uses an empirical formula based on the fluctuations of order, therefore providing the length scale of the average size of the alkyl domain (aggregate) in all directions. However, all the models agree that the average size of the aggregates do not significantly change on increasing *x*, and the number density of aggregates does increase, as shown by the increase in volume fraction and also by the decreasing *d*-spacing (distance between scattering objects).

For *x* = 0.04 and 0.24, data were collected for five isotopic contrasts, Figure 2.13, the different contrasts, in general, indicating similar liquid nanostructuring, Table 2.6. This is expected as the largest differences in SLDs in the system is between the C12 aggregates and the polar networks. However for *x* = 0.04, the data suggests slightly longer length scales for the scattering objects for C12-HD in C2-HH, C12-HH in C2-HD, and C12-HH in C2-HH, but this may just be a product of the uncertainty in the fits as the SANS data for these contrasts is weak, with large error bars and of low intensity. The intensity differences are due to the proportion of deuterium and hydrogen in the samples, higher proportions of hydrogen leading to more incoherent scattering, while the scattering intensity is related to the difference in scattering length density between the two components. By carrying out SANS measurements on multiple contrasts, the fitted and derived parameters, for chemically identical but isotopically different samples, can be averaged. For *x* = 0.04 and 0.24, five contrasts were measured and the average taken are reported along with the standard errors in Table 2.5 and Table 2.6.

Table 2.6: Selected SANS fitting parameters and derived parameters for x = 0.04 and 0.24 for the five different contrasts and their averages. Fitting to the Teubner-Strey model for contrast C12-HD in C2-HH of composition x = 0.04 was poor and is not reported.

		Sphere model		Ellipsoid model			Teubner-Strey model		
Composition, x	Contrast	Radius / nm	Volume fraction	Axial radius / nm	Equatorial radius / nm	Volume fraction	Correlation length / nm	*d*-spacing / nm	Amphiphile strength, *γ*
0.04	C12-HH in C2-DD	0.8	0.02	1.2	0.6	0.03	0.4	4.4	0.5
0.04	C12-DD in C2-HH	0.8	0.04	1.1	0.6	0.04	0.4	4.1	0.4
0.04	C12-HD in C2-HH	0.9	0.02	2.2	0.6	0.02	–	–	–
0.04	C12-HH in C2HD	1.1	0.00	2.7	0.7	0.00	0.6	11.7	0.8
0.04	C12-HH in C2HH	1.0	0.02	3.0	0.6	0.02	0.6	9.9	0.8
0.04	Average	0.93±0.05	0.017±0.005	2.0±.03	0.62±0.02	0.02±0.01	0.50±0.04	7.51±1.66	0.62±0.09
0.24	C12-HH in C2-DD	0.8	0.10	1.4	0.6	0.12	0.6	4.0	0.1
0.24	C12-DD in C2-HH	0.8	0.15	1.3	0.6	0.18	0.5	4.0	0.2
0.24	C12-HD in C2-HH	0.8	0.15	1.0	0.7	0.16	0.6	3.6	0.0
0.24	C12-HH in C2HD	0.9	0.06	1.4	0.7	0.07	0.6	4.2	0.1
0.24	C12-HH in C2HH	0.8	0.04	1.2	0.6	0.05	0.6	3.8	0.1
0.24	Average	0.82±0.02	0.11±0.02	1.24±0.06	0.65±0.01	0.11±0.02	0.57±0.02	3.9±0.1	0.09±0.02

2.6.2. Intermediate Compositions of $[C_{12}C_1im][Tf_2N]$ where $0.24 \leq x \leq 0.52$

SANS data for the ionic liquid mixtures for $0.24 \leq x \leq 0.52$ are shown in Figure 2.15. Three different compositions were studied; $x = 0.32$ for two isotropic contrasts, C12-HH in C2-DD and C12-DD in C2-HH; and three contrasts (C12-HD in C2-HH, C12-HH in C2-HD, and C12-HH in C2-HH) were studied for two compositions ($x = 0.24$, 0.52), for which the standard error is reported along with the average of the derived parameters, Table 2.7.

The system undergoes significant organisational change in this compositional range. The nanostructure of the IL mixtures changes from aggregates of C12 alkyl chains to ILs where the volume fraction of the system occupied by the C12 chains is large enough that they are able to percolate to form a continuous, apolar subphase. Qualitatively this can be seen visually in Figure 2.15 by the appearance of the PNPP at intermediate q values of ~1.2 to 2.5 nm. When $x > 0.24$ the data no longer fit to shape-based scattering models, thus they will not be discussed.

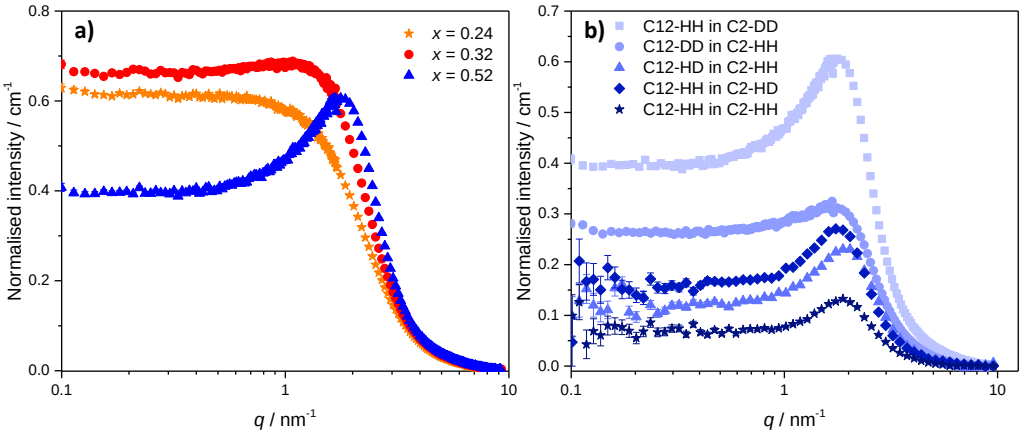

Figure 2.15: SANS data for $[C_2C_1im\text{-}d_{11}]_{1-x}[C_{12}C_1im]_x[Tf_2N]$; a) where $0.24 \leq x \leq 0.52$ and; b) all contrasts for $x = 0.52$. All the data are normalised to the background.

The SANS data, for $0.24 \leq x \leq 0.52$ fit well to the Teubner-Strey model as shown in Figure 2.14 and Figure 2.16. The PNPP starts to emerge visibly around 1.5 nm^{-1}, when $x = 0.32$, yet it is likely that there is a small PNPP component to the $x = 0.24$ data as the shape based models fit poorly. The PNPP emerging around $x = 0.32$ agrees with previously reported SAXS data and MD simulations,[91, 104] and this data fit well to the Lorentz + Peak Lorentz model when there is a defined PNPP, $x > 0.32$.

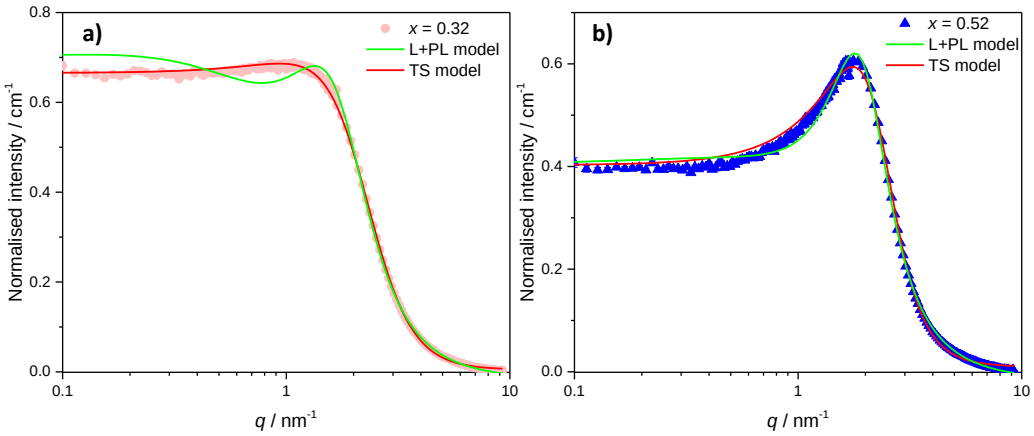

Figure 2.16: SANS data for $[C_2C_1im\text{-}d_{11}]_{1-x}[C_{12}C_1im]_x[Tf_2N]$ (fits to other contrasts are similar): a) x = 0.32 and *b*) x = 0.52. Fits to the Lorentz + Peak Lorentz (L+PL model) and Teubner-Strey (TS model) are shown in green and red, respectively. All the data are normalised to the background.

The amphiphile strength parameters from the TS models for x = 0.24 to x = 0.52 show a decrease from 0.1 to -0.5. The value has changed sign, indicating a change in structure from isolated aggregates to a bicontinuous system. The *d*-spacing decreases dramatically between x = 0.24 to 0.25 from 4.0 nm to 3.1 nm, consistent with a significant structural change in the liquids, as the aggregates begin to coalesce to form an apolar network within the IL.

Table 2.7: Derived parameters for the Teubner-Strey, peak Lorentz (PL) and Lorentz (L) + Peak Lorentz models for all compositions. Data are average values from fitting of both the C12-HH in C2-DD and C12-DD in C2-HH contrasts at that composition, except at x = 0.24, 0.52 and 0.87 where averages and standard errors from five compositions and repeat measurements are given.

		Teubner-Strey model			Lorentz + Peak Lorentz model		
Composition, *x*	PNPP position / nm^{-1}	Correlation length /nm	*d*-spacing / nm	Amphiphile strength, *γ*	Correlation length / nm	*d*-spacing / nm	Scatterer size / nm
0	-	-	-	-	-	-	-
0.01	-	0.5	4.5	0.3	-	-	-
0.04	-	0.50±0.04	7.51±1.66	0.62±0.09	-	-	-
0.16	-	0.5	4.4	0.4	-	-	-
0.24	-	0.6±0.01	4.0±0.1	0.1±0.02	-	-	-
0.32	1.5	0.6	3.7	-0.1	1.1	4.3	1.0
0.52	1.8	1.0±0.07	3.0±0.05	-0.6±0.05	0.8±0.08	3.4±0.05	1.2±0.06
0.74	2.2	1.1	2.7	-0.7	0.8	2.9	1.3
0.87	2.3	1.5±0.08	2.6±0.04	-0.9±0.01	1.6±0.3	2.8±0.04	1.5±0.07
0.96	2.4	1.6	2.5	-0.9	-	2.6	1.5
0.99	2.5	1.8	2.4	-0.9	-	2.5	1.6
1	2.3	1.9	2.5	-0.9	-	2.7	1.9

2.6.3. High Compositions of $[C_{12}C_1im][Tf_2N]$ where $x \geq 0.52$

SANS data for the ionic liquid mixtures for $x \geq 0.52$ are shown in Figure 2.17. Six different compositions were studied (x = 0.52, 0.74, 0.87, 0.96, 0.99, 1) for two isotropic contrasts, C12-HH in C2-DD and C12-DD in C2-HH. Three additional contrasts (C12-HD in C2-HH, C12-HH in C2-HD, and C12-HH in C2-HH) were studied for two compositions (x = 0.52, 0.87), for which standard error is reported along with the average of the derived parameters, Table 2.7.

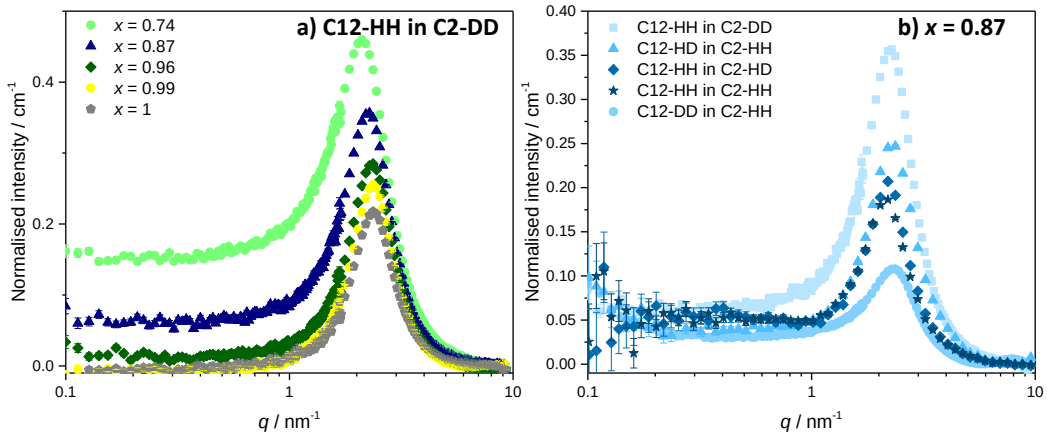

Figure 2.17: SANS data for $[C_2C_1im\text{-}d_{11}]_{1-x}[C_{12}C_1im]_x[Tf_2N]$: a) x > 0.52; b) all contrasts for x = 0.87.

The SANS data, in this compositional range, are dominated by a large PNPP, which is characteristic of the scattering seen in nanostructured pure ILs such as $[C_{12}C_1im][Tf_2N]$.[81] The position of the PNPP moves linearly to higher q between x = 0.52 and 0.99, increasing from 1.8 nm^{-1} to 2.5 nm^{-1}, after which there is a shift to 2.3 nm^{-1} when x = 1. There is also, in addition to the PNPP, some scattering at lower q at x = 0.52, which reduces in intensity with increasing x. In this compositional range, the data were fitted to the Teubner-Strey, peak Lorentz and Lorentz + peak Lorentz models, Figure 2.18.

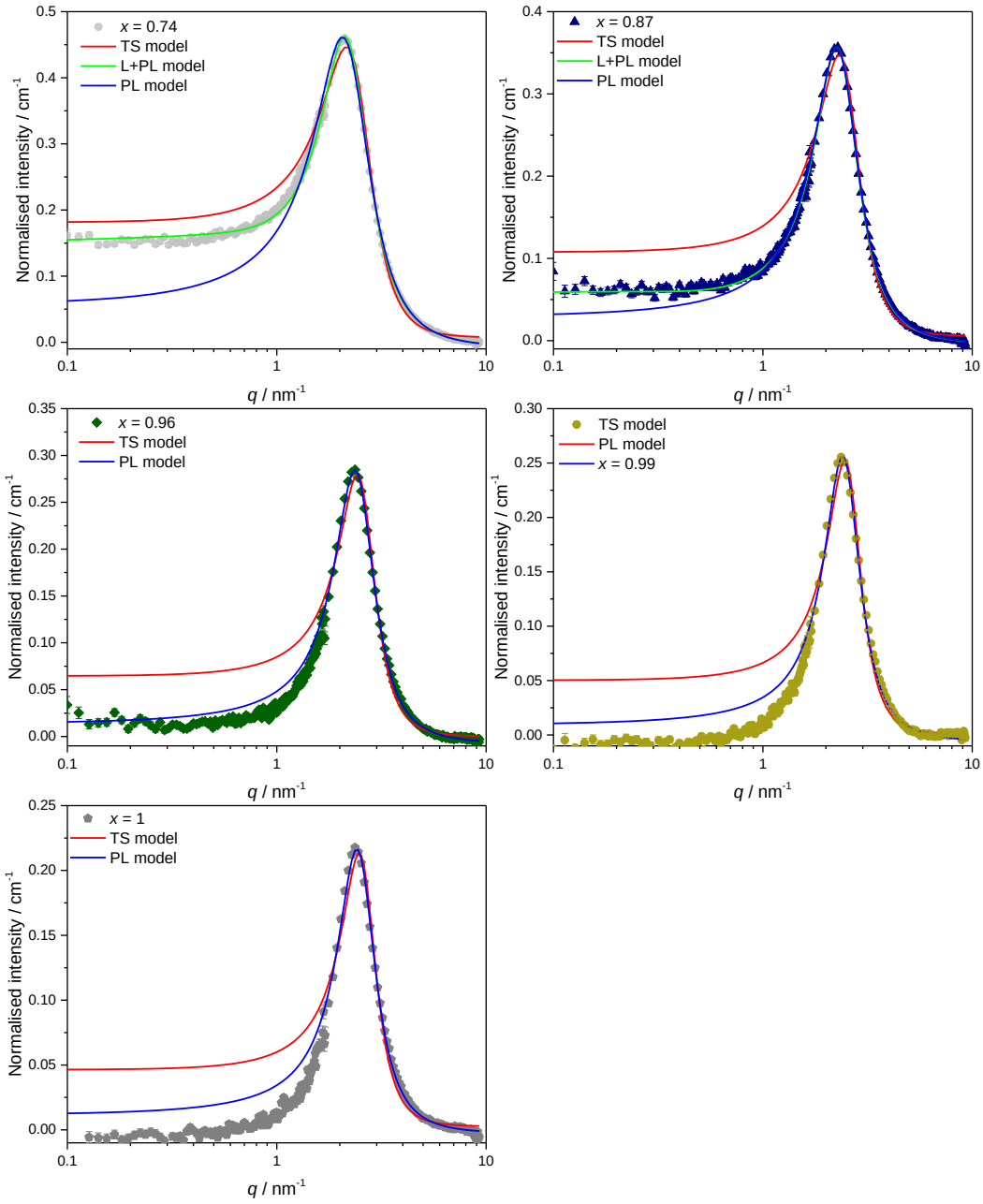

Figure 2.18: Fits to the Teubner-Strey (TS) model, Lorentz + Peak Lorentz (L+PL) model and peak Lorentz (PL) model are shown in red, green, and blue respectively for $[C_2C_1im\text{-}d_{11}]_{1-x}[C_{12}C_1im]_x[Tf_2N]$ where x = 0.74, 0.87, 0.96, 0.99. All the data are normalised to the background.

The TS model overestimates the amount of low-q scattering, while the peak Lorentz model underestimates the amount of low-q scattering for x = 0.52, 0.74, and 0.87. A Lorentz component was added to the peak Lorentz to account for the extra scattering (L+PL). The L+PL model has been used successfully to describe ultra-flexible microemulsions that do not have a sharp interface between the two phases.[103]

Within this compositional range, the structure can be described as a bicontinuous (percolated) network of polar domains containing $[Tf_2N]^-$ anions, $[C_2C_1im]^+$ cations,

and imidazolium head groups of the $[C_{12}C_1im]^+$ cations, and a continuous apolar domain containing the C12 alkyl chains of the $[C_{12}C_1im]^+$ cations. This is indicated by the clear PNPP and the TS model's amphiphile strength values being between 0 and -1. With increasing *x,* the PNPP moves to higher *q*, which is associated with a decrease in *d*-spacing, from 3.0 nm for *x* = 0.52 to 2.5 nm for *x* = 1, in the TS and PL models. This is indicative of a contraction of the bilayer structure and agrees with SAXS data.[91] An argument can be made that this contraction is due either to interdigitation, or folding, of the alkyl chains, but this is inconsistent with molecular dynamic simulations, which suggest there is little change in interdigitation with increasing *x*.[104] The correlation length and scatterer size also tell a different story, the correlation lengths and scatterer size of the TS and PL models indicate that the alkyl chain region length scale increases with increasing *x*, from ~1 nm at *x* = 0.52 to 1.9 nm at *x* = 1. This can be explained by considering the polar network length scale, which can be inferred by looking at the difference in length scale between the *d*-spacing and correlation length, Table 2.8. As *x* increases, the length scale of the polar network decreases down to the length associated with pure $[C_{12}C_1im][Tf_2N]$. The polar domain length scale decreases as the amount of $[C_2C_1im]^+$ in the system reduces (*x* increases). When large amounts of $[C_2C_1im]^+$ are present, they are incorporated into the polar network, resulting in its volume expanding. Thus, when less $[C_2C_1im]^+$ is present, the polar network shrinks back down to the size of the network in pure $[C_{12}C_1im][Tf_2N]$. This is compounded by the alkyl chain domain increasing in volume inducing a structural change in the polar network, as the alkyl chains are attached to the imidazolium cations. The polar network must stretch, or expand slightly, to account for the increasing alkyl chain domain upon increasing *x*. Molecular dynamic simulations suggest that the position of the COP changes with increasing *x*, indicating a change in distances between anions.[91] The global effect of these changes, in both the polar and apolar networks, results in a reduction in the distance between the centre of the polar network, separated by the alkyl chains (bilayer thickness), giving rise to the change in the PNPP position and the *d*-spacing.

Table 2.8: Polar length scale calculated by the difference between the *d*-spacing and correlation lengths from the derived parameters for the Teubner-Strey, and the difference between the *d*-spacing and scatterer size for the peak Lorentz (PL) or Peak Lorentz models. For all compositions the average of the two models is reported, excluding $x \leq 0.24$ as these could not be fitted to a Lorentzian peak thus only the TS parameters are used. Data are also average values from fitting of both the C12-HH in C2-DD and C12-DD in C2-HH contrasts.

Composition, x	Polar length scale / nm
0	–
0.01	4.0
0.04	3.8
0.16	3.9
0.24	3.4
0.32	3.2
0.52	2.3
0.74	1.6
0.87	1.3
0.96	1.0
0.99	0.8
1	0.7

2.6.4. Summary of the Structural Changes with Changing Composition

A summary of selected fitting and derived parameters from the Teubner-Strey, Peak Lorentz and Lorenz + peak Lorentz models are shown in Figure 2.20. It was possible to fit the Teubner-Strey model across the whole composition range, but at higher mole fractions of $[C_{12}C_1im][Tf_2N]$, the model did not fit well but the derived parameters have comparable length scale dimensions to the better fitting PL or L+PL models. Thus, the TS model can be used to describe the SANS data across all compositions.

The amphiphile strength parameter (γ) from the TS model suggests the structure of the system. When the amphiphile strength is positive but less than one ($x \leq 0.24$) aggregates form, while when γ is negative ($x \geq 0.24$) a bicontinuous structure is present. The change in sign of γ (Lifshitz line) can be associated with a percolation threshold, where the C12 alkyl chains occupy enough volume to form a continuous domain within the liquid, and is best described as a bicontinuous network of polar and apolar domains. It is possible to deduce from the data that the percolation threshold, when γ changes sign, occurs at $x \sim 0.28$ in this IL mixture. A cartoon representation of the proposed nanostructure is provided in Figure 2.19 to aid interpretation.

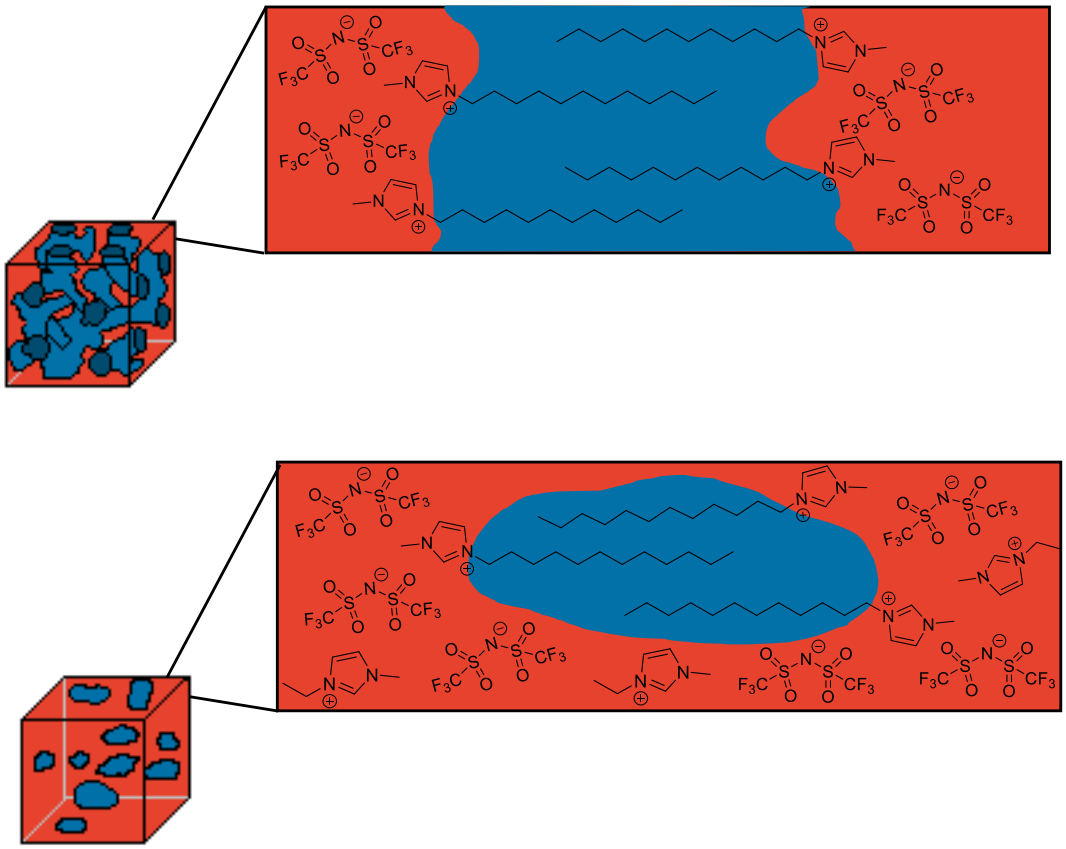

Figure 2.19: A cartoon representation of the different nanostructures proposed. Top, the bicontinuous structure; bottom, the aggregate structure.

As *x* increases, the *d*-spacing decreases smoothly from 4.5 nm at $x = 0$ to 2.5 nm at $x = 1$, which is accompanied by an increase in volume fraction of aggregates (from the shape-based models) at low mole fractions. The decrease in *d*-spacing in these mixtures is related to distance between the scattering objects, which in the case of aggregates is the distance between aggregates, while in the case of a bicontinuous network, it is the bilayer size.

The correlation length increases from 0.5 nm for $x = 0.01$ to 1.9 nm for $x = 1$. When aggregates are present ($x < 0.24$), the correlation length is associated with the length of the density fluctuation of the aggregate domains. This remains almost constant because the size of the aggregates does not fluctuate greatly. However, when the aggregates coalesce into a bicontinuous structure ($-1 < \gamma < 0$, $x > 0.24$), the correlation length now represents the alkyl chain domain length scale, as this is the length scale over which the correlation decays, indicating that the size of the alkyl chain domain increases upon increasing *x*.

Initially as *x* increases the polar length scale remains flat, this is representative of the length scale that the ordering in the polar network decays over. After $x > 0.24$ the

polar length scale decreases down to the length of the polar network in pure $[C_{12}C_1im][Tf_2N]$ as there is less $[C_2C_1im]^+$ available to swell the polar network.

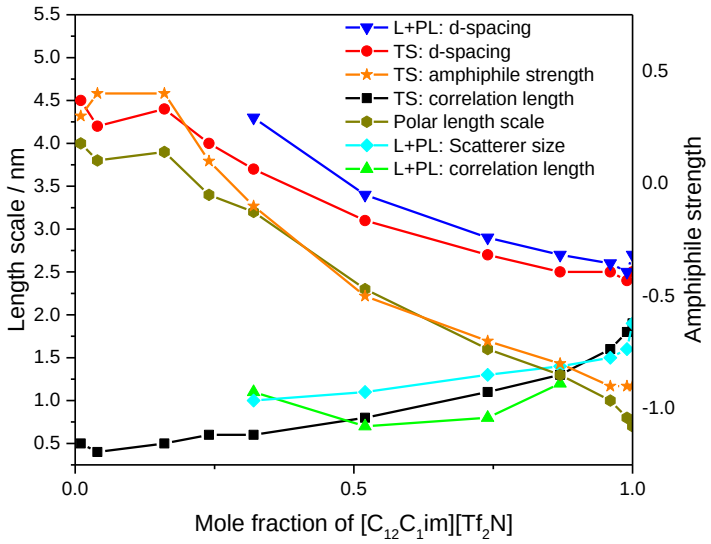

Figure 2.20: A summary of selected fitting and derived parameters from the Teubner-Strey model (TS), Lorentz (L) + peak Lorentz (PL) model. Data are averaged values for the $[C_2C_1im\text{-}d_{11}]_{1-x}[C_{12}C_1im]_x[Tf_2N]$ and $[C_2C_1im]_{1-x}[C_{12}C_1im\text{-}d_{31}]_x[Tf_2N]$ contrasts. Where a Lorentzian component of the L+PL model is missing, the fitting was done to a PL model only.

Molecular dynamics simulations on $[C_2C_1im]_{1-x}[C_{12}C_1im]_x[Tf_2N]$ (where x = 0, 0.04, 0.24, 0.32, 0.52, 0.74, 0.87, and 1) are reported by Bruce *et al*. in a comprehensive study of this binary IL mixture.[91] The calculated structure factors are in agreement with the SANS and SAXS data reported in the paper, as well as the SANS data presented in this thesis. The PNPP in the SAXS data starts to present around x = 0.24 and is well developed at x = 0.32, which is consistent with the SANS data in this chapter. Bruce *et al*. also report on the shape of the aggregates which was obtained by analysis of the MD simulation box. They describe a picture where smaller aggregates are prolate in shape that develop into progressively more globular shapes as their size increases. These globular shapes can be thought of as fragments of an apolar network. This is consistent with the SANS data modelling were at low x the data fits well to prolate shaped aggregates, while at higher x the data fits well to the Teubner-Strey model for a bicontinuous network.

Triolo *et al*. provide SAXS data for the binary IL mixtures of $[C_1C_1im]_{1-x}[C_{12}C_1im]_x[Tf_2N]$.[86] This is a similar system to the one investigated in this chapter, where a long chain IL is mixed with a short chain IL, with both ILs having a common anion. The mole fraction at which the PNPP begins to appear in Triolo's

system (x = 0.15), this is lower than that for the system studies here (x = 0.24). Both systems develop a more distinct PNPP as the mole fraction of the long chain IL increases, while also shifting to higher q. Triolo *et al*. modelled their SAXS data to a sphere model at low mole fractions, while at higher mole fractions a hard-interacting sphere model was added to fit the emerging peak in the data. It would be interesting to fit Triolo's data to the same models as used in this thesis to enable a direct comparison of the fitting parameters, especially the Teubner-strey model which could provide an indication of the structure of the system with its amphiphile strength parameter.

2.6.5. The Effect of Temperature on the Mixtures

Variable temperature studies were carried out on three compositions (x = 0.01, 0.24, and 0.74) with two contrasts (C12-HH in C2-DD and C12-DD in C2-DD), at two temperatures (20 and 60 °C). Mixtures with a low mole fraction of $[C_{12}C_1im][Tf_2N]$ (x = 0.01) were fitted to the ellipsoid and TS models, while the intermediate and high mole fraction mixtures (x = 0.24 and 0.74, respectively) were fitted to the TS model, Figure 2.21. Selected fitting and derived parameters are shown in

Table 2.9, the average of the two contrasts is reported.

There is no significant change in the d-spacing or correlation length upon heating the mixtures from 20 to 60 °C, for x = 0.24 and 0.74, even though visually the SANS scattering intensity has decreased. However the amphiphile strength increases upon increasing temperature, indicating $[C_{12}C_1im]^+$ is acting as a weaker amphiphile, suggesting that the system becomes more disordered. For x = 0.01 there is a decrease in d-spacing and axial radius on increasing the temperature, which could be due to uncertainty in the fits due to the low intensity of the scattering data.

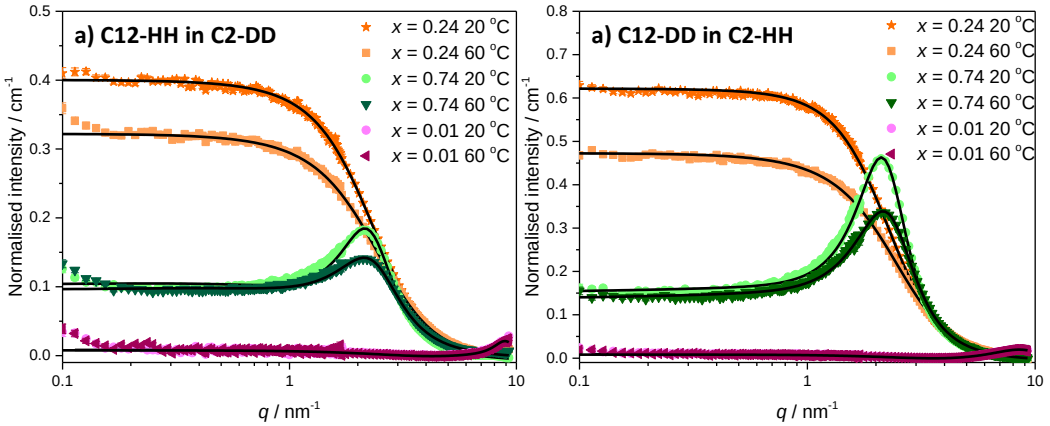

Figure 2.21: Variable temperature SANS data for three compositions (x = 0.01, 0.24 and 0.74): a) for $[C_2C_1im\text{-}d_{11}]_{1-x}[C_{12}C_1im]_x[Tf_2N]$ (C12-HH in C2-DD), and b) for $[C_2C_1im]_{1-x}[C_{12}C_1im\text{-}d_{31}]_x[Tf_2N]$ (C12-DD in C2-HH). Fits to the most appropriate scattering model are shown in black. All the data are normalised to the background.

Table 2.9: SANS fitting and derived parameters. Data are average values from fitting of both the C12-HH in C2-DD and C12-DD in C2-HH contrasts at that composition.

		Ellipsoid model			Teubner-Strey model		
Composition, x	Temperature / °C	R_a / nm	R_b / nm	Volume fraction	Correlation length / nm	d-spacing / nm	Amphiphile strength, γ
0.01	60	1.4	0.8	0.01	0.5	7.3	0.7
0.01	20	0.9	0.8	0.01	0.5	4.5	0.3
0.24	60	-	-	-	0.5	3.9	0.3
0.24	20	-	-	-	0.6	4.0	0.1
0.74	60	-	-	-	0.9	2.6	-0.6
0.74	20	-	-	-	1.1	2.7	-0.7

2.6.6. Effect of Water on the Mixtures

The effect of water on the SANS data for two compositions (x = 0.24 and 1) was investigated. Although these ILs are hydrophobic, in that they are not miscible with water, they will absorb some moisture and this can affect the physical properties, including their structure.[65] All ILs reported in this chapter were synthesised under anhydrous conditions, where appropriate, and dried carefully and stored in a N_2-filled glovebox prior to transport to the beamlines. Although the mixtures were prepared in air and the cuvettes filled in air, the exposure time to moisture in the air was minimised as much as possible as the cuvettes were sealed after filling. In order to investigate the effects of large amounts of water on the structure of these ILs the two compositions were saturated with H_2O by shaking the samples with water, letting the

two phases separate and partitioning off the water-saturated IL layer. The SANS data are shown in Figure 2.22, while the fitting and derived parameters are in Table 2.10.

When C12-DD was saturated with water (x = 1) the scattering increases slightly, yet the derived parameters from both the TS and PL models show little difference. Hence, there appears to be no significant difference in the structure of C12-DD when water was added. However, when water was added to the IL mixture composition where x = 0.24 there was a larger difference in the scattering profile and the derived parameters differ significantly. The addition of water results in both the *d*-spacing and amphiphile strength increasing. Adding water swells the polar domain, as illustrated by larger distances between aggregates (*d*-spacing), as well as leading to a more disordered system, illustrated by the amphiphile strength value increasing. The observation of a water effect in the IL mixture where x = 0.24 and not for x = 1 may be due to the difference in liquid structure between the samples, aggregates of C12 alkyl chains and bicontinuous network respectively. However, it is most likely due to the $[C_{12}C_1im][Tf_2N]$ being more hydrophobic than the x = 0.24 mixture, as it has a significantly higher volume fraction being taken up by the apolar alkyl chains.

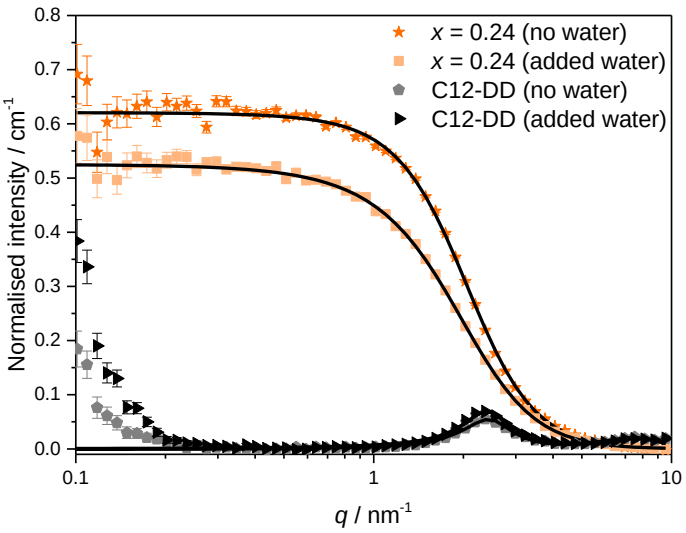

Figure 2.22: SANS data for H_2O saturated samples and the same compositions without added water.

Table 2.10: SANS fitting and derived parameters for H_2O saturated samples and the same compositions without added water.

		Teubner-Strey model			Peak Lorentz model	
Composition	Added water	Correlation length / nm	*d*-spacing / nm	Amphiphile strength, *γ*	*d*-spacing / nm	Scatterer size / nm
x = 0.24 (averaged)	No	0.6	4.0	0.1	–	–
x = 0.24 (C12-HH in C2-DD)	Yes	0.6	4.9	0.3	–	–
C12-DD (averaged)	No	2.3	2.5	-0.9	2.7	1.9
C12-DD	Yes	2.4	2.5	-0.9	2.6	1.8

2.7. SANS of Binary mixtures of $[C_nC_1im][Tf_2N]$ in $[C_2C_1im][Tf_2N]$

SANS experiments were performed on a range of compositions of the binary mixtures of $[C_nC_1im][Tf_2N]$ in $[C_2C_1im][Tf_2N]$ ($[C_2C_1im]_{x-1}[C_nC_1im]_x[Tf_2N]$) ionic liquids (*n* = 12, 10, 8, 6, 4). The compositions and contrasts investigated are given in Table 2.11. The SANS data for the C*n*-DD in C2-HH mixtures where *n* = 4, 6, 8, and 10, are provided in Figure 2.23. In this section the Teubner-Strey model is used to describe all the SANS data. This model was chosen as it has proven itself as a robust model across the whole composition range for the C12 in C2 mixtures reported in Section 2.6 and it gives comparable length scales to the other models. The main focus in this section is on the structural parameters derived from the SANS data, as the fits are very similar to the C12 in C2 mixtures reported in the previous section.

A discussion of the effect of decreasing the chain length of the long alkyl chain component ($[C_nC_1im][Tf_2N]$) in the IL mixtures has upon the structure of the mixtures is presented in three different sections. Firstly, the effect on the amphiphile strength parameter is discussed, followed by the effect on the length scale parameters (*d*-spacing and correlation length), and then finally a summary of the structural changes.

Table 2.11: Mixtures and contrasts used in the present SANS studies.

Isotopic contrast	Compositions, *x*
$[C_2C_1im\text{-}d_{11}]_{1-x}[C_{12}C_1im]_x[Tf_2N]$ (C12-HH in C2-DD)	0, 0.01, 0.04, 0.16, 0.24, 0.32, 0.52, 0.74, 0.87, 0.96, 0.99, 1
$[C_2C_1im]_{1-x}[C_{12}C_1im\text{-}d_{31}]_x[Tf_2N]$ ((C12-DD in C2-HH))	0, 0.01, 0.04, 0.16, 0.24, 0.32, 0.52, 0.74, 0.87, 0.96, 0.99, 1
$C_2C_1im\text{-}d_{11}]_{1-x}[C_{10}C_1im]_x[Tf_2N]$ (C10-HH in C2-DD)	0, 0.01, 0.03, 0.12, 0.18, 0.25, 0.44, 0.65, 0.74, 0.84, 0.96, 0.99, 1
$[C_2C_1im]_{1-x}[C_{10}C_1im\text{-}d_{27}]_x[Tf_2N]$ ((C10-DD in C2-HH))	0, 0.01, 0.03, 0.12, 0.18, 0.25, 0.44, 0.65, 0.74, 0.84, 0.96, 0.99, 1
$[C_2C_1im\text{-}d_{11}]_{1-x}[C_8C_1im]_x[Tf_2N]$ ((C8-HH in C2-DD)	0, 0.01, 0.03, 0.12, 0.18, 0.25, 0.44, 0.67, 0.83, 0.95, 0.99, 1
$[[C_2C_1im]_{1-x}[C_8C_1im\text{-}d_{23}]_x[Tf_2N]$ (C8-DD in C2-HH)	0, 0.01, 0.03, 0.12, 0.18, 0.25, 0.44, 0.67, 0.83, 0.95, 0.99, 1
$[C_2C_1im\text{-}d_{11}]_{1-x}[C_6C_1im]_x[Tf_2N]$ (C6-HH in C2-DD)	0, 0.01, 0.03, 0.13, 0.19, 0.27, 0.46, 0.69, 0.84, 0.95, 0.99, 1
$[C_2C_1im]_{1-x}[C_6C_1im\text{-}d_{19}]_x[Tf_2N]$ (C6-DD in C2-HH)	0, 0.02, 0.03, 0.13, 0.19, 0.27, 0.46, 0.69, 0.84, 0.95, 0.99, 1
$[C_2C_1im\text{-}d_{11}]_{1-x}[C_4C_1im]_x[Tf_2N]$ (C4-HH in C2-DD)	0, 0.01, 0.03, 0.14, 0.21, 0.28, 0.48, 0.71, 0.85, 0.95, 0.99, 1
$[C_2C_1im]_{1-x}[C_4C_1im\text{-}d_{15}]_x[Tf_2N]$ (C4-DD in C2-HH)	0, 0.01, 0.03, 0.14, 0.21, 0.29, 0.44, 0.70, 0.85, 0.95, 0.99, 1

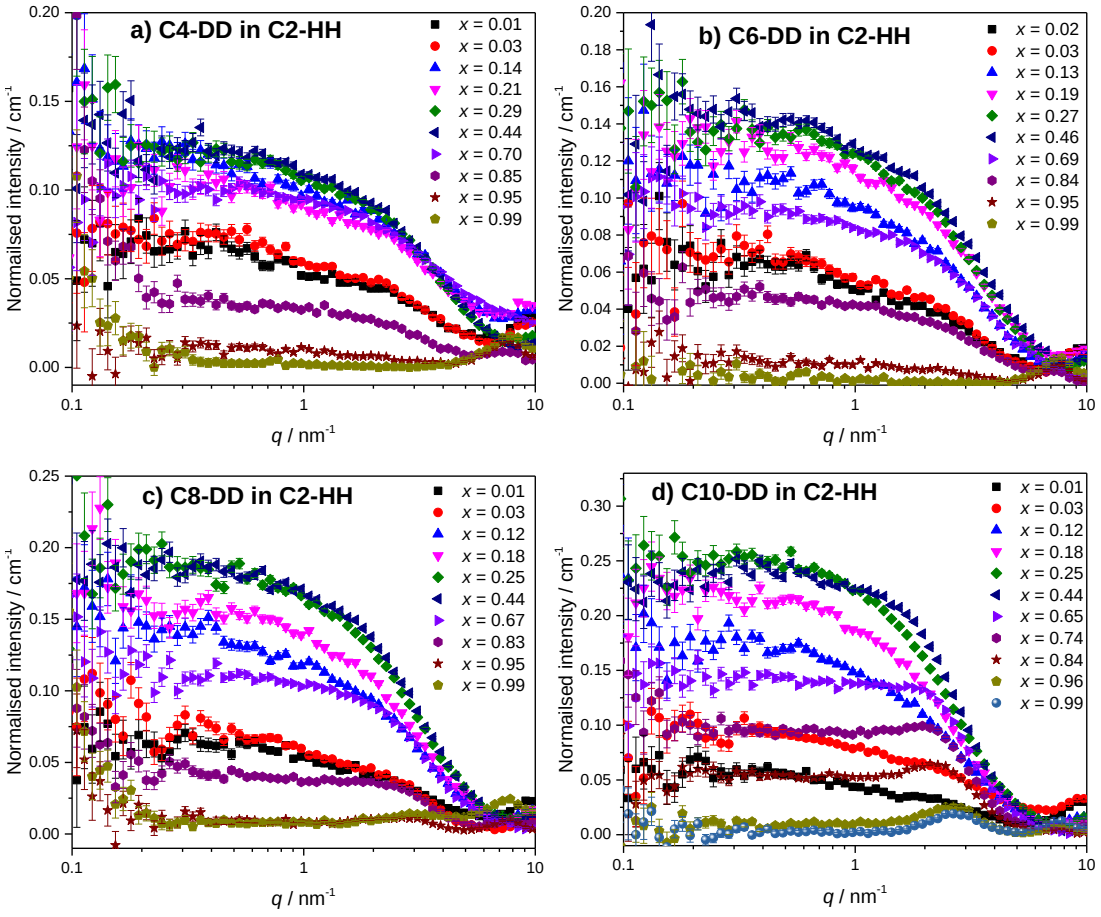

Figure 2.23:SANS data for: a) $[C_2C_1im]_{1-x}[C_4C_1im\text{-}d_{15}]_x[Tf_2N]$;
b) $[C_2C_1im]_{1-x}[C_6C_1im\text{-}d_{19}]_x[Tf_2N]$; c) $[C_2C_1im]_{1-x}[C_8C_1im\text{-}d_{23}]_x[Tf_2N]$;
d) $[C_2C_1im]_{1-x}[C_{10}C_1im\text{-}d_{27}]_x[Tf_2N]$. All the data are normalised to the background.

2.7.1. Amphiphile Strength Parameter

The amphiphile strength parameters for all the mixtures and compositions under study in this section are shown in Figure 2.24. The data are averaged values for the $[C_2C_1im\text{-}d_{11}]_{1-x}[C_nC_1im]_x[Tf_2N]$ and $[C_2C_1im]_{1-x}[C_nC_1im\text{-}d_{n\times2+7}]_x[Tf_2N]$ contrasts, where n = 12, 10, 8, and 6. The $[C_2C_1im\text{-}d_{11}]_{1-x}[C_4C_1im]_x[Tf_2N]$ and $[C_2C_1im]_{1-x}[C_4C_1im\text{-}d_{15}]_x[Tf_2N]$ mixtures are not included as they essentially have no scattering from alkyl chain aggregates at q < 4 nm, thus do not display any long length scale alkyl chain organisation.

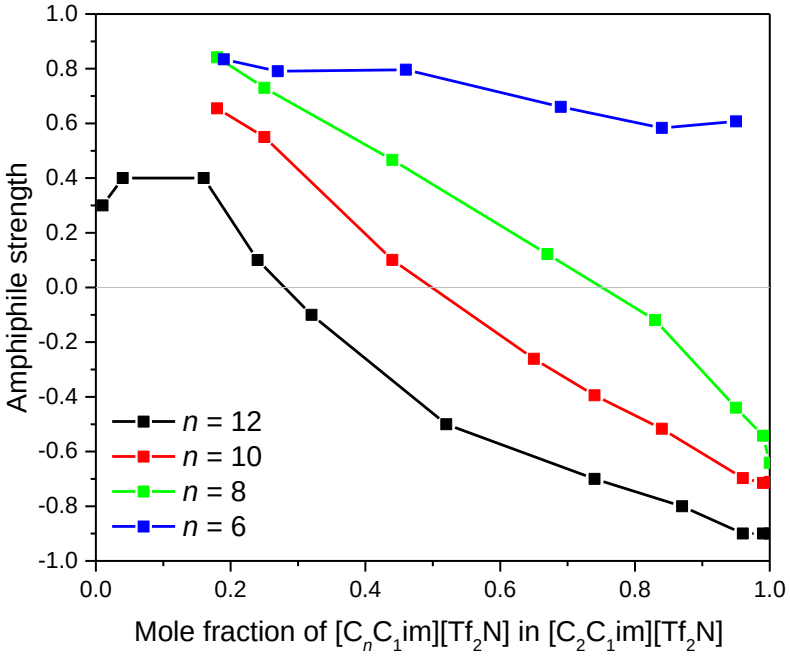

Figure 2.24: The amphiphile strength parameter from the Teubner-Strey model for $[C_2C_1im]_{1-x}[C_nC_1im]_x[Tf_2N]$. The data are averaged values for the $[C_2C_1im\text{-}d_{11}]_{1-x}[C_nC_1im]_x[Tf_2N]$ and $[C_2C_1im]_{1-x}[C_nC_1im\text{-}d_{n\times2+7}]_x[Tf_2N]$ contrasts, where n = 12, 10, 8, and 6. The grey horizontal line is the Lifshitz line.

The profiles of the amphiphile strength plots are similar for the different chain length mixtures ($[C_2C_1im]_{x-1}[C_nC_1im]_x[Tf_2N]$ when $n \geq 8$, in that, at lower mole fractions aggregate structures are present, as indicated by the amphiphile strength value being positive. On increasing the mole fraction the amphiphile strength parameter decreases in value, crossing the Lifshitz line, indicating that the aggregates have coalesced resulting in percolation of the alkyl chains throughout the liquid, *i.e.* a bicontinuous structure. The percolation threshold is reached at different mole fractions for each set of chain length mixtures, increasing linearly with increasing n, with the

lowest mole fraction (x ~ 0.28), for n = 12, followed by x ~ 0.50 for m = 10, and then x ~ 0.75 for m = 8 mixtures, Figure 2.25.

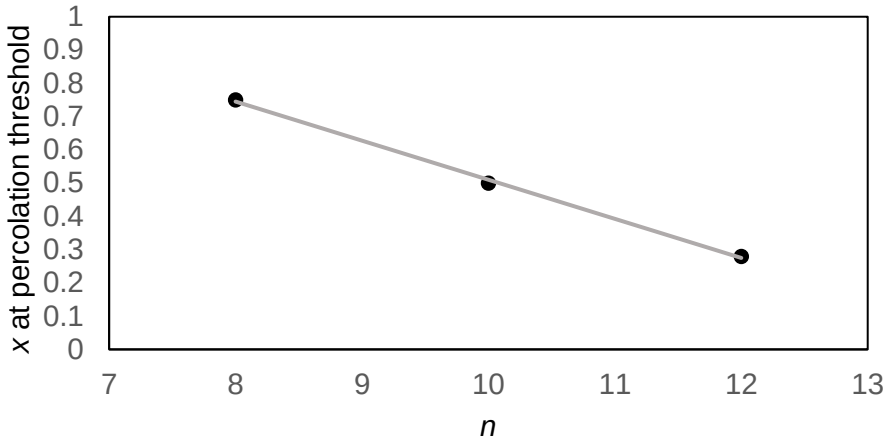

Figure 2.25: Linear regression analysis between alkyl chain length n in the IL mixtures of $[C_2C_1im]_{x-1}[C_nC_1im]_x[Tf_2N]$ and the mole fraction (x) at which the percolation threshold is reached.

A convenient way to look at this trend is to analyse the volume fraction occupied by the apolar alkyl chains, of the $[C_nC_1im][Tf_2N]$ component of the mixture, at the percolation threshold. It might be expected that the apolar network is formed when a specific volume fraction of alkyl chains is reached. Hence, shorter chains have less apolar volume so more of them are needed to reach the volume fraction required for percolation. To this end the mole fraction, at which the mixtures cross over the Lifshitz line (the percolation threshold), has been plotted against the approximate volume fraction of the alkyl chains at this composition, Figure 2.26. The figure does not indicate that the alkyl chain volume fraction is the only driving force behind percolation. The apolar volume fraction needed to cross the Lifshitz line is not constant, in fact it increases as alkyl chain length decreases. The relationship between the percolation threshold and the chain length is more complex than simply filling space.

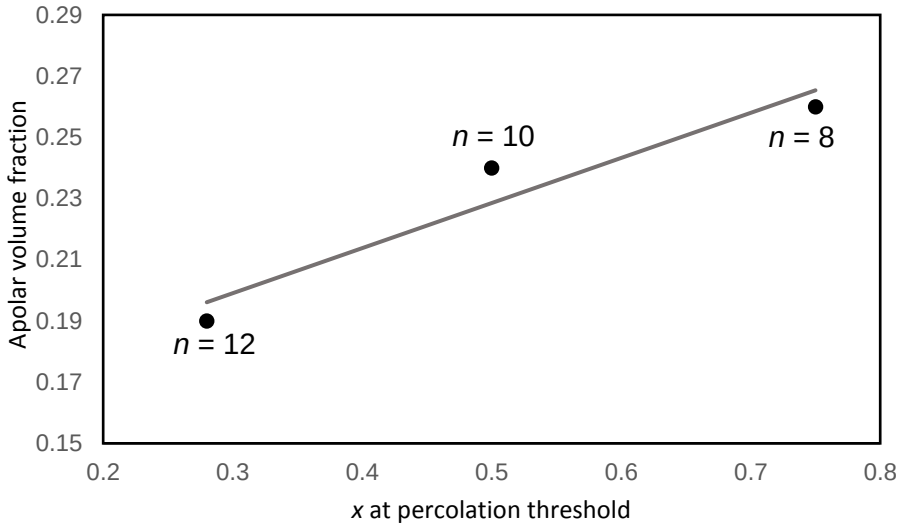

Figure 2.26: Linear regression analysis between the mole fraction (x) at which the percolation threshold is reached in $[C_2C_1im]_{x-1}[C_nC_1im]_x[Tf_2N]$ IL mixtures with the apolar mole fraction of the liquids.

While neither the SANS data show any scattering from alkyl chain aggregates at $q < 4$ nm for pure $[C_2C_1im][Tf_2N]$ and $[C_6C_1im][Tf_2N]$, thus no alkyl chain aggregation, the $[C_2C_1im]_{1-x}[C_6C_1im]_x[Tf_2N]$ mixtures display some structuring, in that aggregates are present. At both extremes of the compositional range, $x > 0.19$ and $x < 0.95$, no alkyl chain structuring is observed in the SANS data. At low x the SANS data fits suggest no alkyl chain aggregation, this is most likely due to there not being enough aggregates in the liquid to scatter strongly enough. On increasing x, to $x > 0.19$, the fits to the SANS data show aggregation of the C6 chains. However, when x is increased further to $x > 0.95$ the structure is lost, this is because the C6 alkyl chains are no longer acting as amphiphiles. As more $[C_6C_1im]^+$ is added (increasing x) the liquid is becoming more apolar, conversely less $[C_2C_1im]^+$ cations are in the mixture thus the polarity of the mixture is effectively being reduced. When the mixture is highly polar the C6 alkyl chains are amphiphilic enough to aggregate, upon reducing the liquids polarity the amphilicity of $[C_6C_1im][Tf_2N]$ is no longer a strong enough driving force to result in aggregation.

2.7.2. Length Scale Parameters

The two length scale parameters derived from the Teubner-Strey model are d-spacing and correlation length (ξ). When the liquid has an aggregate structure, the d-spacing is related to the distance between the aggregates and the correlation length is

associated with the density fluctuations within the aggregates, which can be interpreted as the alkyl chain aggregate size. For correlated structures, such as the bicontinuous structure, the *d*-spacing is related to the periodic distances in the structure, or the bilayer size, while the correlation length is related to the alkyl chain domain length scale. The length scale parameters for all the mixtures and compositions under study in this section are shown in Figure 2.27.

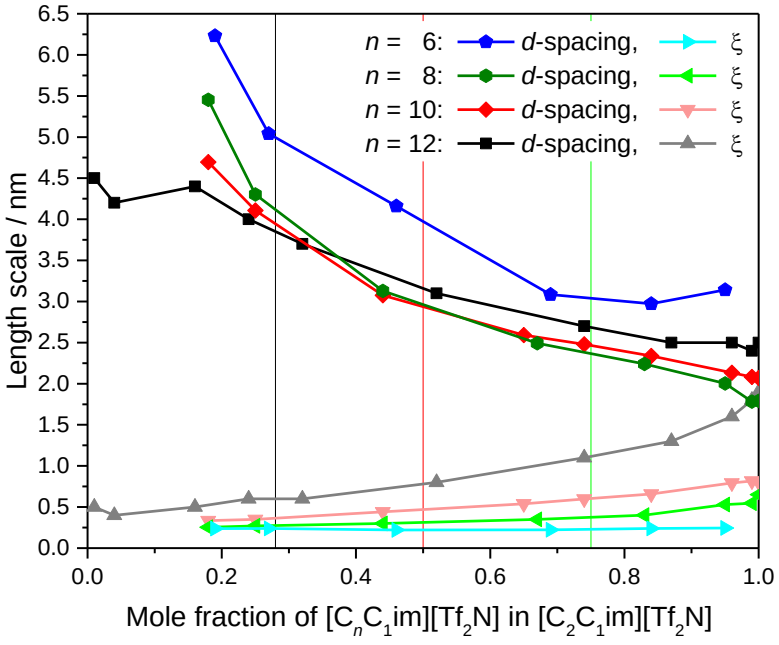

Figure 2.27: The length scale parameters from the Teubner-Strey model for $[C_2C_1im]_{1-x}[C_nC_1im]_x[Tf_2N]$, where ξ is the correlation length. The data are averaged values for the $[C_2C_1im\text{-}d_{11}]_{1-x}[C_nC_1im]_x[Tf_2N]$ and $[C_2C_1im]_{1-x}[C_nC_1im\text{-}d_{n\times2+7}]_x[Tf_2N]$ contrasts, where n = 12, 10, 8, and 6. The black, red, and green vertical lines represent the mole fraction where the Lifshitz line is crossed for n = 12, 10, and 8 respectively.

The length scale parameters for the different chain length mixtures, $([C_2C_1im]_{x-1}[C_nC_1im]_x[Tf_2N]$ when $n \geq 8$, all follow similar trends, in that, before the percolation threshold the *d*-spacings decrease while the correlation lengths stay almost constant, and once the percolation threshold is reached, the *d*-spacings decrease while the correlation lengths increase.

Before percolation, when the system can be described as consisting of aggregates, the smaller chain length mixtures have larger *d*-spacings and smaller correlation lengths, at a specific *x*. This is intuitive, since the alkyl chain becomes shorter the aggregates also become smaller (shorter correlation length), as shorter chains are less voluminous, thus the aggregates are smaller so can be further apart. This effect

is also compounded by the prospect of their being fewer aggregates upon decreasing the alkyl chain length, at a specific value of *x*, as the ILs are less amphiphilic, as shown by reaching the percolation threshold at higher *x*, there is a higher chance an alkyl chain will be isolated and not be involved in aggregation.

Once the percolation threshold is reached, for each chain length mixture, the ordering of *d*-spacings changes so that the longer chain length mixtures have the longer *d*-spacings. This is because the length scale of the apolar network is related to the alkyl chain length, thus the longer the alkyl chain length the larger the *d*-spacing. The *d*-spacings continue to decrease as *x* increases, until they reach the value of the pure $[C_nC_1im][Tf_2N]$ ILs, as there are less $[C_2C_1im][Tf_2N]$ to increase the volume of the polar network. The correlation lengths increase after the percolation threshold is reached, this increase in most pronounced when $n = 12$ and less so with decreasing *n*, the reason behind this is not fully understood.

For the $n = 6$ mixtures the *d*-spacing decreases from 6.2 nm at $x = 0.19$ to 3.0 nm at $x = 0.84$, before increasing to 3.1 nm at $x = 0.95$, while the correlation remains constant around 0.2 nm. Thus providing a picture of aggregates that are increasing in number yet remaining a similar size. This is consistent with what has been reported for the longer chain systems in the regions where aggregates dominate.

2.7.3. Summary of the Structural Changes with Changing Composition

Decreasing the alkyl chain length of $[C_nC_1im]_x[Tf_2N]$ in binary mixtures of $[C_nC_1im][Tf_2N]$ in $[C_2C_1im][Tf_2N]$ for $n = 12, 10, 8, 6, 4$, has an interesting effect upon the liquid structure. As the chain length decreases from $n = 12$ to $n = 6$, at mole fractions before the percolation threshold is reached, the aggregate size decreases, as indicated by the smaller correlation lengths and the aggregates being further away from each other (larger *d*-spacing). This is intuitive, since the alkyl chain becomes shorter the aggregates also become smaller, as shorter chains are less voluminous, thus the aggregates are smaller so can be further apart. This effect is also compounded by the prospect of their being fewer aggregates upon decreasing the alkyl chain length, at a specific value of *x*, as the ILs are less amphiphilic, there is a higher chance an alkyl chain will be isolated and not be involved in aggregation. After the mixtures cross the Lifshitz line, where the aggregates coalesce to form a bicontinuous structure, the *d*-spacings decrease at a slower rate and the correlation lengths begin to increase, being most pronounced when $n = 12$ and less clear with the shorter chain lengths. The decrease in *d*-spacing is related to the polar network

reducing in volume on decreasing mole fraction of $[C_2C_1im]^+$ (increasing *x*), with its value converging on the *d*-spacing found in the pure $[C_nC_1im][Tf_2N]$ ILs. The percolation threshold was found not to be directly related a specific alkyl chain volume fraction. Additionally, when *n* = 4, no alkyl chain structuring is observed, indicating that $[C_4C_1im][Tf_2N]$ in not a strong enough amphiphile to aggregate within $[C_2C_1im][Tf_2N]$.

2.8. SANS of Binary mixtures of $[C_{12}C_1im][Tf_2N]$ in $[C_mC_1im][Tf_2N]$

SANS experiments were performed on a range of compositions of the binary mixtures of $[C_{12}C_1im][Tf_2N]$ in $[C_mC_1im][Tf_2N]$ ($[C_mC_1im]_{x-1}[C_{12}C_1im]_x[Tf_2N]$) (*m* = 8, 6, 4, 2). The compositions and contrasts investigated are given in Table 2.12. The SANS data for the C12-DD in C*m*-HH mixtures where *m* = 2, 4, and 6 are provided in Figure 2.28.

In this section the Teubner-Strey model is used to describe the SANS data. This model was chosen as it has proven itself as a robust model across the whole composition range for the C12 in C2 mixtures reported in Section 2.6 and it gives comparable length scales to the other models. The main focus in this section is on the structural parameters derived from the SANS data, as the fits are very similar to the C12 in C2 mixtures reported in the previous section.

The discussion of the effect that increasing the chain length of the short alkyl chain component of the IL mixture from *m* = 2 to *m* = 6 , while keeping the long alkyl chain length constant, has upon the structure of the mixtures is presented in two different sections firstly, the effect on the amphiphile strength parameter, secondly, the effect on the length scale parameters (*d*-spacing and correlation length). Then a more discussion of the SANS data collected for the C12 in C8 mixtures is given as the data did not follow the trend seen in the other mixtures. Then finally, a summary of the structural changes is presented.

Table 2.12: Mixtures and contrasts used in the SANS studies under Heading 2.8.

Isotopic contrast	Compositions
$[C_2C_1im\text{-}d_{11}]_{1-x}[C_{12}C_1im]_x[Tf_2N]$ (C12-HH in C2-DD)	x = 0, 0.01, 0.04, 0.16, 0.24, 0.32, 0.52, 0.74, 0.87, 0.96, 0.99, 1
$[C_2C_1im]_{1-x}[C_{12}C_1im\text{-}d_{31}]_x[Tf_2N]$ (C12-DD in C2-HH)	x = 0, 0.01, 0.04, 0.16, 0.24, 0.32, 0.52, 0.74, 0.87, 0.96, 0.99, 1
$[C_4C_1im\text{-}d_{15}]_{1-x}[C_{12}C_1im]_x[Tf_2N]$ (C12-HH in C4-DD)	x = 0, 0.01, 0.04, 0.16, 0.24, 0.32, 0.52, 0.74, 0.87, 0.96, 0.99, 1
$[C_4C_1im]_{1-x}[C_{12}C_1im\text{-}d_{31}]_x[Tf_2N]$ (C12-DD in C4-HH)	x = 0, 0.01, 0.04, 0.16, 0.24, 0.32, 0.52, 0.74, 0.87, 0.96, 0.99, 1
$[C_6C_1im\text{-}d_{19}]_{1-x}[C_{12}C_1im]_x[Tf_2N]$ (C12-HH in C6-DD)	x = 0, 0.01, 0.04, 0.16, 0.24, 0.32, 0.52, 0.74, 0.87, 0.96, 0.99, 1
$[[C_8C_1im]_{1-x}[C_{12}C_1im\text{-}d_{31}]_x[Tf_2N]$ (C12-DD in C6-HH)	x = 0, 0.01, 0.04, 0.16, 0.24, 0.32, 0.52, 0.67, 0.74, 0.87, 0.96, 0.99, 1
$[C_2C_1im\text{-}d_{11}]_{1-x}[C_{12}C_1im]_x[Tf_2N]$ (C12-HH in C8-DD)	x = 0, 0.01, 0.04, 0.16, 0.24, 0.32, 0.52, 0.67, 0.74, 0.87, 0.96, 0.99, 1
$[C_2C_1im]_{1-x}[C_{12}C_1im\text{-}d_{31}]_x[Tf_2N]$ (C12-DD in C8-HH)	0, 0.01, 0.04, 0.16, 0.24, 0.32, 0.52, 0.67, 0.74, 0.87, 0.96, 0.99, 1

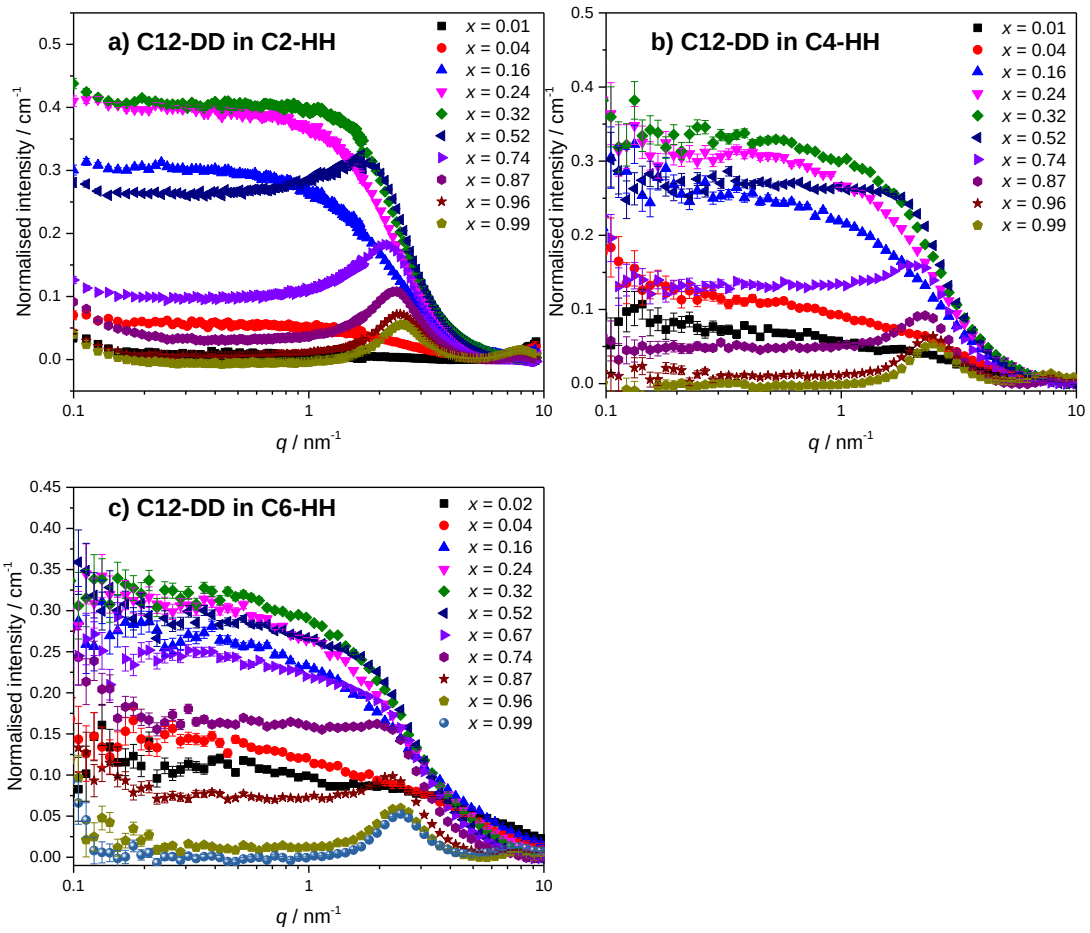

Figure 2.28: SANS data for: a) $[C_2C_1im]_{1-x}[C_{12}C_1im\text{-}d_{31}]_x[Tf_2N]$; b) $[C_4C_1im]_{1-x}[C_{12}C_1im\text{-}d_{31}]_x[Tf_2N]$; c) $[C_6C_1im]_{1-x}[C_{12}C_1im\text{-}d_{31}]_x[Tf_2N]$. All the data are normalised to the background.

2.8.1. Amphiphile Strength Parameters

The amphiphile strength parameters for the mixtures of m = 2, 4, 6 ($[C_mC_1im]_{x\text{-}1}[C_{12}C_1im]_x[Tf_2N]$) are shown in Figure 2.29. The data are averaged values for the $[C_mC_1im\text{-}d_{2m+7}]_{1\text{-}x}[C_{12}C_1im]_x[Tf_2N]$ and $[C_mC_1im]_{1\text{-}x}[C_{12}C_1im\text{-}d_{31}]_x[Tf_2N]$ contrasts.

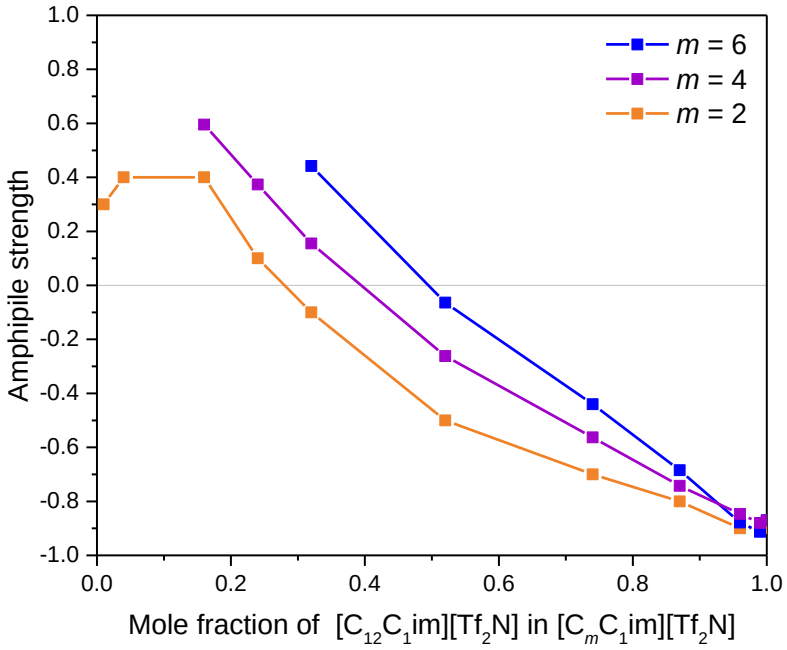

Figure 2.29: The amphiphile strength parameter from the Teubner-Strey model for $[C_mC_1im]_{1\text{-}x}[C_{12}C_1im]_x[Tf_2N]$. The data are averaged values for the $[C_mC_1im\text{-}d_{2m+7}]_{1\text{-}x}[C_{12}C_1im]_x[Tf_2N]$ and $[C_mC_1im]_{1\text{-}x}[C_{12}C_1im\text{-}d_{31}]_x[Tf_2N]$ contrasts, where m = 6, 4, and 2. The grey horizontal line is the Lifshitz line.

The profiles of the amphiphile strength plots are similar for the different chain length mixtures ($[C_mC_1im]_{x\text{-}1}[C_{12}C_1im]_x[Tf_2N]$, m = 6, 4, 2), in that, at lower mole fractions aggregate structures are present, as indicated by the amphiphile strength value being positive. On increasing the mole fraction the amphiphile strength parameter decreases in value, crossing the Lifshitz line, indicating that the aggregates have coalesced resulting in percolation of the alkyl chains throughout the liquid, *i.e.* a bicontinuous structure. The percolation threshold is reached at different mole fractions for each set of chain length mixtures, increasing linearly with increasing m, with the lowest mole fraction (x ~ 0.28), for m = 2, followed by x ~ 0.40 for m = 4, and then x ~ 0.50 for m = 6 mixtures, Figure 2.30.

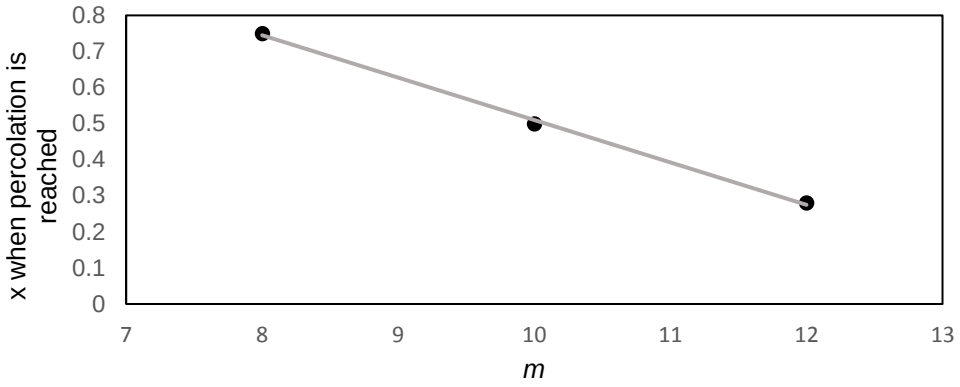

Figure 2.30: Linear regression analysis between alkyl chain length *m* in the IL mixtures of $[C_mC_1im]_{x\text{-}1}[C_{12}C_1im]_x[Tf_2N]$ and the mole fraction (*x*) at which the percolation threshold is reached.

It could be imagined that the percolation threshold is reached when a specific volume fraction of apolar alkyl chains is reached within the mixture. The relationship between the percolation threshold and the volume fraction occupied by the apolar alkyl chains is shown in Figure 2.31, where the alkyl volume fractions are estimated as the volume fraction occupied by the alkyl chains of both components in the mixture. The figure does not indicate that the total alkyl volume fraction of the mixtures is the only driving force behind percolation, as the apolar volume fraction needed to reach percolation is not coherent between the different mixtures, indeed a larger apolar volume fraction is needed to reach percolation upon increasing the alkyl chain length of the shorter chain component (*m*).

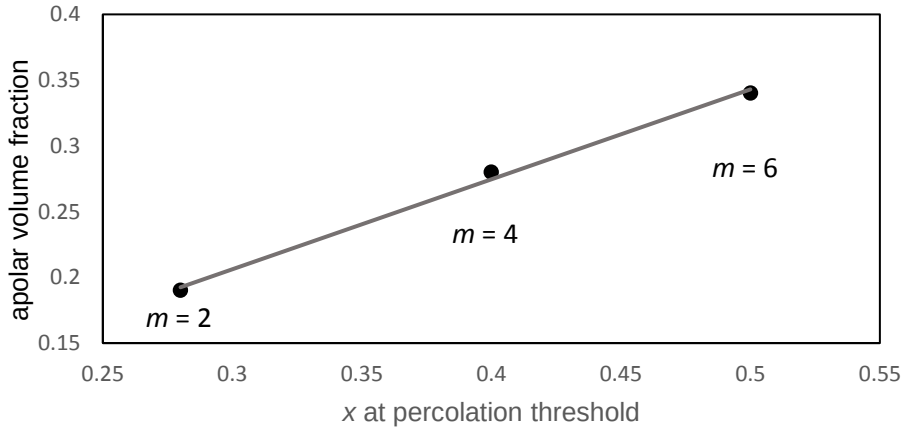

Figure 2.31: Linear regression analysis between the mole fraction (*x*) at which the percolation threshold is reached in $[C_mC_1im]_{x\text{-}1}[C_{12}C_1im]_x[Tf_2N]$ IL mixtures with the apolar mole fraction of the liquids.

2.8.2. Length Scale Parameters

The length scale parameters from fitting to the Teubner-Strey model for m = 6, 4, 2, in $[C_mC_1im]_{x-1}[C_{12}C_1im]_x[Tf_2N]$ are shown in Figure 2.32.

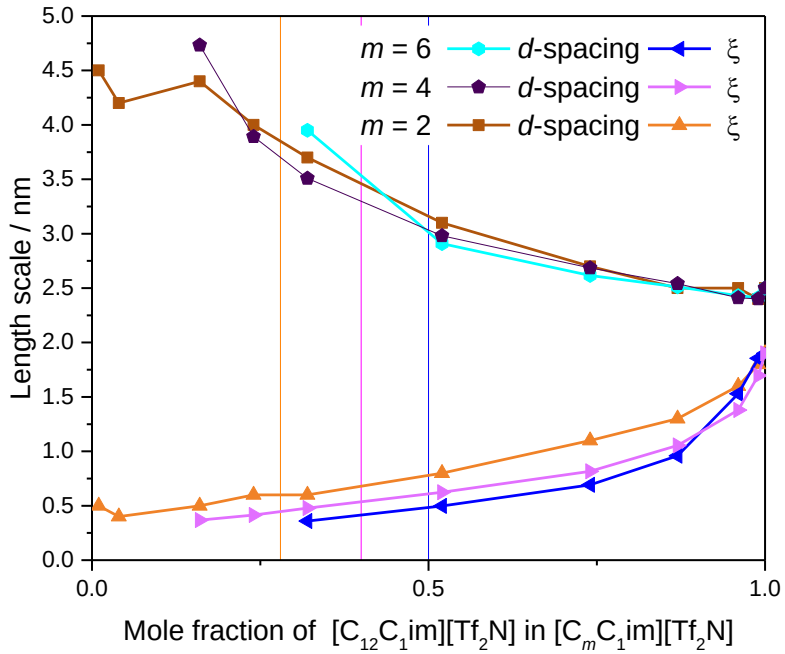

Figure 2.32: The length scale parameters from the Teubner-Strey model $[C_mC_1im\text{-}d_{2m+7}]_{1-x}[C_{12}C_1im]_x[Tf_2N]$, where ξ is the correlation length. The data are averaged values for the $[C_mC_1im\text{-}d_{2m+7}]_{1-x}[C_{12}C_1im]_x[Tf_2N]$ and $[C_mC_1im]_{1-x}[C_{12}C_1im\text{-}d_{31}]_x[Tf_2N]$ contrasts, where m = 6, 4, 2. The orange, pink, and blue vertical lines represent the mole fraction where the Lifshitz line is crossed for n = 6, 4, and 2 respectively.

The length scale parameters for the different chain length mixtures, ($[C_mC_1im]_{x-1}[C_{12}C_1im]_x[Tf_2N]$ when n = 6, 4, 2, all follow similar trends, in that, before the percolation threshold the d-spacings decrease while the correlation lengths stay almost constant, and once the percolation threshold is reached, the d-spacings decrease, while the correlation lengths increase.

Before percolation, when the system can be described as consisting of aggregates, the mixtures with larger m have longer d-spacings and shorter correlation lengths, at a given mole fraction. The longer d-spacings can be explained by the C12 chains aggregates being separated by more voluminous $[C_mC_1im]^+$ cations, as m increases. While the shorter correlation lengths can be rationalised as resulting from smaller C12 chain aggregates being present, due to the driving force behind the aggregation of

the C12 chains reducing, as *m* increases, thus the hydrophobic effect is weaker, that is an isolated C12 chain in $[C_2C_1im][Tf_2N]$ is less favourable than an isolated chain in $[C_6C_1im][Tf_2N]$.

After percolation all the *d*- spacings, at a given *x*, are congruent between the different mixtures, while the correlation lengths are shorter for the longer chain length mixtures, portraying a system where the apolar alkyl chain bilayer becomes shorter on increasing *m*, yet the periodic distance is remaining constant. An argument could be made that this is the result of the longer alkyl chains of $[C_mC_1im]^+$ cations causing the polar network of the bilayer to become more voluminous as *m* increases, this increase in volume is compensated for by the apolar layer contracting and widening. The difference in correlation lengths, between the different mixtures, reduces as *x* increases as the system starts to resemble pure $[C_{12}C_1im][Tf_2N]$.

2.8.3. Binary mixtures of $[C_{12}C_1im][Tf_2N]$ in $[C_8C_1im][Tf_2N]$

The SANS study of the binary mixtures of $[C_{12}C_1im][Tf_2N]$ in $[C_8C_1im][Tf_2N]$ ($[C_8C_1im]_{x\text{-}1}[C_{12}C_1im]_x[Tf_2N]$) has been singled out as it warrants a more detailed explanation, owing to the observation that it does not follow the trends of the other mixtures presented above. The SANS data for both contrasts (C12-DD in C8-HH and C12-HH in C2-DD) are shown in Figure 2.33. The IL mixture of $[C_{12}C_1im][Tf_2N]$ in $[C_8C_1im][Tf_2N]$ is distinct from all the previous mixtures in this chapter as both pure components have a bicontinuous structure, they both show PNPPs in the SANS experiments and have negative amphiphile strengths, when fit to the Teubner-Strey model (Section 2.5.2). On mixing these two ILs it was expected that they would be compatible and form bicontinuous structures with length scales intermediate of the two components, so that all compositions would show a PNPP. However, this is not the case as can be seen in Figure 2.33, where in most cases the PNPP is absent.

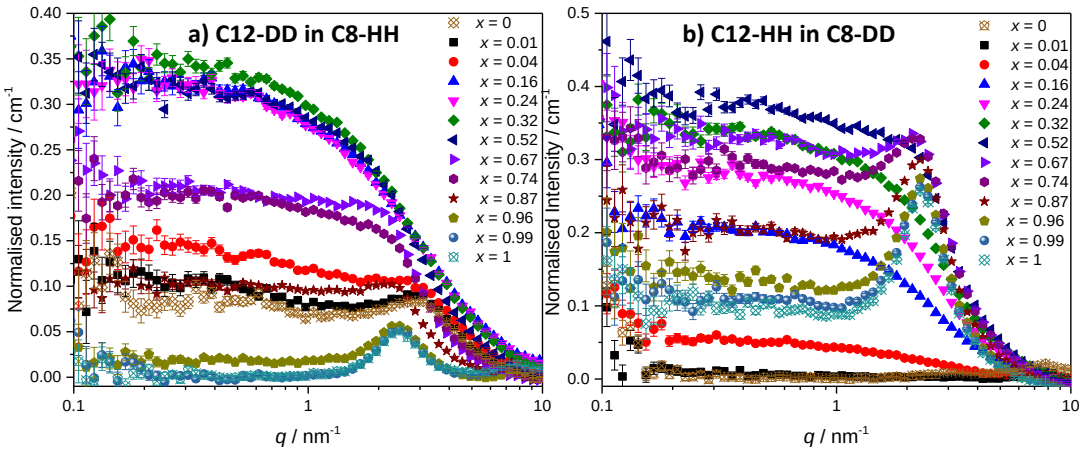

Figure 2.33: SANS data for all compositions for: a) $[C_8C_1im]_{1-x}[C_{12}C_1im\text{-}d_{31}]_x[Tf_2N]$ (C12-DD in C8-HH); b) $[C_8C_1im\text{-}d_{23}]_{1-x}[C_{12}C_1im]_x[Tf_2N]$ (C12-HH in C8-DD).

Fitting to the models used previously proved to be hard for these mixtures, as the Teubner-Strey model was found to fit poorly across most of the compositional range ($0.24 < x < 0.96$) for both contrasts, Figure 2.34. The data fit well to the Lorentz + peak Lorentz model over most of the composition range except at $x = 0.16$, 0.24, 0.32 for C12-DD in C8-HH, and $x = 0.01$, 0.04, 0.16 for C12-HH in C2-DD, where only a Lorentz component was requited to fit the data at lower q (> 4 nm^{-1}), Figure 2.35. The d-spacing decreases slowly after $x = 0.32$ while the scatter size increases in length, with a discontinuity in the data below $x = 0.32$. As the SANS data do not fit well to the Teubner-Strey model, and there is a discontinuity in the parameters derived from the Lorentz + peak Lorentz model suggests that the data, in some cases, might not be representative of the ordering in the IL mixtures. This could be due to a poor contrast between the apolar and polar components in the liquid.

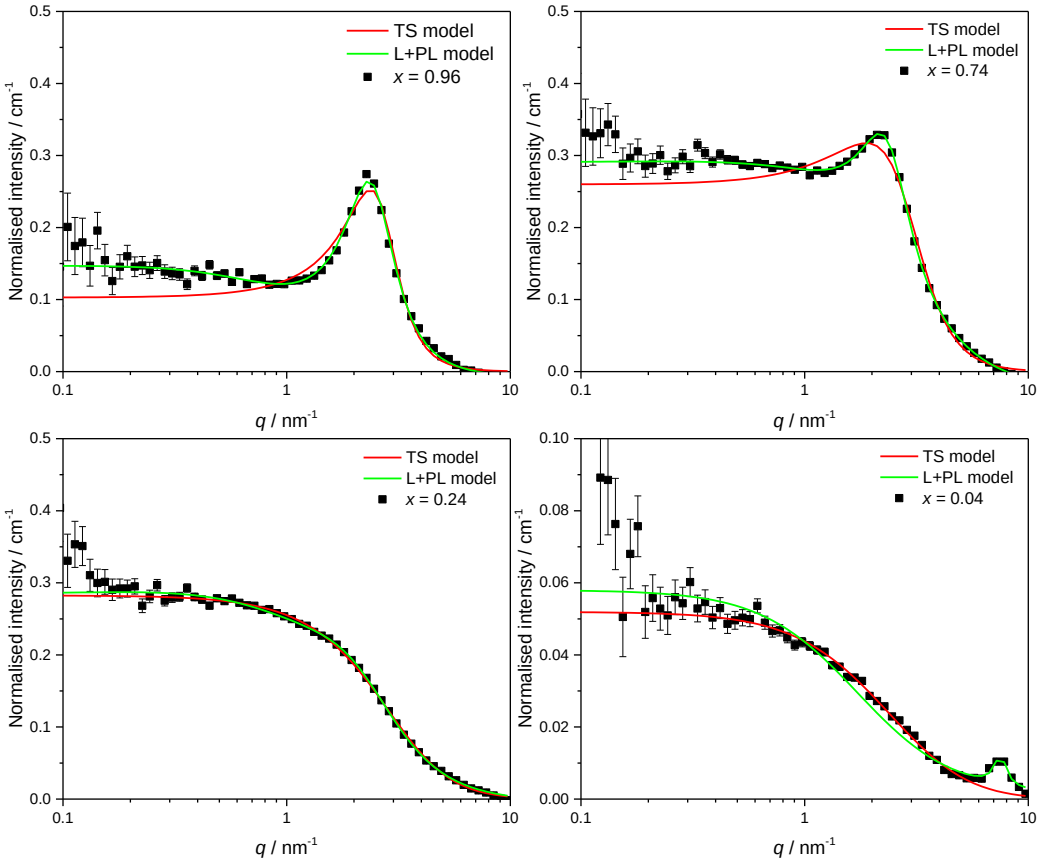

Figure 2.34: Fits to the Teubner-Strey (TS) model and Lorentz + Peak Lorentz (L+PL) models and peak Lorentz (PL) model are shown in red and green, respectively for $[C_8C_1im\text{-}d_{23}]_{1-x}[C_{12}C_1im]_x[Tf_2N]$ where x = 0.04, 0.24, 0.74, 0.96. The PL component of the P+PL model was used to model the data below q ~ 4 nm^{-1}, except for x = 0.04 where the PL component was used to model the COP.

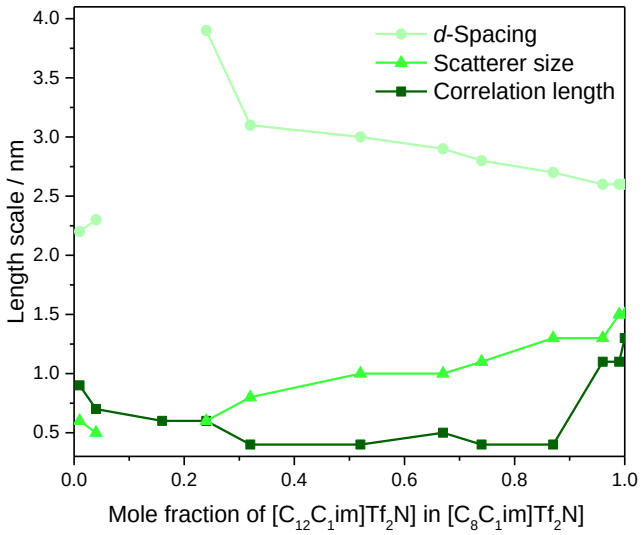

Figure 2.35: Derived parameters for the Lorentz + Peak Lorentz model for all compositions. Data are average values from fitting of both the C12-HH in C8-DD and C12-DD in C8-HH contrasts at that composition, except where stated in the main text.

To see if this is the case small-angle X-ray scattering (SAXS) measurements were conducted on a subset of the compositions of C12-HH in C8-DD (x = 0.01, 0.04, 0.16, 0.24, 0.52, 0.87, 0.99), Figure 2.36. The SAXS data shows that all the compositions contain PNPPs, suggesting that they all have a bicontinuous structure. This is in stark contrast to the SANS data where the PNPP is absent for most of the compositions.

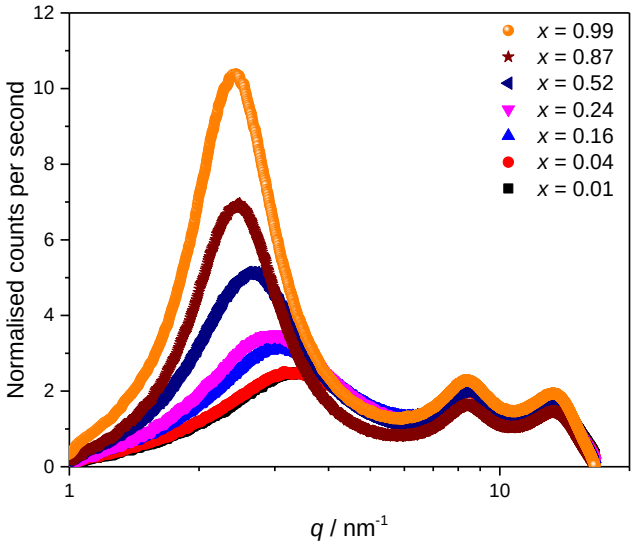

Figure 2.36: SAXS data for x = 0.01, 0.04, 0.16, 0.24, 0.52, 0.87, 0.99 of $[C_8C_1im\text{-}d_{23}]_{1-x}[C_{12}C_1im]_x[Tf_2N]$ (C12-HH in C8-DD).

The absence of PNPPs in the SANS data, and the presence of PNPPs in all of the SAXS data can be attributed to poor contrast between the apolar and polar components in the SANS experiments. Hence, the estimated SLD difference between the apolar alkyl chain component and the polar component of the mixtures was calculated using a group contribution scheme, Figure 2.37. For the polar component, the SLD was estimated using the molar ratio and densities of $[C_1C_1im][Tf_2N]$ and $[C_1C_1im\text{-}d_9][Tf_2N]$, the density of $[C_1C_1im\text{-}d_9][Tf_2N]$ being estimated from the density and molecular mass of $[C_1C_1im][Tf_2N]$ and the molecular mass of the deuterated analogue.[91, 105] SLDs of the apolar alkyl chains were calculated using the molar ratio and densities of decane for the C12 alkyl chains and hexane for C8 alkyl chains. It can be seen from the absolute difference in the SLDs of the two components, that there is a region where the contrast will be poor, so that SANS will not be able to differentiate between the ordered polar and apolar domains in the liquids, since it is this contrast that is the origin of the PNPP.

The calculated SLD difference between the polar and apolar components can be related to the absence of a PNPP in the SANS data, Figure 2.33, for the C12-HH in

C8-DD mixtures a PNPP is visible in the SANS data when the SLD difference is above 2.3 $\times 10^{-6}$ A^2, which occurs at $x \geq 0.74$. However, the relationship between the SLD difference for the C12-DD in C8-HH mixtures and the appearance of a PNPP is more complex. The PNPP can only be seen, in the SANS data for these mixtures, when $x \geq 0.87$ which corresponds to an SLD difference of 1.1 $\times 10^{-6}$ A^2. Conversely, lower mole fractions ($x \leq 0.32$) have an SLD difference of more than 1.1 $\times 10^{-6}$ A^2, yet the SANS data do not show a PNPP. This is because at lower x the mixture is more proteo-rich, which results in more incoherent scattering, thus a larger SLD difference is needed in order to be able to detect the PNPP.

The absence of a PNPP in some of the SANS experiments and the presence of a PNPP for all of the compositions in the SAXS experiments demonstrates the usefulness of complimentary SANS and SAXS experiments.

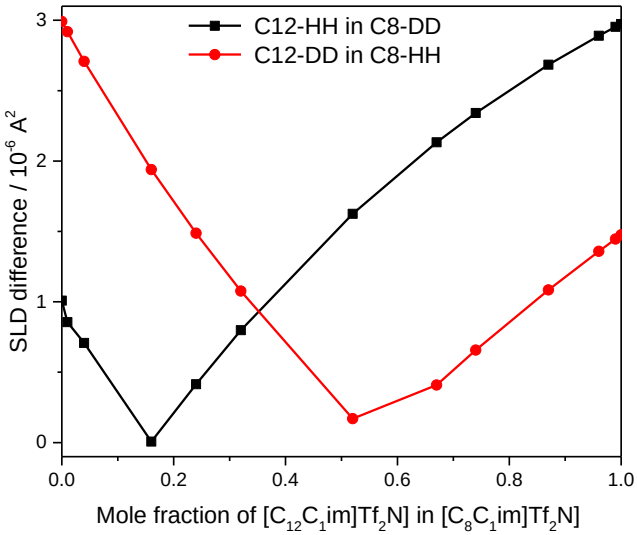

Figure 2.37: SLD difference between the polar component and apolar component of $[C_{12}C_1im\text{-}d_{31}][Tf_2N]$ in $[C_8C_1im][Tf_2N]$ and of $[C_{12}C_1im][Tf_2N]$ in $[C_8C_1im\text{-}d_{23}][Tf_2N]$ (C12-DD in C8-HH and C12-HH in C8-DD, respectively).

The SAXS data were fitted to a peak Lorentz + peak Lorentz + peak Lorentz model, where the PNPP, COP and CP were all fit as individual Lorentzian peaks. The parameters derived for the peak Lorentz component for the PNPP are shown in Figure 2.38. From this it can be seen that upon increasing the mole fraction of $[C_{12}C_1im][Tf_2N]$ in $[C_8C_1im][Tf_2N]$ both the *d*-spacing and scatterer size length scales increase smoothly. The *d*-spacing increases from 1.8 nm for $x = 0.01$ to 2.6 nm for $x = 0.99$ and the scatterer size increases from 0.6 nm for $x = 0.01$ to 1.3 nm for $x = 0.99$. As all the SAXS data shows a PNPP peak, these mixtures are all interpreted as having a

bicontinuous structure. On increasing *x* the *d*-spacing and scatterer sizes both increase at the same rate, giving the picture of an increasing bilayer length scale due to more volume being taken up by the apolar alkyl chains. While the length scale of the polar network stays constant around 1.3 nm (the difference between the *d*-spacing and the scatterer size).

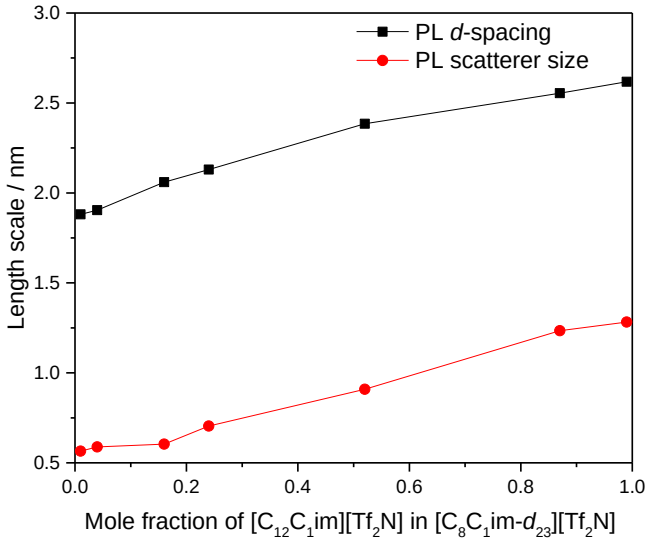

Figure 2.38: The derived parameters for the PNPP peak Lorentz (PL) component of the PL+PL+PL model, fitted to SAXS data of $[C_{12}C_1im]_{1-x}[C_8C_1im\text{-}d_{23}]_x[Tf_2N]$.

2.8.4. Summary of Structural Changes with Changing Composition

Increasing the chain length of the short alkyl chain component of the IL mixture systems of $[C_mC_1im]_{x-1}[C_{12}C_1im]_x[Tf_2N]$ where m = 8, 6, 4, 2, has a wide range of effects on the structure of the systems, as determined by SANS, and SAXS for the m = 8 mixtures.

The IL mixtures, where m = 2, 4, and 6, can all be described in the same way, that is the apolar alkyl chains aggregate at low mole fractions of $[C_{12}C_1im]^+$ and form bicontinuous structures upon increasing mole fraction. The mole fraction at which the percolation threshold is met is dependent on m, with the mixtures with a shorter m crossing the Lifshitz line at lower x. The length scales associated with the aggregate size, and the length scale of the apolar domains in the bicontinuous network, were found to be dependent on the mole fraction, increasing as x increases, while the *d*-spacings decrease on increasing x. When the mixtures display a bicontinuous network the length scale of the apolar region increases as m decreases, at a given x,

unless *x* is high then the length scale tends towards the value of pure $[C_{12}C_1im][Tf_2N]$. The percolation threshold was found not to be only related to an apolar volume fraction.

All the *m* = 8 mixtures can be depicted as having a bicontinuous structure and the periodicity of the bilayer increases on increasing *x*.

2.9. Conclusions on Structural Changes for $[C_nC_1im][Tf_2N]$ in $[C_mC_1im][Tf_2N]$ Ionic Liquid Mixtures

A detailed SANS study on pure IL mixtures and their binary mixtures of $[C_nC_1im][Tf_2N]$ in $[C_2C_1im][Tf_2N]$ and $[C_{12}C_1im][Tf_2N]$ in $[C_mC_1im][Tf_2N]$, where *n* = 4, 6, 8, 10, 12 and *m* = 2, 4, 6, 8, over a wide range of compositions and isotopic contrasts has been conducted.

Analysis of the SANS data for the pure ILs ($[C_nC_1im][Tf_2N]$, *n* = 2, 4, 6, 8, 10, 12) revealed that bilayer formation occurs after the chain length is *n* ≥ 8, where the bicontinuous network can be described as consisting of a network of apolar alkyl chains within a network of the cationic imidazolium headgroups and $[Tf_2N]^-$ anions. On increasing the chain length, *n,* of $[C_nC_1im][Tf_2N]$, the bilayer length scale increases, due to the increasing length of the alkyl chain increasing the distance between the polar network. This interpretation is consistent with the MD simulations carried out by Shimizu *et al*. who suggest that the PNPP is well defined by $[C_7C_1im][Tf_2N]$ and that the length scale of the apolar network increases with increasing *n*.[81]

Analysis of the SANS data for the IL mixtures revealed that several different fitting models can be used and that the most appropriate often depends on the composition of the IL mixture. As exemplified by the IL mixtures of $[C_2C_1im]_{x-1}[C_{12}C_1im]_x[Tf_2N]$, when *x* < 0.24, the SANS data are described well by shape-based (sphere and ellipsoid) and Teubner-Strey models. Whereas when *x* ≥ 0.24, the data are well described by the Teubner-Strey model. For *x* ≥ 0.74, the data can additionally be described well by the Lorentz + peak Lorentz model, while *x* ≥ 0.96 compositions are described well by the peak Lorentz model. The Teubner-Strey model is a particularly powerful model for the understanding of these systems as it can fit the data across the whole composition range, along with providing length scales as well as an indication of the structure in the system, and thus was used as the main model to describe the structure of the IL mixtures. The SANS fitting models suggest that the

liquid structure, for the binary IL mixtures of these ILs, depends extensively upon the composition.

For the IL mixtures of $[C_2C_1im]_{x-1}[C_nC_1im]_x[Tf_2N]$, where n = 12, 10, or 6, it was found that at lower mole fraction compositions the mixtures contain small aggregates of alkyl chains and their number density increases with increasing x. It is likely that at intermediate mole fractions small local bilayer structures are present and on increasing x the percolation threshold is reached, where all the Cn alkyl chains coalesce to form a continuous apolar network. Thus the structure can now be described as a bicontinuous network with both apolar and polar domains. As x increases further, the bilayer length scale decreases until the length scale is that of pure $[C_nC_1im][Tf_2N]$. The length scales of the aggregates and the bicontinuous network have been related to the length of the longest alkyl chain in the mixture. The mole fraction at which the percolation threshold is reached increases with decreasing n, indicating that more Cn chains are need to form a bicontinuous network on decreasing n. It was hypothesised that this was simply a space filling issue, however apolar volume fractions were found not to be directly related to the mole fraction at which percolation was achieved. This could be a result of the shorter alkyl chain mixtures not preferentially aggregating as strongly, as presumably an isolated C12 chain in $[C_2C_1im][Tf_2N]$ is more unfavourable than an isolate C8 chain. Additionally, this could be related to the length of the chain, in that to percolate all the chains need to be part of the same network, to do this they all need to be in contact with each other, this is likely easier with longer chains as they span more space. When n = 4 only small alkyl chain aggregates are formed, while when n = 4 no alkyl chain ordering is observed.

Temperature-dependent SANS studies on $[C_2C_1im]_{1-x}[C_{12}C_1im]_x[Tf_2N]$, suggest that the structures of the mixtures remains similar, yet they become more disordered on increasing temperature. The structural change upon addition of water was found to be dependent upon composition. Thus when x = 0.24 the water appears to be incorporated into the polar structure, whereas, when x = 1 water does not change the structural parameters as the IL is assumed too hydrophobic.

For the IL mixtures of $[C_mC_1im]_{x-1}[C_{12}C_1im]_x[Tf_2N]$, where m = 2, 4, 6, it was found that the structures present are similar to the set of mixtures described above, in that, at low mole fractions of $[C_{12}C_1im]^+$ small aggregates form and upon increasing the mole fraction these aggregates coalesce forming a bicontinuous network, as the alkyl chains percolate throughout the IL structure. The mole fraction at which the percolation threshold is reached increases with m. This could be a result of the C12 alkyl chains having a stronger driving force behind chain aggregation when in the

smaller chain length mixtures, in comparison to the longer chain lengths, thus the hydrophobic effect is weaker as presumably an isolated C12 chain in $[C_2C_1im][Tf_2N]$ is more unfavourable than an isolate C12 chain in $[C_6C_1im][Tf_2N]$. Additionally, this could be related to the length of the chain, in that to percolate all the C12 chains need to be part of the same network, to do this they all need to be in contact with each other. This is most likely harder to achieve, when the polar network is more voluminous, due to it containing the shorter alkyl component along with the imidazolum headgroups and the $[Tf_2N]^-$ anions.

Analysis of the SANS data for *m* = 8 mixtures proved challenging as the scattering data did not show prominent PNPPs. To help understand the SANS data complimentary SAXS data was collected for a subset of the range. The SAXS data shows that all the compositions have a PNPP, thus can be depicted as a system that always consists of a bicontinuous structure, no matter what the mole fraction. The length scales of the fits can be related to an increase in apolar network on increasing mole fraction. The absence of a PNPP in most of the SANS data was related to small SLD differences between the apolar and polar networks. The *m* = 8 mixtures highlight the power of conducting complimentary SANS and SAXS experiments.

Overall, this study demonstrates that a mixture of two ionic liquids, with different cations but a common anion, display a wide range of structural chemistry. Ionic liquid mixtures can be exploited to access a range of different structures, and thus properties, simply by changing their composition.

3. Liquid-Crystalline Ionic Liquids as Reaction Media

3.1. Introduction

Solvent choice is often a crucial part in optimising the outcome of chemical reactions. Solvent properties (*e.g.* boiling point, density, polarity, and structure) can influence the outcome of the reaction by encouraging reaction pathways by stabilisation of one transition state over another. Also, having control over the reaction temperature and the solubility of the reagents and products affects the reaction outcome. Being able to control a reaction by simply changing the solvent is a powerful tool that is used on a range of scales daily, from the laboratory to industrial plants. Recently ILs have presented themselves as a unique solvent class with properties considerably different to conventional organic solvents. However, these solvents all exhibit no long-range ordering, that is they are all isotropic fluids. Anisotropic reaction media have the potential to influence the outcome of reactions by placing electronic and/or steric restrictions on the reactants, products, or transition states. Liquid-crystalline materials are anisotropic fluids that can provide such an ordered reaction media to potentially influence the stereochemical outcome and/or reaction rate.

3.1.1. Neutral Liquid Crystalline Materials as Reaction Media

Structurally ordered reaction media such as liquid-crystalline materials have received attention due to their potential to influence the outcome of reactions. In the 1970s and 1980s, neutral thermotropic LCs as reaction solvents was a hot topic.[106] A handful of unimolecular thermal reactions, such as the system investigated in this chapter, were investigated. For example, the Claisen rearrangement was reported by Bacon *et al.*, Scheme 3.1.(a).[107] who reported that the Clasien rearrangement was faster in the nematic phase than in the isotropic phase.[108] However a detailed study conducted by Dewar and Nahlovsky later contradicted this finding and showed that there was no change in kinetics upon the transition from the nematic phase to the isotropic phase.[109] Saeva *et al.* demonstrated that a chiral nematic liquid crystal affected the stereochemical outcome of a Claisen rearrangement (Scheme 3.1.(b)).[110] When the reaction was conducted in the isotropic phase of the LC, the product had no optical activity, whereas when the reaction was conducted in a chiral nematic phase the

product was optically active, with one enantiomer being favoured over the other, however the authors do not report the enantiomeric excess. The authors propose that the helical structure in the chiral nematic phase preferentially allows the rotation of the allyl group in one direction over the other.

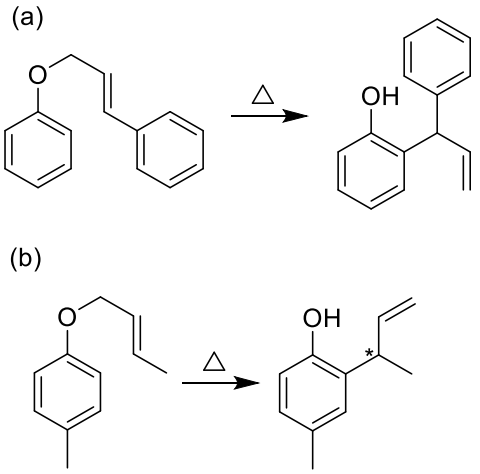

Scheme 3.1: The Claisen rearrangement investigated by; a) Bacon *et al.*; b) Saeva *et al*.

Many different types of reaction have been investigated in neutral LCs yet difficulties permeated through the literature. Neutral thermotropic LCs generally do not have large LC windows, and the addition of reactant(s) into the LC phases tends to disrupt them resulting in loss of ordering, which exhibits itself as either a narrowing or loss of the LC phase window. Another issue is that the neutral thermotropic LCs are not very flexible solvents, and generally only dissolve reactants of a similar polarity and shape. Liquid-crystalline ionic liquids (LCILs) can potentially overcome these difficulties, as they can solvate a wide range of different substrates and their LC windows are generally wide, in comparison to neutral LCs.

3.1.2. Liquid-Crystalline Ionic Liquids as Reaction Media

There are a small number of reports in the literature of LCILs being used as reaction solvents. The extensive 57 page review entitled “Ionic Liquid Crystals” by Binnemans in 2005 contained only a small section (150 words) on the use of LCILs as organised reaction media.[25] While only 2 pages were given in the 165 page 2016 review by Goossens *et al.* entitled “Ionic Liquid Crystals: Versatile Materials”.[5] This illustrates

the lack of research in this area. To date there have been two directions taken for the use of LCILs as reaction media. The first was to use the neat LCIL and dissolve the substrate(s) into the LCIL as a solvent.[111, 112] The second direction has been to confine the LCILs to a solid support.[113, 114] Supported ionic liquid crystal phase materials (SILCPs) have a very thin layer of a LCIL anchored to a porous support by physisorption or by covalent bonds. SILCPs have been investigated as catalyst supports and CO_2 adsorption materials at low pressures.[115, 116] Utilisation of LCILs has also facilitated the synthesis of inorganic nanomaterials such as graphene sheets and copper(I) chloride nanoparticles.[117] This Introduction will concentrate on the use of neat LCIL as reaction media.

Lee *et al.* carried out a Diels-Alder reaction in the LCIL $[C_{12}Him]Cl$ and reported on the stereoselectivity, Scheme 3.2.[111] The *exo* product was favoured over the *endo* product with an *exo*/*endo* ratio of 54:46 in the LCIL, which is higher than the isotropic molecular solvent they used as a comparison (ethanol, 12:88). In this case $[C_{12}Him]Cl$ was synthesised by the addition of a slight excess of 12 M HCl to dodecylimidazole. No attempt was made to remove the water added, or excess HCl, which could have an effect upon the stereochemical outcome of the reaction. The authors only compared the *exo*/*endo* ratio of the reaction in the LCIL to ethanol, so in this case the effect observed could be attributed to changing the solvent and not a liquid-crystalline effect. Indeed studies by Welton *et al.* and Dyson *et al.* reported considerable differences in the *exo*/*endo* ratio for a range of different ILs and conventional solvents for the Diels-Alder reaction between cyclopentadiene and methyl acrylate, Scheme 3.3.[118-121] They attribute these differences to the hydrogen bond donator ability of the solvent, which can interact with the carbonyl on the methyl acrylate. The stronger the hydrogen bond donation ability of the solvent the more the endo product is favoured.

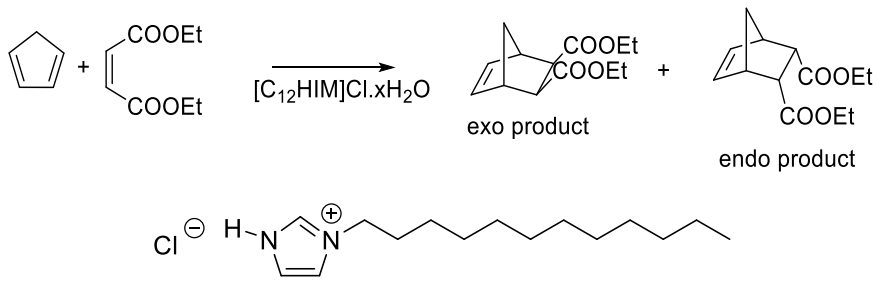

$[C_{12}Him]Cl$

Scheme 3.2: Diels-Alder system studied by Lee *et al*.[111]

Do and Schmitzer reported on an intramolecular Diels-Alder reaction in a LCIL with a crystal smectic T phase, where an intramolecular Diels-Alder reaction was favoured in comparison to an isotropic IL.[122] They proposed that this was due to the reactant being well dispersed in the LCIL and the reactant conformation leading to the intramolecular product being favoured in the smectic T phase. This study only compares the reaction outcome of one LCIL with one IL, which leaves the interpretation up for debate as the chemical differences between the solvents could be responsible for the outcome in addition to, or instead of, an LC effect.

Bruce *et al.* carried out a detailed study of a similar Diels-Alder reaction in 5 LCILs and 10 ILs, all imidazolium based, Scheme 3.3.[123] This system was chosen as Welton *et al.* had previously investigated the same system in ionic liquids and some conventional molecular solvents.[118] Thus, robust benchmark data were available to verify their own studies as three of the ILs chosen by Bruce *et al.* were also used by Welton *et al*. Upon careful analysis of the stereoselectivity of the reactions in the ILs and LCILs, a small but significant effect was assigned to the change from isotropic liquid into the liquid-crystalline state, with the *exo*/*endo* ratio changing, with the selectivity ranging from 76:24 to 82:18.

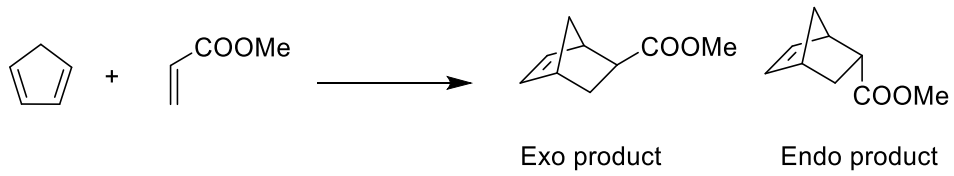

Scheme 3.3: The Diels-Alder system investigated by Welton *et al.*,[118-120] Dyson *et al.*,[121] and Bruce *et al*. [123]

By looking at patterns in the *endo*/*exo* ratio upon changing the solvents, a liquid-crystalline effect was identified, with the LCILs favouing the *exo* product with respect to the isotropic ILs. The authors went to a significant effort to deconvolute the effect of changing the alkyl chain, anion, and phase by comparing the reaction in 19 different solvents, along with complementary MD simulations. The conclusions drawn were similar to those of Welton *et al.*, in that the ability of the solvent to hydrogen bond to the carbonyl oxygen on the methyl acrylate promotes the *endo* transition state. The liquid-crystalline effect is attributed to the ordering in the LCILs effectively restricting

some protons on the imidazolium cation from hydrogen bonding with the methyl acrylate carbonyl, thus reducing the polarity of the solvent leading to the favourability of the *exo* transition state. The MD simulations also suggest that the *exo* transition state preferentially hydrogen bonds to the imidazolium cation due its more exposed carbonyl group.

In more recent, unpublished work Bruce *et al.* investigated a Claisen rearrangement in a range of LCs and LCILs, Scheme 3.4.[124] This system was chosen as it is a pericyclic reaction, similar to the Diels-Alder reaction and it was expected that order in the reaction solvent may influence the rate and/or selectivity of the reaction.

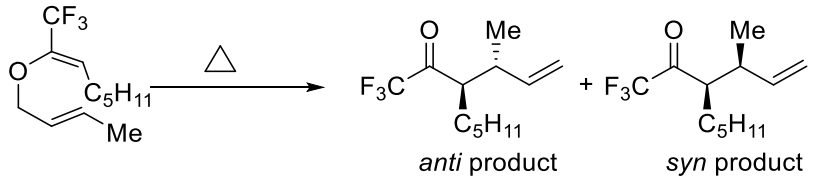

Scheme 3.4: The Claisen rearrangement studied by Bruce *et al*. [124]

The Claisen rearrangement was monitored by *in situ* ^{19}F nuclear magnetic resonance (NMR) spectroscopy over the bicontinuous cubic-to-isotropic phase transition in the LCIL [fan-C_{10}-NEt_3][BF_4], Figure 3.1, however no discontinuity in the rate was observed upon change in phase. Additionally, the Claisen substrate had poor solubility in the short chain IL [C_2C_1im][Tf_2N] and the rate of reaction in [fan-C_{10}-NEt_3][BF_4] and its precursor 3,4,5-tris(dodecyloxy)benzyl chloride were almost identical. Thus, it was proposed that the Claisen rearrangement occurred in the disordered alkyl chain region of the LCILs and as such no liquid-crystalline effect is observed.

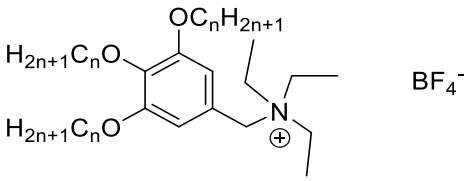

[Fan-C_{10}-NEt_3][BF_4] | Cr · 42 · Cub_{bi} · 82 · Iso

Figure 3.1: Structure of [3,4,5-tris(decyloxy)benzyl]triethylammonium tetrfluoroborate ([fan-C_{10}-NEt_3][BF_4]) and its mesomorphic behaviour, transition temperatures are given in ° C; Cr, crystal; Cub_{bi}, bicontinuous cubic; Iso, isotropic.

It was predicted that by introducing a charge into a similar system, that undergoes a pericyclic rearrangement (*e.g.* by changing from an allyl ether to an allyl enammonium) the reactant would interact more with the ordered charged regions of the LCILs and thus a liquid-crystalline effect might be expected.

3.2. Aims

The research detailed in this chapter aimed to contribute to the study of ordered reaction media and its effect upon the outcome of reactions. The ordered reaction media under investigation are LCILs. In order to be able to derive kinetic parameters in a complex media such as a LCILs, an appropriate method needed to be developed. To develop such a method the reaction under investigation was monitored in a conventional solvent, followed by a range of ionic liquids and finally in LCILs. The system under investigation is that of an allyl enammonium that undergoes an aza-Claisen rearrangement. To ascertain if the ordering of the LCILs can influence the outcome of the aza-Claisen rearrangement, the reaction was monitored through a range of temperatures that spans one phase transition of the solvent.

3.3. Aza-Claisen Rearrangement Monitored by *in situ* ^{1}H NMR Spectroscopy

The rate of the aza-Claisen rearrangement of enammonium bromide (**1**-Br**,** Scheme 3.5) was investigated using *in situ* ^{1}H NMR spectroscopy.

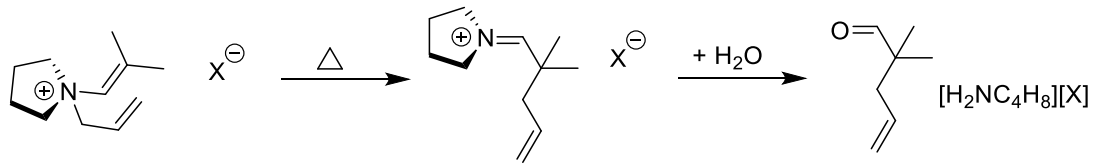

1-X **2**-X **3**

Scheme 3.5: The aza-Claisen rearrangement of 1-X, X = Br, BF_4.

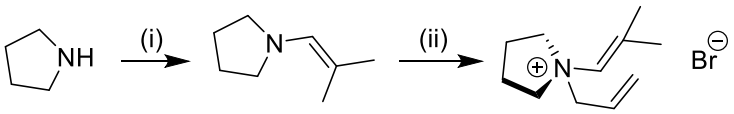

1-Br

Scheme 3.6: The synthetic route to enammnoium bromide **1**-Br. (i) isobutyraldehyde, anhydrous K_2CO_3, diethyl ether, 0 °C, 24 h; (ii) allyl bromide, acetonitrile, –20 °C, 24 h.

1-Br was synthesised in two steps, Scheme 3.6, firstly isobutyraldehyde was added to pyrrolidine in the presence of potassium carbonate to yield 2-methylpropenyl pyrolidine. Then 2-methylpropenyl pyrolidine underwent quaternisation to afford the enammnoium bromide **1**-Br.

The enammonium bromide **1**-Br, Scheme 3.5, undergoes an aza-Claisen rearrangement to yield iminium **2**-Br, which subsequently undergoes hydrolysis to yield the aldehyde **3**, the water needed for the hydrolysis is present in the solvent and trace ammounts are sufficient.

In the first instance the aza-Claisen rearrangement was investigated by ^{1}H NMR spectroscopy in acetonitrile, followed by two ionic liquids, namely $[C_4C_1im][Tf_2N]$ and $[C_8C_1im]Br$, and finally in the LCILs $[fan\text{-}C_n\text{-}NEt_3][BF_4]$. The kinetic parameters and the viability of the method will be discussed.

3.3.1. *In situ* Monitoring of the Aza-Claisen Rearrangement in Acetonitrile-d_3

Acetonitrile was chosen as a solvent to investigate the kinetics of this reaction, as it is a typical example of a conventional organic solvent in which **1**-Br has good solubility. To make the ^{1}H NMR spectra easier interpret, deuterated acetonitrile was used.

In a typical procedure for the aza-Claisen rearrangement in acetonitrile-d_3, enammonium bromide (**1**-Br, 10-13 mg) was dissolved in acetonitrile-d_3 (0.5 cm^3) to make a 0.08-0.11 mol dm^{-3} solution, and heated inside a 500 MHz NMR spectrometer in a standard capped 5 mm NMR tube. Proton NMR spectra were acquired periodically to monitor the reaction kinetics over a temperature range.

An example of the ^{1}H NMR spectra obtained while following the rearrangement are shown in Figure 3.2. The rate constant at each reaction temperature was calculated using the absolute values of the ^{1}H NMR spectrometer response for an appropriate proton environment, in this case the bleaching of a methyl group on **1**-Br was used in order to calculate the first order rate constant.

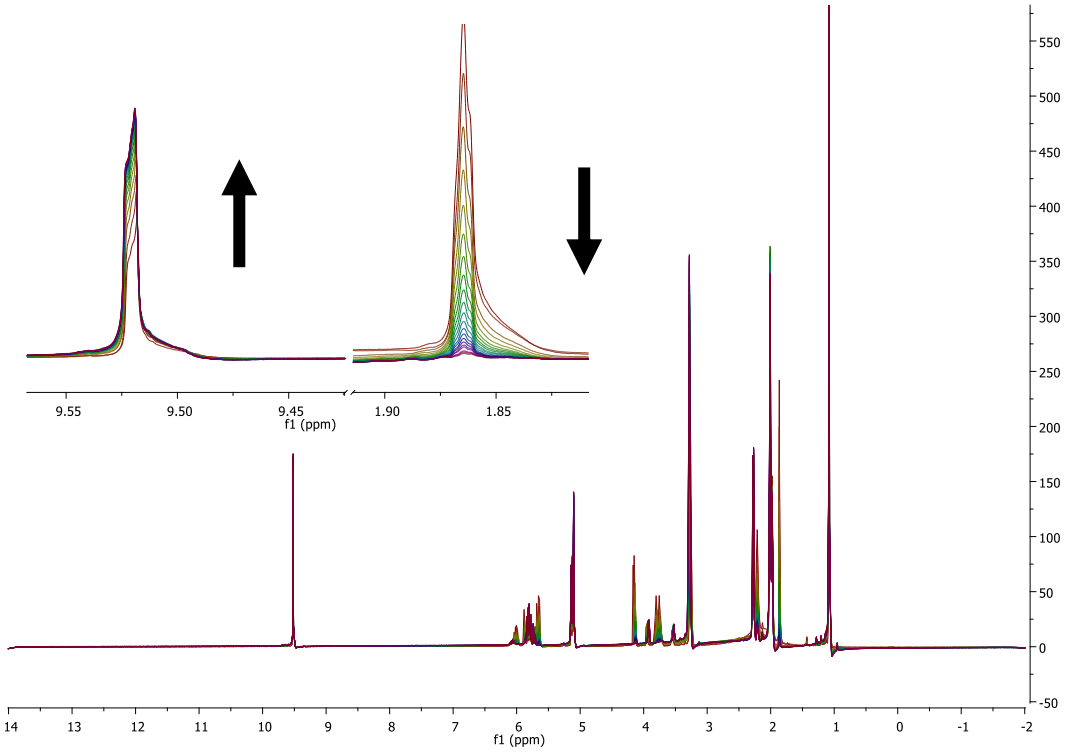

Figure 3.2: ^{1}H NMR spectra of the rearrangement of **1**-Br in acetonitrile-d_3. Inserted are expansions of the decay of a methyl signal on **1**-Br at 1.87 ppm and the appearance of the aldehyde proton of **3** at 9.52 ppm.

Once the spectrometer response was collected the data were plotted to calculate the rate constant. To do so, the first-order rate equation, Equation 3.1, is rearranged to Equation 3.2, and then both sides of the equation are integrated to give Equation 3.3. Equation 3.3 can then be rearranged to give Equation 3.4, that can be plotted as a y = mx + c plot to yield a straight line. An example plot is given in Figure 3.3.

Equation 3.1 $$\text{rate} = -\frac{d[A]}{dt} = k[A]$$

Equation 3.2 $$\frac{d[A]}{[A]} = -k\,dt$$

Equation 3.3 $$\ln[A] - \ln[A]_0 = -kt$$

Equation 3.4 $$\ln[A] = -kt + \ln[A]_0$$

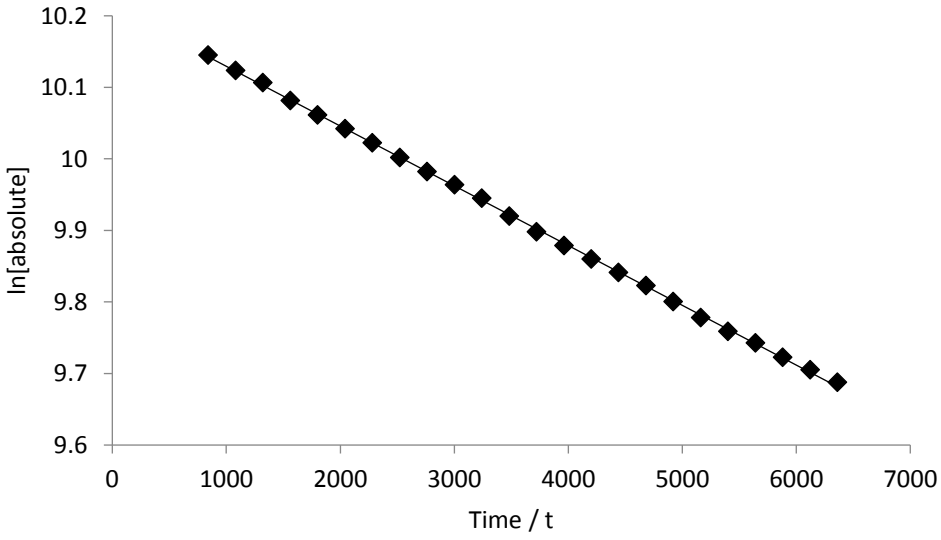

Figure 3.3: First-order rate plot of the rearrangement of **1**-Br in acetonitrile-d_3 at 50 °C.

The aza-Claisen rearrangement in acetonitrile-d_3 was monitored by *in situ* ^{1}H NMR spectroscopy over a temperature range of 40 – 70 °C in 5 °C increments. The calculated rate constants and their standard error, as given by Excel's 'Analysis Toolpak' linear regression tool, are shown in Table 3.1.

Table 3.1: Rate constants (*k*) at different temperatures for the rearrangement of **1**-Br in acetonitrile-d_3.

Reaction temperature / °C	k / × 10^{-5} s^{-1}
40.0	2.22 ± 0.06
40.0	2.24 ± 0.05
45.0	4.27 ± 0.02
45.0	3.52 ± 0.01
50.0	7.46 ± 0.09
50.0	8.35 ± 0.03
55.0	14.8 ± 0.1
60.0	24.1 ± 0.6
60.0	22.8 ± 0.3
60.0	26.2 ± 0.5
60.0	27.5 ± 0.6
65.0	43.9 ± 0.1
65.0	42.0 ± 0.4
70.0	93.5 ± 0.7
70.0	80.9 ± 0.9

The activation parameters for the rearrangement can be calculated from Eyring plots, where the enthalpy and entropy of activation ($\Delta H^{\neq}$ and $\Delta S^{\neq}$ respectively) can be found by plotting $\ln\frac{k}{T}$ against $\frac{1}{T}$. The rate of reaction as a function of temperature can be described by the Eyring equation, Equation 3.5.

Equation 3.5 $$k = \frac{k_B T}{h} e^{-\Delta G^{\neq}/RT}$$

Where $\Delta G^{\neq}$ is the Gibbs energy of activation, k_B is the Boltzman constant, h is Planks constant and T is temperature. The Gibbs energy of activation can be expressed as in Equation 3.6.

Equation 3.6 $$\Delta G^{\neq} = \Delta H^{\neq} - T\Delta S^{\neq}$$

Where $\Delta H^{\neq}$ is the enthalpy of activation and $\Delta S^{\neq}$ is the entropy of activation. Division of Equation 3.5 by T and substitution of $\Delta G^{\neq}$ gives Equation 3.7 in the logarithmic form.

Equation 3.7 $$\ln\frac{k}{T} = \ln\frac{k_B}{h} - \frac{\Delta H^{\neq}}{R}\frac{1}{T} + \frac{\Delta S^{\neq}}{R}$$

A plot of Equation 3.7, was constructed to determine the enthalpy of activation ($\Delta H^{\neq}$) and the entropy of activation ($\Delta S^{\neq}$), and values of $\Delta H^{\neq} = 105 \pm 2$ kJ mol^{-1} and $\Delta S^{\neq} = 1 \pm 6$ J K^{-1} mol^{-1} were found, Figure 3.4. These data provide a good benchmark to compare the rates of reaction for this rearrangement in different LC and isotropic ILs.

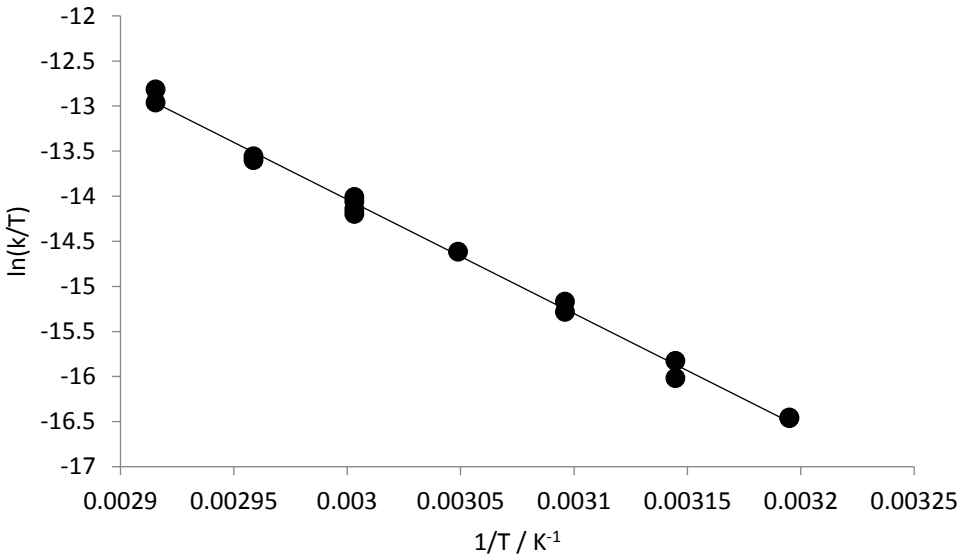

Figure 3.4: Eyring plot for the aza-Claisen rearrangement of **1**-Br in acetonitrile-d_3.

3.3.2. *In situ* Monitoring of the Aza-Claisen Rearrangement in Ionic Liquids

Generally, upon going from a conventional liquid, such as acetonitrile, to an IL, and then to a LCIL, the viscosity increases, which can lead to poor resolution in ^{1}H NMR spectroscopy. To assess the ease of *in situ* monitoring by ^{1}H NMR spectroscopy, the kinetics of the aza-Claisen rearrangement in two ILs were investigated. The ionic liquids chosen were 1-butyl-3-methylimidazolium bis(trifuoromethylsulfonyl)amide, [C_4C_1im][Tf_2N] and 1-octyl-3-methylimidazolium bromide, [C_8C_1im]Br, Figure 3.5. [C_4C_1im] [Tf_2N] is a relatively low viscosity ionic liquid (0.52 P at 25 ˚C) while [C_8C_1im]Br is more viscous (72.45 P at 25 ˚C).[125, 126] These two ionic liquids were

chosen to determine if the increase in viscosity would inhibit the ability to obtain kinetic data from ^{1}H NMR spectroscopy. Another consideration is that there will now be no deuterated solvent for the NMR spectrometer to lock onto, although a deuterated co-solvent can be added into the reaction mixture. However, such co-solvents can interfere with the reaction kinetics, as has been demonstrated by Harper *et al*. a number of times,[127-129] and so another method, and the one explored here, is to add a sealed glass capillary containing a lock solvent into the NMR tube.[130] The lock solvent ideally has a strong deuterium signal, as its volume is low when compared to the volume of the reaction mixture, D_2O was used in this case.

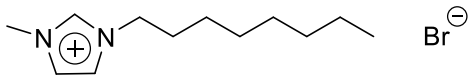

$[C_8C_1im]Br$

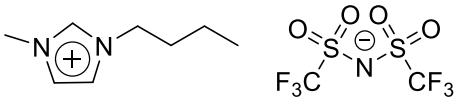

$[C_4C_1im][Tf_2N]$

Figure 3.5: The structure of $[C_8C_1im]Br$ and $[C_4C_1im][Tf_2N]$.

The aza-Claisen rearrangement in $[C_4C_1im][Tf_2N]$ at 60 °C with a D_2O insert was monitored by ^{1}H NMR spectroscopy and the first-order rate plots are shown in Figure 3.6. Duplicate experiments gave almost identical rate constants, $k = 4.30 \times 10^{-4} \pm 6 \times 10^{-6}$ s^{-1} and $k = 4.2 \times 10^{-4} \pm 1 \times 10^{-5}$ s^{-1}.

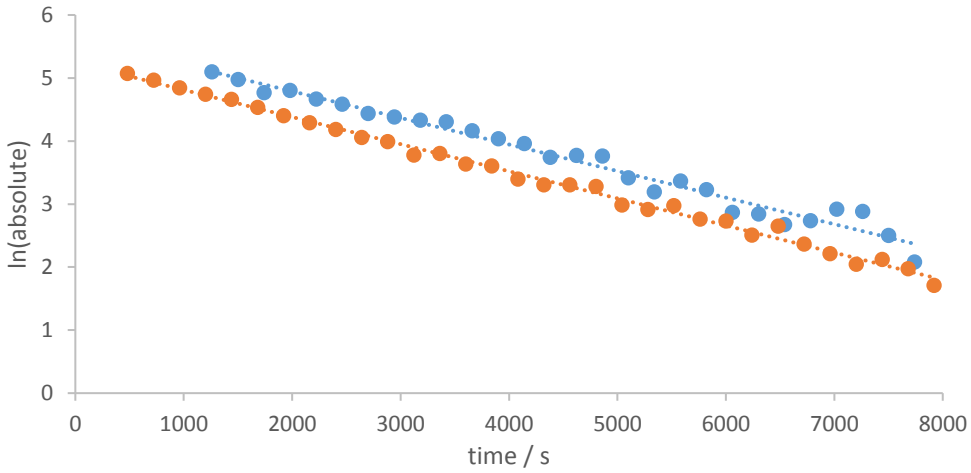

Figure 3.6: Two first-order rate plots for the aza-Claisen rearrangement in $[C_4C_1im][Tf_2N]$ at 60 ˚C, obtained using ^1H NMR spectroscopy with a D_2O lock insert.

The aza-Claisen rearrangement in $[C_8C_1im]Br$ was monitored *via* ^1H NMR spectroscopy at 60 ˚C, to assess if the reaction can be followed in a more viscous ionic liquid. Monitoring the rearrangement in $[C_8C_1im]Br$ proved to be unsuccessful as the ^1H signals that are not obscured by the $[C_8C_1im]Br$ signals are too weak and broad to provide reliable integrals for kinetic data, Figure 3.7.

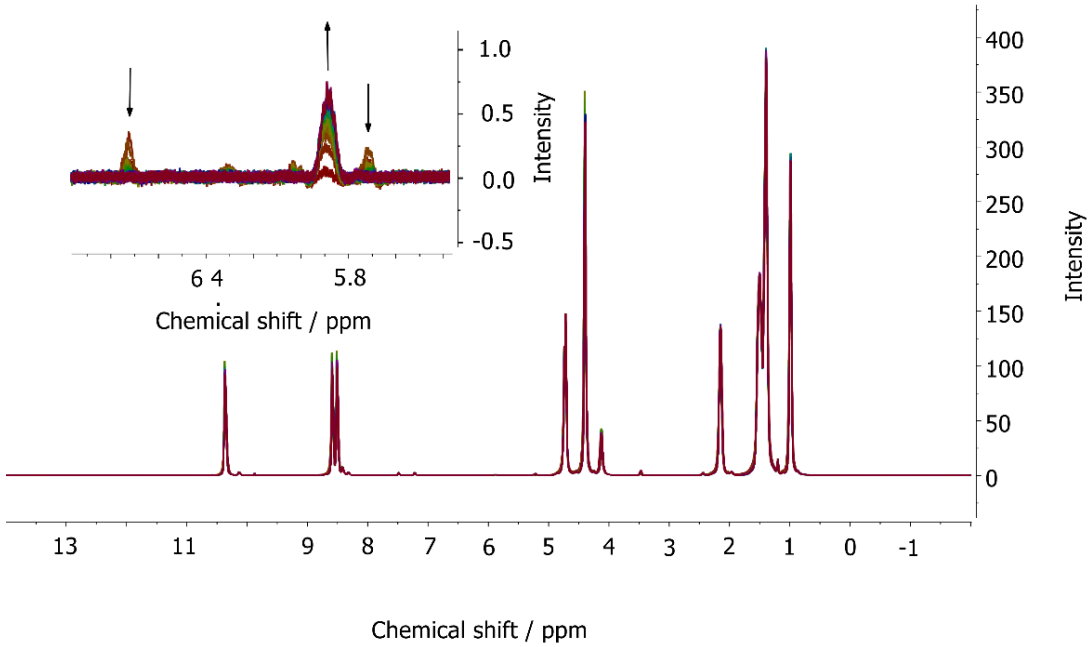

Figure 3.7: ^1H NMR spectra of the rearrangement of **1**-Br in $[C_8C_1im]Br$. Inserted are expansions of the decay of **1**-Br and the production of **3**.

As conventional ^{1}H NMR spectroscopy proved to be an inadequate method for monitoring the rearrangement in the viscous [C_8C_1im]Br medium, an alternative method was required. High-resolution magic angle spinning (HRMAS) ^{1}H NMR spectroscopy has proven to be an effective technique for observation of simple molecules in ILs,[131] therefore it is investigated as a technique to monitor the rearrangement of **1**-Br in ionic liquids and liquid-crystalline ionic liquids. It should be noted that direct comparisons of the rates obtained using HRMAS and high-resolution NMR spectroscopy cannot be made as the temperature was not calibrated correctly for the HRMAS experiments. In the first instance, [C_4C_1im][Tf_2N] was syringed into a magic angle spinning rotor and ^{1}H NMR spectra taken with and without spinning at 4000 Hz. The spinning of the sample at the magic angle had a profound effect upon the appearance the spectra, Figure 3.8, so that the signals become sharper and better defined, the insert in Figure 3.8 illustrates this well. Without spinning the signal was broad and features were unclear (red spectra), whereas with spinning the signal is a sharper, well-resolved triplet (blue spectra).

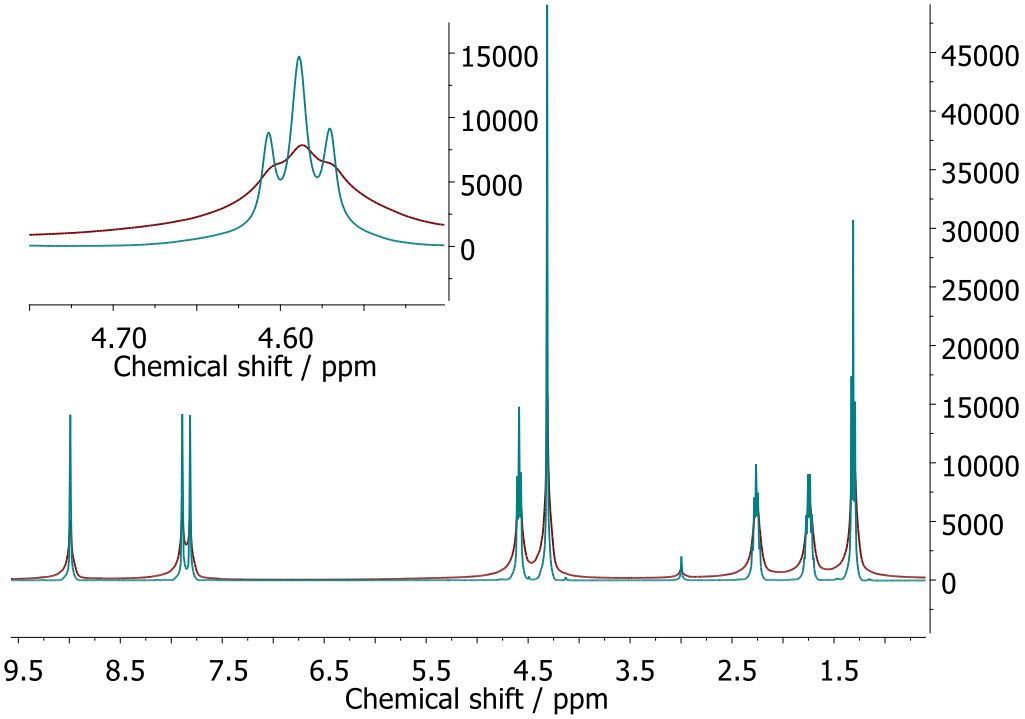

Figure 3.8: HRMAS ^{1}H NMR spectra of [C_4C_1im][Tf_2N] without spinning (red spectra) and with spinning (blue spectra, 4000 Hz) at 290 K. Insert, expansion of N-C*H*2 signal.

HRMAS ^{1}H NMR spectra were recorded on a second sample, this time containing the aza-Claisen substrate (**1**-Br, 5.0 mg) dissolved in [C_4C_1im][Tf_2N] (50 µl) at 60 ˚C and

the stacked spectra are presented in Figure 3.9, while the first-order kinetic plot is presented in Figure 3.10

The rate constant for the rearrangement calculated using HRMAS ^{1}H NMR spectroscopy was $k = 2.11 \times 10^{-4} \pm 2 \times 10^{-6}$ s^{-1}. This rate constant cannot be directly compared to those obtained using high-resolution spectroscopy, however, they are similar in magnitude. HRMAS has therefore helped to increase the resolution of the ^{1}H NMR spectra of the IL [C_4C_1im][Tf_2N] and kinetics of the rearrangement can be followed.

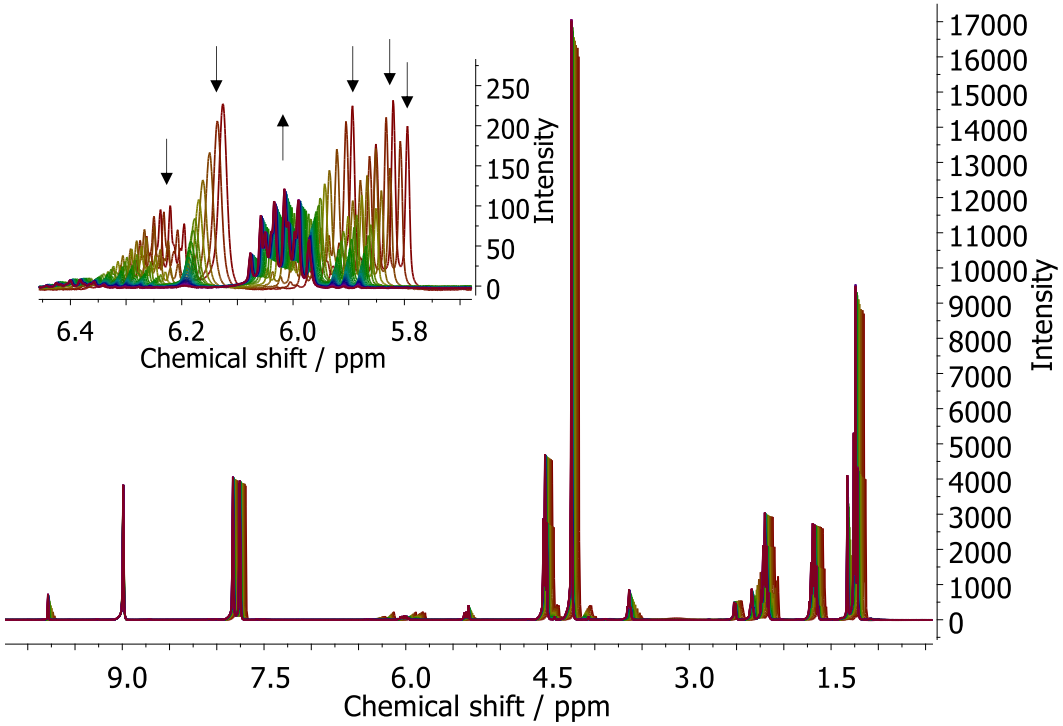

Figure 3.9: HRMAS ^{1}H NMR spectra of the rearrangement of **1**-Br in [C_4C_1im][Tf_2N] at 60 °C. The insert is an expansion of the 5.9 – 6.4 ppm range and the arrows indicate peak intensity change over time.

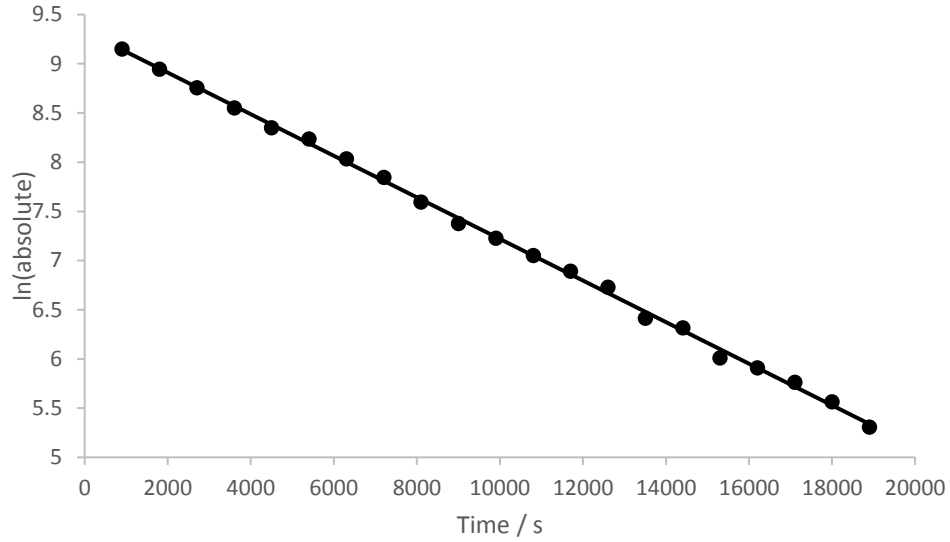

Figure 3.10: First-order rate plot for the rearrangement of **1**-Br in [C_4C_1im][Tf_2N] at 60 ˚C, attained using HRMAS ^{1}H NMR spectroscopy.

3.3.3. *In situ* Monitoring of the Aza-Claisen Rearrangement in Liquid-Crystalline Ionic Liquids

As indicated before, [C_4C_1im][Tf_2N] has a low viscosity (for an IL) hence, it is not surprising that it is possible to follow a reaction in such a solvent using ^{1}H NMR spectroscopy. HRMAS ^{1}H NMR spectroscopy has provided a way to gain sharper spectra and thus possibly better-quality kinetic data. Instead of changing the solvent to [C_8C_1im]Br, to establish if the kinetics can be followed in a more viscous solvent, as was explored before, a LCIL was used as the next solvent, as the ultimate aim was to follow the rearrangement in a liquid-crystalline environment. The liquid-crystalline ionic liquid was (3,4,5-tris(decyloxy)benzyl)triethylammonium tetrfluoroborate ([fan-C_{10}-NEt_3][BF_4]) which has the following phase sequence upon heating; crystalline 42 °C bicontinuous cubic 82 °C isotropic, Figure 3.11.[132]

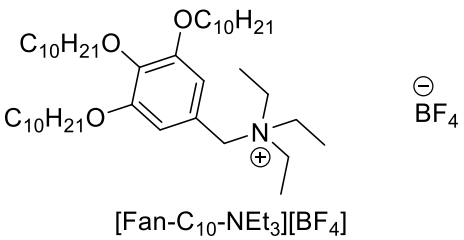

[Fan-C_{10}-NEt_3][BF_4]

Figure 3.11: Structure of (3,4,5-tris(decyloxy)benzyl)trimethylammonium tetrfluoroborate, [fan-C_{10}-NEt_3][BF_4].

For comparisons to be drawn, a ^{1}H NMR spectrum in CD_3Cl was acquired of [fan-C_{10}-NEt_3][BF_4], along with a ^{1}H NMR spectrum of neat [fan-C_{10}-NEt_3]BF_4 in the Cub_{bi} mesophase at 63 ˚C, using the high-resolution spectrometer, Figure 3.12. As [fan-C_{10}-NEt_3][BF_4] is solid at room temperature, a MAS rotor was packed with solid [fan-C_{10}-NEt_3][BF_4] (48.5 mg) and the aza-Claisen substrate (**1**-Br, 3.0 mg) was added on top then mixed physically. HRMAS ^{1}H NMR spectra (4000 Hz) were taken over a range of temperatures to establish if this technique would provide suitable spectra for kinetic studies; the temperatures shown here are 17, 67, and 82 ˚C, Figure 3.13. At 17 ˚C [fan-C_{10}-NEt_3][BF_4] is in the crystalline state and the HRMAS NMR spectrum is broad and almost featureless when compared to the spectra at higher temperatures. On heating the sample into the cubic mesophase (Figure 3.13, 67 °C, green), the spectrum clarity has improved in comparison to the ^{1}H NMR spectrum acquired on the high-resolution spectrometer, although not enough to be able to extract kinetic data. Upon further heating the sample into the isotropic IL (Figure 3.13, 82 °C, blue), the signals in the spectrum become sharper and better resolved, although, most splitting patterns are still unresolved. Although the clarity of spectra acquired using HRMAS ^{1}H NMR spectroscopy improved upon going from the crystalline solid phase into the Cub_{bi} mesophase and finally into the isotropic phase, the spectra were not of a high enough quality for kinetic studies.

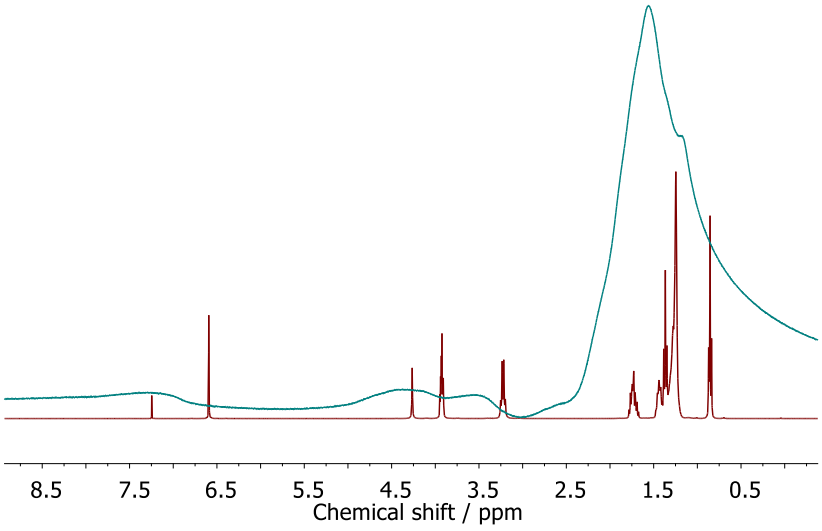

Figure 3.12: ^{1}H NMR spectra of [fan-C_{10}-NEt_3][BF_4], dissolved in CD_3Cl, red, neat at 63 ˚C (Cub_{bi}), Blue.

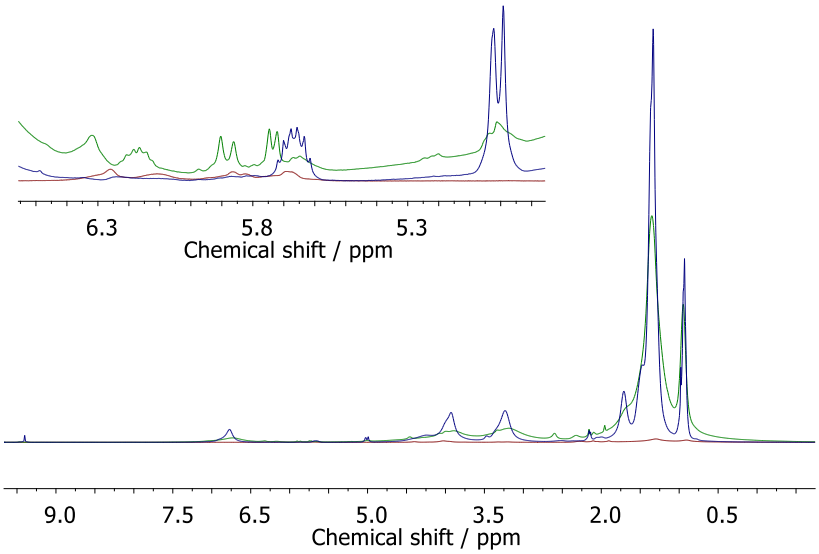

Figure 3.13: HRMAS ^{1}H NMR spectra of **1**-Br in [fan-C_{10}-NEt_3][BF_4] at different temperatures; red 17 ˚C (crystalline), green 67 ˚C (Cub_{bi}) , blue 82 ˚C (isotropic liquid).

3.4. Aza-Claisen Rearrangement Monitored by *in situ* IR Spectroscopy

As it is not possible to monitor the rearrangement by *in situ* ^{1}H NMR and HRMAS NMR spectroscopy in viscous media, an alternative technique is required; a promising alternative is infrared (IR) spectroscopy.

3.4.1. Aza-Claisen Rearrangement in Acetonitrile

To determine the viability of using *in situ* infrared spectroscopy to monitor the reaction kinetics, the rearrangement of **1**-Br (54.6 mg) in acetonitrile (1.5 cm^3, 0.140 mol dm^{-3}) was followed. An oil bath was set to 60 ˚C and aliquots of the reaction mixture taken every 30 minutes and an IR spectrum acquired on a Bruker Alpha Fourier transform infrared (FTIR) spectrometer without any work up. Figure 3.14 shows the overlaid IR spectra.

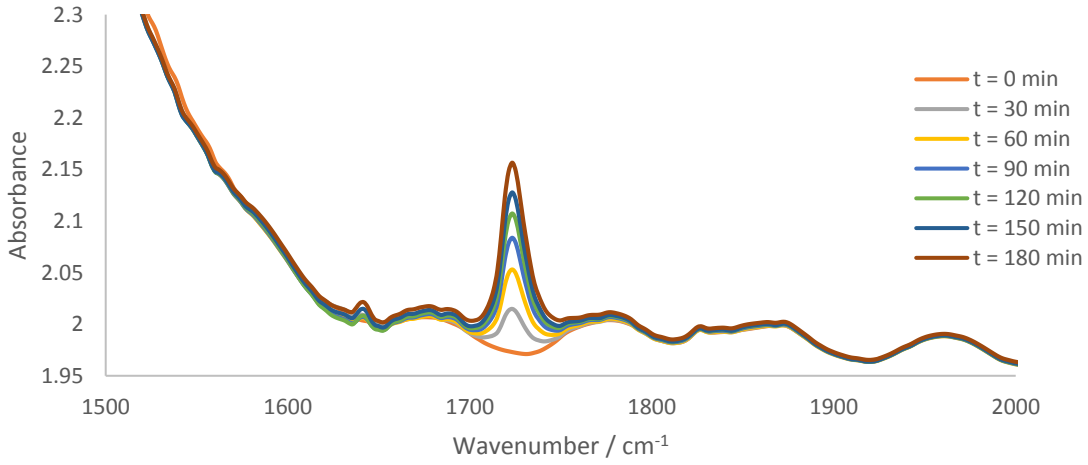

Figure 3.14: IR spectra, in the range of 1500 – 2000 cm^{-1}, of the aza-Claisen rearrangement of **1**-Br in acetonitrile upon heating to 60.0 °C.

From this basic study it was clear that the rearrangement could be monitored by an increase in the absorbance at 1723 cm^{-1} due to the carbonyl group on the aldehyde **3** being formed. A more detailed study of the kinetics was carried out using a ReactIR iC10.

The ReactIR allows *in situ* FTIR spectroscopy in real time for monitoring of reactions. The peak absorbance intensity at 1725 cm^{-1} was followed over time to gain kinetic data. As the aldehyde formation was now being followed rather than the bleach of the enammonium bromide, an assumption that the hydrolysis of the iminium intermediate is appreciably faster that the rearrangement of the substrate was made. This is a reasonable assumption, as the rearranged iminium product is not observed in the ^{1}H NMR spectra (**1**-Br, acetonitrile-d_3).

ReactIR was used to monitor the rearrangement of enammonium bromide in acetonitrile at approximately 60 ˚C. Two experiments were carried out: Firstly the oil bath temperature was set to 60.0 ˚C, which results in a reaction temperature lower than 60.0 °C due to heat transfer losses. Secondly, the temperature was monitored using a thermocouple which was placed directly into the reaction mixture. The temperature difference between the oil bath and the reaction mixture temperature was significant, so that when the oil bath temperature was set to 64.1 ˚C the reaction mixture temperature was 60.2 ˚C

The appearance of the carbonyl stretch of the aldehyde (**3**) was monitored over time, Figure 3.15, and a rate constant calculated. Assuming that the rate of aldehyde formation, and therefore intensity increase, is inversely proportional to the depletion of the aza-Claisen substrate **1**-Br, the rate constant can be calculated.

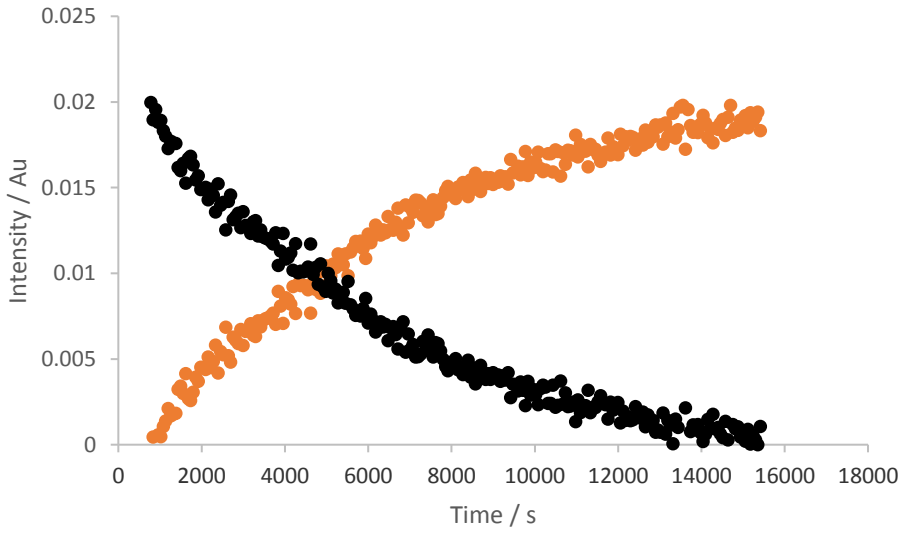

Figure 3.15: Carbonyl stretch of **3** (1725 cm^{-1}) intensity, orange. Calculated enammonium bromide depletion, black.

From the calculated depletion of the enammnoium bromide, first-order rate plots can be constructed and hence rate constants determined, Figure 3.16 and Table 3.2.

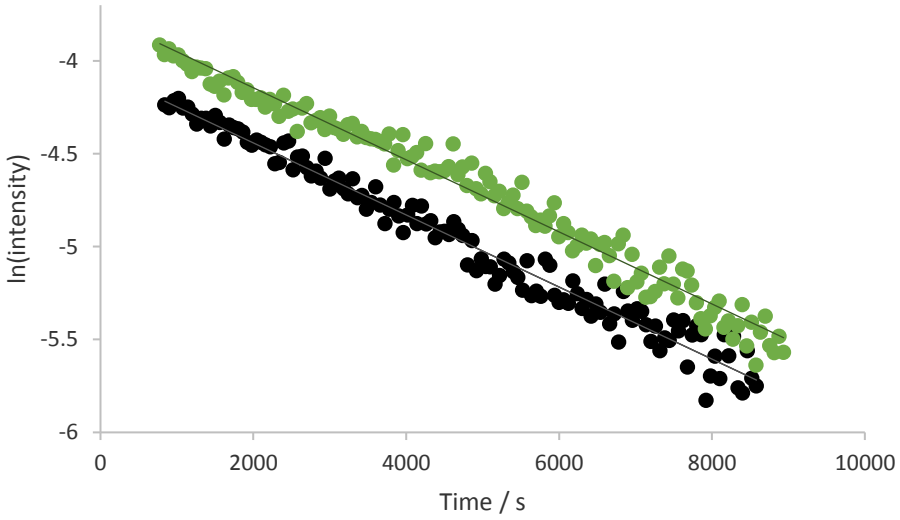

Figure 3.16: First-order rate plot from ReactIR Data. Oil bath temperature 60.0 ˚C, green; Thermocouple temperature 60.2 °C, black.

Interestingly, the rate constants obtained from the reactIR experiments do not correlate correctly with reaction temperature, Table 3.2. The rate is expected to increase with increasing temperature, as observed with the *in situ* ^{1}H NMR spectroscopy data. In this case the rate constant remained constant upon increasing temperature. Also the rate constants obtained from the ReactIR experiments are slightly smaller than that obtained by *in situ* ^{1}H NMR spectroscopy, which is likely a result of experimental error as no repeat measurements were conducted.

Table 3.2: Rate constants of the aza-Claisen rearrangement of **1**-Br in acetonitrile as determined by *in situ* FTIR spectroscopy.

Method	Temp / ˚C	k / × 10^{-4} s^{-1}
In situ FTIR spectroscopy	Probe 60.2	1.94 ± 0.03
In situ FTIR spectroscopy	Oil bath 60.0	1.94 ± 0.03
In situ ^{1}H NMR spectroscopy [a]	60.0	2.51 ± 0.09

a, Reaction conducted in acetonitrile-d_3 and the rate constant is an average of four experiments

3.4.2. Aza-Claisen Rearrangement in Ionic Liquids

Following on from the ReactIR work in acetonitrile, the same procedure was used in an attempt to follow the kinetics of the rearrangement in $[C_4C_1im][Tf_2N]$. Firstly solution IR spectra using a Bruker Alpha TF-IR were attained of the pure $[C_4C_1im][Tf_2N]$, **1**-Br in $[C_4C_1im[Tf_2N]$, and then spectra recorded on heating at 60 ˚C in an oil bath. To obtain the spectra, the enammnoium bromide (**1**-Br, 19.0 mg) was dissolved in $[C_4C_1im][Tf_2N]$ (1.0 cm^3) and heated to 60 °C and aliquots taken at 30, 60 and 180 minutes. The IR spectra showed little observable change over the course of the reaction. This is because the starting material and product IR signals overlap the solvent signals. Interestingly a carbonyl signal is absent even after 180 minutes. This could be either due to the aldehyde carbonyl stretch of **3** being shifted and broadened due to the hydrogen bonding with the acidic protons on $[C_4C_1im][Tf_2N]$, or it could be due to the $[C_4C_1im][Tf_2N]$ not containing enough water to hydrolyse the rearranged product **2**-Br into the aldehyde. However, the most likely reason is that the hydrolysis of the iminium (**2**-Br) has become the rate determining step of the reaction due to $[C_4C_1im][Tf_2N]$ stabilising the iminium towards hydrolysis. ILs containing $[Tf_2N]^-$ such as $[C_4C_1im][Tf_2N]$ and $[C_4C_1pyrr][Tf_2N]$ (1-butyl-1-methylpyrrolidinium bis(trifluoromethylsulfonyl)imide, Figure 1.1) have been shown to hydrolytically stabilise highly moisture sensitive compounds such as PCl_3, which usually must be used under highly anhydrous conditions.[133, 134] PCl_3 was shown to be stable in $[C_4C_1pyrr][Tf_2N]$ even when the IL had not been dried and under stirring in air for weeks.[133].

3.5. Aza-Claisen Rearrangement Monitored by *ex situ* ^{1}H NMR Spectroscopy

As a method to directly monitor the rearrangement under investigation has proven hard, an indirect method is required. Aliquots of the reaction mixture were taken at regular intervals and dissolved in chloroform-d. The aliquots were then stored at – 20 ºC and each aliquot was examined using ^{1}H NMR spectroscopy at 0 °C. The rate of rearrangement is very low at these temperatures, so it was assumed that the reaction had stopped at the time that the aliquots had been taken.

3.5.1. Aza-Claisen Rearrangement in Acetonitrile

To validate the aliquot-^{1}H NMR spectroscopy method, it was carried out in acetonitrile so that a comparison can be made to the *in situ* ^{1}H NMR spectroscopy kinetic data. The kinetics of each reaction were determined by normalising a signal from the aza-Claisen substrate (**1**-Br, N-C*H*$_2$, *δ* 4.36 – 4.14 ppm) to a signal from the aldehyde product (**3**, CO*H*, *δ* 9.45). In a typical procedure the aza-Claisen precursor, **1**-Br (0.02 g), was dissolved in the acetonitrile (1 cm^3) that had been preheated to the reaction temperature. As had been established using the ReactIR, oil bath temperatures are different to the reaction temperature so a thermocouple is placed in the reaction solvent to determine the true reaction temperature. Table 3.3 tabulates the rate and temperatures of the aza-Claisen rearrangement of **1**-Br in acetonitrile monitored by taking aliquots. These results are comparable to the results obtained by *in situ* ^{1}H NMR spectroscopy, as shown by the Eyring polts in Figure 3.17.

Table 3.3: Kinetic data for the aza-Claisen rearrangement of **1**-Br in acetonitrile, monitored by aliquot-^{1}H NMR spectroscopy.

Temperature/ °C	k / ×10^{-4} s^{-1}
58.7	2.09 ± 0.04
58.7	2.14 ± 0.09
73.3	41.6 ± 0.5

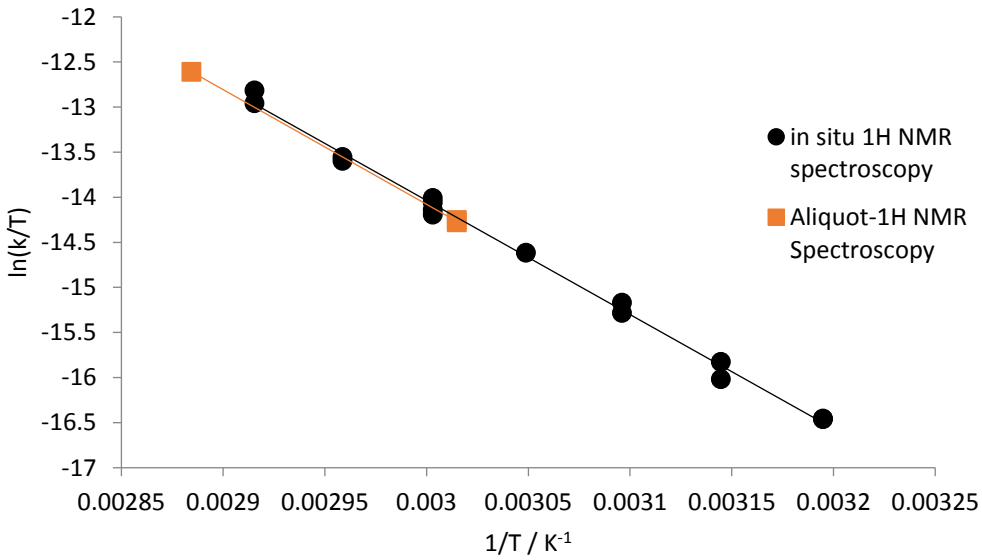

Figure 3.17: Eyring plot for the aza-Claisen rearrangement of **1**-Br in acetonitrile. Orange data points are obtained by taking aliquots, black data points are obtained from *in situ* ^{1}H NMR spectroscopy.

3.5.2. Aza-Claisen Rearrangement in Liquid Crystalline Ionic Liquids

Once the aliquot-^{1}H NMR spectroscopy method had been validated by comparison with the *in situ* data, the rearrangement was investigated in two LCILs using [fan-C_n-NEt_3][BF_4] (*n* = 10, 12), which display bicontinuous cubic and columnar mesophases, Table 3.4. The kinetics were monitored across a range of temperatures that spanned phase transitions in the LCILs to better understand if the liquid-crystalline order was affecting the rearrangement. With [fan-C_{10}-NEt_3][BF_4] as the solvent the bicontinuous cubic-to-isotropic phase transition was investigated, while the bicontinuous cubic-to-columnar phase transition was observed in [fan-C_{12}-NEt_3][BF_4]. It was not possible to monitor across the columnar-to-isotropic transition as the rearrangement proceeds too quickly at that temperature.

Table 3.4: Mesophase behaviour of [fan-C_n-NEt_3][BF_4], *n* = 10, 12. Cr, crystalline; Cub, bicontinuous cubic; Col, columnar; Iso, isotropic.

Liquid-crystalline ionic liquid	Phase behaviour, temperatures are in °C
[Fan-C_{10}-NEt_3][BF_4]	Cr 42 Cub 82 Iso
[Fan-C_{12}-NEt_3][BF_4]	Cr 32 Cub 49 Col 126 Iso

Dissolving a solute in a liquid-crystalline solvent can have a profound effect upon the phase transitions observed, as the solute can disturb the mesophase ordering.[135] In an effort to reduce this, an anion exchange reaction was performed on the aza-Clasien substrate **1**-Br, to yield **1**-BF_4, so that the counter anions were the same. To ensure good mixing of the substrate in the solvent, **1**-BF_4 and [fan-C_{10}-NEt_3][BF_4] were dissolved in dichloromethane and stirred together for 10 min at 0 °C. Then the solvent was removed under reduced pressure to yield the mixture as a colourless solid. The same procedure was used to mix **1**-BF_4 with [fan-C_{12}-NEt_3][BF_4]. Both mixtures were stored at –20 °C.

The liquid-crystalline properties of the two mixtures were investigated by polarising optical microscopy (POM) and differential scanning calorimetry (DSC) and the phase transitions on the first heating are reported in Table 3.5. The first heat is reported, as the reaction kinetics will be investigated on the first heat of these mixtures. In both cases the liquid crystalline windows were reduced, with both the melting and clearing points perturbed slightly.

Table 3.5: Thermal properties of mixtures of [fan-C_n-NEt_3][BF_4] + **1**-BF_4 (n = 10, 12) on the first heat. Cr, crystalline; Cub_{bi}, bicontinuous cubic; Col, columnar; Iso, isotropic.

	Phase behaviour temperatures are in °C
[Fan-C_{10}-NEt_3][BF_4] + **1**-BF_4	Cr 46 Cub_{bi} 73 Iso
[Fan-C_{12}-NEt_3][BF_4] + **1**-BF_4	Cr 41 Cub_{bi} 61 Col 121 Iso

The kinetics of the rearrangement of **1**-BF_4 in [fan-C_n-NEt_3][BF_4] was investigated using the aliquot-^{1}H NMR spectroscopy method described above, although with [fan-C_n-NEt_3][BF_4] as the solvent, the hydrolysis of the rearranged product to form the aldehyde is slow. This was evident by the reduced intensity of the aldehyde proton signal compared to what was to be expected, along with the presence of additional signals between δ 5.95 – 5.00 ppm in the spectra (Figure 3.18), the region of the spectrum where the alkene protons appear for **1**-X, **2**-X and **3**, Scheme 3.7.

The green spectrum (Figure 3.18), which represents the rearrangement of **1**-Br in acetonitrile after reacting at 73 °C for 1800 s, shows two overlapping doublets at δ 5.10 – 5.03 ppm. One has a *J*-coupling of 10 Hz which is from the *cis*-proton of **3** (H_f), and the other with a *J*-coupling of 17 Hz due to H_e coupling with the *trans*-proton of the alkene, Scheme 3.7. The red spectrum represents the rearrangement of **1**-BF_4 in acetonitrile, after reacting at 81 °C for 660 s, also shows this splitting pattern, shifted downfield, while also having additional signals at δ 5.24 – 5.18 ppm. This has a similar splitting pattern with J = 10 and 17 Hz. These signals can be assigned to the cis-proton (H_d) and the tran-proton (H_c) of **2**-BF_4. The absolute integral values of these signals along with the doublet of H_a (δ 5.62, d, J = 10 Hz red spectrum) were normalised to each other and first-order rate plots constructed to obtain the rate constants, Table 3.6.

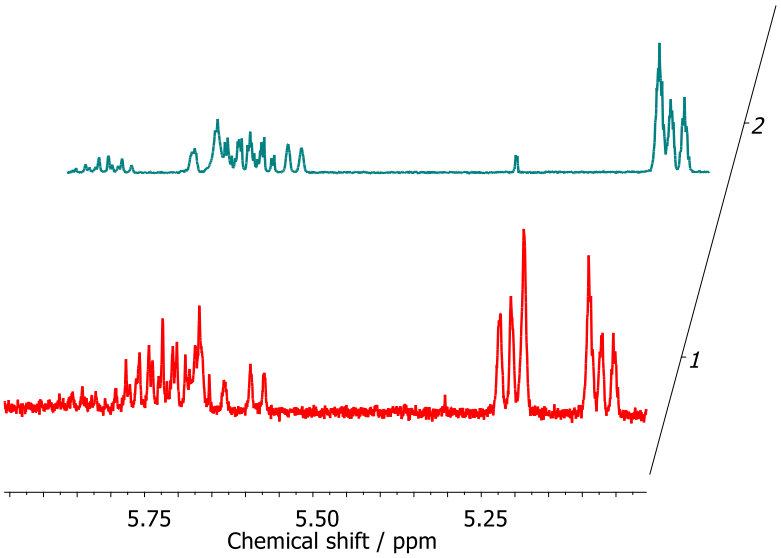

Figure 3.18: ^{1}H NMR (500 MHz, $CDCl_3$) spectra of; red, the rearrangement of **1**-BF_4 in [fan-C_{12}-NEt_3][BF_4] at 81 °C after 660 s; green, the rearrangement of **1**-Br in acetonitrile at 73 °C after 1800 s.

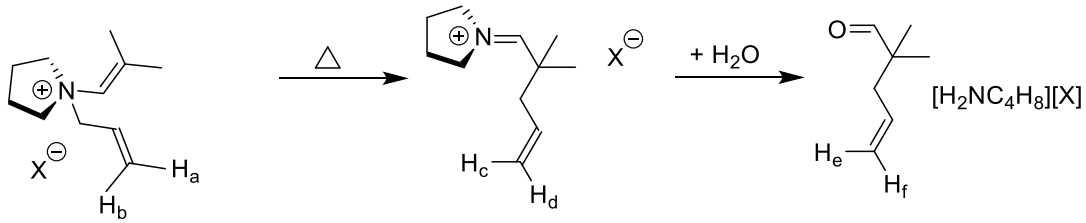

1-*X* **2**-*X* **3**

Scheme 3.7: The aza-Claisen rearrangement of **1**-X, X = Br, BF_4 with terminal alkene protons labelled.

Table 3.6: Rate constants for the rearrangement of **1**-BF_4 in [fan-C_n-NEt_3][BF_4] (n = 10, 12)

Solvent	Reaction temperature / °C	k / × 10^{-4} s^{-1}
[Fan-C_{10}-NEt_3][BF_4]	47.7	0.84 ± 0.04
[Fan-C_{10}-NEt_3][BF_4]	62.4	5.5 ± 0.2
[Fan-C_{10}-NEt_3][BF_4]	58.4	3.5 ± 0.1
[Fan-C_{10}-NEt_3][BF_4]	59.4	4.09 ± 0.04
[Fan-C_{10}-NEt_3][BF_4]	66.5	8.1 ± 0.5
[Fan-C_{10}-NEt_3][BF_4]	69.9	11.7 ± 0.5
[Fan-C_{10}-NEt_3][BF_4]	76.8	21.8 ± 0.7
[Fan-C_{10}-NEt_3][BF_4]	79.0	33 ± 2
[Fan-C_{10}-NEt_3][BF_4]	86.0	57 ± 1
[Fan-C_{10}-NEt_3][BF_4]	87.7	75 ± 2
[Fan-C_{12}-NEt_3][BF_4]	45.6	0.62 ± 0.07
[Fan-C_{12}-NEt_3][BF_4]	47.0	0.72 ± 0.04
[Fan-C_{12}-NEt_3][BF_4]	53.2	1.4 ± 0.1
[Fan-C_{12}-NEt_3][BF_4]	57.2	1.9 ± 0.04
[Fan-C_{12}-NEt_3][BF_4]	66.7	7.28 ± 0.08
[Fan-C_{12}-NEt_3][BF_4]	69.8	11.3 ± 0.3
[Fan-C_{12}-NEt_3][BF_4]	76.9	21 ± 1
[Fan-C_{12}-NEt_3][BF_4]	81.2	29 ± 2

The activation parameters for the rearrangement of **1**-BF_4 in [fan-C_n-NEt_3][BF_4] were calculated from Eyring plots, presented for each LCIL. The data are fitted separately for each of the phases of the solvent, as well as being fitted across the whole temperature range. [Fan-C_{10}-NEt_3][BF_4] is presented in Figure 3.19 and [fan-C_{12}-NEt_3][BF_4] in Figure 3.20. The activation parameters are summarised in Table 3.7.

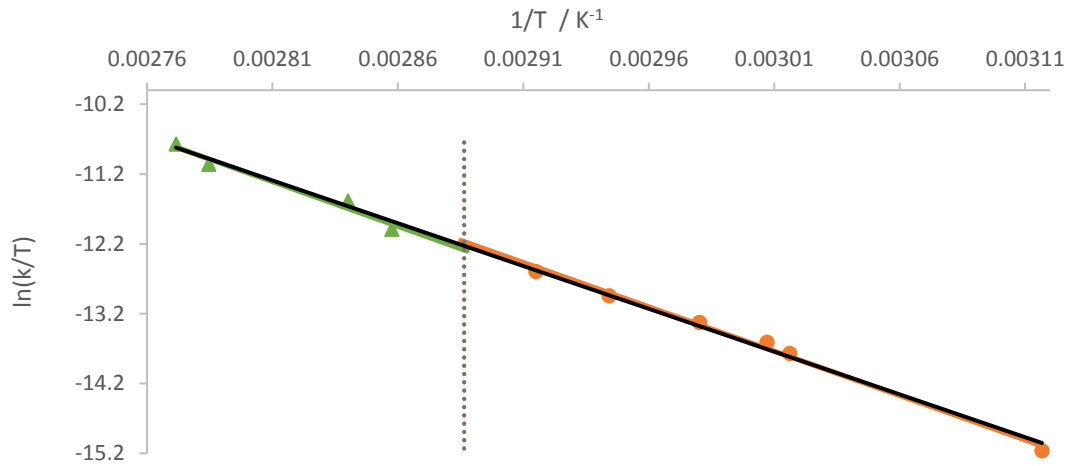

Figure 3.19: Eyring plot of the aza-Claisen rearrangement of **1**-BF_4 in [fan-C_{10}-NEt_3][BF_4] in the bicontinuous cubic phase (orange circles) and isotropic phase (green triangles). The phase transition is at the grey dotted line (73 °C).

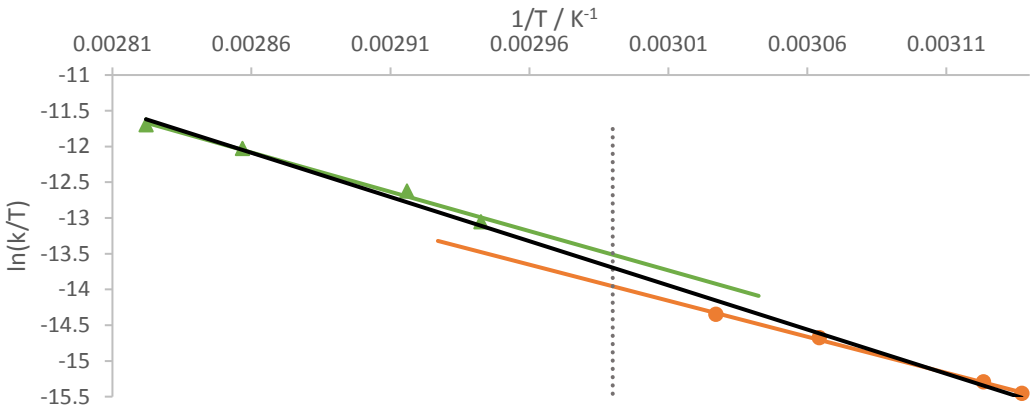

Figure 3.20: Eyring plot of the aza-Claisen rearrangement of **1**-BF_4 in [fan-C_{12}-NEt_3][BF_4], in the bicontinuous cubic phase (orange circles) and columnar phase (green triangles), the black regressions line is for all the data. The phase transition is at the grey dotted line (61 °C).

Table 3.7: Activation parameters for the rearrangement of **1**-BF_4 in [fan-C_n-NEt_3][BF_4] (n = 10, 12) and **1**-Br in acetonitrile-d_3.

Solvent (phase)	$\Delta H^{\neq}$ / kJ mol^{-1}	$\Delta S^{\neq}$ / J K $^{-1}$ mol^{-1}
[Fan-C_{10}-NEt_3][BF_4]	102 ± 2	-5 ± 6
[Fan-C_{10}-NEt_3][BF_4] (Iso)	106 ± 13	7 ± 35
[Fan-C_{10}-NEt_3][BF_4] (Cub)	105 ± 4	6 ± 12
[Fan-C_{12}-NEt_3][BF_4]	103 ± 3	-4 ± 9
[Fan-C_{12}-NEt_3][BF_4] (Cub)	84 ± 3	-63 ± 8
[Fan-C_{12}-NEt_3][BF_4] (Col)	91 ± 6	-37 ± 18
Acetonitrle-d_3 (Iso)	105 ± 2	1 ± 6

The Eyring plot for [fan-C_{10}-NEt_3][BF_4] across the phase transition, black regression line in Figure 3.19, shows no discontinuity at the bicontinuous cubic to isotropic phase transition at 73 °C. As there is not a discontinuity in the Eyring plot it can be concluded that the rate of reaction is only dependent on temperature, and that the ordering in the bicontinuous cubic phase does not have an effect on the activation parameters when compared to the isotropic phase. This can also be demonstrated by the individual Eyring plots for the bicontinuous cubic and isotropic phase (Figure 3.19 orange and green, respectively), as these are in agreement with the regression across the two phases. This conclusion is also exemplified by the enthalpy and entropy of activation values for [fan-C_{10}-NEt_3][BF_4], Table 3.7, calculated across the phase transition, which show that the parameters from each phase (isotropic and bicontinuous cubic), are well within experimental error of each other.

The effect of the transition from the bicontinuous cubic to columnar phase of [fan-C_{12}-NEt_3][BF_4] can be viewed in two ways. Firstly, when an Eyring plot across the transition is constructed, the regression line fits quite well, although some data points do not fit the line as well as others, Figure 3.20, black line. The enthalpy and entropy of activation values obtained from this plot are consistent with the values obtained when [fan-C_{10}-NEt_3][BF_4] is used as the solvent, Table 3.7. Thus both the transition from the bicontinuous cubic to the columnar phase, and the change from [fan-C_{10}-NEt_3][BF_4] to [fan-C_{12}-NEt_3][BF_4], has no effect upon the activation vales of the rearrangement. However, an alternative view can be gained from looking at the Eyring plots for the bicontinuous cubic and columnar phases separately, Figure 3.20 orange and green, respectively. The regression lines for each phase are visibly different and a small discontinuity can be discerned. If real, and not due to scatter in the data, this could indicate that there is a small effect on the rearrangement upon going from the bicontinuous cubic to the columnar phase of [fan-C_{12}-NEt_3][BF_4]. The

activation parameters for each phase are reported in Table 3.7 and both the enthalpy and entropy of activation are different in the two phases, with the values in the bicontinuous cubic phase being lower than in the columnar phase. Although the errors reported in the table result in the values overlapping, they can tentatively be considered to be different enough to conclude that the phase effects the parameters. This is because, in comparison the Eyring plots for [fan-C_{10}-NEt_3][BF_4], there is a large change in activation parameters when the reaction is followed across the phase transition.

3.6. Conclusions

The use of neutral LCs as reaction media to influence the rate of reaction and/or stereo-/regio- chemical outcome of reactions has received little attention since the 1980s.[106] This is due to neutral LCs generally having small LC ranges that narrow, or are lost completely on addition of solutes. The use of LCILs as media to influence the chemical outcome of reactions has received little attention, even though LCILs generally exhibit large LC ranges which are more resilient to the addition of solutes. The limited literature concentrates on bimolecular thermal reactions such as the Diels alder systems examined by lee *et al.*, Do and Schmitzer, and Bruce *et al.*, along with the unimolecular Claisen rearrangement by Bruce *et al*.[5, 25, 111, 122-124] The Diels alder systems studied distinguish a liquid-crystalline effect, that is, the liquid-crystalline ordering in the solvent had an influence over the stereochemical outcome of the reaction. Conversely, the Claisen rearrangement demonstrated no liquid-crystalline effect as the rate of reaction remained unchanged upon phase change of the LCIL.

The aza-Claisen rearrangement of **1**-BF_4 was investigated in LCILs [fan-C_{10}-NEt_3][BF_4] and [fan-C_{12}-NEt_3][BF_4] to determine if the liquid-crystalline ordering of these solvents affects the reaction kinetics. First-order rate constants were recorded and then activation parameters determined from Eyring plots. The transition from the bicontinuous cubic phase to the isotropic phase of [fan-C_{10}-NEt_3][BF_4] was found to have little or no effect upon the enthalpy or entropy of activation of the rearrangement, however the transition between the bicontinuous cubic phase and columnar phase of [fan-C_{12}-NEt_3][BF_4] may show some discontinuity, as the enthalpy and entropy of activation appear to change slightly across the phase transition.

It is perhaps not surprising that there is no change in the activation parameters on transitioning from the bicontinuous cubic phase to the isotropic phase, as the short-range ordering in both phases will be very similar. The isotropic phase of some

ionic liquids, even those that do not exhibit a liquid-crystalline phase, still have some structure, for example [$C_nC_1$im][Tf_2N] ionic liquids form continuous apolar and polar networks when $n < 6$. [79, 81] The same can be considered to occur in the isotropic phase of [fan-C_{10}-NEt_3][BF_4]. The continuous polar and apolar networks in the isotropic phase will be similar to that in the bicontinuous cubic phase, over a short distance. The aza-Claisen substrate cannot distinguish between the two phases, as the substrate will be most strongly influenced by the ordering of the solvent molecules around it. The viscosity of the solvent appears not to have an effect on the activation parameters, as the viscosity is higher in the cubic phase than in the isotropic phase, yet the parameters are the same in both phases. Welton *et al*. showed that viscosity does not effect a bimolecular Diels-Alder reaction, thus it may be expected that a unimolecular reaction shows the same.[118]

There is then a small effect upon the activation parameters of the rearrangement on transition from the bicontinuous cubic phase to the columnar phase. In this instance, unlike in the bicontinuous cubic-to-isotropic phase transition, there is a change in the anisotropy of the system. The substrate has proven to be sensitive to this change in anisotropy, such that the enthalpy of activation changes by + 7 kJ mol^{-1} and the entropy of activation changes by + 26 J K^{-1} mol^{-1}, upon the bicontinuous cubic-to-columnar phase transition.

Increasing the chain length from $n = 10$ to $n = 12$ in [fan-C_n-NEt_3][BF_4] also changes the activation parameter values in the bicontinuous cubic phase, with the enthalpy of activation decreasing by 21 kJ mol^{-1}, and the entropy of activation decreasing by 69 J K mol^{-1}. Assuming that the viscosity does not influence the parameters, which can be presumed, as they do not change in [fan-C_{10}-NEt_3][BF_4] upon going through the bicontinuous cubic to isotropic phase, which is associated with a very substantial change in viscosity, then the difference must be due to something else. The mesophase is the same in both cases, bicontinuous cubic, so the difference could be due to the change in polarity. Upon changing from [fan-C_{10}-NEt_3][BF_4] to [fan-C_{12}-NEt_3][BF_4] there are six more methylene groups, introducing more apolar character to the solvent. Other reactions in ionic liquids have shown to be alkyl chain length dependent. For example a decrease in reaction rate is observed as the alkyl chain length on the IL increases for, a Beckman rearrangement,[136] some hydrogenation reactions,[137, 138] and some dimerisations.[139, 140] This was usually attributed to a change in solubility of the reactants, as increasing the alkyl chain length on the IL cation results in a decrease of the polarity of the solvent..

The observation that [C_4C_1im][Tf_2N] is able to hydrolytically stabilise the highly moisture sensitive hydrolysis of the iminium (**2**-Br) into the aldehyde (**3**) is noteworthy.

There is little literature on this however, it appears the ILs with $[Tf_2N]^-$ anions are able to stabilise compounds which usually require highly anhydrous conditions.[133, 134] This is remarkable as even dry ILs, which contain *ca.* 0.1 wt% of water, have a ratio of 1 water molecule per 50 IL anion-cation pairs, while dry tetrahydrofuran has a ratio of 1 water molecule for every 5000 tetrahydrofuran molecules (0.005 wt% water). [133] The ability of these ILs to preclude decomposition of highly water sensitive compounds is an interesting observation that could be exploited for reactions and storage mediums.

Perhaps the notion that the global ordering of a solvent influencing the reaction outcome is incorrect, in fact, the effect may be more subtle. The local ordering that the solute is able to see is likely to play a dominant role in the reaction outcome. For example, the availability of part of the solvent may be restricted in one phase over another resulting in a different outcome, such as suggested by Welton *et al*. and Bruce *et al.* through their work on a bimolecular Diels-Alder reaction. [118, 123]

4. Stilbazolium-based Liquid-Crystalline Ionic Liquids

4.1. Introduction

As discussed in Chapter 3 by using [3,4,5-tris(alkyloxy)benzyl]triethylammonium tetrfluoroborates (Figure 4.1), the nanostructured ordering present in liquid crystals has the potential to influence the rate and/or stereo- or region-chemical outcome of a reaction.[106] Monitoring the reaction over the phase transitions proved to be a powerful technique to determine if the phase ordering is affecting the outcome of the reaction. These studies showed that while the rate was affected by the LC phase, the changes were small. Part of the reason for this may have been the rather small charged area of the mesophase in which the reaction was taking place and so consideration was given to the design of new materials where this changed polar volume may be more extensive.

a)

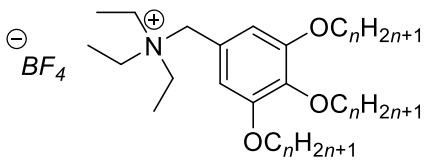

[Fan-C_n-NEt_3][BF_4]

n	Phase behaviour / °C
10	Cr 42 Cub_{bi} 82 Iso
12	Cr 32 Cub_{bi} 49 Col 126 Iso

b)

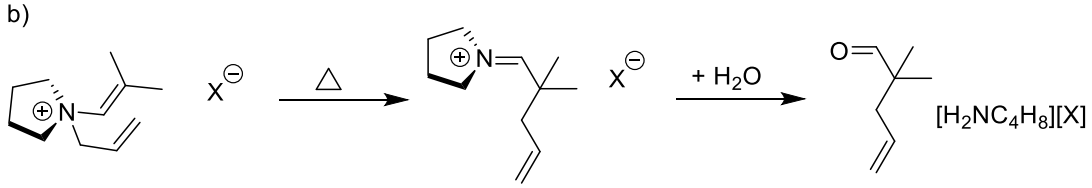

Figure 4.1: a) Structure of [3,4,5-tris(decyloxy)benzyl]triethylammonium tetrfluoroborate ([fan-C_n-NEt_3][BF_4] and its mesomorphic behaviour, transition temperatures (° C). Cr, crystal; Cub_{bi}, bicontinuous cubic; Iso, isotropic; b) the aza-Claisen rearrangement studied in Chapter 3.

Fan-shaped (or wedge-shaped) moieties, such as 3,4,5-tris(alkyloxy)benzyl groups, have been used to promote mesomorphism in thermotropic liquid crystals.[141, 142] Kato

et al. were the first to report fan-shaped imidazolium-based LCILs in the 2000s,[132, 143, 144] followed by reports of fan-shaped ammonium,[145, 146] phosphonium,[146] and pyridinium-based LCILs.[147] Most of these salts display liquid-crystalline properties, exhibiting either hexagonal columnar or cubic phases.

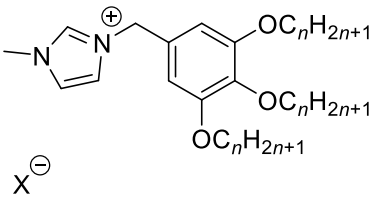

4-*n*-X

n = 8, 12, 16, 18

X = BF_4, PF_6, CF_3SO_3, Tf_2N

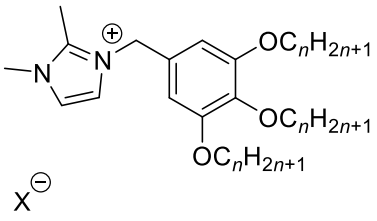

5-*n*-X

n = 12

X = BF_4, PF_6, CF_3SO_3, Tf_2N

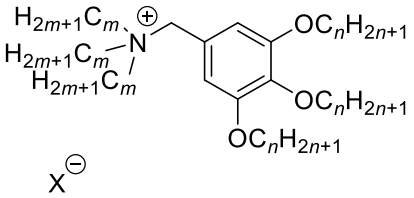

6-*m*/*n*-X

n = 10 ,12, 14

m = 1, 2, 3

X = BF_4, PF_6, CF_3SO_3

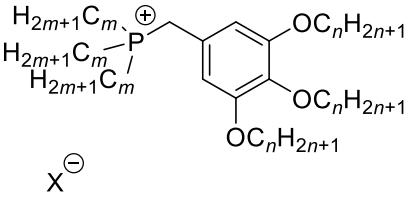

7-*m*/*n*-X

n = 10 ,12, 14

m = 1, 2, 3

X = BF_4

Figure 4.2: Imidazolium, ammonium and phosphonium-based, wedge-shaped LCILs.

The imidazolium-based materials (**4**-*n*-X, Figure 4.2) display exclusively hexagonal columnar phases, unless the anion is large and the alkyl chain length is short, (X = $[Tf_2N]^-$ and *n* = 8 or 12) then no mesomorphism is observed.[132, 144] The mesophase formation is a product of the nanosegregation of the alkyl chains from the anions and the imidazolium group of the cation. Increasing the alkyl chain length (*n*) results in the melting point increasing, while the clearing points decrease with increasing anion size. The stability of the mesophase follows the same trend as found in

1-alky-3-methylimidazolium salts, where the mesophase is stabilised in the order of X = BF_4^- > PF_6^- > $CF_3SO_3^-$, reflecting anion size.[30] Increasing the size at the apex of the materials, by introducing a methyl group at the 2-position of the imidazolium group, results in columnar hexagonal mesophase formation in all cases, except when X = Tf_2N^-, were no mesophase is formed (**5**-*n*-X, Figure 4.2.(b)).[144] Interestingly, **4**-12-CF_3SO_3 is not liquid crystalline, whereas its bulkier analogue **5**-12-CF_3SO_3 exhibits a columnar hexagonal phase between 66 and 85 °C. This can be explained by the larger cation being accommodated into a mesophase as the cationic imidazolium part is also larger. Thus, the volume fractions and shape of the cationic, anionic and apolar parts of the materials, all play an important role in mesophase formation.

Ammonium-based analogues of the fan-shaped imidazolium-based LCILs have also been reported **6**-*m*/*n*-X, Figure 4.2.[145, 146, 148] These LCILs exhibit columnar hexagonal mesophases, as well as also showing cubic mesophases. The different phase behaviours displayed can be attributed to the size, shape and charge density of the cationic group. By increasing the size of the group at the apex, from imidazolium to triethylammonium, the interfacial curvature is reduced so a cubic phase can be formed. Additionally, the positive change on the imidazolium head group is more delocalised, than in the ammonium cation, resulting in a stronger interaction between the cation and anion leading to lower melting and clearing points. The effect of changing the size of the apex group was investigated systematically in a series of ammonium and phosphonium-based fan-shaped LCILs by changing the length of the alkyl chains attached to the ammonium/phosphonium group, **6**-*m*/*n*-X, **7**-*m*/*n*-X, respectively (Figure 4.2).[146] The trimethylammonium salts (**6**-1/*n*-BF_4) only show columnar hexagonal phases, and the triethylammonium salts (**6**-2/*n*-BF_4) show both columnar hexagonal and bicontinuous cubic phases, which clear at higher temperatures than the analogous phosphonium salts. Further increasing the alkyl chain length to propyl (**6**-3/*n*-BF_4) leads to mesophase suppression, except for **6**-3/14-BF_4, where the hexagonal columnar phase is present. When there is a small cationic headgroup (*m* = 1), the molecules are highly tapered, thus they self-organise into a columnar hexagonal mesophase, with high interfacial curvature. On increasing *m* to *m* = 2, the headgroup size increases, leading to a less tapered molecule, resulting in the molecules being able to self-organise into a cubic phase (which has a lower interfacial curvature), along with a columnar phase. However, increasing the headgroup size further, to *m* = 3, reduces the taper of the molecule to the point where no mesophase is present. However, by increasing the length of the three alkyloxy chains to tetradecyl (*n* = 14), a more tapered molecule is again realised and a columnar phase is seen. Another factor affecting the mesophase properties is the

strength of the electrostatic interaction between the cationic group and the anion. When increasing *m* from 1 to 3, the strength of the interaction is reduced as the ammonium cation is becoming sterically less accessible due to the increasing alkyl chain length and the charge is a little more dispersed. The reduction in this interaction reduces the clearing temperature.

Pyridinium-based taper-shaped analogues have also been reported, **8**-X, Figure 4.3.[147] Only when a small anion was used (**8**-Br) a columnar mesophase is present and larger anions proved to have a destabilising effect on the liquid-crystalline properties, as when X = NO_3^-, BF_4^-, or PF_6^-, no mesophases were present. Perhaps by increasing the nanosegregation, by either decreasing the length if the alkyloxy chain on the pyridine part or increasing the alkyloxy chain lengths on the 3,4,5-tris(alkyoxy)benzyl part, can mesophases be achieved with the larger anions. Another possible option to induce mesophase formation is to elongate the cationic pyridinium part to help accommodate the larger anions.

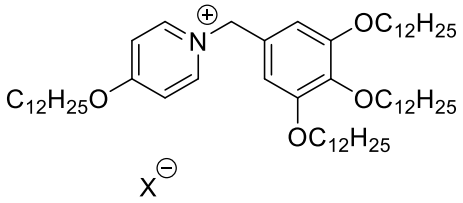

8-X
X = Br, NO_3, BF_4, PF_6

Figure 4.3: Pyridinium-based, wedge-shaped LCILs.

Elongation of the cationic pyridinium part of the molecules could be achieved by swapping the pyridinium cation for a stilbazolium cation. Stilbazoles have been used to form LCILs upon complexation with silver(I), Figure 4.4.[33, 35] The silver(I) complexes are formally ionic species however, they have low conductivity in the nematic phase indicating that they form tight ion pairs. This allows these complexes to form the nematic phase, which is rare for ionic liquids, as the usual electrostatic interactions that promotes smectic mesomorphic are largely absent.

a)

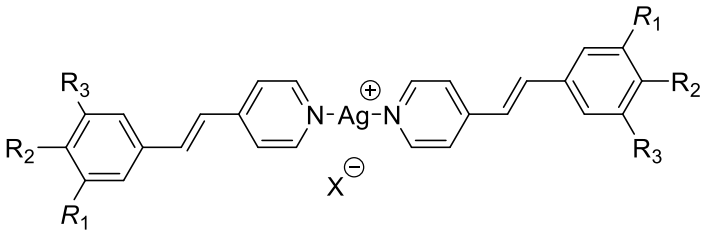

R = H, OC_nH_{2n+1}
X = CF_3SO_3, $O_3SOC_mH_{2m+1}$

Figure 4.4: Chemical structures of anhydrous silver(I) stilbazole complexes.

Stilbazole-based LCILs have also been prepared by simple quaternisation with alkyl halides to yield *N*-(n-alkyl)stilbazolium halides, Figure 4.5. [149] All these exhibit smectic phases, except for some of the iodide analogues which are not mesogenic. The clearing temperature for these was high, often >200 °C, which results in partial decomposition on clearing, as noted by the decreasing clearing temperature on successive differential scanning calorimetry runs.

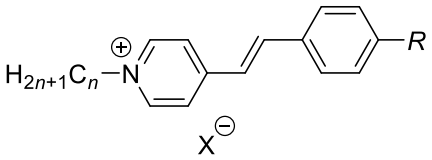

R = H, OH, OCH_3
n = 14, 16, 18, 20, 22
X = Br, I

Figure 4.5: Structures of *N*-(n-alkyl)stilbazolium halides, reported by Israel *et al*.[149]

By combining the fan-shaped 3,4,5-alkyloxybenzyl group and the alkyloxystilbazole group, a novel series of materials can be synthesised, Figure 4.6. The design of the molecules provides a platform for a series to be made by either changing the length of the alkoxy chains on the 3,4,5-alkyoxybenzyl or alkoxystilbazolium groups, as well as chaining the cation. Furthermore the nature of the terminal chains could be different in the two moieties. The synthesis and thermal properties of a small series of [fan-C_n-SB-C_m][X] salts is presented in this chapter.

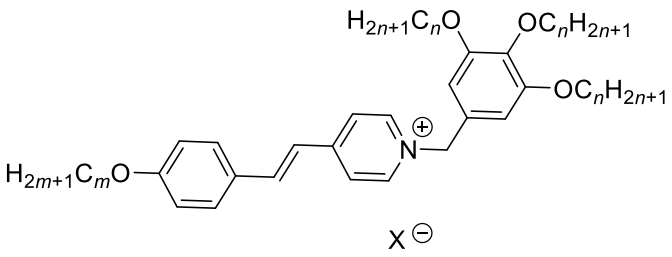

[Fan-C_n-SB-C_m][X]

n = 10, 12, 14
m = 6, 12
X = Cl, BF_4

Figure 4.6: Stilbazolium-based, wedge-shaped LCILs.

4.2. Synthesis

The synthesis of the stilbazolium-based, fan-shaped salts ([fan-C_n-SB-C_m][X]) is shown in Scheme 4.1. The 3,4,5-tris(alkyloxy)benzyl chlorides (provided by the Bruce group) and 4-alkoxystilbazoles were synthesised according to literature procedures.[132, 150] Then the stilbazolium-based fan-shaped ILs were prepared by the quaternisation reaction of 4-alkyloxystilbazole with 3,4,5-tris(alkyloxy)benzyl chloride, while subsequent anion exchange, with sodium tetrafluoroborate, afforded the stilbazolium-based tetrafluoroborate salts. Care was taken after the quarterisation step to protect the salts from light as they were found to undergo *trans* to *cis* isomerisation under ambient light conditions. This is evident by the depletion of the AB signal from the *trans* protons on the alkene, $^2J_{HH}$ = 16.1 Hz, and the appearance of a new AB signal from *cis* protons on the alkene, $^2J_{HH}$ = 12.0 Hz, in the ^{1}H NMR spectrum, Figure 4.7. After a short period of time, just 1.5 h, the isomerisation is observed, and after 22 h the *cis*:*trans* ratio is 0.83:1.00, which remained unchanged upon further exposure to ambient light. No such isomerisation was reported for the alkyl stilbazolium halides, Figure 4.5, or the silver(I) stilbazole complexes.[149 33, 35]

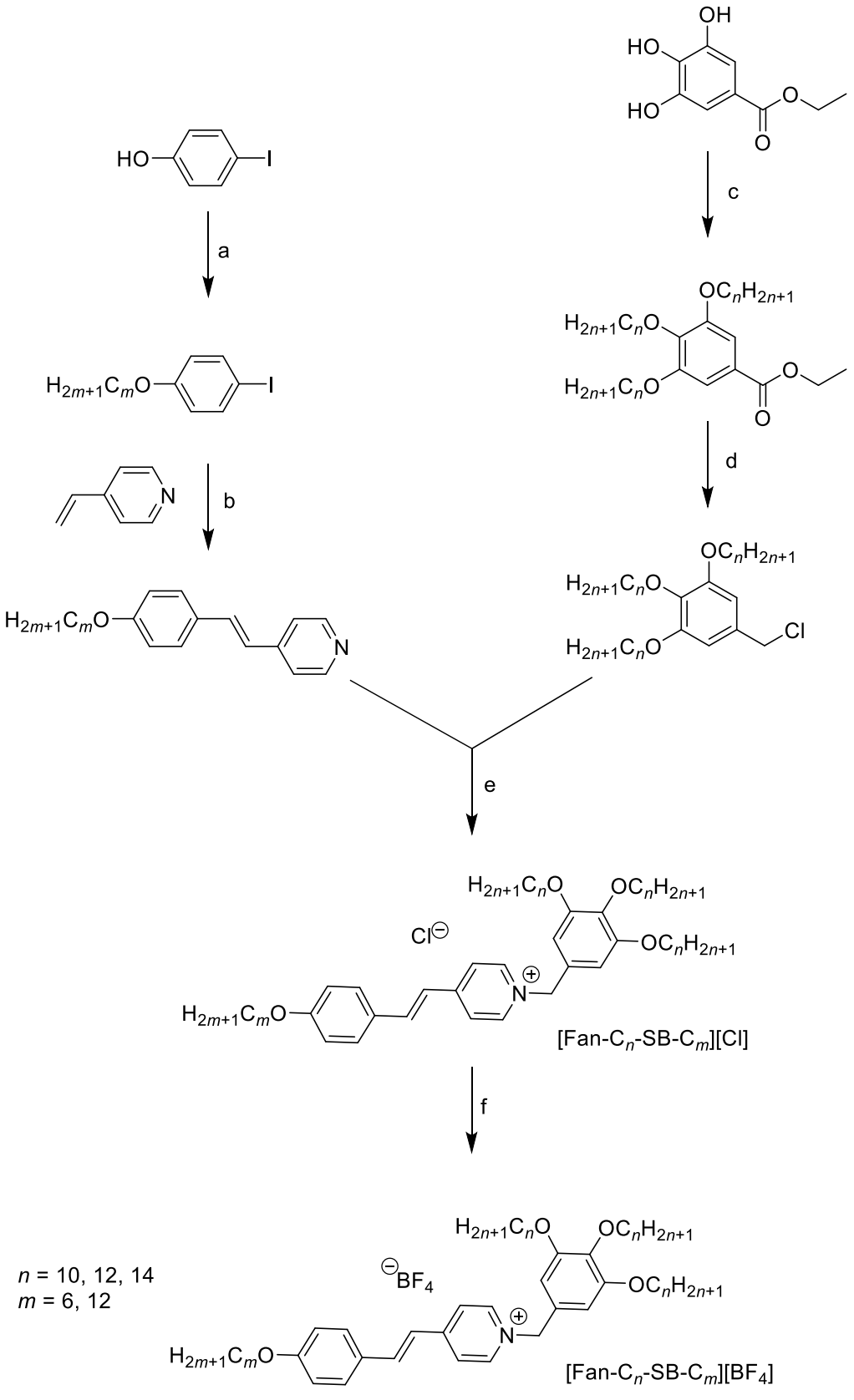

Scheme 4.1: Synthesis of stilbazolium-based fan-shaped ionic liquids: a) BrC_mH_{2m+1}, K_2CO_3, acetone; b) palladium(II) acetate, triethylamine, acetone; c) BrC_nH_{2n+1}, K_2CO_3, dimethylformamide; d) i) $LiAlH_4$, tetrahydrofuran, ii) $SOCl_2$, CH_2Cl_2; e) acetonitrile; f) $NaBF_4$, CH_2Cl_2.

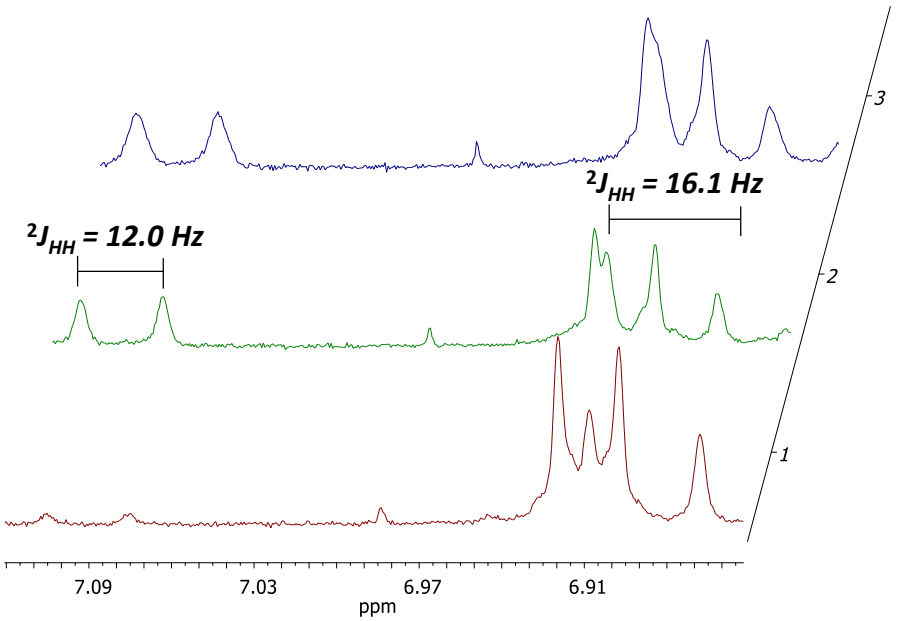

Figure 4.7: ^{1}H nuclear magnetic resonance spectrum of [fan-C_{14}-SB-C_{12}][BF_4], in the C=C*H* region, after illumination under ambient light conditions in CD_2Cl_2 after 1.5 h (1, red) 22 h (2, green) and 6 days (3, blue).

4.3. Thermal Behaviour

The thermal phase behaviour of the [fan-C_n-SB-C_m][BF_4] salts were investigated using polarising optical microscopy (POM) and differential scanning calorimetry (DSC). The thermal behaviour of the chloride salts were not investigated fully as they underwent decomposition upon heating, thus they were changed into the tetrafluoroborate salts and it is these that were characterised fully, Table 4.1. The decomposition of ILs upon heating is common, with reports that it is to be expected for halide salts, especially near their clearing temperatures.[25, 149, 151] For example the chloride and bromide salts of [$C_nC_1$im][X] have a tendency to decompose, whereas the tetrafluoroborate analogues have a higher thermal stability.[30, 152-154]

Table 4.1: Thermal data for [fan-C_n-SB-C_m][BF_4] salts.

Compound	Transitions / °C[a]
[Fan-C_{10}-SB-C_6][BF_4]	g 50 Cr_2 95 Iso
[Fan-C_{12}-SB-C_6][BF_4]	g 14 Cr_1 26 Cr_2 59 Cr_3 91 Iso
[Fan-C_{14}-SB-C_6][BF_4]	Cr_1 29 Cr_2 71 Cr_3 87 Iso
[Fan-C_{10}-SB-C_{12}][BF_4]	Cr_1 38 Cr_2 103 Iso
[Fan-C_{12}-SB-C_{12}][BF_4]	Cr_1 26 Cr_2 37 Cr_3 86 Iso
[Fan-C_{14}-SB-C_{12}][BF_4][b]	Cr_1 37 Cr_2 87 Iso

g, glass: Cr, crystal; Iso, isotropic. [a]The transition temperatures are DSC onset temperatures on the second heat. [b]The transition to the isotropic phase is only seen in the DSC trace on the first heat.

Figure 4.8: Polarising optical microscopy images [Fan-C_{12}-SB-C_{12}][BF_4] at 69 °C after cooling from the isotropic liquid phase at 10 °C min^{-1}.

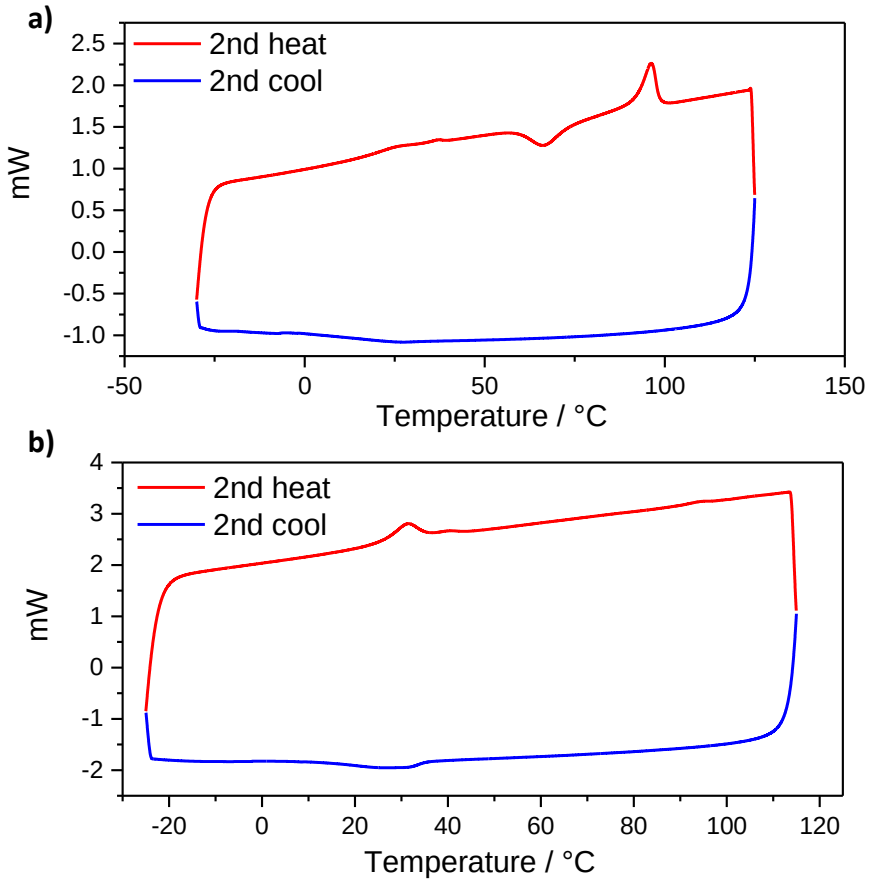

Figure 4.9: DSC for the second heating and cooling cycles, at a heating and cooling rate of 10 °C min^{-1}, for a) [fan-C_{12}-SB-C_6][BF_4] and b) [fan-C_{12}-SB-C_{12}][BF_4].

A POM image of [fan-C_{12}-SB-C_{12}][BF_4] and DSC traces for [fan C_{12}-SB-C_6][BF_4] and [fan-C_{12}-SB-C_{12}][BF_4] are shown in Figure 4.8 and Figure 4.9, respectively. POM studies of the [fan-C_n-SB-C_m][BF_4] salts show that they are not liquid-crystalline compounds as demonstrated by the POM image in Figure 4.8, showing the stilbazolium salt slowly crystallising upon cooling from the isotropic liquid. The DSC traces support this conclusion and additionally shows that some of the compounds have glassy states (Figure 4.9.a). The second and third heating cycles and the first, second and third cooling cycles are consistent suggesting good thermal stability of the salts.

4.4. Conclusions

Disappointingly no liquid-crystalline properties are present in any of the [fan-C_n-SB-C_m][BF_4] salts, as seen by POM investigations. Perhaps the tetrafluoroborate anion is too large to facilitate a liquid crystalline phase, as is seen for the pyridinium analogues, **8**-X, Figure 4.3, or the molecule is bent and preventing mesophase formation.

One possible way to induce a mesophase into this system is to increase the length of the alkyl chains to increase the amphilicity of the molecules, another way to do this is to increase the number of alkoxy chains on the stilbazolium end of the salts. The latter method has been used to great effect with 2-aryl substituted imidazolium LCILs, Figure 4.10. By increasing the number of alkyloxy chains on the 2-aryl group from one to two, the salt changes from showing no mesophase behaviour to being liquid-crystalline.

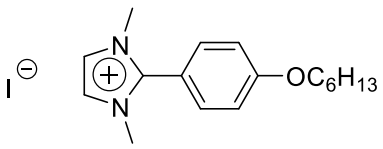

Cr 123 Iso (°C)

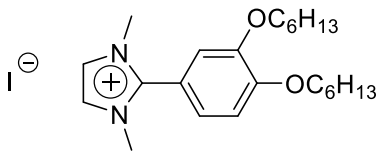

Cr_1 33 Cr_2 99 Cr_3 106 SmX 124 SmA 147 Iso (°C)

Figure 4.10: T he chemical structure and phase behaviour of 2-arylsubstituted imidazolium LCILs. Cr, crystal; Iso, isotropic; SmX, unidentified smectic phase :SmA, smectic A.

Alternatively, dimeric salts, which can be thought of as two fan-shaped moieties attached together by an alkyl chain, at their apexes, have been used to increase the mesophase windows of their monomeric analogues. Bruce *et al.* prepared a series of dimeric imidazolium-based LCILs which have high thermal stabilities and display large

hexagonal columnar mesophase windows, in some cases over 200 °C. In comparison to their monomeric analogues they have more stable mesophases that clear at higher temperatures and have larger windows.[155] Dimeric pyridinium LCILs have also been prepared and these too exhibit hexagonal columnar phases that have higher clearing temperatures and larger mesophase windows than their monomeric analogues.[156] Interestingly some of the dimeric pyridinium analogues display liquid crystalline behaviour even though the corresponding monomeric analogue does not, for example **8**-BF_4 (Figure 4.3) is not liquid crystalline whereas the decyl bridged dimeric analogue has a hexagonal columnar mesophase between 14 and 84 °C, Figure 4.11.

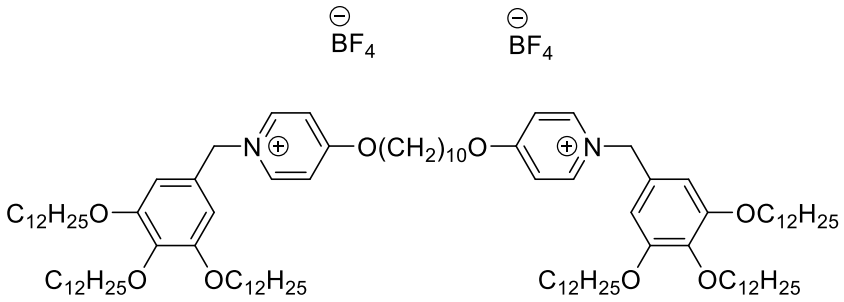

Cr 14 Col_h 84 Iso (°C)

Figure 4.11: Structure and phase behavious of a bis(pyridinium) LCIL. Cr, crystal; Col_h, columnar hexagonal; Iso, isotropic.

The fan-shaped stilbazoium-based salts, even if they were liquid-crystalline, would not be practical to use as ordered reaction media due to them readily undergoing *trans*-to-*cis* isomerisation under ambient light conditions. One possible way to eliminate this is by removing the alkene group and directly joining the two rings, to form a phenylpyridium group.

5. Experimental

5.1. General

Reagents and solvents were obtained from Sigma-Aldrich or Alfa Aesar and used without further purification, unless otherwise stated.

All air-sensitive experimental procedures were performed under an inert atmosphere of nitrogen using standard Schlenk line and glovebox techniques.

Toluene was purified using an Innovative Technologies anhydrous solvent engineering system. Dichloromethane, acetonitrile and hexane were purified by distillation using calcium hydride (for dichloromethane and acetonitrile) and sodium (for hexane) as drying agents. 1-Methylimidazole and [D_3]-1-methylimidazole were dried over calcium hydride and distilled under reduced pressure (10^{-3} mbar). Purification of the non–deuterated bromoalkanes was performed by distillation immediately prior to use, in the presence of activated 4 Å molecular sieves under nitrogen (1-bromoethane) or under reduced pressure. Deuterium oxide (99.9% D), [D_5]-1-bromoethane (99.0% D), and [D_1]-methanol (99.0% D) were obtained from Aldrich and used without further purification. [D_3]-1-iodomethane (99+% D) was purchased from Acros and used as received. [D_{25}]-1-bromododecane was provided by the ISIS deuteration facility and used as received. [D3]-methyl iodide (99+% D) was purchased from Acros and used as received. [D_{21}]-1-bromodecane was provided by the ISIS deuteration facility and used as received. [D_9]-1-bromobutane (98.0% D) was purchased from Goss Scientific. [D_5]-1-bromoethane (99.0% D), [D_{13}]-1-bromohexane (98.0% D), and [D_{17}]-1-bromooctane (98.0% D) from Sigma Aldrich and used as received. (3,4,5-Tris(decyloxy)benzyl)triethylammonium chloride and (3,4,5-tris(dodecyloxy)benzyl)triethylammonium chloride were synthesised by Yanan Gao. [C_6C_1im]Br was prepared by Iman Khazal and [C_6C_1im][Tf_2N] was prepared by Iman Khazal then dried by Christopher Cabry. [C_8C_1im]Br, [C_8C_1im][Tf_2N], [C_2C_1im-d_8]Br, [C_2C_1im-d_8][Tf_2N], and [C_2C_1im-d_{11}][Tf_2N] were prepared by Lucía D'Andrea. [C_4C_1im]Br, [C_4C_1im][Tf_2N], [$C_{10}C_1$im]Br, [$C_{10}C_1$im][Tf_2N], [C_2C_1im-d_8]Br, [C_2C_1im-d_8][Tf_2N], [C_2C_1im-d_{11}][Tf_2N], [C_4C_1im-d_{12}]Br, [C_4C_1im-d_{12}][Tf_2N], [C_4C_1im-d_{15}][Tf_2N], [$C_{10}C_1$im-d_{24}]Br, [$C_{10}C_1$im-d_{24}][Tf_2N], [$C_{10}C_1$im-d_{27}][Tf_2N], were prepared by Sarah Kirchhecker.

^{1}H and $^{13}C\{^{1}H\}$ nuclear magnetic resonance spectroscopy (NMR) was recorded on either a Jeol ECS400 or a Jeol ECX400 (400 MHz ^{1}H NMR spectra, 101 MHz $^{13}C\{^{1}H\}$ NMR spectra, 376 MHz $^{19}F\{^{1}H\}$ NMR spectra) or a Bruker AV500 (500 MHz ^{1}H NMR spectra, 126 MHz ^{13}C NMR spectra, 471 MHz ^{19}F NMR spectra) at 298 K, unless stated otherwise. Chemical shifts are usually reported in ppm (δ) relative to the residual solvent peak. The coupling constant (J) are recorded in hertz (Hz) and the splitting patterns are allocated as s, singlet, d, doublet, t, triplet, q, quartet, AA'XX', magnetically inequivalent coupling of para-disubstituted benzenes.

CHN microanalyses was conducted on final compounds using an Exeter Analytical CE440 elemental analyser.

Mass spectrometry was performed using a Bruker micro-TOF mass spectrometer for electrospray mass spectrometry (ESI).

The thermal transitions were recorded on a Mettler Toledo DSX822^{e} differential scanning calorimeter (DSC) using STAR^{e} software at a heating and cooling rate of 10 °C min^{-1} unless stated otherwise. The calorimeter was calibrated against a pure indium standard (melting point = 156.6 °C, ΔH = 28.5 J g^{-1}).

5.2. 1-Ethyl-3-methylimidazolium bromide, $[C_2C_1im]Br$

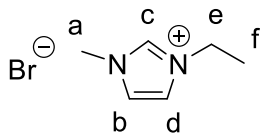

1-Ethyl-3-methylimidazolium bromide was prepared according to the literature method.[157] Distilled 1-methylimidazole (91.7 g, 89.0 cm^{3}, 1.12 mol) was added dropwise to an excess of freshly distilled 1-bromoethane (133.8 g, 92.0 cm^{3}, 1.23 mol). The mixture was stirred for 15 min at 50 °C, until the initial turbidity disappeared, and then for 2 h at 70 °C. Upon cooling to 0 °C, a white solid formed, which was ground in a glovebox. The solid was treated with ethyl acetate (20 cm^{3}) and stirred at −10 °C for 1 h under nitrogen. After removing the solvent *via* cannula filtration, the white solid was dried under vacuum (10^{-2} mbar) at 60 °C for 6 h (185.7 g, 87%).

^{1}H NMR (400 MHz, DMSO-d_6, 293 K), δ (ppm): 9.29 (*s*, Hc, 1H), 7.87 (*m*, Hd, 1H), 7.78 (*m*, Hb, 1H), 4.24 (*q*, J = 7.3 Hz, He, 2H), 3.90 (*s*, Ha, 3H), 1.44 (*t*, J = 7.3 Hz, Hf, 3H).

5.3. 1-Butyl-3-methylimidazolium bromide, [C_4C_1im]Br

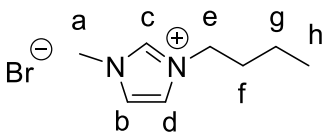

Distilled 1-methylimidazole (4 cm^3, 47.3 mmol) was added dropwise to a 10 mol% excess of freshly distilled 1-bromobutane (5.6 cm^3, 52.0 mmol). The mixture was stirred at room temperature for 20 min, 50 °C for 20 min, and then for 2 h at 70 °C. Upon cooling to –20 °C a white solid formed, which was ground under a blanket of ethyl acetate, followed by stirring in ethyl acetate at −10 °C for 1 h under nitrogen. After the solvent was removed via cannula filtration, the white solid was dried under vacuum (10^{-2} mbar) at room temperature for 2 h followed by 60 °C for 8 h to yield the product as a white solid (10.2 g, 98%).

^{1}H NMR (400 MHz, acetone-d_6). δ (ppm): 10.19 (s, Hc, 1H), 8.05 (t, J = 1.8 Hz, Hd, 1H), 7.96 (t, J = 1.7 Hz, Hb, 1H), 4.47 (t, J = 7.3 Hz, He, 2H), 4.12 (s, Ha, 3H), 1.98 – 1.86 (m, Hf, 2H), 1.42 – 1.28 (m, Hg, 2H), 0.92 (t, J = 7.4 Hz, Hh, 3H).

5.4. 1-Hexyl-3-methylimidazolium bromide, [C_6C_1im]Br

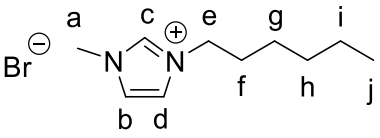

Distilled 1-methylimidazole (155.3 g, 150 cm^3, 1.89 mol) was added dropwise to freshly distilled 1-bromohexane (178.75 g, 152 cm^3, 1.08 mol) and dry toluene (150 cm^3). The mixture was stirred at 60 °C overnight. Once cooled the toluene was removed *via* cannula transfer, the ionic liquid was washed with dry toluene (3 × 50 cm^3). The product was then dried under vacuum (10^{-1} mbar) to yield a white solid. This solid was ground in a glove box and then dried under reduced pressure (10^{-2} mbar) at 60 °C for several days. The product was obtained as a white solid.

^{1}H NMR (400 MHz, D_2O). δ (ppm): 10.29 (s, Hc, 1H), 8.13 (t, J = 1.8 Hz, Hd, 1H), 8.04 (t, J = 1.7 Hz, Hb, 1H), 4.48 (t, J = 7.3 Hz, He, 2H), 4.13 (s, Ha, 3H), 2.00 – 1.89 (m, Hf, 2H), 1.40 – 1.22 (m, Hg,h,i 6H), 0.85 (t, J = 7.1 Hz, Hj, 3H).

5.5. 1-Octyl-3-methylimidazolium bromide, [C_8C_1im]Br

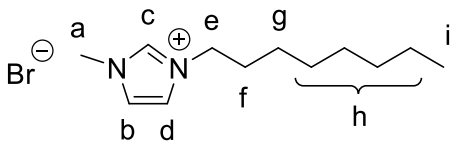

Distilled 1-methylimidazole (71.1 g, 69 cm^3, 0.87 mol) was added dropwise to freshly distilled 1-bromooctane (178.9 g, 160 cm^3, 0.93 mol) and dry toluene (150 cm^3). The mixture was stirred at 60 °C overnight. Once cooled the toluene was removed *via* cannula transfer. The product was then dried under vacuum (10^{-1} mbar) to yield a yellow oil. This oil was then dried under reduced pressure (10^{-2} mbar) at 60 °C for 4 days (215.6 g, 90 %)

^{1}H NMR (400 MHz, D_2O), δ (ppm): 7.46 (d, $^4J_{HH}$ = 2.0 Hz, Hd, 1H), 7.42 (d, $^4J_{HH}$ = 2.0 Hz, Hb, 1H), 4.16 (t, $^3J_{HH}$ = 7.0 Hz, He, 2H), 3.86 (s, Ha, 3H), 1.87-1.79 (m, Hf, 2H), 1.27-1.18 (m, Hg,h, 10H), 0.81 (t, $^3J_{HH}$ = 7 Hz, Hi, 3H).

5.6. 1-Decyl-3-methylimidazolium bromide, [$C_{10}C_1$im]Br

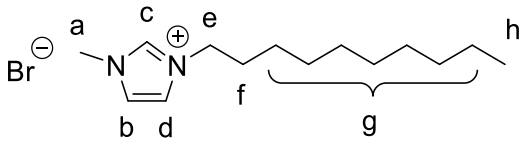

Freshly distilled 1-bromodecane (3.26 cm^3, 15.72 mmol) and a slight excess of distilled 1-methylimidazole (1.05 eq, 1.316 cm^3, 16.52 mmol) were combined in dry toluene and stirred 24 h at 60 °C. The solvent and excess reagents were removed under vacuum (10^{-2} mbar) at 60 °C (7 days) to yield a colourless oil (6.28 g, 80%).

^{1}H NMR (400 MHz, $CDCl_3$). δ (ppm): 10.31 (s, Hc, 1H), 7.59 (t, J = 1.8 Hz, Hd, 1H), 7.41 (t, J = 1.8 Hz, Hb, 1H), 4.29 – 4.25 (m, He, 2H), 4.08 (s, Ha, 3H), 1.92 – 1.79 (m, Hf, 2H), 1.35 – 1.12 (m, Hg, 14H), 0.81 (t, J = 6.9 Hz, Hh, 3H).

5.7. 1-Dodecyl-3-methylimidazolium bromide, $[C_{12}C_1im]Br$

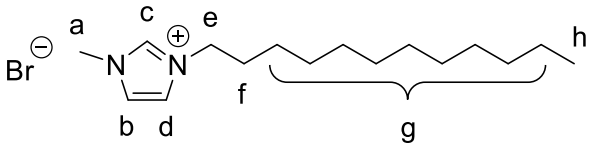

A slight excess of freshly distilled 1-bromododecane (183.7 g, 177.0 cm^3, 0.73 mol), distilled 1-methylimidazole (56.6 g, 55.0 cm^3, 0.69 mol) and dry toluene (150 cm^3) were heated at 60 °C under nitrogen for 12h. The homogeneous solution obtained was concentrated under vacuum (10^{-2} mbar) at 60 °C to give a white solid, which was ground in a glovebox and further dried under vacuum at 60 °C for 7 days (219.0 g, 96%).

^{1}H NMR (400 MHz, D_2O). δ (ppm): 7.42 (s, Hd, 1H), 7.37 (s, Hb, 1H), 4.13 (t, J = 6.7 Hz, He, 2H), 3.83 (s, Ha, 3H), 1.85-1.80 (m, Hf, 2H), 1.22 (m, Hg, 18H), 0.81 (t, J = 5.6 Hz, Hh, 3H).

5.8. 1-Ethyl-3-methylimidazolium bis(trifluoromethylsulfonyl)imide, $[C_2C_1im][Tf_2N]$

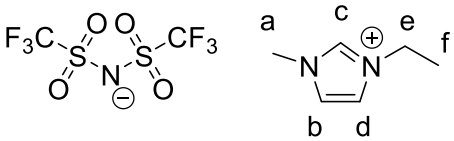

A solution of $[C_2C_1im]Br$ (35.0 g, 0.18 mol) in deionised water (150 cm^3) was treated with a solution of $LiTf_2N$ (53.2 g, 0.18 mol) in deionised water (150 cm^3). The biphasic system was stirred overnight at room temperature, under an atmosphere of nitrogen. An aqueous extraction (8 × 50 cm^3) was performed to remove the lithium halide until no precipitation of AgBr occurred in the aqueous phase upon addition of $AgNO_3$

solution. The colourless oil was then dried under vacuum (10^{-3} mbar) at 60 °C for 4 days (51.1 g, 71%).

^{1}H NMR (400 MHz, acetone-d_6). δ (ppm): 8.79 (s, Hc, 1H), 7.59 (s, Hd, 1H), 7.52 (s, Hb, 1H), 4.36 (q, J = 7.0 Hz, He, 2H), 4.02 (s, Ha, 3H), 1.63 (t, J = 7.0 Hz, Hf 3H).

5.9. 1-Butyl-3-methylimidazolium bis(trifluoromethylsulfonyl)imide, [C_4C_1im][Tf_2N]

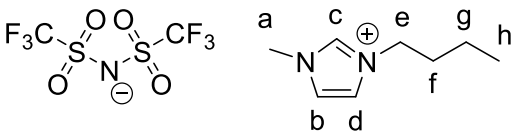

A solution of [C_4C_1im]Br (7.88 g, 36.0 mmol) in deionised water (50 cm^3) was treated with a solution of LiTf_2N (10.33 g, 36.0 mmol) in deionised water (50 cm^3). The biphasic system was stirred overnight at room temperature, under an atmosphere of nitrogen. An aqueous extraction was performed to remove the lithium halide until no precipitation of AgBr occurred in the aqueous phase upon addition of $AgNO_3$ solution. The colourless oil was then dried under vacuum (10^{-2} mbar) at 60 °C for 4 days (13.62 g, 90%).

^{1}H NMR (400 MHz, DMSO-d_6). δ (ppm): 9.10 (s, Hc, 1H), 7.76 (t, J = 1.8 Hz, Hd, 1H), 7.69 (t, J = 1.7 Hz, Hb, 1H), 4.15 (t, J = 7.2 Hz, He, 2H), 3.84 (s, Ha, 3H), 1.82 – 1.69 (m, Hf, 2H), 1.34 – 1.18 (m, Hg, 2H), 0.90 (t, J = 7.4 Hz, Hh, 3H).

5.10. 1-Hexyl-3-methylimidazolium bis(trifluoromethylsulfonyl)imide, [C_6C_1im][Tf_2N]

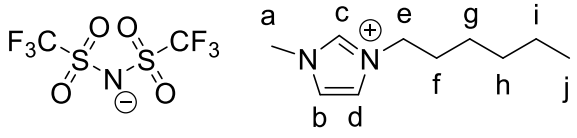

A solution of [C_6C_1im]Br (27.6 g, 0.112 mol) in deionised water (150 cm^3) was treated with a solution of LiTf_2N (32.41 g, 0.112 mol) in deionised water (150 cm^3). The biphasic system was stirred overnight at room temperature, under an atmosphere of

nitrogen. An aqueous extraction (8 × 70 cm^3) was performed to remove the lithium halide until no precipitation of AgBr occurred in the aqueous phase upon addition of $AgNO_3$ solution. The pale yellow oil was then dried under vacuum (10^{-3} mbar) at 60 °C for 4 days.

^{1}H NMR (400 MHz, acetone-d_6). δ (ppm): 8.90 (s, Hc, 1H), 7.69 (t, J = 1.8 Hz, Hd, 1H), 7.62 (t, J = 1.8 Hz, Hb, 1H), 4.31 (t, J = 7.4 Hz, He, 2H), 4.01 (s, Ha, 3H), 1.97 – 1.86 (m, Hf, 2H), 1.40 – 1.24 (m, Hg,h,I, 6H), 0.86 (t, J = 7.1 Hz, Hj, 3H).

5.11. 1-Octly-3-methylimidazolium bis(trifluoromethylsulfonyl)imide, [C_8C_1im][Tf_2N]

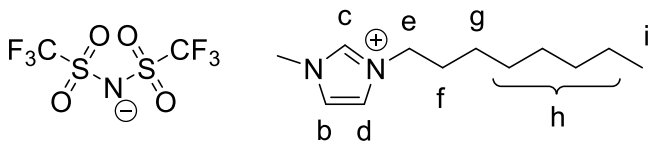

[C_8C_1im]Br (38.17 g, 0.14 mol) was dissolved in distilled water (100 cm^3) and an aqueous solution (150 cm^3) of LiTf_2N (40.46 g, 0.14 mol) were added under stirring. The reaction was stirred overnight then an aqueous extraction was performed to remove the lithium halide until no precipitation of AgBr occurred in the aqueous phase upon addition of $AgNO_3$ solution. The solid was dried under vacuum (10^{-3} mbar) to yield the product as a colourless liquid (59.0 g, 90%).

^{1}H NMR (400 MHz, acetone-d_6, 294 K), δ (ppm): 9.09 (*s*, Hc, 1H), 7.81 (*t*, $^4J_{HH}$ = 1.8 Hz, Hd, 1H), 7.75 (*t*, $^4J_{HH}$ = 1.8 Hz, Hb, 1H), 4.39 (*t*, $^3J_{HH}$ = 7.4 Hz, He, 2H), 4.09 (*s*, Ha, 3H), 1.96 (*br quint*, $^3J_{HH}$ = 7.4 Hz, Hf, 2H), 1.39-1.27 (*m*, Hg,h, 10H), 0.86 (*t*, $^3J_{HH}$ = 7 Hz, Hi, 3H).

5.12. 1-Decyl-3-methylimidazolium bis(trifluoromethylsulfonyl)imide, $[C_{10}C_1im][Tf_2N]$

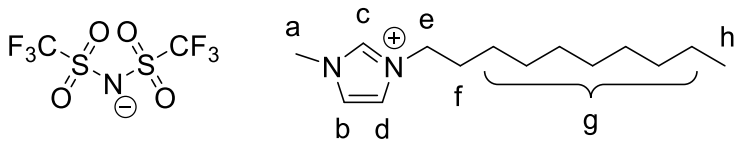

$[C_{10}C_1im]Br$ (6.28 g, 20.7 mmol) was dissolved in distilled water and an aqueous solution of $LiTf_2N$ (5.94 g, 20.7 mmol) were added under stirring. The reaction was stirred overnight then an aqueous extraction was performed to remove the lithium halide until no precipitation of AgBr occurred in the aqueous phase upon addition of $AgNO_3$ solution. The solid was dried under vacuum (10^{-2} mbar) to yield the product as a colourless liquid (10.24 g, 98%).

^{1}H NMR (400 MHz, DMSO-d_6). δ (ppm): 9.09 (s, Hc,1H), 7.76 (t, J = 1.7 Hz, Hd, 1H), 7.69 (t, J = 1.7 Hz, Hb, 1H), 4.14 (t, J = 7.2 Hz, He, 2H), 3.84 (s, Ha, 3H), 1.83 – 1.69 (m, Hf, 2H), 1.36 – 1.14 (m, Hg, 14H), 0.85 (t, J = 6.8 Hz, Hh, 3H).

5.13. 1-Dodecyl-3-methylimidazolium bis(trifluoromethylsulfonyl)imide, $[C_{12}C_1im][Tf_2N]$

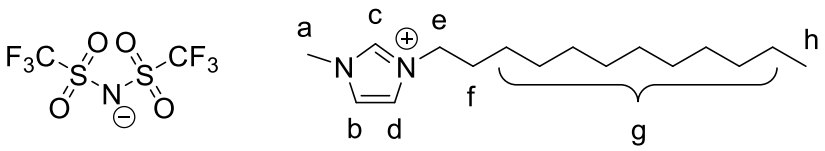

A solution of $[C_{12}C_1im]Br$ (58.1 g, 0.18 mol) and deionised water (150 cm^3) was treated with $LiTf_2N$ (50.9 g, 0.18 mol) in deionised water (150 cm^3). The biphasic system was stirred overnight at room temperature, under and atmosphere of nitrogen. The ionic liquid phase was separated and thoroughly washed with deionised water (8 × 70 cm^3). Then an aqueous extraction was performed to remove the lithium bromide until no precipitation of AgBr occurred in the aqueous phase upon addition of $AgNO_3$ solution. The pale-yellow oil was then dried under vacuum (10^{-2} mbar) at 60 °C for 4 days (80.6 g, 86%).

^{1}H NMR (400 MHz, acetone-d_6). δ (ppm): 8.78 (s, Hc, 1H), 7.56 (m, Hd, 1H), 7.50 (s, Hb, 1H), 4.28 (t, J = 7.0 Hz, He, 2H), 3.99 (s, Ha, 3H), 2.00-1.93 (m, Hf, 2H), 1.30 (m, Hg, 18H), 0.92 (t, J = 6.6 Hz, Hh, 3H).

5.14. Sodium imidazolate

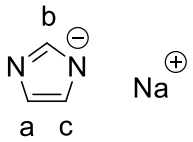

Deprotonation of imidazole was performed following a literature method with some modifications.[157] A suspension of sodium hydride (2.05 g, 85.4 mmol) in dry acetonitrile (150 cm^3) was cooled in an ice bath under a nitrogen atmosphere. Imidazole (5.53 g, 81.2 mmol) was ground into a fine powder and slowly added over a course of 3 h. A gentle effervescence of hydrogen occurred during addition. After 24 h of stirring, the solvent was removed under vacuum (10^{-1} mbar). Due to the hygroscopic nature of the product, the work-up was performed under nitrogen. The white solid was washed with dry hexane (4 $\times$ 30 cm^3) and dried at 100 °C under reduced pressure (10^{-1} mbar) for 1-2 h (6.93 g, 95%).

^{1}H NMR (400 MHz, D_2O). δ (ppm): 7.78 (s, Hb, 1H), 7.14 (s, Ha,c, 2H).

5.15. [D_3]-1-Methylimidazole

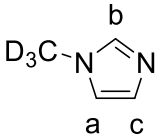

Methylation of sodium imidazolate was carried out following a literature method with some modifications.[157] Finely ground sodium imidazolate (28.00 g, 0.31 mol) was suspended in dry acetonitrile (350 cm^3) under nitrogen and cooled down in an ice/salt bath to –15 °C. To this, [D_3]-iodomethane (45.18 g, 19.4 cm^3, 0.31 mol) was added dropwise over a course of 3 h, during which time a yellow colour evolved. The resulting

mixture was stirred at –15 °C for 3 – 5 additional h and then allowed to warm to room temperature. After 3 days of stirring, the solvent was removed under vacuum (10^{-1} mbar) to give an orange residue, which was then extracted with dry dichloromethane (6 × 100 cm^3) *via* cannula transfer. A yellowish oil was obtained after removal of the dichloromethane under reduced pressure. The product was purified by vacuum distillation (10^{-1} mabr) . The colourless liquid obtained (19.4 g, 73%) was stored at 4 °C under nitrogen. The degree of deuteration on the methyl group was quantitative.

^{1}H NMR (400 MHz, DMSO-d_6). δ (ppm): 7.60 (s, Hb,1H), 7.15 (s, Hc, 1H), 6.91 (s, Ha, 1H).

5.16. [D_8]-1-Ethyl-3-methylimidazolium bromide, [C_2C_1im-d_8]Br

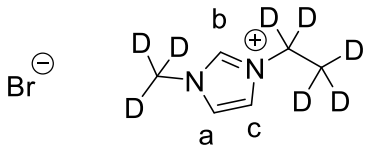

This product was prepared according to a literature method[1]. Distilled [D_3]-1-methylimidazole (3.92 g, 46.0 mmol) was added dropwise to a 10 mol% excess of [D_5]-bromoethane (5.70 g, 50.0 mmol). The mixture was stirred at room temperature for 20 min, 50 °C for 20 min, and then for 2 h at 70 °C. Upon cooling to room temperature, a white solid formed, which was ground under a blanket of ethyl acetate, followed by stirring in ethyl acetate at −10 °C for 1 h under nitrogen. After the solvent was removed *via* cannula filtration, the white solid was dried under vacuum (10^{-2} mbar) at room temperature for 2 h followed by 60 °C for 8 h (9.02 g, 98%). The degree of deuteration on the ethyl group was quantitative, as determined by ^{1}H NMR spectroscopy.

^{1}H NMR (400 MHz, acetone-d_6). δ (ppm): 10.08 (s, Hb, 1H), 7.86 (s, Hc, 1H), 7.77 (s, Ha, 1H).

5.17. [D_{12}]-1-Butyl-3-methylimidazolium bromide, [C_4C_1im-d_{12}]Br

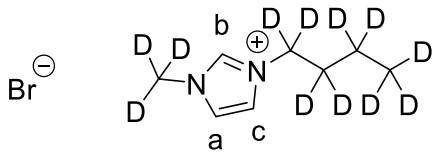

This product was prepared according to a literature method[1]. Distilled [D_3]-1-methylimidazole (1.72 g, 20.4 mmol) was added dropwise to a 10 mol% excess of [D_9]-bromobutane (3.28 g, 22.5 mmol). The mixture was stirred at room temperature for 20 min, 50 °C for 20 min, and then for 2 h at 70 °C. Upon cooling to room temperature a white solid formed, which was ground under a blanket of ethyl acetate, followed by stirring in ethyl acetate at −10 °C for 1 h under nitrogen. After the solvent was removed *via* cannula filtration, the white solid was dried under vacuum (10^{-2} mbar) at room temperature for 2 h followed by 60 °C for 8 h (4.68 g, 99%). The degree of deuteration on the butyl group was quantitative, as determined by ^{1}H NMR spectroscopy.

^{1}H NMR (400 MHz, acetone-d_6). δ (ppm): 10.09 (s, Hb, 1H), 7.83 (t, J = 1.8 Hz, Hc, 1H), 7.78 (t, J = 1.8 Hz, Ha, 1H).

5.18. [D_{16}]-1-Hexy-3-methylimidazolium bromide [C_6C_1im-d_{16}]Br

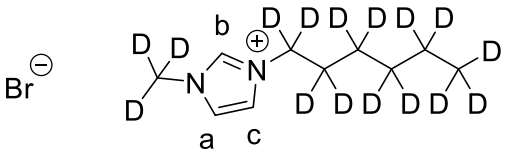

Distilled [D_3]-1-methylimidazole (1.61 g, 19.0 mmol) was added dropwise to a slight excess of [D_{13}]-bromohexane (3.54 g, 19.9 mmol). The mixture was stirred at room temperature for 20 min, then 60 °C for 21 h under an atmosphere of nitrogen. The excess [D_{13}]-bromohexane was removed under reduced pressure (10^{-3} mbar) at 60 °C for 9 h to yield a white solid (4.88 g, 98%). The degree of deuteration on the hexyl group was quantitative, as determined by ^{1}H NMR spectroscopy.

^{1}H NMR (400 MHz, D_2O). δ (ppm): 8.70 (t, J = 1.6 Hz, Hb, 1H), 7.46 (t, J = 1.8 Hz, Hc, 1H), 7.41 (t, J = 1.8 Hz, Ha, 1H).

5.19. [D_{20}]-1-Octyl-3-methylimidazolium bromide, [C_8C_1im-d_{20}]Br

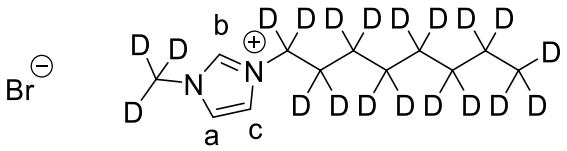

A slight excess of distilled [D_3]-1-methylimidazole (1.51 g, 17.7 mmol) was added dropwise to [D_{17}]-bromooctane (3.48 g, 16.6 mmol). The mixture was stirred at room temperature for 20 min, then 60 °C for 23 h under an atmosphere of nitrogen. The excess [D_3]-1-methylimidazole was removed under reduced pressure (10^{-3} mbar) at 60 °C for 9 h to yield a white solid (4.86 g, 99%). The degree of deuteration on the octyl group was quantitative, as determined by ^{1}H NMR spectroscopy.

^{1}H NMR (400 MHz, $CDCl_3$). δ (ppm): 10.37 (s, Hb, 1H), 7.55 (t, J = 1.6 Hz, Hc, 1H), 7.38 (t, J = 1.6 Hz, Ha, 1H).

5.20. [D_{24}]-1-Decyl-3-methylimidazolium bromide, [$C_{10}C_1$im-d_{24}]Br

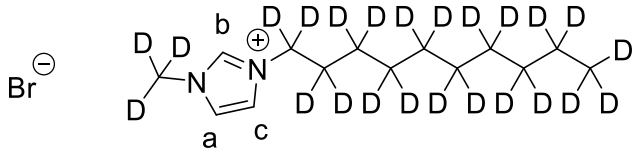

[D_{21}]-bromodecane (1.80 g, 7.44 mmol) and a slight excess of [D_3]-1-methylimidazole (1.07 eq, 0.6774 g, 7.96 mmol) were combined in dry toluene and stirred for 48 h at 60 °C. The solvent and excess reagents were removed under vacuum (10^{-2} mbar) at 60 °C for 7 days to yield a colourless oil (1.97 g, 81%). The degree of deuteration on the decyl group was quantitative, as determined by ^{1}H NMR spectroscopy.

^{1}H NMR (400 MHz, acetone-d_6). δ (ppm): 9.86 (s, Hb, 1H), 7.82 (t, *J* = 1.8 Hz, Hc, 1H), 7.76 (t, *J* = 1.8 Hz, Ha, 1H).

5.21. [D_{28}]-1-Dodecyl-3-methylimidazolium bromide, [$C_{12}C_1$im-d_{28}]Br

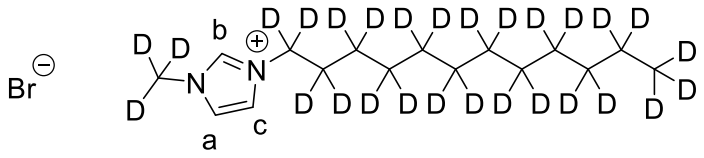

[D_{25}]-1-bromododecane (2.98 g, 2.5 cm^3, 10.9 mmol), an excess of distilled [D_3]-1-methylimidazole (0.99 g, 0.88 cm^3, 11.7 mmol) and dry toluene (2.5 cm^3) were heated at 60 °C under nitrogen overnight. The solvent was then removed under vacuum (10^{-2} mbar) and the product was further dried at 60 °C for 5-8 h to give a white gel. The sample was left in an ice/NaCl bath overnight to promote precipitation. The white solid obtained was ground in a glovebox and further dried under vacuum for 2 h to yield the product (3.62 g, 93%). The degree of deuteration on the dodecyl group was quantitative, as determined by ^{1}H NMR spectroscopy.

^{1}H NMR (400 MHz, D_2O). δ (ppm): 7.42 (s, Hc, 1 H), 7.37 (s, Ha, 1 H).

5.22. [D_8]-1-Ethyl-3-methylimidazolium bis(trifluoromethylsulfonyl)imide, [C_2C_1im-d_8][Tf_2N]

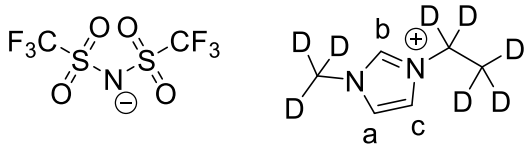

A solution of [C_2C_1im-d_8]Br (9.02 g, 45.3 mmol) in deionised water (7 cm^3) was treated with a solution of $LiTf_2N$ (13.66 g, 47.6 mmol) in deionised water (8 cm^3). The biphasic system was stirred overnight at room temperature, under an atmosphere of nitrogen. The ionic liquid phase was separated and washed with deionised water until no precipitation of AgBr occurred in the aqueous phase upon addition of $AgNO_3$ solution. The organic layer was then dried under vacuum (10^{-3} mbar) at 60 °C for 8 h to yield a colourless oil (16.62 g, 92%). The degree of deuteration on the ethyl group remained unchanged during the metathesis step, as determined by ^{1}H NMR spectroscopy. The compound was taken to the next step without characterisation.

5.23. [D_{12}]-1-Butyl-3-methylimidazolium bis(trifluoromethylsulfonyl)imide, [C_4C_1im-d_{12}][Tf_2N]

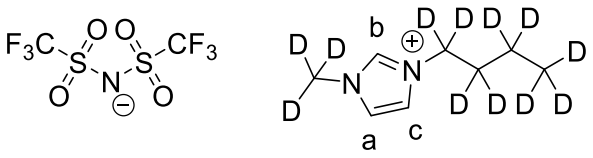

A solution of [C_4C_1im-d_{12}]Br (4.68 g, 20.2 mmol) in deionised water (6 cm^3) was treated with a solution of $LiTf_2N$ (6.10 g, 20.2 mmol) in deionised water (6 cm^3). The biphasic system was stirred overnight at room temperature, under an atmosphere of nitrogen. The ionic liquid phase was separated and washed with deionised water until no precipitation of AgBr occurred in the aqueous phase upon addition of $AgNO_3$ solution. The organic layer was then dried under vacuum (10^{-2} mbar) at 60 °C for 8 h to yield a colourless oil (7.73 g, 88%). The degree of deuteration on the butyl group remained unchanged during the metathesis step, as determined by ^{1}H NMR spectroscopy. The compound was taken to the next step without characterisation.

5.24. [D_{16}]-1-Hexyl-3-methylimidazolium bis(trifluoromethylsulfonyl)imide, [C_6C_1im-d_{16}][Tf_2N]

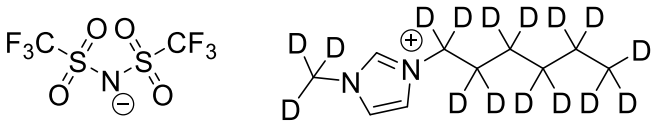

A solution of [C_6C_1im-d_{16}]Br (4.88 g, 18.5 mmol) in deionised water (10 cm^3) was treated with a solution of $LiTf_2N$ (5.32 g, 18.5 mmol) in deionised water (10 cm^3). The biphasic system was stirred overnight at room temperature, under an atmosphere of nitrogen. The ionic liquid phase was separated and washed with deionised water until no precipitation of AgBr occurred in the aqueous phase upon addition of $AgNO_3$ solution. The organic layer was then dried under vacuum (10^{-3} mbar) at 60 °C for 19 h to yield a colourless oil (7.77 g, 90%). The degree of deuteration on the hexyl group

remained unchanged during the metathesis step, as determined by ^{1}H NMR spectroscopy. The compound was taken to the next step without characterisation.

5.25. [D_{20}]-1-Octyl-3-methylimidazolium bis(trifluoromethylsulfonyl)imide, [C_8C_1im-d_{20}][Tf_2N]

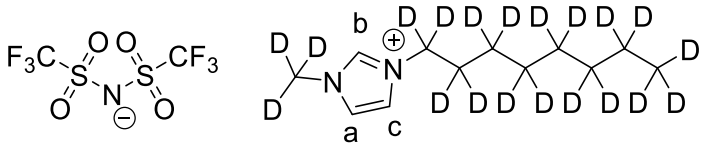

A solution of [C_8C_1im-d_{20}]Br (4.86 g, 16.5 mmol) in deionised water (10 cm^3) was treated with a solution of LiTf_2N (4.72 g, 16.5 mmol) in deionised water (10 cm^3). The biphasic system was stirred overnight at room temperature, under an atmosphere of nitrogen. The ionic liquid phase was separated and washed with deionised water until no precipitation of AgBr occurred in the aqueous phase upon addition of $AgNO_3$ solution. The organic layer was then dried under vacuum (10^{-3} mbar) at 60 °C for 10 h to yield a colourless oil (6.24 g, 77%). The degree of deuteration on the octyl group remained unchanged during the metathesis step, as determined by ^{1}H NMR spectroscopy.

^{1}H NMR (400 MHz, CD_2Cl_2). δ (ppm): 8.71 (s, Hb, 1H), 7.32 – 7.31 (m, Ha,c, 2H).

5.26. [D_{24}]-1-Decyl-3-methylimidazolium bis(trifluoromethylsulfonyl)imide, [$C_{10}C_1$im-d_{24}][Tf_2N]

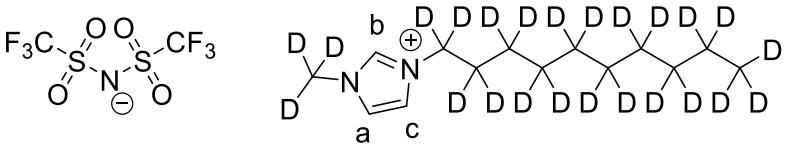

A solution of [$C_{10}C_1$im-d_{24}]Br (1.97 g, 6.0 mmol) in deionised water (5 cm^3) was treated with a solution of LiTf_2N (1.82 g, 6.3 mmol) in deionised water (5 cm^3). The biphasic system was stirred overnight at room temperature, under an atmosphere of nitrogen. The ionic liquid phase was separated and washed with deionised water until no

precipitation of AgBr occurred in the aqueous phase upon addition of $AgNO_3$ solution. The organic layer was then dried under vacuum (10^{-2} mbar) at 60 °C overnight to yield a colourless oil (3.02 g, 95%). The degree of deuteration on the decyl group remained unchanged during the metathesis step, as determined by ^{1}H NMR spectroscopy.

^{1}H NMR (400 MHz, acetone-d_6). δ (ppm): 9.07 (s, Hb, 1H), 7.80 (s, Hc, 1H), 7.74 (s, Ha, 1H).

5.27. [D_{28}]-1-Dodecyl-3-methylimidazolium bis(trifluoromethylsulfonyl)imide, [$C_{12}C_1$im-d_{28}][Tf_2N]

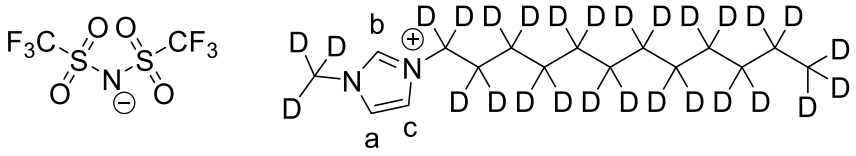

A solution of [$C_{12}C_1$im-d_{28}]Br (3.46 g, 9.6 mmol) and water (10 cm^3) was treated with $LiTf_2N$ (2.81 g, 9.8 mmol) in deionised water (10 cm^3). The biphasic system was stirred overnight at room temperature. After this time, the IL phase was separated and the aqueous phase extracted with dichloromethane (3 × 15 cm^3). The organic layers were combined and thoroughly washed with deionised water (8 × 30 cm^3). The ionic liquid phase was separated and washed with deionised water until no precipitation of AgBr occurred in the aqueous phase upon addition of $AgNO_3$ solution. The ionic liquid was then dried under vacuum (10^{-3} mbar) at 60 °C for 8 h to give a colourless oil (4.88 g, 90%). The degree of deuteration on the dodecyl group remained unchanged during the metathesis step, as determined by ^{1}H NMR spectroscopy.

^{1}H NMR (400 MHz, acetone-d_6). δ (ppm): 8.78 (s, Hb, 1 H), 7.56 (m, Hc, 1 H), 7.50 (s, Ha, 1 H).

5.28. [D_{11}]-1-Ethyl-3-methylimidazolium bis(trifluoromethylsulfonyl)imide, [C_2C_1im-d_{11}][Tf_2N]

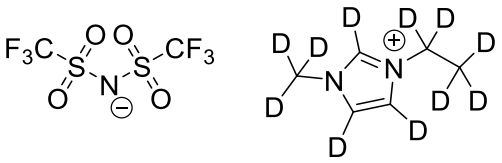

This product was prepared following a literature method.[91, 157] [C_2C_1im-d_8][Tf_2N] (16.62 g, 41.5 mmol) was dissolved in [D_1]-methanol (102 cm^3), treated with caesium hydroxide monohydrate (2.05 g, 11.65 mmol) and stirred for 24 h at 50 °C under nitrogen. The mixture was neutralised with an 80% aqueous solution of bis(trifluoromethylsulfonyl)amide diluted 1:3 in D_2O, and the solvent was removed under vacuum (10^{-2} mbar). The residue was partitioned between dichloromethane and deuterium oxide. The layers were separated and the aqueous layer was extracted with dichloromethane. The combined organic layers were washed 3 times with deuterium oxide, and the solvent was removed under vacuum (10^{-2} mbar). The resulting colourless oil was dried under vacuum (10^{-3} mbar) at 60 °C for 6 h (16.09 g, 96%). The ^{1}H-NMR spectrum (CD_2Cl_2, 0.5 cm^3) of [C_2C_1im-d_{11}][Tf_2N] (47.9 mg, 0.119 mmol) in the presence of hexamethylbenzene (6.0 mg, 0.037 mmol) as an internal reference, revealed a degree of deuteration of 93% on the C2 position of the aromatic ring and 93% on the C4 and C5 positions.

5.29. [D_{15}]-1-Butyl-3-methylimidazolium bis(trifluoromethylsulfonyl)imide, [C_4C_1im-d_{15}][Tf_2N]

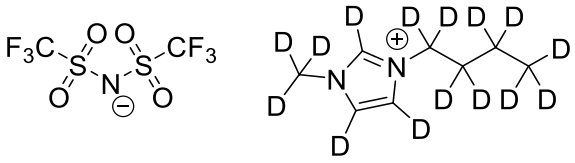

This product was prepared following a literature method.[91, 157] [C_4C_1im-d_{12}][Tf_2N] (7.73 g, 17.9 mmol) was dissolved in [D_1]-methanol (44 cm^3), treated with caesium hydroxide monohydrate (0.88 g, 5.00 mmol) and stirred for 24 h at 50 °C under nitrogen. The mixture was neutralised with an aqueous solution (80%) of

bis(trifluoromethylsulfonyl)amide diluted 1:3 in D_2O, and the solvent was removed under vacuum (10^{-2} mbar). The residue was partitioned between dichloromethane and deuterium oxide. The layers were separated and the aqueous layer was extracted with dichloromethane. The combined organic layers were washed three times with deuterium oxide, and the solvent was removed under vacuum (10^{-2} mbar). The resulting colourless oil was dried under vacuum (10^{-2} mbar) at 60 °C for 6 h (7.48 g, 96%). The ^{1}H-NMR spectrum (CD_2Cl_2, 0.5 cm^3) of [C_4C_1im-d_{15}][Tf_2N] (168.9 mg, 0.389 mmol) in the presence of hexamethylbenzene (6.7 mg, 0.041 mmol) as an internal reference, revealed a degree of deuteration of 98% on the C2 position of the aromatic ring and 92% on the C4 and C5 positions.

5.30. [D_{19}]-1-Hexyl-3-methylimidazolium bis(trifluoromethylsulfonyl)imide, [C_6C_1im-d_{19}][Tf_2N]

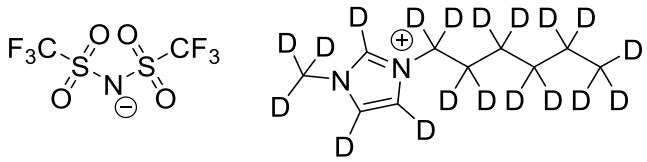

This product was prepared following a literature method.[91, 157] [C_6C_1im-d_{16}][Tf_2N] (7.77 g, 16.8 mmol) was dissolved in [D_1]-methanol (40.0 cm^3), treated with caesium hydroxide monohydrate (0.84 g, 5.00 mmol) and stirred for 24 h at 50 °C under nitrogen. The mixture was neutralised with an 80% aqueous solution of bis(trifluoromethylsulfonyl)amide, and the solvent was removed under vacuum (10^{-1} mbar). The residue was partitioned between dichloromethane and deuterium oxide. The layers were separated and the aqueous layer was extracted with dichloromethane. The combined organic layers were washed with deuterium oxide (3 × 15 cm^3), and the solvent was removed under vacuum (10^{-2} mbar). The resulting colourless oil was dried under vacuum (10^{-3} mbar) at 60 °C for 6.5 h (7.55 g, 97%). The ^{1}H-NMR spectrum (CD_2Cl_2, 0.5 cm^3) of [C_6C_1im-d_{19}][Tf_2N] (51.73 mg, 0.11 mmol) in the presence of hexamethylbenzene (10.26 mg, 0.06 mmol) as an internal reference, revealed a degree of deuteration of 84% on the C2 position of the aromatic ring and 90% on the C4 and C5 positions.

5.31. [D_{23}]-1-Octyl-3-methylimidazolium bis(trifluoromethylsulfonyl)imide, [C_8C_1im-d_{23}][Tf_2N]

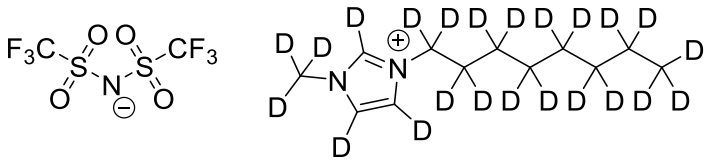

This product was prepared following a literature method.[91, 157] [C_8C_1im-d_{20}][Tf_2N] (6.24 g, 12.6 mmol) was dissolved in [D_1]-methanol (30.0 cm^3), treated with caesium hydroxide monohydrate (0.63 g, 3.78 mmol) and stirred for 24 h at 50 °C under nitrogen. The mixture was neutralised with an 80% aqueous solution of bis(trifluoromethylsulfonyl)amide, and the solvent was removed under vacuum (10^{-2} mbar). The residue was partitioned between dichloromethane and deuterium oxide. The layers were separated and the aqueous layer was extracted with dichloromethane. The combined organic layers were washed with deuterium oxide (3 × 15 cm^3), and the solvent was removed under vacuum (10^{-2} mbar). The resulting colourless oil was dried under vacuum (10^{-3} mbar) at 60 °C for 6 h (6.00 g, 96%). ^{1}H NMR spectroscopy (CD_2Cl_2, 0.5 cm^3) of [C_8C_1im-d_{23}][Tf_2N] (0.211 g, 0.423 mmol) in the presence of hexamethylbenzene (7.37 mg, 0.045 mmol) as an internal reference, revealed a degree of deuteration of 87% on the C2 position of the aromatic ring and 91% on the C4 and C5 positions.

5.32. [D_{27}]-1-Decyl-3-methylimidazolium bis(trifluoromethylsulfonyl)imide, [$C_{10}C_1$im-d_{27}][Tf_2N]

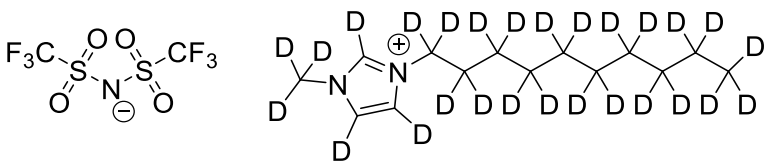

This product was prepared following a literature method.[91, 157] [$C_{10}C_1$im-d_{24}][Tf_2N] (3.02 g, 5.73 mmol) was dissolved in [D_1]-methanol (14 cm^3), treated with caesium hydroxide monohydrate (0.28 g, 1.6 mmol) and stirred for 24 h at 50 °C under nitrogen. The mixture was neutralised with an 80% aqueous solution of

bis(trifluoromethylsulfonyl)amide diluted 1:3 in D_2O, and the solvent was removed under vacuum (10^{-2} mbar). The residue was partitioned between dichloromethane and deuterium oxide. The layers were separated and the aqueous layer was extracted with dichloromethane. The combined organic layers were washed 3 times with deuterium oxide, and the solvent was removed under vacuum (10^{-2} mbar). The resulting colourless oil was dried under vacuum (10^{-2} mbar) at 60 °C for 6 h (2.91 g, 97%). ^{1}H-NMR spectroscopy (CD_2Cl_2, 0.5 cm^3) of [$C_{10}C_1$im-d_{27}][Tf_2N] (0.040 g, 0.0753 mmol) in the presence of hexamethylbenzene (3.1 mg, 0.063 mmol) as an internal reference, revealed a degree of deuteration of 89% on the C^2 position of the aromatic ring, and 92% on the C^4 and C^5 positions, whereas the degree of deuteration on the alkyl groups was quantitative.

5.33. [D_{31}]-1-Dodecyl-3-methylimidazolium bis(trifluoromethylsulfonyl)imide, [$C_{12}C_1$im-d_{31}][Tf_2N]

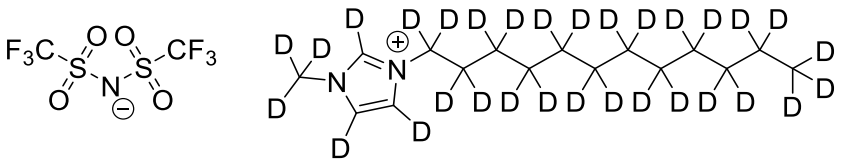

This product was prepared following a literature method.[91, 157] [$C_{12}C_1$im-d_{28}][Tf_2N] (5.85 g, 10.5 mmol) was dissolved in [D_1]-methanol (21.2 g, 26 cm^3, 0.64 mol), treated with caesium hydroxide monohydrate (0.52 g, 3.1 mmol) and stirred for 24 h at 50 °C under nitrogen. The mixture was neutralised with 1:3 v/v H[Tf_2N]/D_2O (where H[Tf_2N] is a commercially available 80% aqueous solution of bis(trifluoromethylsulfonyl)imide), and the solvent was removed under vacuum (10^{-2} mbar). The residue was partitioned between dichloromethane (20 cm^3) and deuterium oxide (20 cm^3). The layers were separated and the aqueous phase was extracted with dichloromethane (15 cm^3). The combined organic layers were washed with deuterium oxide (3 × 15 cm^3), and the solvent was subsequently removed under vacuum (10^{-2} mbar). The resulting colourless oil was dried under vacuum (10^{-3} mbar) at 60 °C for 6 h (5.52 g, 94%). ^{1}H-NMR spectroscopy (CD_2Cl_2, 0.5 cm^3) of [$C_{12}C_1$im-d_{31}][Tf_2N] (0.264 g, 0.0469 mmol) in the presence of hexamethylbenzene (10.23 mg, 0.063 mmol) as an internal reference, revealed a degree of deuteration of 94% on the C^2 position of the aromatic ring, and 95% on the C^4 and C^5 positions, whereas the degree of deuteration on the alkyl groups was quantitative.

5.34. [D_5]-1-Ethyl-3-methylimidazolium bromide, [C_2C_1im-d_5]Br

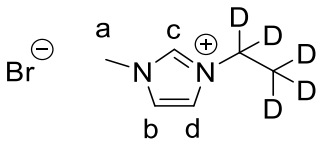

Distilled 1-methylimizazole (3.55 g, 3.44 cm^3, 43.2 mmol) was added dropwise to a 10% excess of [D_5]-bromoethane (5.42 g, 3.55 cm^3, 47.6 mmol). The mixture was stirred at 50 °C for 15 min, and then for 2 h at 70 °C. Upon cooling to room temperature, a white solid formed, which was ground in a glovebox. The solid was treated with ethyl acetate (20 cm^3) and stirred at -10 °C for 1 h under nitrogen. After the solvent was removed via cannula, the white solid was dried under vacuum (10^{-2} mbar) at room temperature for 2 h followed by 60 °C for 8 h (7.847 g, 93%).

^{1}H NMR (400 MHz, dimethyl sulfoxide-d_6, 293 K) δ (ppm): 9.28 (s, Ha, 1H), 7.84 (m, Hd, 1H), 7.75 (m, Hb, 1H), 3.86 (s, Ha, 3H).

5.35. [D_5]-1-Ethyl-3-methylimidazolium bis(trifluoromethylsulfonyl)imide, [C_2C_1im-d_5][Tf_2N]

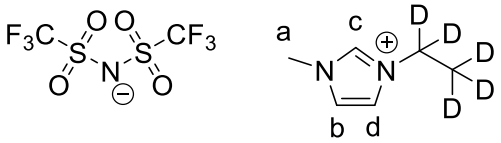

A solution of [C_2C_1im-d_5]Br (7.748 g, 39.5 mmol) in deionised water (7 cm^3) was treated with a solution of LiTf_2N (11.34 g, 39.5 mmol) in deionised water (8 cm^3). The biphasic system was stirred overnight at room temperature, under nitrogen. The ionic liquid phase was separated and the aqueous phase extracted with dichloromethane (3 × 10 cm^3). The combined organic phases were washed with deionised water until no precipitation of AgBr occurred in the aqueous phase upon addition of $AgNO_3$ solution. The organic layer was then dried under vacuum (10^{-2} mbar) at 60 °C for 8 h to yield a colourless oil (12.96 g, 83%).

^{1}H NMR (400 MHz, acetone-d_6). δ (ppm): 8.97 (s, Hc, 1H), 7.74 (m, Hd, 1H), 7.67 (m, Hb, 1H), 4.04 (s, Ha, 3H).

5.36. [D_{25}]-1-Dodecyl-3-methylimidazolium bromide, [$C_{12}C_1$im-d_{25}]Br

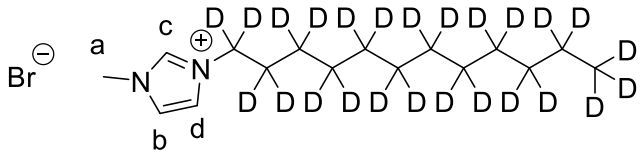

[D_{25}]-bromododecane (5.0 g, 18.2 mmol), 3% excess of freshly distilled 1-methylimidazole (1.54 g, 1.5 cm^3, 18.8 mmol) and dry toluene (4 cm^3) were heated at 60 °C under nitrogen overnight. The homogeneous solution obtained was concentrated and dried under vacuum (10^{-2} mbar) at 60 °C for 6 h. Once the liquid was cooled to room temperature a white solid was formed (6.049 g, 95%).

^{1}H NMR (400 MHz, acetone-d_6). δ (ppm): 8.45 (s, Hd, 1H), 8.43 (s, Hb, 1H), 4.80 (s, Ha, 3H).

5.37. [D_{25}]-1-Dodecyl-3-methylimidazolium bis(trifluoromethylsulfonyl)imide, [$C_{12}C_1$im-d_{25}][Tf_2N]

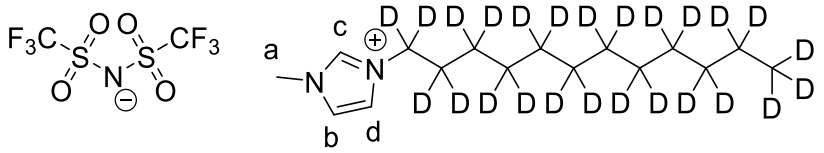

A solution of [$C_{12}C_1$im-d_{25}]Br (6.049 g, 17.0 mmol) in water (12 cm^3) was treated with $LiTf_2N$ (4.871 g, 17.0 mmol) in deionised water (12 cm^3). The biphasic system was stirred overnight at room temperature under nitrogen. The ionic liquid phase was separated and the aqueous phase extracted with dichloromethane (3 × 20 cm^3). The combined organic layers were washed with deionised water until no precipitation of AgBr occurred in the aqueous phase upon addition of $AgNO_3$ solution. The organic layer was then dried under vacuum (10^{-2} mbar) at 60 °C for 7 h to yield a colourless oil (8.91 g, 94%).

^{1}H NMR (400 MHz, acetone-d_6). δ (ppm): 9.01 (s, Hc, 1H), 7.76 (m, Hd, 1H), 7.70 (m, Hb, 1H), 4.05 (*s*, Ha, 3H).

5.38. 1-(2-Methylprop-1-en-1-yl) pyrrolidine

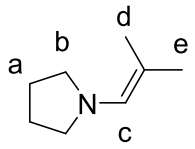

Anhydrous K_2CO_3 (2.76 g, 0.02 mol) was added to a solution of isobutyraldehyde (2.88 g, 0.04 mol) and pyrrolidine (5.68 g, 0.08 mol) in 20 cm^3 of diethyl ether at 0 °C. The reaction was stirred for 24 h. The solution was distilled under reduced pressure (10^{-2} mbar) to yield the product as a clear liquid (3.63 g, 73%).

^{1}H NMR (400 MHz, $CDCl_3$). δ (ppm): 5.60 (septet, $^4J_{HH}$ = 1.3 Hz, Hc, 1H), 2.94 – 2.90 (m, Hb, 4H), 1.76 (m, Ha, 4H), 1.68 (d, $^4J_{HH}$ = 0.6 Hz, Hd, 3H), 1.61 (d, $^4J_{HH}$ = 0.9 Hz, He, 3H).

^{13}C{^{1}H} NMR (101 MHz, $CDCl_3$). δ ppm: 134.53, 114.10, 53.67, 24.84, 22.91, 17.8.

5.39. 1-(2-Methylprop-1-en-1-yl)-1-(prop-2-en-1-yl) pyrrolidinium bromide

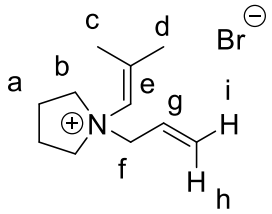

Ice cold allyl bromide (1.06 g 8.79 mmol) was added drop wise to a solution of 1-(2-methylprop-1-en-1-yl) pyrolidine (1.00 g, 7.99 mmol) in acetonitrile (1 cm^3) at 0 °C with stirring. The reaction was cooled to -20 °C and left for 24 h. The solvent was removed under reduced pressure (10^{-1} mbar) and the solids washed with diethyl ether (3 × 2 cm^3) and dried under reduced pressure (10^{-2} mbar) then crystallised from room temperature acetonitrile to yield a white microcrystalline solid (0.97 g, 50%).

^{1}H NMR (500 MHz, CD_3CN). δ (ppm): 5.92 (ddt, J_{HH} = 17.3, 10.1, 7.2 Hz, Hg, 1H), 5.83 (s, He, 1H), 5.61 (dd, $^3J_{HH}$ = 17.0, $^2J_{HH}$ = 1.0 Hz, Hh, 1H), 5.55 (d, J_{HH} = 10.2 Hz,

Hi, 1H), 4.11 (d, J_{HH} = 7.2 Hz, Hf, 2H), 3.74 (m, Hb 2H), 3.62 (m, Hb, 2H), 2.08 (m, Ha, 4H), 1.91 (d, $^4J_{HH}$ = 1.3 Hz, Hc/d, 3H), 1.75 (d, $^4J_{HH}$ = 1.3 Hz, Hc/d, 3H).

ESI: (m/z). Found: 166.1588 $[M]^+$, calculated for $C_{11}H_{20}N$: 166.1590 $[M]^+$.

5.40. 1-(2-Methylprop-1-en-1-yl)-1-(prop-2-en-1-yl) pyrrolidinium tetrafluoroborate

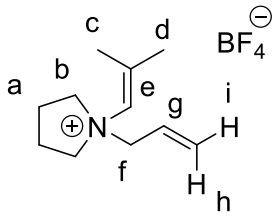

Silver tetrafluoroborate (0.307 g, 1.58 mmol) was added to a solution of 1-(2-methylprop-1-en-1-yl)-1-(prop-2-en-1-yl) pyrrolidinium bromide (0.3887 g, 1.58 mmol) in methanol (4 cm^3) at -20 ˚C and left to react for 24 h. Insoluble AgBr was filtered through a celite pad and washed with ice cold methanol (3 × 2 cm^3). The solvent was removed under reduced pressure (10^{-2} mbar) at 0 °C to yield the desired product (0.3612, 90%).

^{1}H NMR (400 MHz, $CDCl_3$). δ (ppm): 5.94 – 5.82 (m, Hg, 1H), 5.69 (dd, J = 17.0, 0.9 Hz, Hh, 1H), 5.69 (bs, He, 1H), 5.63 (d, J = 10.2 Hz, Hi, 1H), 4.22 (d, J = 7.2 Hz, Hf, 2H), 3.95 – 3.86 (m, Hb, 2H), 3.78 – 3.68 (m, Hb, 2H), 2.40 – 2.29 (m, Ha, 2H), 2.21 – 2.12 (m, Ha, 2H), 2.03 (d, $^4J_{HH}$ = 1.4 Hz, Hc/d, 3H), 1.87 (d, $^4J_{HH}$ = 1.5 Hz, Hc/d, 3H).

^{19}F{^{1}H} NMR (376 MHz $CDCl_3$). δ (ppm): -152.11.

CHN: This substrate undergoes an aza-Claisen rearrangement followed by hydrolysis at room temperature preventing an accurate CHN analysis.

5.41. (3,4,5-Tris(decyloxy)benzyl)triethylammonium tetrafluoroborate

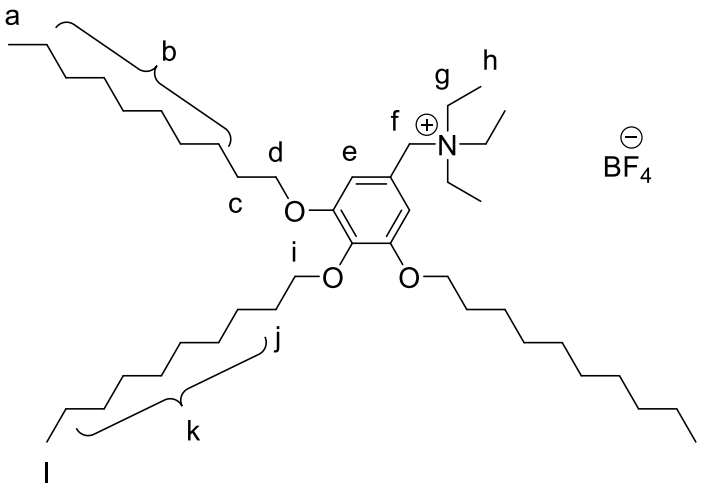

(3,4,5-Tris(decyloxy)benzyl)triethylammonium chloride (8.0408 g, 11.56 mmol) was dissolved in methanol (30 cm^3). A solution of silver tetrafluoroborate (2.250 g, 11.56 mmol) in methanol (20 cm^3) was then added dropwise. The mixture was stirred at room temperature for 2 h. The insoluble silver chloride was filtered through a celite pad, the solids washed with methanol and dichloromethane. The filtrate was collected and the solvent removed under reduced pressure (10^{-3} mbar) to yield the product (8.0442 g, 93%)

^{1}H NMR (400 MHz, $CDCl_3$). δ (ppm): 6.60 (s, He, 2H), 4.27 (s, Hf, 2H) 3.94 (t, J_{HH} = 6.5 Hz, Hd, 4H), 3.93 (t, J_{HH} = 6.1 Hz, Hi, 2H), 3.23 (d, J_{HH} = 6.6 Hz, Hg, 6H), 1.80 – 1.66 (m, Hc,j, 6H), 1.50 – 1.16 (m, Hb,k,h, 51H), 0.86 (t, J = 6.8 Hz, Ha,l, 9H).

^{13}C{^{1}H} NMR (101 MHz, $CDCl_3$). δ (ppm): 153.65, 140.13, 121.55, 110.78, 73.62, 69.52, 61.62, 52.75, 32.04, 32.02, 30.46, 29.85, 29.79, 29.76, 29.71, 29.60, 29.50, 29.47, 26.24, 26.19, 22.80, 22.79, 14.21, 7.93.

ESI. (m/z): Found: 660.6283 $[M]^+$, calculated for $[C_{43}H_{82}NO_3]^+$: 660.6289 $[M]^+$.

CHN. Found: C 68.6; H 11.0%; N 1.9%. Calculated: C 69.05%; H 11.05%; N 1.9%.

5.42. (3,4,5-Tris(dodecyloxy)benzyl)triethylammonium tetrafluoroborate

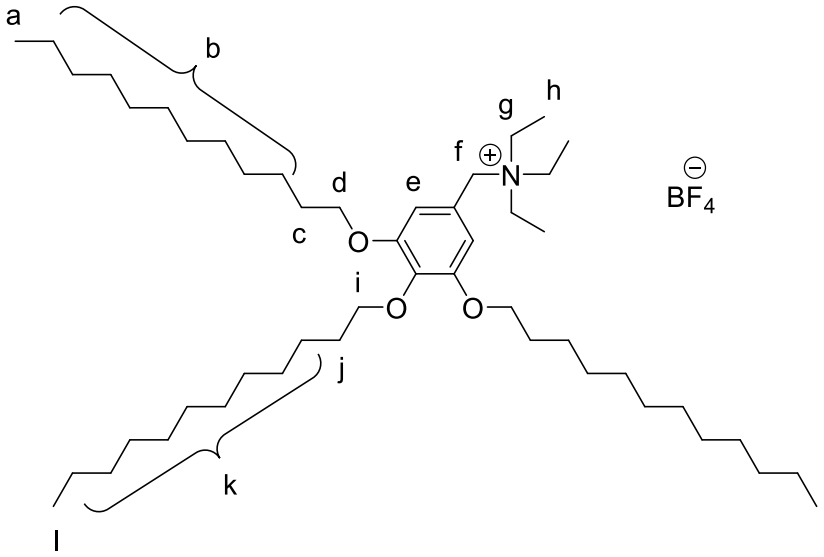

(3,4,5-Tris(dodecyloxy)benzyl)triethylammonium chloride (4.7600 g, 6.10 mmol) was dissolved in methanol (30 cm^3). A solution of silver tetrafluoroborate (1.1869 g, 6.10 mmol) in methanol (20 cm^3) was then added dropwise. The mixture was stirred at room temperature for 2 h. The insoluble silver chloride was filtered through a celite pad, the solids washed with methanol and dichloromethane. The filtrate was collected and the solvent removed under reduced pressure (10^{-3} mbar) to yield the product (4.6278 g, 93%).

^{1}H NMR (400 MHz, $CDCl_3$). δ (ppm): 6.10 (s, He, 2H), 4.29 (s, Hf, 2H) 3.95 (t, J_{HH} = 6.6 Hz, Hd, 2H), 3.94 (t, J_{HH} = 6.2 Hz, Hi, 4H), 3.24 (q, J_{HH} = 6.2 Hz, Hg, 6H), 1.82 – 1.67 (m, Hc,j, 6H), 1.52 – 1.18 (m, Hb,k,h, 63H), 0.87 (t, J = 6.8 Hz, Ha,l, 9H).

$^{13}C\{^1H\}$ NMR (101 MHz, $CDCl_3$). δ (ppm): 153.70, 140.21, 121.52, 110.83, 73.65, 69.57, 61.71, 52.80, 32.07, 32.06, 30.49, 29.90, 29.88, 29.86, 29.83, 29.81, 29.80, 29.75, 29.64, 29.53, 29.51, 26.27, 26.22, 22.82, 14.25, 7.98.

ESI. (m/z): Found: 744.7205 $[M]^+$, calculated for $[C_{49}H_{94}NO_3]^+$: 744.7228 $[M]^+$.

CHN. Found: C 70.8; H 11.5%; N 1.7%. Calculated: C 70.7%; H 11.4%; N 1.7%.

5.43. 4-Dodecyloxyiodobenzene

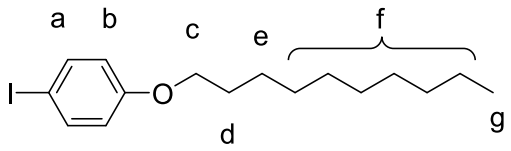

1-Bromododecane (8.23 g, 3.30 mmol), 4-iodophenol (7.26 g, 3.30 mmol) and potassium carbonate (4.56 g, 3.30 mmol) were dissolved in acetone (40 cm^3). The reaction mixture was heated under reflux for 19 h. Water was added to dissolve the potassium bromide and the product extracted with diethyl ether (3 × 10 cm^3). The organic layer was washed with brine (10 cm^3), aqueous sodium hydroxide solution (10%, 10 cm^3) and water (10 cm^3). The organic layer was then dried over anhydrous magnesium sulfate. The product was purified by vacuum distillation (10^{-2} mbar) to yield 4-dodecyloxyiodobenzene (7.46 g, 56%).

^{1}H NMR (400 MHz, $CDCl_3$). δ (ppm): 7.53 (d, $J_{AA'XX'}$ = 8.9 Hz, Ha, 2H), 6.66 (d, $J_{AA'XX'}$ = 8.9 Hz, Hb, 2H), 3.89 (t, J_{HH} = 6.6 Hz, Hc, 2H), 1.81 – 1.71 (m, Hd, 2H), 1.48 – 1.39 (m, He, 2H), 1.39 – 1.21 (m, Hf, 12H), 0.89 (t, J_{HH} = 6.8 Hz, Hg, 3H).

$^{13}C\{^1H\}$ NMR (101 MHz, $CDCl_3$). δ (ppm): 159.10, 138.23, 117.01, 82.51, 68.19, 32.06, 29.80, 29.78, 29.74, 29.71, 29.51, 29.50, 29.28, 26.13, 22.83, 14.28.

5.44. 4-Dodecyloxystilbazole

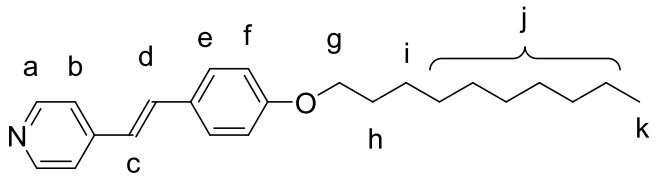

Palladium(II) acetate (0.08 g, 0.36 mol) and triethylamine (10 cm^3) were added to 4-dodecyloxyiodobenzene (3.88 g, 10 mmol) in a Fisher-Porter vessel. To this 4-vinylpyridine (1.89 g, 18 mmol) and acetonitrile (60 cm^3) were added. The vessel was outgassed, placed under an atmosphere of dry nitrogen at constant volume and then heated to 100 ˚C for 96 h with stirring. The solvent was then removed under reduced pressure (10^{-1} mbar) and the resulting solid dissolved in dichloromethane and

then washed with water (4 × 50 cm^3). The organic layer was dried over anhydrous magnesium sulfate and the solvent removed under reduced pressure (10^{-1} mbar). A Soxhlet extraction with petroleum ether (40 – 60 ˚C) was performed. The product was and then crystallised from hot petroleum ether (40 – 60 ˚C) and dried under reduced pressure (10^{-2} mbar) to yield the product (1.47 g, 40%).

^{1}H NMR (400 MHz, $CDCl_3$). δ (ppm): 8.52 (d, $J_{AA'XX'}$ = 5.9 Hz, Ha, 2H), 7.44 (d, $J_{AA'XX'}$ = 8.7 Hz, Hf, 2H), 7.31 (d, $J_{AA'XX'}$ = 6.0 Hz, Hb, 2H), 7.23 (d, J_{AB} = 16.2 Hz, Hd, 1H), 6.89 (d, $J_{AA'XX'}$ = 8.7 Hz, He, 2H), 6.84 (d, J_{AB} = 16.3 Hz, Hc, 1H), 3.96 (t, J_{HH} = 6.6 Hz, Hg, 2H), 1.83 – 1.72 (m, Hh, 2H), 1.51 – 1.38 (m, Hi, 2H), 1.38 – 1.16 (m, Hj, 12H), 0.87 (t, J_{HH} = 6.8 Hz, Hk, 3H).

$^{13}C\{^1H\}$ NMR (101 MHz, $CDCl_3$). δ (ppm): 159.82, 150.06, 145.09, 132.84, 128.67, 128.40, 123.53, 120.64, 114.84, 68.14, 31.94, 29.67, 29.63, 29.42, 29.38, 29.25, 26.05, 22.72, 14.15.

ESI. (m/z): Found: 366.2784 $[M+H]^+$, calculated for $C_{25}H_{36}NO$: 366.2791 $[M+H]^+$.

5.45. *N*-(3,4,5-Tris(alkoxy)benzyl)-4-hexyloxystilbazolium chlorides

In a typical procedure, a solution of 3,4,5-tris(dodecyloxy)benzyl chloride (0.65 g 0.96 mmol) in acetonitrile (5 cm^3) was added to a solution of dodecyloxystilbazole (0.37 g 0.96 mmol) also in acetonitrile (5 cm^3) at room temperature, in the dark. The resulting solution was heated and maintained at 70 °C for 48 h with stirring. Once cooled, the solvent was removed under reduced pressure (10^{-2} mbar) and the resulting yellow solid was washed with petroleum ether (40 – 60 °C) to yield a yellow powder (0.90 g, 90%).

5.45.1. *N*-(3,4,5-Tris(decyloxy)benzyl)-4-hexyloxystilbazolium chloride

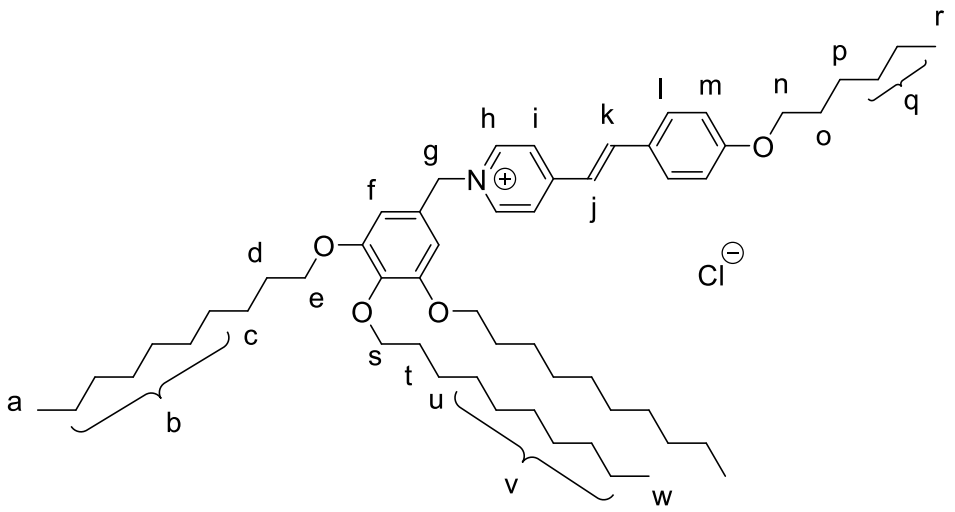

^{1}H NMR (400 MHz, $CDCl_3$). δ (ppm): 9.22 (d, $J_{AA'XX'}$ = 6.3 Hz, Hh, 2H), 7.83 (d, $J_{AA'XX'}$ = 6.5 Hz, Hi, 2H), 7.58 (d, J_{AB} = 15.8 Hz, Hj, 1H), 7.55 (d, $J_{AA'XX'}$ = 8.7 Hz, Hl, 2H), 6.93 (d, $J_{AA'XX'}$ = 8.8 Hz, Hm, 2H), 6.93 (d, J_{AB} = 16.1 Hz, Hk, 1H), 6.78 (s, Hf, 2H), 5.93 (s, Hg, 2H), 4.00 (t, J_{HH} = 6.6 Hz, Hs, 2H), 3.96 (t, J_{HH} = 6.4 Hz, He, 4H), 3.92 (t, J_{HH} = 6.6 Hz, Hn, 2H), 1.84 – 1.68 (m, Hd,o,t, 8H), 1.52 – 1.38 (m, Hc,p,u, 8H), 1.37 – 1.19 (m, Hb,q,v, 40H), 0.95 – 0.82 (m, Ha,r,w, 12H).

^{13}C{^{1}H} NMR (101 MHz, $CDCl_3$). δ ppm: 161.89, 154.00, 153.82, 144.08, 142.05, 139.13, 130.46, 128.28, 127.18, 123.49, 119.66, 115.27, 108.02, 73.60, 69.58, 68.45, 63.64, 32.08, 31.72, 30.50, 29.91, 29.82, 29.77, 29.65, 29.54, 29.26, 26.31, 26.26, 25.83, 22.85, 22.75, 14.28, 14.19.

ESI. (*m/z*): Found: 840.6846 $[M]^+$, calculated for $C_{56}H_{90}NO_4$: 840.6864 $[M]^+$.

5.45.2. *N*-(3,4,5-Tris(dodecyloxy)benzyl-4-hexyloxystilbazolium chloride

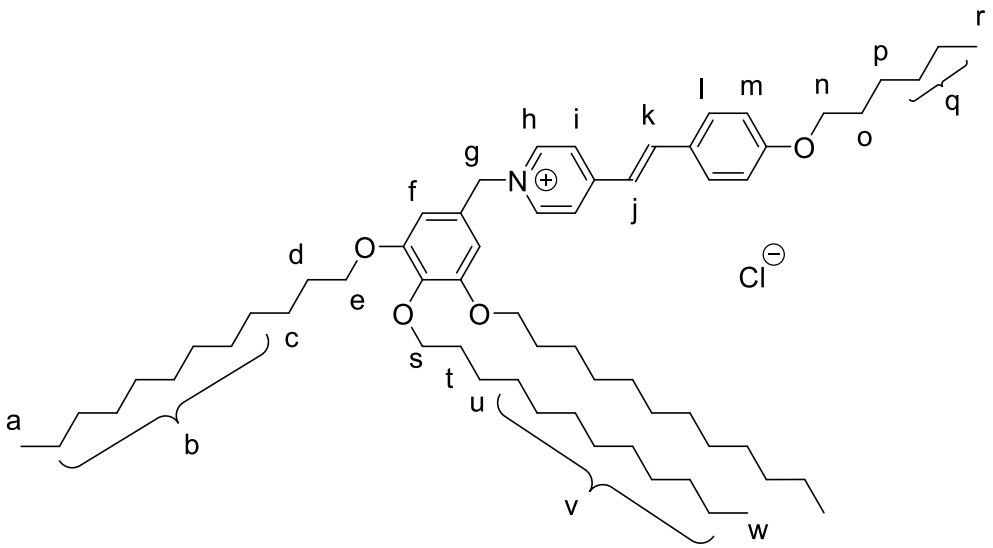

^{1}H NMR (400 MHz, $CDCl_3$). δ (ppm): 9.20 (d, $J_{AA'XX'}$ = 6.4 Hz, Hh, 2H), 7.82 (d, $J_{AA'XX'}$ = 6.3 Hz, Hi, 2H), 7.61 – 7.50 (m, Hj,l, 3H), 6.92 (d, $J_{AA'XX'}$ = 8.8 Hz, Hm, 2H), 6.92 (d, J_{AB} = 16.1 Hz, Hk, 1H), 6.77 (s, Hf, 2H), 5.92 (s, Hg, 2H), 4.04 – 3.89 (m, He,n,s, 8H), 1.85 – 1.65 (m, Hd,o,t, 8H), 1.51 – 1.19 (m, Hc,p,u, 8H), 1.37 – 1.19 (m, Hb,q,v, 52H), 0.92 – 0.82 (m, Ha,r,w, 12H).

^{13}C{^{1}H} NMR (101 MHz, $CDCl_3$). δ (ppm): 161.81, 153.92, 153.73, 144.01, 141.97, 139.06, 130.37, 128.17, 127.09, 123.42, 119.57, 115.19, 107.96, 77.43, 77.11, 76.79, 73.51, 69.51, 68.37, 63.61, 32.01, 31.63, 30.41, 29.84, 29.81, 29.75, 29.70, 29.58, 29.46, 29.17, 26.23, 26.18, 25.74, 22.77, 22.66, 14.19, 14.10.

ESI. (*m/z*): Found: 924.7795 $[M]^+$, calculated for $C_{62}H_{102}NO_4$: 924.7803 $[M]^+$.

CHN. Found: C 71.8%; H 9.7%; N 1.6%. Calculated C 72.5%; H 9.8%; N 1.5%.

5.45.3. *N*-(3,4,5-Tris(tetradecyloxy)benzyl)-4-hexyloxystilbazolium chloride

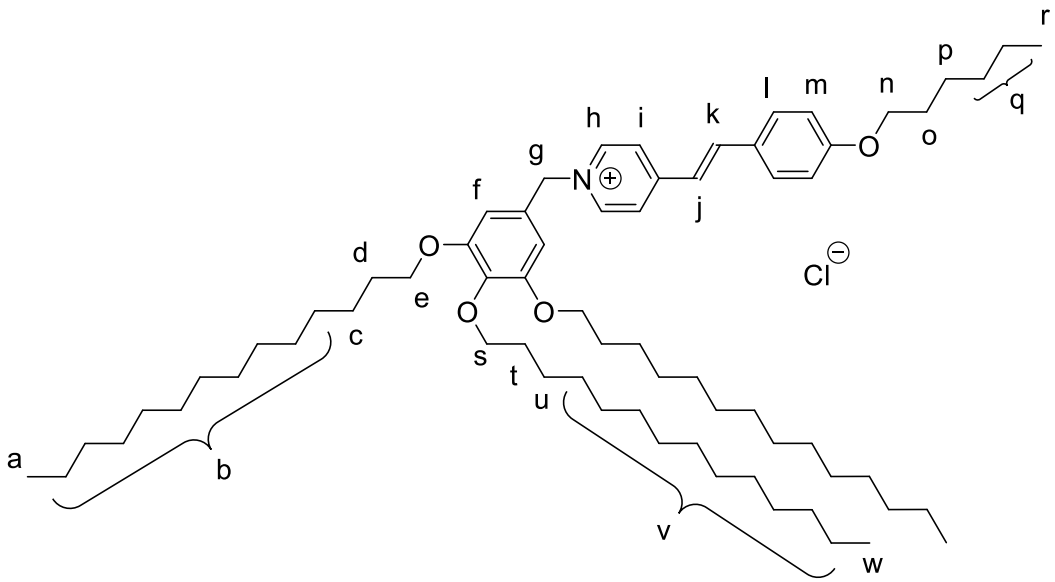

^{1}H NMR (400 MHz, $CDCl_3$). δ (ppm): 9.21 (d, $J_{AA'XX'}$ = 6.8 Hz, Hh, 2H), 7.83 (d, $J_{AA'XX'}$ = 6.8 Hz, Hi, 2H), 7.57 (d, J_{AB} = 16.0 Hz, Hj, 1H), 7.55 (d, $J_{AA'XX'}$ = 8.8 Hz, Hl, 2H), 6.93 (d, J_{AB} = 16.1 Hz, Hk, 1H), 6.93 (d, $J_{AA'XX'}$ = 8.9 Hz, Hm, 2H), 6.75 (s, Hf, 2H), 5.92 (s, Hg, 2H), 4.03 – 3.89 (m, He,n,s, 8H), 1.84 – 1.66 (m, Hd,o,t, 8H), 1.56 – 1.39 (m, Hc,p,u, 8H), 1.37-1.18 (m, Hb,q,v, 64H), 0.92 – 0.82 (m, Ha,r,w, 12H).

^{13}C{^{1}H} NMR (101 MHz, $CHCl_3$). δ (ppm): 161.89, 154.00, 144.08, 142.05, 139.13, 130.45, 128.26, 127.18, 123.49, 119.65, 115.27, 108.03, 77.52, 77.20, 76.88, 73.59, 69.58, 68.45, 63.66, 32.10, 31.72, 30.51, 29.91, 29.85, 29.80, 29.67, 29.55, 29.26, 26.32, 26.27, 25.83, 22.86, 22.75, 14.29, 14.19.

ESI. (*m/z*): Found: 1008.8725 $[M]^+$, calculated for $C_{68}H_{114}NO_4$: 1008.8742 $[M]^+$.

5.45.4. *N*-(3,4,5-Tris(decyloxy)benzyl)-4-dodecyloxystilbazolium chloride

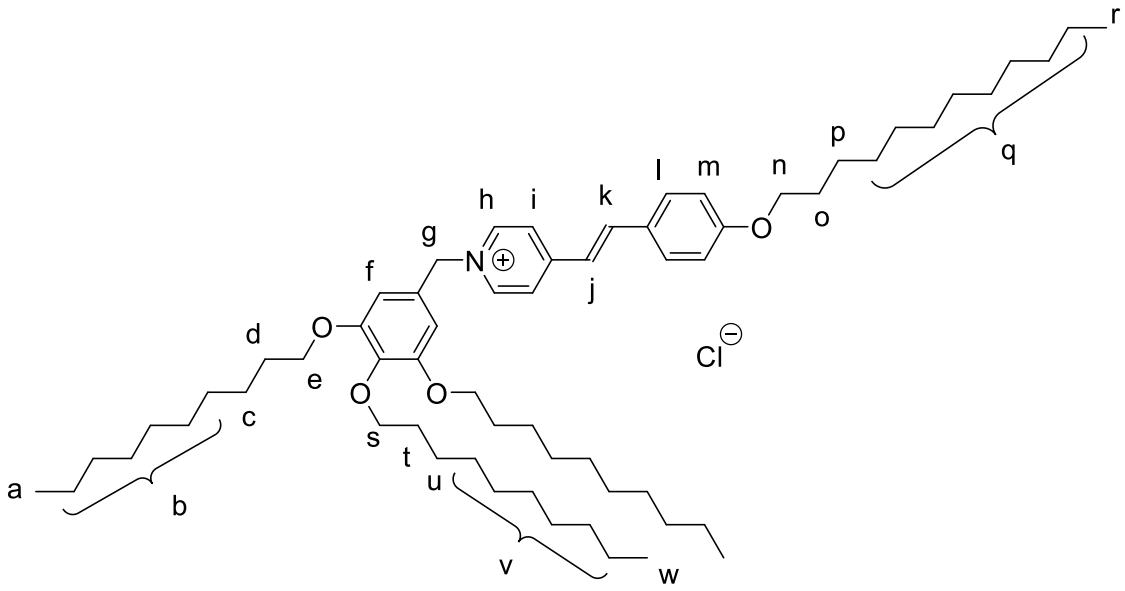

^{1}H NMR (400 MHz, $CDCl_3$). δ (ppm): 9.22 (d, $J_{AA'XX'}$ = 6.3 Hz, Hh, 2H), 7.83 (d, $J_{AA'XX'}$ = 6.4 Hz, Hi, 2H), 7.58 (d, J_{AB} = 15.8 Hz, Hj, 1H), 7.55 (d, $J_{AA'XX'}$ = 8.7 Hz, Hl, 2H), 6.94 (d, $J_{AA'XX'}$ = 8.6 Hz, Hm, 2H), 6.94 (d, J_{AB} = 15.8 Hz, Hk, 1H), 6.78 (s, Hf, 2H), 5.93 (s, Hg, 2H), 4.01 – 3.88 (m, He,n,s, 8H), 1.84 – 1.68 (m, Hd,o,t, 8H), 1.48 – 1.39 (m, Hc,p,u, 8H), 1.38 – 1.20 (m, Hb,q,v, 50H), 0.94 – 0.82 (m, Ha,r,w, 12H).

^{13}C{^{1}H} NMR (126 MHz, $CDCl_3$). δ (ppm): 161.45, 153.65, 153.45, 143.79, 141.58, 138.68, 130.21, 128.41, 127.09, 123.35, 119.54, 114.91, 107.68, 73.29, 69.27, 68.14, 63.25, 31.82, 30.25, 29.65, 29.59, 29.57, 29.52, 29.48, 29.42, 29.32, 29.29, 29.27, 29.24, 29.07, 26.08, 26.00, 25.91, 22.57, 13.99.

ESI. (*m/z*): Found: 924.7883, Calculated ($C_{62}H_{102}NO_4^+$) 924.7803.

5.45.5. *N*-(3,4,5-Tris(dodecyloxy)benzyl)-4-dodecyloxystilbazolium chloride

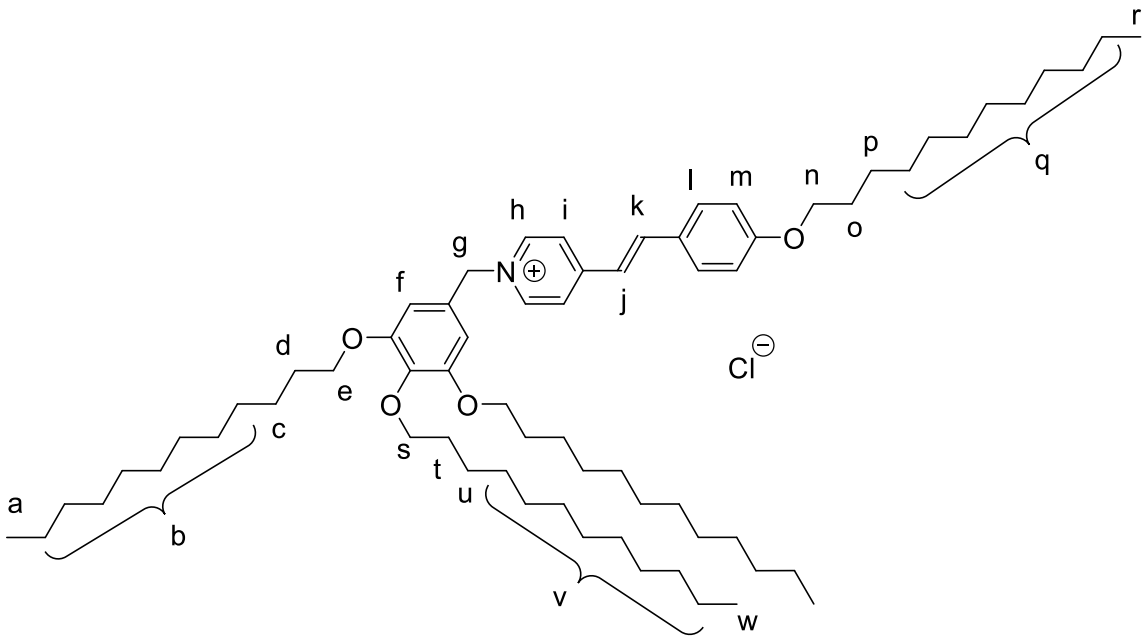

^{1}H NMR (400 MHz, $CDCl_3$). δ (ppm): 9.21 (d, $J_{AA'XX'}$ = 5.4 Hz, Hh, 2H), 7.79 (d, $J_{AA'XX'}$ = 5.7 Hz, Hi, 2H), 7.59 – 7.43 (m, Hj,l, 3H), 6.93 – 6.79 (m, Hm,k,f, 5H), 5.92 (s, Hg, 2H), 4.04 – 3.78 (m, He,n,s, 8H), 1.81 – 1.58 (m, Hd,o,t, 8H), 1.46 – 1.34 (m, Hc,p,u, 8H), 1.33 – 1.10 (m, Hb,q,v, 62H), 0.88 – 0.8 (m, Ha,r,w, 12H).

^{13}C{^{1}H} NMR (126 MHz, $CDCl_3$). δ (ppm): 161.64, 153.77, 153.58, 143.89, 141.78, 138.89, 130.25, 128.19, 127.03, 123.32, 119.49, 115.04, 107.82, 73.37, 69.37, 68.24, 63.41, 31.88, 31.86, 30.30, 29.71, 29.69, 29.63, 29.58, 29.56, 29.53, 29.46, 29.33, 29.30, 29.10, 26.12, 26.06, 25.95, 22.64, 14.06.

ESI. (*m/z*): Found: 1008.8772, Calculated ($C_{68}H_{114}NO_4^+$) 1008.8742.

5.45.6. *N*-(3,4,5-Tris(tetradecyloxy)benzyl)-4-dodecyloxystilbazolium chloride

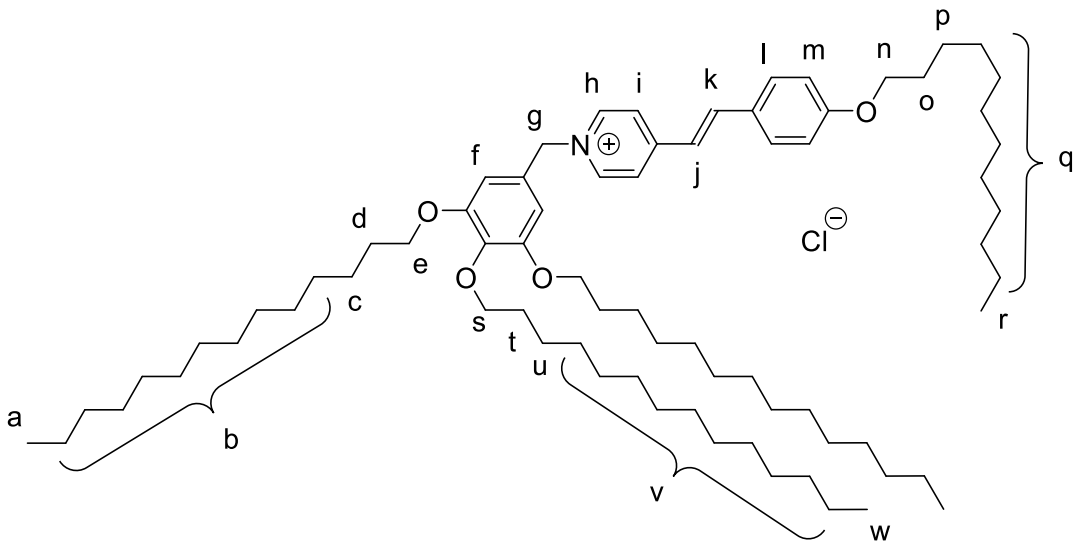

^{1}H NMR (500 MHz, $CDCl_3$). δ (ppm): 9.22 (d, $J_{AA'XX'}$ = 6.4 Hz, Hh, 2H), 7.82 (d, $J_{AA'XX'}$ = 6.5 Hz, Hi, 2H), 7.66 – 7.51 (m, Hj,l, 3H), 6.96 – 6.89 (m, Hm,k, 3H), 6.79 (s, Hf, 2H), 5.94 (s, Hg, 2H), 4.06 – 3.86 (m, He,n,s, 8H), 1.87 – 1.59 (m, Hd,o,t, 8H), 1.51 – 1.39 (m, Hc,p,u, 8H), 1.38 – 1.19 (m, Hb,q,v, 76H), 0.96 – 0.79 (m, Ha,r,w, 12H).

^{13}C{^{1}H} NMR (126 MHz, $CDCl_3$). δ (ppm): 161.70, 153.81, 153.63, 153.16, 143.88, 132.28, 130.25, 127.00, 123.31, 119.47, 115.07, 107.86, 107.01, 73.39, 69.41, 69.09, 68.26, 31.90, 30.31, 29.71, 29.65, 29.60, 29.48, 29.34, 29.11, 26.13, 26.07, 25.96, 22.65, 14.07.

ESI. (*m/z*): Found: 1092.9707, Calculated ($C_{74}H_{1126}NO_4^+$) 1083.9681.

5.46. *N*-(3,4,5-Tris(alkyloxy)benzyl)-4-alkyloxystilbazolium tetrafluoroborates

In a typical procedure, sodium tetrafluoroborate (0.0153 g, 0.139 mmol) was added to a solution of N-(3,4,5-tris(dodecyloxy)benzyl)-4-dodecyloxystilbazolium chloride (0.1455 g, 0.139 mmol) in dichloromethane (5 cm^3) and stirred at room temperature for 2 h in the dark. The yellow solids were filtered and washed with dichloromethane then dried under reduced pressure (10^{-3} mbar) for 1 day in the dark, to yield pure N-(3,4,5-tris(dodecyloxy)benzyl)-4-dodecyloxystilbazolium tetrafluoroborate (0.1455 g, 95%).

5.46.1. *N*-(3,4,5-Tris(decyloxy)benzyl)-4-hexyloxystilbazolium tetrafluoroborate

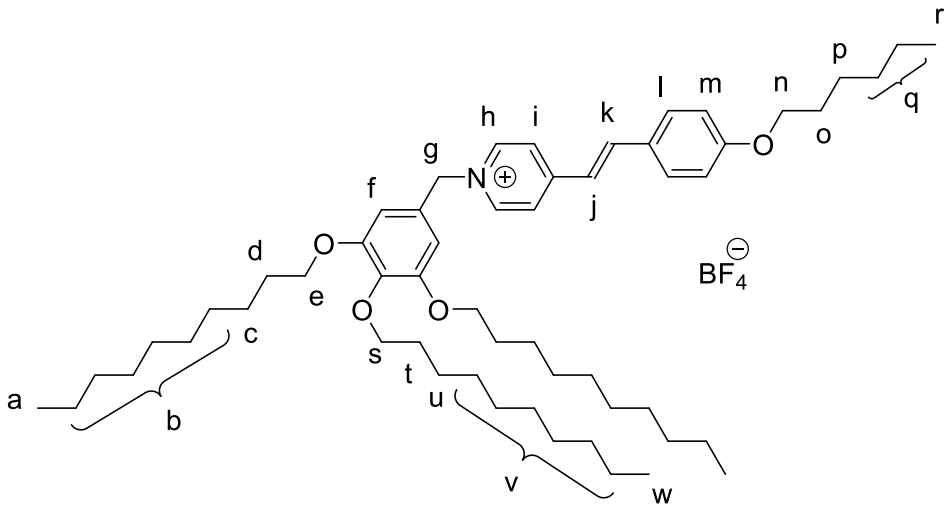

^{1}H NMR (500 MHz, $CDCl_3$). δ (ppm): 8.66 (d, $J_{AA'XX'}$ = 6.5 Hz, Hh, 2H), 7.78 (d, $J_{AA'XX'}$ = 6.6 Hz, Hi, 2H), 7.57 – 7.48 (m, Hj,l, 3H), 6.89 (d, $J_{AA'XX'}$ = 8.8 Hz, Hm, 2H), 6.87 (d, J_{AB} = 15.9 Hz, Hk, 1H), 6.67 (s, Hf, 2H), 5.52 (s, Hg, 2H), 3.99 – 3.85 (m, He,n,s, 8H), 1.83 – 1.64 (m, Hd,o,t, 8H), 1.49 – 1.38 (m, Hc,p,u, 8H), 1.34 – 1.19 (m, Hb,q,v, 40H), 0.93 – 0.84 (m, Ha,r,w, 12H).

^{13}C{^{1}H} NMR (126 MHz, $CDCl_3$). δ (ppm): 161.70, 153.89, 143.32, 141.91, 138.95, 130.39, 127.83, 127.08, 123.43, 119.45, 115.08, 107.57, 73.44, 69.29, 68.28, 63.80, 31.93, 31.59, 30.37, 29.76, 29.70, 29.68, 29.63, 29.52, 29.41, 29.39, 29.13, 26.17, 26.11, 25.68, 22.69, 22.59, 14.11, 14.02.

$^{19}F\{^{1}H\}$ NMR (471 MHz, $CDCl_3$). δ (ppm): -151.58.

ESI. (*m/z*): Found: 840.6883, Calculated ($C_{56}H_{90}NO_4^+$) 840.6864.

CHN. Found: C 71.8%; H 9.7%; N 1.6%. Calculated C 72.5%; H 9.8%; N 1.5%.

5.46.2. *N*-(3,4,5-Tris(dodecyloxy)benzyl)-4-hexyloxystilbazolium tetrafluoroborate

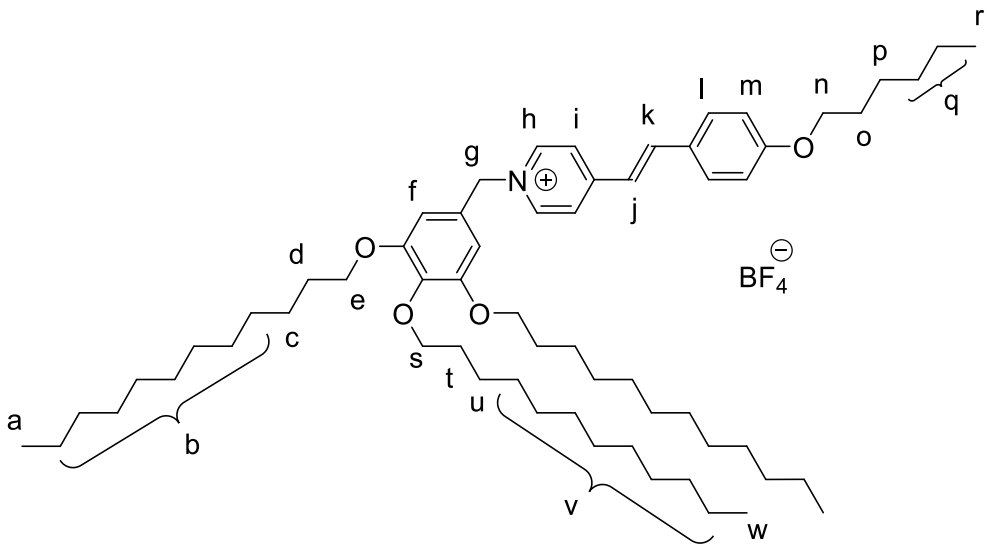

^{1}H NMR (500 MHz, $CDCl_3$). δ (ppm): 8.56 (d, $J_{AA'XX'}$ = 6.5 Hz, Hh, 2H), 7.80 (d, $J_{AA'XX'}$ = 6.3 Hz, Hi, 2H), 7.61 – 7.50 (m, Hj,l, 3H), 6.96 – 6.87 (m, Hk,m, 3H), 6.64 (s, Hf, 2H), 5.49 (s, Hg, 2H), 4.05 – 3.87 (m, He,n,s, 8H), 1.86 – 1.66 (m, Hd,o,t, 8H), 1.51 – 1.40 (m, Hc,p,u, 8H), 1.38 – 1.12 (m, Hb,q,v, 52H), 0.93 – 0.81 (m, Ha,r,w, 12H).

$^{13}C\{^{1}H\}$ NMR (126 MHz, $CDCl_3$). δ (ppm): 161.84, 154.09, 154.04, 143.25, 142.08, 139.11, 130.51, 127.72, 127.14, 123.51, 119.49, 115.21, 107.62, 73.56, 69.37, 68.39, 64.05, 32.05, 31.70, 30.48, 29.88, 29.81, 29.65, 29.51, 29.24, 26.28, 26.23, 25.79, 22.81, 22.71, 14.23, 14.14.

$^{19}F\{^{1}H\}$ NMR (471 MHz, $CDCl_3$). δ (ppm): -151.68.

ESI. (*m/z*): Found: 924.7830, Calculated ($C_{62}H_{102}NO_4^+$) 924.7803.

CHN. Found: C 73.4%; H 9.85%; N 1.4%. Calculated: C 73.6%; H 10.2%; N 1.4%.

5.46.3. *N*-(3,4,5-Tris(tetradecyloxy)benzyl)-4-hexyloxystilbazolium tetrafluoroborate

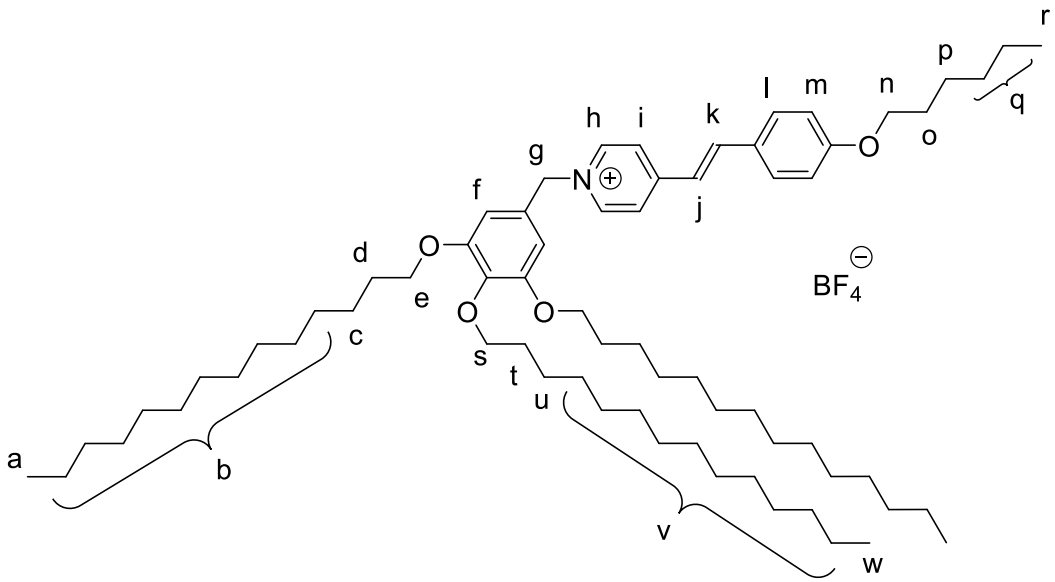

^{1}H NMR (500 MHz, $CDCl_3$). δ (ppm): 8.83 (d, $J_{AA'XX'}$ = 6.6 Hz, Hh, 2H), 7.78 (d, $J_{AA'XX'}$ = 6.6 Hz, Hi, 2H), 7.54 (d, J_{AB} = 16.1 Hz, Hj, 1H) 7.50 (d, $J_{AA'XX'}$ = 8.7 Hz, Hl, 2H), 6.89 (d, $J_{AA'XX'}$ = 8.7 Hz, Hm, 2H) 6.87 (d, J_{AB} = 16.4 Hz, Hk, 1H), 6.70 (s, Hf, 2H), 5.65 (s, Hg, 2H), 4.03 – 3.85 (m, He,n,s, 8H), 1.84 – 1.62 (m, Hd,o,t, 8H), 1.50 – 1.37 (m, Hc,p,u, 8H), 1.35 – 1.17 (m, Hb,q,v, 64H), 0.94 – 0.81 (m, Ha,r,w, 12H).

^{13}C{^{1}H} NMR (126 MHz, $CDCl_3$). δ (ppm): 161.79, 153.97, 153.91, 143.61, 142.01, 139.04, 130.47, 128.04, 127.17, 123.51, 119.57, 115.18, 107.76, 73.53, 69.43, 68.37, 63.79, 32.04, 31.68, 30.47, 29.86, 29.80, 29.64, 29.49, 29.23, 26.28, 26.23, 25.78, 22.80, 22.69, 14.21, 14.12.

^{19}F{^{1}H} NMR (471 MHz, $CDCl_3$). δ (ppm): -151.77.

ESI. (*m/z*): Found: 1008.8763, Calculated ($C_{68}H_{114}NO_4^+$) 1008.8742.

CHN. Found: C 74.2%; H 10.2%; N 1.2%. Calculated: C 74.5%; H 10.5%; N 1.3%.

5.46.4. *N*-(3,4,5-Tris(decyloxy)benzyl)-4-dodecyloxystilbazolium tetrafluoroborate

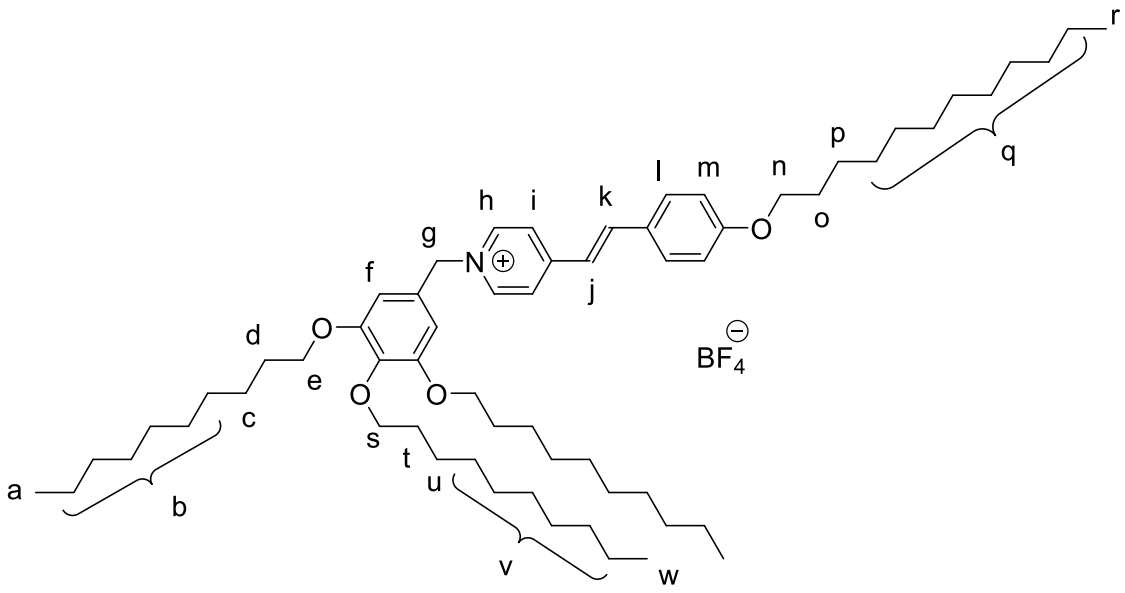

^{1}H NMR (500 MHz, $CDCl_3$). δ (ppm): 8.56 (d, $J_{AA'XX'}$ = 6.3 Hz, Hh, 2H), 7.74 (d, $J_{AA'XX'}$ = 6.3 Hz, Hi, 2H), 7.54 – 7.45 (m, Hj,l, 3H), 6.88 – 6.81 (m, Hk,m, 3H), 6.86 (s, Hf, 2H), 5.44 (s, Hg, 2H), 3.99 – 3.87 (m, He,n,s, 8H), 1.81 – 1.66 (m, Hd,o,t, 8H), 1.48 – 1.38 (m, Hc,p,u, 8H), 1.34 – 1.19 (m, Hb,q,v, 52H), 0.90 – 0.83 (m, Ha,r,w, 12H).

^{13}C{^{1}H} NMR (126 MHz, $CHCl_3$). δ (ppm): 161.91, 154.15, 154.09, 143.27, 142.20, 139.20, 130.52, 127.58, 127.11, 123.53, 119.46, 115.25, 107.68, 73.58, 69.42, 68.43, 64.15, 32.06, 30.49, 29.89, 29.80, 29.75, 29.63, 29.52, 29.29, 26.27, 26.14, 22.83, 14.24.

^{19}F{^{1}H} NMR (471 MHz, $CDCl_3$). δ (ppm): -151.99.

ESI. (*m/z*): Found: 924.7809, Calculated ($C_{62}H_{102}NO_4^+$) 924.7803.

CHN. Found: C 73.6%; H 10.7%; N 1.1%. Calculated: C 73.6%; H 10.2%; N 1.4%.

5.46.5. *N*-(3,4,5-Tris(dodecyloxy)benzyl)-4-dodecyloxystilbazolium tetrafluoroborate

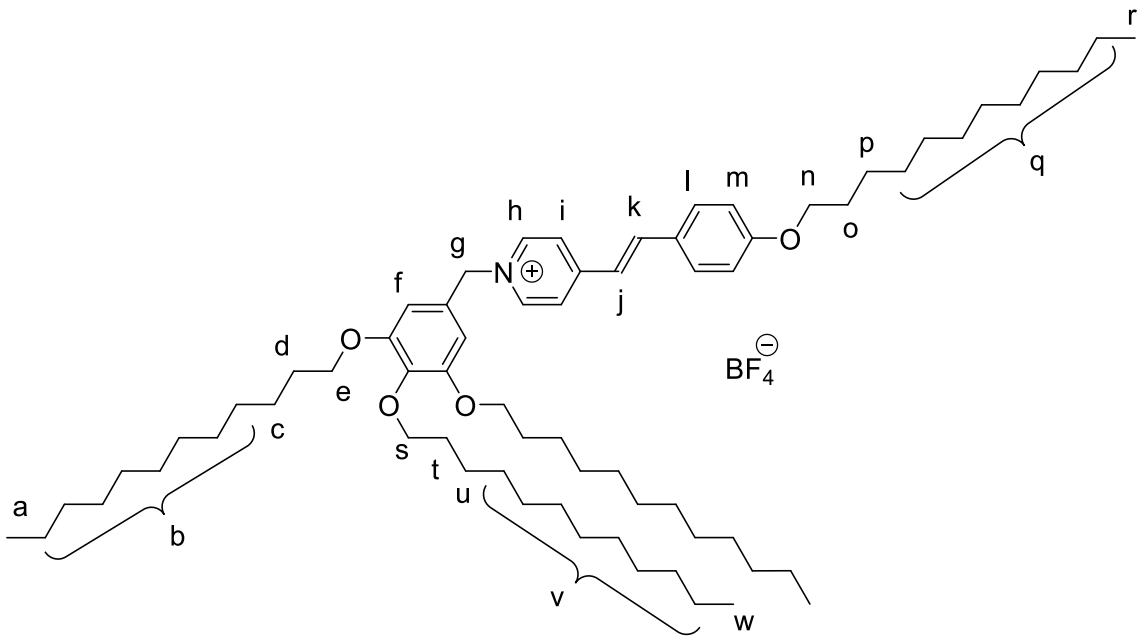

^{1}H NMR (500 MHz, $CDCl_3$). δ (ppm): 8.51 (d, $J_{AA'XX'}$ = 6.2 Hz, Hh, 2H), 7.73 (d, $J_{AA'XX'}$ = 6.4 Hz, Hi, 2H), 7.52 – 7.44 (m, Hj,l, 3H), 6.87 (d, $J_{AA'XX'}$ = 8.7 Hz, Hm, 2H), 6.84 (d, J_{AB} = 16.2 Hz, Hk, 1H), 6.66 (s, Hf, 2H), 5.41 (s, Hg, 2H), 3.99 – 3.87 (m, He,n,s, 8H), 1.82 – 1.66 (m, Hd,o,t, 8H), 1.50 – 1.39 (m, Hc,p,u, 8H), 1.34 – 1.19 (m, Hb,q,v, 64H), 0.92 – 0.83 (m, Ha,r,w, 12H).

^{13}C{^{1}H} NMR (126 MHz, $CDCl_3$). δ (ppm): 161.87, 154.09, 154.06, 143.30, 142.11, 139.14, 130.50, 127.70, 127.13, 123.52, 119.49, 115.22, 107.66, 73.56, 69.40, 68.42, 64.06, 32.06, 30.49, 29.89, 29.81, 29.77, 29.72, 29.65, 29.52, 29.48, 29.30, 26.28, 26.24, 26.14, 22.82, 14.24.

^{19}F{^{1}H} NMR (471 MHz, $CDCl_3$) δ (ppm): -150.47.

ESI. (*m/z*): Found: 1008.8767, Calculated ($C_{68}H_{114}NO_4^+$) 1008.8742.

CHN. Found: C 74.1%; H 10.4%; N 1.25%. Calculated C 74.5%; H 10.5%; N 1.3%.

5.46.6. *N*-(3,4,5-Tris(tetradecyloxy)benzyl)-4-dodecyloxystilbazolium tetrafluoroborate

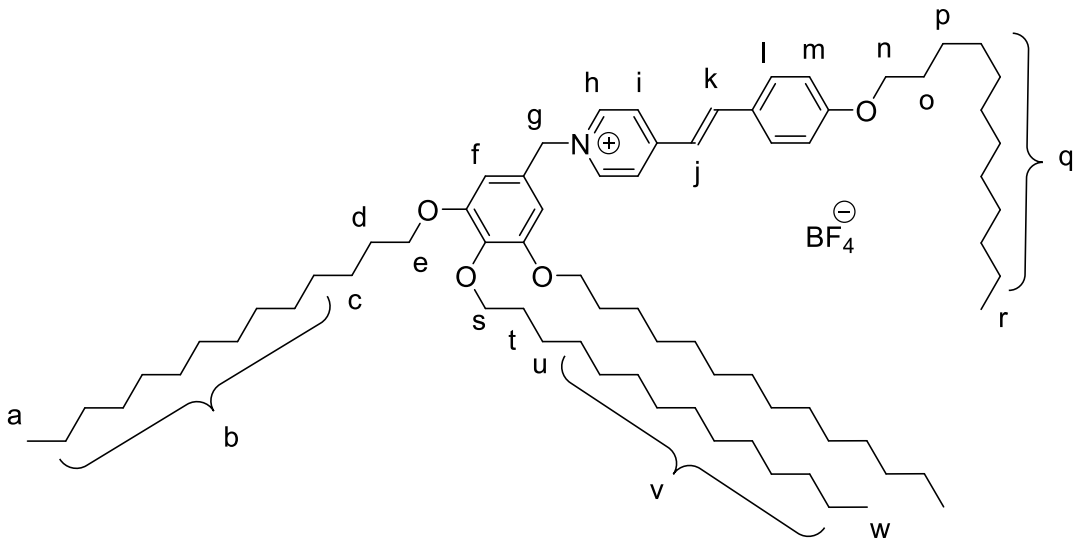

^{1}H NMR (500 MHz, $CDCl_3$). δ (ppm): 8.56 (d, $J_{AA'XX'}$ = 6.6 Hz, Hh, 2H), 7.75 (d, $J_{AA'XX'}$ = 6.7 Hz, Hi, 2H), 7.75 – 7.46 (m, Hj,l, 3H), 6.88 (d, $J_{AA'XX'}$ = 8.8 Hz, Hm, 2H), 6.84 (d, J_{AB} = 16.2 Hz, Hk, 1H), 6.66 (s, Hf, 2H), 5.44 (s, Hg, 2H), 3.99 – 3.88 (m, He,n,s, 8H), 1.83 – 1.66 (m, Hd,o,t, 8H), 1.51 – 1.39 (m, Hc,p,u, 8H), 1.39 – 1.16 (m, Hb,q,v, 76H), 0.92 – 0.83 (m, Ha,r,w, 12H).

^{13}C{^{1}H} NMR (126 MHz, $CDCl_3$). δ (ppm): 161.95, 154.22, 154.11, 143.31, 142.26, 139.23, 130.51, 127.50, 127.06, 123.53, 119.43, 115.27, 107.71, 73.58, 69.44, 68.44, 63.62, 41.32, 32.07, 32.07, 29.89, 29.89, 29.83, 29.83, 29.65, 29.65, 29.53, 29.53, 29.28, 26.28, 26.28, 22.83, 22.83, 14.26, 14.26.

^{19}F{^{1}H} NMR (471 MHz, $CDCl_3$). δ (ppm): -150.87 (BF_4).

ESI. (*m/z*): Found: 1092.9671, Calculated ($C_{74}H_{126}NO_4^+$) 1092.9681.

CHN. Found: C 75.2; H 10.95%; N 1.6%. Calculated: C 75.2%; H 10.8%; N 1.2%.

5.47. Small-angle X-ray scattering measurements

X-ray scattering was performed on a Bruker D8 Discover equipped with a Eurotherm temperature controller and a custom-built bored graphite rod furnace. The radiation was generated was copper Kα (λ = 0.154056 nm) from a 1 μS microfocus source. Diffraction patterns were detected on a 2048 × 2048 pixel Bruker VANTEC 500 area detector. Samples were filled into 1 mm Ø capillary tubes. The data was processed using the DIFFRAC.EVA software.

5.48. Small-angle neutron scattering measurements

SANS was carried out on both the D22 instrument at the ILL (Grenoble, France) and the Sans2d small-angle diffractometer at the ISIS Pulsed Neutron Source (STFC Rutherford Appleton Laboratory, Didcot, U.K.).[96, 158] On D22, two instrument configurations were used λ = 4.6 Å, D = 1.25 m Coll = 5.6 m and D = 8m Coll = 8 m with a detector offset of 400 mm to cover a q-range from 9 × 10^{-3} to 0.9 $Å^{-1}$. The scattering vector q is defined as:

$$q = \frac{4\pi \sin\frac{\theta}{2}}{\lambda}$$

Where θ is the scattered angle and λ is the incident neutron wavelength. The raw scattering data were corrected for the electronic background and empty cell and were normalized on the absolute scale using the attenuated direct beam to calculate the incident flux using the ILL Lamp software (https://www.ill.eu/instruments-support/computing-for-science/cs-software/all-software/lamp/). On Sans2d, a simultaneous Q-range of 0.0045 – 0.7 $Å^{-1}$ was achieved utilizing an incident wavelength range of 1.75 – 16.5 Å and employing an instrument set up of L1 = L2 = 4 m, with the 1 m^2 detector offset vertically 60 mm and sideways 100 mm. The beam diameter was 8 mm. Each raw scattering data set was corrected for the detector efficiencies, sample transmission and background scattering and converted to scattering cross-section data ($\partial\Sigma/\partial\Omega$ *vs* Q) using the instrument-specific software.[96] These data were placed on an absolute scale (cm^{-1}) using the scattering from a standard sample (a solid blend of hydrogenous and perdeuterated polystyrene) in accordance with established procedures.[159] The data was fitted using SasView software.[96]

Abbreviations

[M]	Molecular ion
$\Delta G^{\neq}$	Gibbs energy of activation
$\Delta H^{\neq}$	Enthalpy of activation
$\Delta S^{\neq}$	Entropy of activation
AA'BB'	Magnetically inequivalent coupling of parahydrogen disubstituted benzenes
ACR	Aza-Claisen rearrangement
BMIM	1-Butyl-3-methylimidazolium
bmim	1-Butyl-3-methylimidazolium
C_{12}HIM	1-Dodecyl-3H-imidazolium
C_4C_1IM	1-Butyl-3-methylimidazolium
C_8C_1IM	1-Octyl-3-methylimidazolium
CHN	Carbon hydrogen nitrogen
Col_h	Columnar hexagonal
Col_r	Columnar rectangular
Col_s	Columnar square
COP	Charge ordeing peak
CP	Contact peak
Cub_{bi}	Bicontinuous cubic phase
d	Doublet
DCM	Dichloromethane
DMSO	Dimethyl sulfoxide
DSC	Differential scanning calorimeter
ESI	Electrospray ionisation
Et	Ethyl
FT	Fourier transform
HRMAS	High resolution magic angle spinning
IL	Ionic liquid
IR	Infrared
k	Rate constant
LC	Liquid crystal
LCIL	Liquid-crystalline ionic liquid
m	Multiplet
m/z	Mass/charge
MAS	Magic angle spinning
MD	Molecular dynamic
N	Nematic
N_{col}	Columnar nematic
N_D	Discotic nemaic
NMR	Nuclear magnetic resonance
PL	Peak Lorentz
PNPP	Polar/non-polar peak

POM	Polarising optical microscopy
ppm	Parts per million
q	Quarter
RTIL	Room temperature ionic liquid
s	Singlet
SANS	Small angle neutron scattering
SAXS	Small angle X-Ray scattering
SE	Standard error
SILCP	Supported Ionic liquid crystal phase
SmA	Smectic A
SmB	Smectic B
SmC	Smectic C
SmF	Smectic F
SmI	Smectic I
SmT	Smectic T
t	Triplet
T	Temperature
TF_2N	Bis(trifuoromethylsulfonyl)amide
TS	Teubner-Strey

References

1. S. Gabriel and J. Weiner, *Ber. Dtsch. Chem. Ges.*, 1888, **21**, 2669-2669.
2. M. Freemantle, *An Introduction to Ionic Liquids*, RSC Publishing, 2009.
3. F. H. Hurley and T. P. WIer, *Journal of The Electrochemical Society*, 1951, **98**, 207-212.
4. T. L. Greaves and C. J. Drummond, *Chem. Rev.*, 2008, **108**, 206-237.
5. K. Goossens, K. Lava, C. W. Bielawski and K. Binnemans, *Chem. Rev.*, 2016, **116**, 4643-4807.
6. J. S. Wilkes and M. J. Zaworotko, *J. Chem. Soc., Chem. Commun.*, 1992, 965.
7. J. P. Hallett and T. Welton, *Chem. Rev.*, 2011, **111**, 3508-3576.
8. J. S. Wilkes, *Green Chem.*, 2002, **4**, 73-80.
9. J. W. Goodby, I. M. Saez and S. J. Cowling, in *Supramolecular Chemistry: From Molecules to Nanomaterials*, eds. M. Chierotti, R. Gobetto, P. Gale and J. Steed, John Wiley & Sons, Ltd. Chichester, UK, 2012.
10. D. W. Bruce, *Chem. Rec.*, 2004, **4**, 10-22.
11. P. J. Collings, G. W. Gray, J. W. Goodby and M. Hird, *Introduction to Liquid Crystals*, Routledge, 1997.
12. I. Dierking, in *Textures of Liquid Crystals*, Wiley-VCH Verlag GmbH & Co. KGaA, 2004.
13. G. W. Gray, *Thermotropic Liquid Crystals*, Wiley & Sons, 1987.
14. M. Hird and P. Collings, *Introduction to Liquid Crystals: Chemistry and Physics*, CRC Press, 1997.
15. M. Mitov, *Adv. Mater.*, 2012, **24**, 6260-6276.
16. T. Kato, T. Yasuda, Y. Kamikawa and M. Yoshio, *Chem. Commun.*, 2009, **0**, 729-739.
17. X. Zeng, G. Ungar and M. Imperor-Clerc, *Nat. Mater.*, 2005, **4**, 562-567.
18. C. Tschierske, *J. Mater. Chem.*, 1998, **8**, 1485-1508.
19. C. Tschierske, *J. Mater. Chem.*, 2001, **11**, 2647-2671.
20. C. Tschierske, *Isr. J. Chem.*, 2012, **52**, 935-959.
21. J. W. Goodby, E. J. Davis, R. J. Mandle and S. J. Cowling, *Isr. J. Chem.*, 2012, **52**, 863-880.

22. C. Tschierske, *Chem. Soc. Rev.*, 2007, **36**, 1930-1970.
23. P. Fuchs, C. Tschierske, K. Raith, K. Das and S. Diele, *Angew. Chem. Int. Ed.*, 2002, **41**, 628-631.
24. G. A. Knight and B. D. Shaw, *J. Chem. Soc.*, 1938, **0**, 682-683.
25. K. Binnemans, *Chem. Rev.*, 2005, **105**, 4148-4204.
26. K. V. Axenov and S. Laschat, *Materials*, 2011, **4**, 206-259.
27. L. Douce, J. M. Suisse, D. Guillon and A. Taubert, *Liq. Cryst.*, 2011, **38**, 1653-1661.
28. S. Chen and S. H. Eichhorn, *Isr. J. Chem.*, 2012, **52**, 830-843.
29. C. Tschierske, *Prog. Polym. Sci.*, 1996, **21**, 775-852.
30. A. E. Bradley, C. Hardacre, J. D. Holbrey, S. Johnston, S. E. J. McMath and M. Nieuwenhuyzen, *Chem. Mater.*, 2002, **14**, 629-635.
31. Y. Ji, R. Shi, Y. Wang and G. Saielli, *J. Phys. Chem. B*, 2013, **117**, 1104.
32. P. W. Atkins and J. De Paula, *Physical chemistry*, Oxford University Press, Oxford, 2006.
33. D. W. Bruce, *Acc. Chem. Res.*, 2000, **33**, 831-840.
34. P. H. J. Kouwer and T. M. Swager, *J. Am. Chem. Soc.*, 2007, **129**, 14042-14052.
35. D. W. Bruce, D. A. Dunmur, P. M. Maitlis, P. Styring, M. A. Esteruelas, L. A. Oro, M. B. Ros, J. L. Serrano and E. Sola, *Chem. Mater.*, 1989, **1**, 479-481.
36. D. W. Bruce, D. A. Dunmur, S. A. Hudson, E. Lalinde, P. M. Maitlis, M. P. McDonald, R. Orr, P. Styring, A. S. Cherodian, R. M. Richardson, J. L. Feijoo and G. Ungar, *Mol. Cryst. Liq. Cryst.*, 1991, **206**, 79-92.
37. A. T. Atto, A. H. Al-Dujaili and E. A. Al-Ani, *Acta Polymerica*, 1999, **50**, 313-316.
38. F. Turpin, D. Guillon and R. Deschenaux, *Mol. Cryst. Liq. Cryst.*, 2001, **362**, 171-175.
39. K. Goossens, K. Lava, P. Nockemann, K. Van Hecke, L. Van Meervelt, P. Pattison, K. Binnemans and T. Cardinaels, *Langmuir*, 2009, **25**, 5881-5897.
40. S. Yin, W. Li, J. Wang and L. Wu, *J. Phys. Chem. B*, 2008, **112**, 3983-3988.
41. R. G. Santos-Martell, A. Ceniceros-Olguin, L. Larios-Lopez, R. J. Rodriguez-Gonzalez, D. Navarro-Rodriguez, B. Donnio and D. Guillon, *Liq. Cryst.*, 2009, **36**, 787-797.
42. E. Alami, H. Levy, R. Zana, P. Weber and A. Skoulios, *Liq. Cryst.*, 1993, **13**, 201-212.

43. K. Goossens, K. Lava, P. Nockemann, K. Van Hecke, L. Van Meervelt, K. Driesen, C. Gorller-Walrand, K. Binnemans and T. Cardinaels, *Chem. Eur. J.*, 2009, **15**, 656-674.
44. F. Tittarelli, P. Masson and A. Skoulios, *Liq. Cryst.*, 1997, **22**, 721-726.
45. W. H. Bragg and W. L. Bragg, *Proc. R. Soc. London, A*, 1913, **88**, 428-438.
46. H. Niedermeyer, J. P. Hallett, I. J. Villar-Garcia, P. A. Hunt and T. Welton, *Chem. Soc. Rev.*, 2012, **41**, 7780-7802.
47. G. Chatel, J. F. B. Pereira, V. Debbeti, H. Wang and R. D. Rogers, *Green Chem.*, 2014, **16**, 2051-2083.
48. E. I. Izgorodina and D. R. MacFarlane, *J. Phys. Chem. B*, 2011, **115**, 14659-14667.
49. A. G. Avent, P. A. Chaloner, M. P. Day, K. R. Seddon and T. Welton, *J. Chem. Soc., Dalton Trans.*, 1994, **0**, 3405-3413.
50. P. S. Schulz, N. Müller, A. Bösmann and P. Wasserscheid, *Angew. Chem.*, 2007, **119**, 1315-1317.
51. R. Katoh, M. Hara and S. Tsuzuki, *J. Phys. Chem. B*, 2008, **112**, 15426-15430.
52. E. W. J. Castner, C. J. Margulis, M. Maroncelli and J. F. Wishart, *Annu. Rev. Phys. Chem.*, 2011, **62**, 85-105.
53. H. Weingartner, *Angew. Chem. Int. Ed.*, 2008, **47**, 654-670.
54. D. F. Evans, S. H. Chen, G. W. Schriver and E. M. Arnett, *J. Am. Chem. Soc.*, 1981, **103**, 481-482.
55. J. Dupont, *J. Braz. Chem. Soc.*, 2004, **15**, 341-350.
56. C. Hardacre, J. D. Holbrey, M. Nieuwenhuyzen and T. G. A. Youngs, *Acc. Chem. Res.*, 2007, **40**, 1146-1155.
57. S. Chen, Z. S, X. Lui, J. Wang, J. Wang, K. Dong, J. Sun and B. Xu, *Phys. Chem. Chem. Phys.*, 2014, **16**, 5893-6301.
58. F. C. Gozzo, L. S. Santos, R. Augusti, C. S. Consorti, J. Dupont and M. N. Eberlin, *Chem. Eur. J.*, 2004, **10**, 6187-6193.
59. R. Bini, O. Bortolini, C. Chiappe, D. Pieraccini and T. Siciliano, *J. Phys. Chem. B*, 2007, **111**, 598-604.
60. P. J. Dyson, I. Khalaila, S. Luettgen, J. S. McIndoe and D. Zhao, *Chem. Commun.*, 2004, **0**, 2204-2205.
61. S. Dorbritz, W. Ruth and U. Kragl, *Adv. Synth. Catal.*, 2005, **347**, 1273-1279.
62. W. Xu, E. I. Cooper and C. A. Angell, *J. Phys. Chem. B*, 2003, **107**, 6170-1678.

63. S. S. J. Ho, M. E. Coddens and C. F. Poole, *Org. Mass Spectrom.*, 1985, **20**, 377-397.
64. C. F. Poole, B. R. Kersten, S. S. J. Ho, M. E. Coddens and K. G. Furton, *J. Chromatogr., A*, 1986, **352-425**, 407.
65. U. Schroder, J. D. Wadhawan, R. G. Compton, F. Marken, P. A. Z. Suarez, C. S. Consorti, R. F. de Souza and J. Dupont, *New J. Chem.*, 2000, **24**, 1009-1015.
66. C. J. Margulis, *Mol. Phys.*, 2004, **102**, 829-838.
67. A. Triolo, O. Russina, B. Fazio, R. Triolo and E. Di Cola, *Chem. Phys. Lett.*, 2008, **457**, 362-365.
68. S. M. Urahata and M. C. C. Ribeiro, *J. Chem. Phys.*, 2004, **120**, 1855-1863.
69. Y. Wang and G. A. Voth, *J. Am. Chem. Soc.*, 2005, **127**, 12192-12193.
70. Y. Wang and G. A. Voth, *J. Phys. Chem. B*, 2006, **110**, 18601-18608.
71. J. N. Canongia Lopes, M. F. Costa Gomes and A. A. H. Padua, *J. Phys. Chem. B*, 2006, **110**, 3330-3335.
72. C. Hardacre, J. D. Holbrey, C. L. Mullan, T. G. A. Youngs and D. T. Bowron, *J. Chem. Phys.*, 2010, **133**, 074510.
73. D. V. Wagle, H. Zhao and G. A. Baker, *Acc. Chem. Res.*, 2014, **47**, 2299-2308.
74. E. L. Smith, A. P. Abbott and K. S. Ryder, *Chem. Rev.*, 2014, **114**, 11060-11082.
75. H. Tokuda, K. Hayamizu, K. Ishii, M. A. B. H. Susan and M. Watanabe, *J. Phys. Chem. B*, 2005, **109**, 6103-6110.
76. H. Hamaguchi and R. Ozawa, *Adv. Chem. Phys.*, 2005, **131**, 85-104.
77. T. L. Greaves and C. J. Drummond, *Chem. Soc. Rev.*, 2013, **42**, 1096-1120.
78. E. C. Wijaya, T. L. Greaves and C. Drummond, *Faraday Discuss.*, 2013, **167**, 191-215.
79. R. Hayes, G. G. Warr and R. Atkin, *Chem. Rev.*, 2015, **115**, 6357-6426.
80. O. Russina, A. Triolo, L. Gontrani and R. Caminiti, *J. Phys. Chem. Lett.*, 2012, **3**, 27-33.
81. K. Shimizu, C. E. S. Bernardes and J. N. Canongia Lopes, *J. Phys. Chem. B*, 2014, **118**, 567-576.
82. A. Triolo, O. Russina, H.-J. Bleif and E. Di Cola, *J. Phys. Chem. B*, 2007, **111**, 4641-4644.
83. O. Russina, A. Triolo, L. Gontrani, R. Caminiti, D. Xiao, L. G. Hines, R. A. Bartsch, E. L. Quitevis, N. Plechkova and K. R. Seddon, *J. Phys.-Condes. Matter*, 2009, **21**, 424121.
84. F. Nemoto, M. Kofu and O. Yamamuro, *J. Phys. Chem. B*, 2015, **119**, 5028-5034.

85. A. Triolo, A. Mandanici, O. Russina, V. Rodriguez-Mora, M. Cutroni, C. Hardacre, M. Nieuwenhuyzen, H. J. Bleif, L. Keller and M. A. Ramos, *J. Phys. Chem. B*, 2006, **110**, 21357-21364.
86. O. Russina, F. Lo Celso, N. V. Plechkova and A. Triolo, *J. Phys. Chem. Lett.*, 2017, **8**, 1197-1204.
87. H. V. R. Annapureddy, H. K. Kashyap, P. M. De Biase and C. J. Margulis, *J. Phys. Chem. B*, 2010, **114**, 16838-16846.
88. R. P. Matthews, I. J. Villar-Garcia, C. C. Weber, J. Griffith, F. Cameron, J. P. Hallett, P. A. Hunt and T. Welton, *Phys. Chem. Chem. Phys.*, 2016, **18**, 8608-8624.
89. N. J. Brooks, F. Castiglione, C. M. Doherty, A. Dolan, A. J. Hill, P. A. Hunt, R. P. Matthews, M. Mauri, A. Mele, R. Simonutti, I. J. Villar-Garcia, C. C. Weber and T. Welton, *Chem. Sci.*, 2017, **8**, 6359-6374.
90. A. Klee, S. Prevost and M. Gradzielski, *ChemPhysChem*, 2014, **15**, 4032-4041.
91. D. W. Bruce, C. P. Cabry, J. N. C. Lopes, M. L. Costen, L. D ̧ Andrea, I. Grillo, B. C. Marshall, K. G. McKendrick, T. K. Minton, S. M. Purcell, S. Rogers, J. M. Slattery, K. Shimizu, E. Smoll and M. A. Tesa-Serrate, *J. Phys. Chem. B*, 2017, **121**, 6002-6020.
92. *Structure from Diffraction Methods*, John Wiley & Sons, Ltd, 2014.
93. R. J. Roe, *Methods of X-Ray and Neutron Scattering in Polymer Science*, Oxford University Press, 2000.
94. *Neutron Scattering in Novel Materials*, World Scientific Publishing Co. Pte. Ltd, 2000.
95. J. Chadwick, *Nature*, 1932, **129**, 312-312.
96. www.sasview.org.
97. M. Teubner and R. Strey, *J. Chem. Phys.*, 1987, **87**, 3195-3200.
98. K. V. Schubert, R. Strey, S. R. Kline and E. W. Kaler, *J. Chem. Phys.*, 1994, **101**, 5343-5355.
99. A. A. Freitas, K. Shimizu and J. N. Canongia Lopes, *J. Chem. Eng. Data*, 2014, **59**, 3120-3129.
100. K. Shimizu and J. N. Canongia Lopes, *Fluid Phase Equilib.*, 2016, **418**, 181-191.
101. K. Shimizu, M. Tariq, A. A. Freitas, A. A. H. Pádua and J. N. C. Lopes, *J. Braz. Chem. Soc.*, 2016, **27**, 349-362.
102. K. Shimizu and J. N. Canongia Lopes, *J. Mol. Liq.*, 2015, **210**, 257-263.

103. S. Prevost, T. Lopian, M. Pleines, O. Diat and T. Zemb, *J. Appl. Crystallogr.*, 2016, **49**, 2063-2072.
104. C. P. Cabry, L. D'Andrea, K. Shimizu, I. Grillo, P. Li, S. E. Rogers, D. W. Bruce, J. N. Canongia Lopes and J. M. Slattery, *Faraday Discussions*, 2017, DOI: 10.1039/C7FD00167C.
105. M. A. A. Rocha, C. M. S. S. Neves, M. G. Freire, O. Russina, A. Triolo, J. A. P. Coutinho and L. M. N. B. F. Santos, *J. Phys. Chem. B*, 2013, **117**, 10889-10897.
106. R. G. Weiss, *Tetrahedron*, 1988, **44**, 3413-3475.
107. W. E. Bacon and G. H. Brown, *Molecular Crystals*, 1969, **6**, 155-159.
108. W. E. Bacon and G. H. Brown, *Mol. Cryst. Liq. Cryst.*, 1971, **12**, 229-236.
109. M. J. S. Dewar and B. D. Nahlovsky, *J. Am. Chem. Soc.*, 1974, **96**, 460-465.
110. F. D. Saeva, P. E. Sharpe and G. R. Olin, *J. Am. Chem. Soc.*, 1975, **97**, 204-205.
111. C. K. Lee, H. W. Huang and I. J. B. Lin, *Chem. Commun.*, 2000, **0**, 1911-1912.
112. J. Yang, F. F. Li, J. A. Zhang, J. Li and W. X. Wang, *Helv. Chim. Acta*, 2010, **93**, 1653-1660.
113. C. P. Mehnert, R. A. Cook, N. C. Dispenziere and M. Afeworki, *J. Am. Chem. Soc.*, 2002, **124**, 12932-12933.
114. C. P. Mehnert, *Chem. Eur. J.*, 2005, **11**, 50-56.
115. X. Wang, M. Sobota, F. T. U. Kohler, B. Morain, B. U. Melcher, M. Laurin, P. Wasserscheid, J. Libuda and K. Meyer, *J. Mater. Chem.*, 2012, **22**, 1893-1898.
116. S. Tanaka, K. Kida, H. Fujimoto, T. Makino and Y. Miyake, *Langmuir*, 2011, **27**, 7991-7995.
117. A. Safavi, M. Tohidi, F. A. Mahyari and H. Shahbaazi, *J. Mater. Chem.*, 2012, **22**, 3825-3831.
118. A. Aggarwal, N. L. Lancaster, A. R. Sethi and T. Welton, *Green Chem.*, 2002, **4**, 517-520.
119. R. Bini, C. Chiappe, V. L. Mestre, C. S. Pomelli and T. Welton, *Org. Biomol. Chem.*, 2008, **6**, 2522-2529.
120. R. Bini, C. Chiappe, V. L. Mestre, C. S. Pomelli and T. Welton, *Theor. Chem. Acc.*, 2009, **123**, 347-352.
121. A. Vidiš, C. A. Ohlin, G. Laurenczy, E. Küsters, G. Sedelmeier and P. J. Dyson, *Adv. Synth. Catal.*, 2005, **347**, 266-274.
122. T. D. Do and A. R. Schmitzer, *RSC Adv.*, 2015, **5**, 635-639.
123. D. W. Bruce, Y. Gao, J. N. Canongia Lopes, K. Shimizu and J. M. Slattery, *Chem. Eur. J.*, 2016, **22**, 16113-16123.

124. Y. Gao, J. M. Slattery and D. W. Bruce, *Unpublished work*.
125. G. Singh and A. Kumar, *Indian J. Chem. Sect A-Inorg. Bio-Inorg. Phys. Theor. Anal. Chem.*, 2008, **47**, 495-503.
126. D. Shen, X. Li, Q. Kang, H. Zhang and Y. Qi, *Analytica Chimica Acta*, 2006, **566**, 19-28.
127. S. T. Keaveney and J. B. Harper, *RSC Adv.*, 2013, **3**, 15698-15704.
128. M. Yau Hon, T. Keaveney Sinead, J. Butler Bradley, E. L. Tanner Eden, S. Guerry Max, R. D. George Stephen, H. Dunn Michelle, K. Croft Anna and B. Harper Jason, *Pure Appl. Chem.*, 2013, **85**, 1979-1990.
129. S. T. Keaveney, K. S. Schaffarczyk McHale, R. S. Haines and J. B. Harper, *Org. Biomol. Chem.*, 2014, **12**, 7092-7099.
130. B. J. Butler, D. S. Thomas, J. M. Hook and J. B. Harper, *Magn. Reson. Chem.*, 2014, **54**, 423-428.
131. A. Rencurosi, L. Lay, G. Russo, D. Prosperi, L. Poletti and E. Caneva, *Green Chem.*, 2007, **9**, 216-218.
132. M. Yoshio, T. Mukai, H. Ohno and T. Kato, *J. Am. Chem. Soc.*, 2004, **126**, 994-995.
133. E. Amigues, C. Hardacre, G. Keane, M. Migaud and M. O'Neill, *Chem. Commun.*, 2006, 72-74.
134. D. S. Silvester, L. Aldous, M. C. Lagunas, C. Hardacre and R. G. Compton, *J. Phys. Chem. B*, 2006, **110**, 22035-22042.
135. W. J. Leigh, *Can. J. Chem.*, 1985, **63**, 2736-2741.
136. A. Zicmanis, S. Katkevica and P. Mekss, *Catal. Commun.*, 2009, **10**, 614-619.
137. J. Wang, R. Qin, H. Fu, J. Chen, J. Feng, H. Chen and X. Li, *Tetrahedron: Asymmetry*, 2007, **18**, 847-851.
138. Z. Baan, Z. Finta, G. Keglevich and I. Hermecz, *Green Chem.*, 2009, **11**, 1937-1940.
139. P. Wasserscheid, C. M. Gordon, C. Hilgers, M. J. Muldoon and I. R. Dunkin, *Chem. Commun.*, 2001, 1186-1187.
140. P. Wasserscheid, C. Hilgers and W. Keim, *J. Mol. Catal. A: Chem.*, 2004, **214**, 83-90.
141. C. Tschierske, *Prog. Polym. Sci.*, 1996, **21**.
142. K. Borisch, S. Diele, P. Goring, H. Muller and C. Tschierske, *Liq. Cryst.*, 1997, **22**, 427-443.

143. M. Yoshio, T. Kagata, K. Hoshino, T. Mukai, H. Ohno and T. Kato, *J. Am. Chem. Soc.*, 2006, **128**, 5570-5577.
144. M. Yoshio, T. Ichikawa, H. Shimura, T. Kagata, A. Hamasaki, T. Mukai, H. Ohno and T. Kato, *B. Chem. Soc. Jpn.*, 2007, **80**, 1836-1841.
145. T. Ichikawa, M. Yoshio, A. Hamasaki, T. Mukai, H. Ohno and T. Kato, *J. Am. Chem. Soc.*, 2007, **129**, 10662-10663.
146. T. Ichikawa, M. Yoshio, A. Hamasaki, S. Taguchi, F. Liu, X. B. Zeng, G. Ungar, H. Ohno and T. Kato, *J. Am. Chem. Soc.*, 2012, **134**, 2634-2643.
147. A. Pană, F. L. Badea, M. Iliș, T. Staicu, M. Micutz, I. Pasuk and V. Cîrcu, *J. Mol. Struct.*, 2015, **1083**, 245-251.
148. T. Ichikawa, M. Yoshio, A. Hamasaki, J. Kagimoto, H. Ohno and T. Kato, *J. Am. Chem. Soc.*, 2011, **133**, 2163-2169.
149. D. Ster, U. Baumeister, J. L. Chao, C. Tschierske and G. Israel, *J. Mater. Chem.*, 2007, **17**, 3393-3400.
150. C. B. Ziegler and R. F. Heck, *J. Org. Chem*, 1978, **43**, 2941-2946.
151. A. Getsis and A. V. Mudring, *Cryst. Res. Technol.*, 2008, **43**, 1187-1196.
152. K. Goossens, P. Nockemann, K. Driesen, B. Goderis, C. Gorller-Walrand, K. Van Hecke, L. Van Meervelt, E. Pouzet, K. Binnemans and T. Cardinaels, *Chem. Mater.*, 2008, **20**, 157-168.
153. J. D. Holbrey and K. R. Seddon, *J. Chem. Soc., Dalton Trans.*, 1999, **13**, 2133-2139.
154. I. Lopez-Martin, E. Burello, P. N. Davey, K. R. Seddon and G. Rothenberg, *ChemPhysChem*, 2007, **8**, 690.
155. Y. Gao, J. M. Slattery and D. W. Bruce, *New J. Chem.*, 2011, **35**, 2910-2918.
156. A. Pană, M. Iliș, T. Staicu, I. Pasuk and V. Cîrcu, *Liq. Cryst.*, 2016, **43**, 381-392.
157. R. Giernoth and D. Bankmann, *Eur. J. Org. Chem.*, 2008, 2881-2886.
158. R. K. Heenan, S. E. Rogers, D. Turner, A. E. Terry, J. Treadgold and S. M. King, *Neutron News*, 2011, **22**, 19-21.
159. G. D. Wignall and F. S. Bates, *J. Appl. Crystallogr.*, 1987, **20**, 28.